



The  
University  
Of  
Sheffield.

**Vibrational Spectroscopic Applications of Fourier Transform  
Infrared and Raman Spectroscopy in Biochemistry and  
Microbiology**

**Muneera Shamikh Alrasheedi**

*A thesis submitted in partial fulfilment of the requirements for the degree of  
Doctor of Philosophy*

The University of Sheffield  
Faculty of Science  
Department of Chemistry

September 2021



## **Acknowledgements**

Firstly, I would like to thank my God for giving me the strength to complete this project. I would also like to extend my deepest gratitude to my supervisor Dr. Michael Hippler for all his valuable patience, support and advice, without him it would not have been possible for me to finish this work as he has helped me a lot in many ways during this project.

Also, I would like to thank Ph.D. student George D Metcalfe for his practical help and guidance provided during this work, in particular in the TMAO project for working with me in this part. I would also like to say thank you to the rest of the Hippler group. I am very grateful for Prof. Jeff Green to read and comment on my TMAO chapter. I would like to thank the Ministry of Education of Saudi Arabia for funding my studentship. I am very grateful to the University of Sheffield Chemistry Department for facilitating my research.

Finally, I would like to extend my thanks to my parents, my husband and my children for their continued support throughout my PhD and helping me to get the strong motivation to finish this work. Thanks to my siblings who always provide encouragement, they are truly the best family anyone could have, for that I am privileged.

## Abstract

Vibrational spectroscopy has a number of applications due to its high sensitivity and selectivity, including the distinction of isotopomers, making it a powerful analytical technique. Unlike typical chromatographic methods that require sampling, vibrational spectroscopic methods give *in situ* data acquisition in a closed system, with high time resolution. These advantages make vibrational spectroscopy suitable for monitoring rapidly developing biological processes. A number of applications of both infrared and Raman spectroscopies are presented in this thesis, including the monitoring of metabolites produced and consumed by microbiological cultures and volatiles released during fruit ripening.

A home-built 2.0 m pathlength multiple-pass absorption White cell was constructed, characterised and employed for long-path Fourier Transform Infrared (FTIR) Spectroscopy. CO<sub>2</sub>, acetaldehyde and ethanol production were monitored by FTIR spectroscopy during both *Escherichia coli* growth and banana ripening. Other volatiles, such as ethyl acetate and the ripening hormone ethylene, were also monitored during fruit ripening. Cavity Enhanced Raman Spectroscopy (CERS) was used to monitor the consumption of IR inactive O<sub>2</sub> by bacterial cultures and bananas transitioning from aerobic respiration to fermentation. H<sub>2</sub> production was also monitored using CERS for anaerobic cultures of *E. coli*.

Alongside FTIR and CERS, TMAO reduction by *E. coli* cultures was monitored using *in situ* optical density measurements and liquid phase Raman spectroscopy to monitor TMAO, glucose, acetate, formate and monobasic and dibasic phosphate. Phosphate anion concentration could be used to calculate the pH of the growth medium using a modified Henderson Hasselbalch equation. Deuterated formate (formate-d) could be distinguished from unlabelled formate allowing the monitoring of exogenous formate metabolism and the link to H<sub>2</sub> production in the presence of TMAO.

FTIR and CERS are proven to be cost-effective, highly specific analytical methods in biochemistry and bioscience, complementing and in some cases superseding existing conventional techniques. They also offer new possibilities for mechanistic insights in biochemistry and display a significant promise for measuring isotopically labelled bioassays.

## Abbreviations

ADP	Adenosine Diphosphate
ATP	Adenosine Triphosphate
CCD	Charge-Coupled Device
CERS	Cavity Enhanced Raman Spectroscopy
CRDS	Cavity Ring Down Spectroscopy
CW	Continuous Wave
DM	Dichroic mirror
DMSO	Dimethyl Sulfoxide
<i>E. coli</i>	<i>Escherichia coli</i>
EPR	Electron Paramagnetic Resonance Spectroscopy
FIA	Faraday isolator assembly
FTIR	Fourier Transform Infrared
FWHM	Full Width at Half Maximum
Hz	Hertz
K	Kelvin
kHz	Kilohertz
LB	Lysogeny Broth
LD	Laser Diode
LOD	Limit of Detection
mbar	Millibar
MIR	Mid-infrared
mV	Millivolt

mW	MilliWatt
NAD	Nicotinamide adenine dinucleotide
NAD <sup>+</sup>	Nicotinamide adenine dinucleotide (oxidised)
NADH	Nicotinamide adenine dinucleotide (reduced)
NIR	Near-infrared
NMR	Nuclear Magnetic Resonance Spectroscopy
OD	Optical Density
<i>p</i>	Pressure
PA	photoacoustic
PD	Photodiode
ppb	Part-per-billion
ppm	Part-per-million
TMA	Trimethylamine
TMAO	Trimethylamine Oxide
$\tilde{\nu}$	wavenumber
V	Volt
W	Watt
$\lambda$	wavelength

# Table of Contents

Acknowledgements.....	3
Abstract.....	4
Abbreviations.....	5
Table of Contents.....	7
Chapter 1 – General Introduction .....	12
1.1 Gas Analysis by Spectroscopic Techniques.....	12
1.1.1 Fundamentals of the Theory of Vibrational Spectroscopy .....	12
1.1.2 Limitations of the Harmonic Oscillator Approximation .....	15
1.1.3 Selection Rules for Vibrational Transitions.....	17
1.1.4 Rotational Fine Structure .....	19
1.2 Vibrational Spectroscopy Techniques for Gas Analysis .....	20
1.2.1 Fourier-Transform Infrared (FTIR) Spectroscopy .....	20
1.2.2 Multipass Cells.....	22
1.2.3 Approach of Cavity Ring-Down Spectroscopy (CRDS) .....	26
1.2.4 Cavity Enhanced Absorption Spectroscopy (CEAS) and Related Approaches .....	30
1.2.5 Raman Spectroscopy.....	31
1.3 <i>Escherichia coli</i> : A Model Bacterium.....	35
1.3.1 The metabolic modes of <i>Escherichia coli</i> .....	35

1.4 Aims and Thesis Structure.....	42
Chapter 2 – Long Path Multiple Pass White Cell Construction and Characterisation for FTIR Spectroscopy.....	45
Abstract .....	45
2.1 Introduction .....	46
2.1.1 Obtaining High Sensitivity with FTIR Spectroscopy .....	46
2.1.2 Aims .....	49
2.2 Experimental.....	50
2.2.1 White Cell Components and Assembly .....	50
2.2.2 White Cell Connected to FTIR by using Transfer Optics.....	52
2.2.3 Determination of Pathlength.....	55
2.3 Results & Discussion.....	59
2.3.1 Visible Alignment and Construction of the White Cell.....	59
2.3.2 Pathlength Determination with C <sub>2</sub> H <sub>2</sub> .....	60
2.4 Conclusions and Future Work.....	64
Chapter 3 - Construction and Characteristics of a Cavity Enhanced Raman Spectroscopy (CERS) Experiment.....	66
Abstract .....	66
3.1 Introduction .....	66
3.1.1 Aims .....	72
3.2 Experimental .....	74

3.2.1 Cavity Enhanced Raman Spectroscopy with Optical Feedback.....	74
3.2.2 Laser Alignment.....	77
3.3 Results & Discussion.....	78
3.3.1 Nitrogen and Air.....	78
3.4 Conclusions and Future Works.....	80
Chapter 4 - Long-Path FTIR and CERS Analysis of Volatiles Produced by Bananas During Respiration and Fermentation.....	83
Abstract .....	83
4.1 Introduction .....	84
4.1.1 Overview of Fruit Ripening.....	84
4.1.2 Major Factors Affecting Ripening of Climacteric Fruits.....	85
4.1.3 Ethylene Biosynthesis.....	86
4.1.4 Ethylene Signalling Pathway.....	87
4.1.5 Respiratory Biochemistry (Respiration in Plants) .....	87
4.1.6 Aroma of Fruits.....	91
4.1.7 Banana.....	92
4.1.8 Anaerobic Respiration and its Products.....	92
4.1.9 Methodology for Investigating the Production of Volatiles in Fruits.....	93
4.1.10 Aims.....	95
4.2 Experimental Details.....	96
4.2.1 FTIR Measurements.....	97

4.2.2 CERS Measurements.....	98
4.3 Results & Discussion.....	99
4.3.1 Gas Phase FTIR spectroscopy with White cell for ethylene, CO <sub>2</sub> , acetaldehyde, ethyl acetate and ethanol analysis.....	99
4.3.2 Spectroscopic analysis of volatiles produced by banana.....	104
4.4 Conclusions & Future Work.....	111
Chapter 5- Advanced Analytical Techniques for Monitoring the Effect of Oxygen and Exogeneous Deuterated Formate on Trimethylamine-N-Oxide Reduction and H <sub>2</sub> Production by <i>E. coli</i> .....	114
Abstract .....	114
5.1 Introduction .....	115
5.1.1 The metabolic hierarchy of <i>E. coli</i> and its regulation.....	115
5.1.2 TMAO respiration by bacteria.....	116
5.1.3 TMAO reductase.....	117
5.1.4 Formate and H <sub>2</sub> Production.....	120
5.1.5 Analytical techniques for determining TMAO and TMA.....	121
5.1.6 Aims .....	124
5.2 Experimental.....	126
5.2.1 Experimental set-up.....	126
5.2.2 Spectroscopic monitoring of TMAO reduction by <i>E. coli</i> .....	128
5.2.1.1 White cell FTIR spectroscopy analysis for CO <sub>2</sub> and ethanol.....	128
5.2.2.2 Liquid Raman spectroscopy for phosphates, formate, acetate, glucose and TMAO analysis .....	131

5.2.2.3 FTIR spectroscopy for TMA and NH <sub>3</sub> analysis.....	136
5.2.2.4 CERS measurements for H <sub>2</sub> , N <sub>2</sub> , CO <sub>2</sub> and O <sub>2</sub> .....	142
5.3 Results & Discussion.....	146
5.3.1 Anaerobic TMAO Respiration.....	146
5.3.2 Aerobic TMAO Respiration.....	151
5.3.3 Anaerobic 20 mM TMAO and 20 mM Formate-d.....	155
5.4 Conclusions and Future works.....	157
Chapter 6 - Conclusions and Outlook .....	160
References .....	163

## Chapter 1- General Introduction

This thesis is about the development and characterisation of advanced analytical techniques using vibrational spectroscopies for chemical analysis, and their applications in the biosciences and biotechnology. This chapter provides an introduction to vibrational spectroscopy and its key associated theories as well as background information to the metabolic pathways studied in this thesis.

### 1.1 Gas Analysis by Spectroscopic Techniques

Spectroscopic techniques rely on the interaction between electromagnetic radiation and the target analytes.<sup>1</sup> Spectroscopic methods can be applied to identify gaseous species *in situ* and non-destructively without the requirement for sample taking, unlike chromatographic techniques or mass spectrometry. Spectroscopic techniques are useful for tracking processes with rapid or intricate kinetics. Although the most commonly used approach to spectroscopic gas detection is direct absorption measurements employing the Beer-Lambert law, other techniques can include indirect and extremely sensitive gas molecular measurements, such as photoacoustic (PA) spectroscopy and cavity-ring down spectroscopy (CRDS).<sup>2</sup> Furthermore, Raman scattering is an alternative optical approach for gas analysis that depends on different optical phenomena. In Raman spectroscopy, the limited proportion of light scattered with characteristic wavelength shifts shows the properties of the sample analytes.

#### 1.1.1 Fundamentals of the Theory of Vibrational Spectroscopy

The easiest and most commonly used optical detection method for gases is direct infrared (IR) absorption spectroscopy. UV/vis absorptions are in general much stronger than IR absorptions. However, only a limited number of gases have absorption bands ideal for analytical applications in the visible and near-UV regions. Furthermore, smaller gaseous molecules only have extreme electronic transitions near or inside the vacuum UV region.<sup>3</sup> These bands are usually broad and overlap with other components of the atmosphere, which makes them less beneficial for analytical applications due to the lack of selectivity.<sup>4</sup>

The molecule's absorption of IR radiation contributes to transitions between two vibrational and rotational modes of the molecule, unlike absorption at visible or UV wavelengths<sup>5</sup>, which happens due to transitions between electronic states. The vibrational

energy of the molecule is quantised, which means that only certain, characteristic energy steps occur in a vibrational transition.

The energy supplied to a system by the frequency ( $\nu$ ) of the photon absorbed or lost by emission, is followed by the Planck-Einstein relationship,

$$E = h\nu = \frac{hc}{\lambda} = hc\tilde{\nu} \quad (1)$$

$E$  denotes the photon's energy and  $h$  is Planck's constant. In molecular spectroscopy, the corresponding photon's energy can also be converted to wavelength ( $\lambda$ ) or wavenumber ( $\tilde{\nu}$ ) values. These values are more widely used quantities in spectroscopy.  $c$  represents the speed of light in vacuum. Since light absorption corresponds to the transition between two states, the energy absorbed by a photon correlates to the difference of energy between two states. Therefore equation (2) can be derived as:

$$\Delta E = h\nu = \frac{hc}{\lambda} = hc\tilde{\nu} \quad (2)$$

$\Delta E$  is the energy difference between two states. Since vibrational energy levels are more closely spaced than e.g., electronic states, lower energy IR radiation can be used to excite such transitions. Compared to IR photons, microwave or radio-wave radiation has less energies. Microwave and radio-wave radiation can be used to detect molecular rotation transitions, electronic spin (Electron Paramagnetic Resonance Spectroscopy, EPR) or nuclear spin (Nuclear Magnetic Resonance Spectroscopy, NMR) transitions which have low energies.

$G(\nu)$  are vibrational term values representing the absolute energies in wavenumber units of vibrational states. One single stretching vibrational mode is present for a diatomic gas, for instance carbon monoxide (CO), which leads to the extension and compression along the molecular axis. The vibrational states of a diatomic molecule are defined to a first approximation using a quantised version of the harmonic oscillator as shown in the following equation,

$$G(\nu) = \left(\nu + \frac{1}{2}\right)\tilde{\nu} \quad \nu = 0,1,2, \dots \quad (3)$$

$\nu$  indicates the vibrational quantum number (in increasing order of energy for vibrational states) and  $G(\nu)$  is the vibrational term value.  $\tilde{\nu}$  ( $\text{cm}^{-1}$ ) is the vibrational wavenumber written as:

$$\tilde{\nu} = \frac{1}{2\pi c} \sqrt{\frac{k}{m_{\text{Reduced}}}}, m_{\text{Reduced}} = \frac{m_1 m_2}{m_1 + m_2} \quad (4)$$

where  $c$  is the speed of light in vacuum,  $k$  is the force constant,  $m_{\text{Reduced}}$  is the reduced mass and  $m_1$  and  $m_2$  are the masses of the two different atoms involved in the stretching vibration. Equation (3) predicts the energy for every vibrational level for a single vibrational mode of a molecule. As  $\tilde{\nu}$  is equal to the difference between  $G(0)$  and  $G(1)$  in the harmonic oscillator approximation, this indicates that the energy of absorption of an IR photon in a fundamental  $G(0)$  to  $G(1)$  transition should be equal to  $\tilde{\nu}$ . Hence, the bond stiffness (via the force constant as a measurement of bond strength) and reduced mass (mass of the atoms in the vibrational mode) directly influence the absorption wavenumber. The present formula shows the basis of molecular identification using IR absorption spectroscopy.

Multiple vibrational modes in polyatomic molecules are described approximately as the sum of individual, independent vibrations (normal mode vibrations) like the stretching vibration of a diatomic molecule introduced above. These vibrations still resemble simple stretching or bending vibrations because even in large molecules, the vibrations are localised to just a few atoms. The characteristic stretching and bending modes are representative and characteristic of certain functional groups (group vibrations). Figure 1.1 shows the potential of the energy of a harmonic vibrational mode for diatomic molecules as a function of internuclear separation in a one-dimensional framework.  $^{12}\text{CO}_2$  and  $^{13}\text{CO}_2$  are examples of isotopomers that can be distinguished by vibrational spectroscopy due to the dependence of the fundamental vibrational frequency on the reduced mass. This dependence allows for isotope labelling and tracer studies. It works for stable isotopes since the isotopomer selectivity depends on the reduced mass in vibrational spectroscopy. This isotopic labelling in vibrational spectroscopy is especially sensitive to isotopic replacement of light components, such as proton/deuteron exchange, against the total mass of a fragment molecule or a molecular ion since such a replacement will produce a large isotope shift.

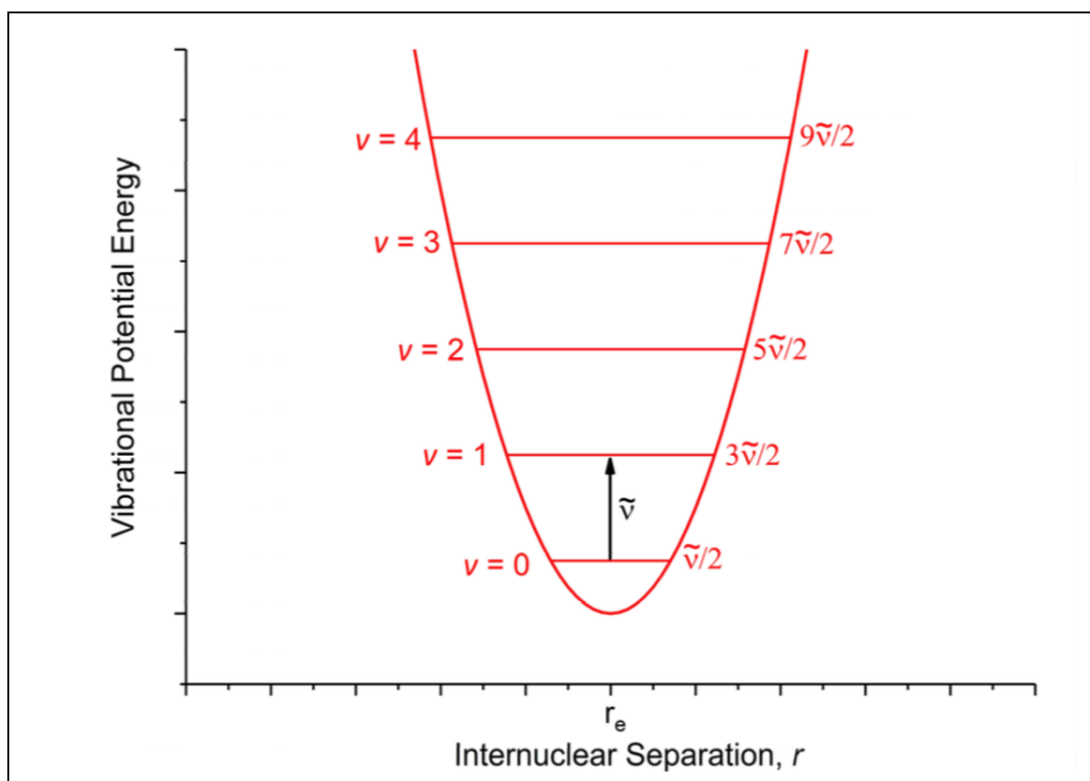


**Figure 1.1** – The potential energy of a harmonic vibrational mode for diatomic molecules as a function of internuclear separation in a one-dimensional framework. The vibrational quantum number ( $\nu$ ), the wavenumber ( $\tilde{\nu}$ ), and the equilibrium intermolecular separation ( $r_e$ ) are displayed.

### 1.1.2 Limitations of the Harmonic Oscillator Approximation

The harmonic oscillator approximation describes well a molecule's vibrational activity close to the equilibrium geometry, that is at low vibrational excitation. However, this approximation fails to explain the molecular vibrational behaviour in higher vibrational modes due to the more displaced internuclear separation from the equilibrium bond length. The actual energy of the vibrational potential energy surface is increasing more towards smaller internuclear separations than in the harmonic approximation due to the repulsive force generated from the electron clouds of the atoms. Furthermore, a completely bonded molecule is predicted by the harmonic oscillator model and the molecule will not dissociate even at infinite internuclear separation. This forecast is unphysical since bond separation will inevitably happen if two nuclei are pushed sufficiently apart.

A better definition of the actual potential surface of energy is derived from the Morse potential as represented by:

$$V(r) = D_e(1 - e^{-\alpha(r-r_e)})^2, \quad \alpha = \sqrt{\frac{k}{2D_e}} \quad (5)$$

$V(r)$  is the potential energy of the vibration,  $D_e$  is the well depth's potential energy,  $r$  is the internuclear separation,  $r_e$  is the equilibrium internuclear separation,  $D_0$  is the dissociation energy from the zero point energy and  $k$  is the force constant. If  $r$  approaches zero, this equation rises in energy more rapidly to infinity and if  $r$  approaches infinity its energy approaches bond dissociation. The vibrational state energies are expressed as:

$$G(v) = \left(v + \frac{1}{2}\right) \tilde{\nu} - \frac{\tilde{\nu}^2}{4D_e} \left(v + \frac{1}{2}\right)^2, \quad v = 0, 1, 2, \dots \quad (6)$$

where  $v$ ,  $G(v)$  and  $\tilde{\nu}$  are defined in the previous description.<sup>4</sup> The extra quadratic term suggests that the separation between vibrational states is not constant but decreases with increasing quantum number, unlike the harmonic oscillator. The prediction of molecular dissociation by the Morse potential is presented in Figure 1.2. As can be seen, the curve approximates dissociation when the internuclear separation increases, indicating bond dissociation.

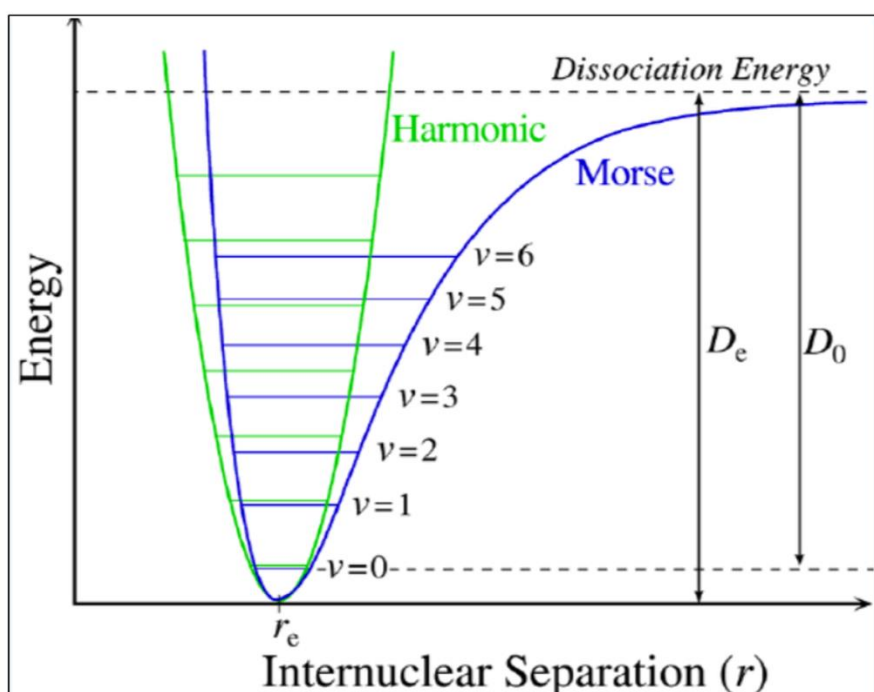


**Figure 1.2** – The overlapping of two curves representing the Morse and harmonic vibrational potential energy of a diatomic molecule.  $D_0$  is the dissociation energy from the zero point energy and  $D_e$  is the potential energy well depth.<sup>4</sup>

### 1.1.3 Selection Rules for Vibrational Transitions

A transition between two vibrational states corresponds to IR radiation absorbed by a molecule. Not all transitions are feasible, some transitions are strong and allowed, whereas others are totally forbidden and some are slightly permitted so that the relative intensity of the absorption band is low and can only be detected with a sensitive apparatus.

For allowed IR transitions, a change in the electric dipole moment related to the accompanying vibrational mode must occur. For a linear molecule, the number of vibrational degrees of freedom is equal to  $3N - 5$  and for a non-linear molecule,  $3N - 6$ , where  $N$  denotes the number of atoms in the molecule. Only one degree of freedom and a single-mode vibrational mode applies to diatomic molecules ( $N = 2$ ). Heteronuclear diatomic molecules such as CO and NO will fulfil the selection rule as they have a permanent electric dipole moment; any change in internuclear separation will inevitably result in a change in the dipole moment. IR absorption is prohibited for homonuclear molecules because for any distortion along the bond axis, the electric dipole moment remains zero. Since Raman spectroscopy has different selection rules requiring a change of polarizability during the vibration, the excited vibrational states of homonuclear molecules can be accessed by Raman spectroscopy instead.

Multiple vibrational modes occur in polyatomic molecules. As an example, the three CO<sub>2</sub> vibrational modes and their fundamental wavenumbers are shown in Figure 1.3. Based on the calculation, CO<sub>2</sub> has four degrees of vibrational freedom. However, the two bending modes are degenerate, moving in-plane and out-of-plane. Molecules that are centrosymmetric at equilibrium position have no permanent electric dipole moment. CO<sub>2</sub> is such an example since the molecule is linear and the distance of the two oxygen atoms with central carbon is the same, there is no net permanent electric dipole moment. The symmetry of CO<sub>2</sub> is broken by bending and asymmetric stretching modes where the oxygen atoms are either now not directly opposite to each other, or one of them closer to the carbon atom compared the other one, contributing to a transition in the electrical dipole moment. As a consequence, both the bending and asymmetric (or antisymmetric) modes are IR active and IR spectroscopy will observe absorption bands corresponding to both vibrations. The symmetric stretching mode, however, distorts the lengths of the C=O bond but it maintains the molecule's symmetry so that all bond lengths increase and decrease simultaneously, resulting in no net change in the moment of the electric dipole. Therefore, no accompanying absorption band can be observed in the IR

absorption spectrum, and the mode is IR inactive. This symmetric stretching mode, however, is Raman active. Hence Raman spectroscopy can be used to detect this mode.

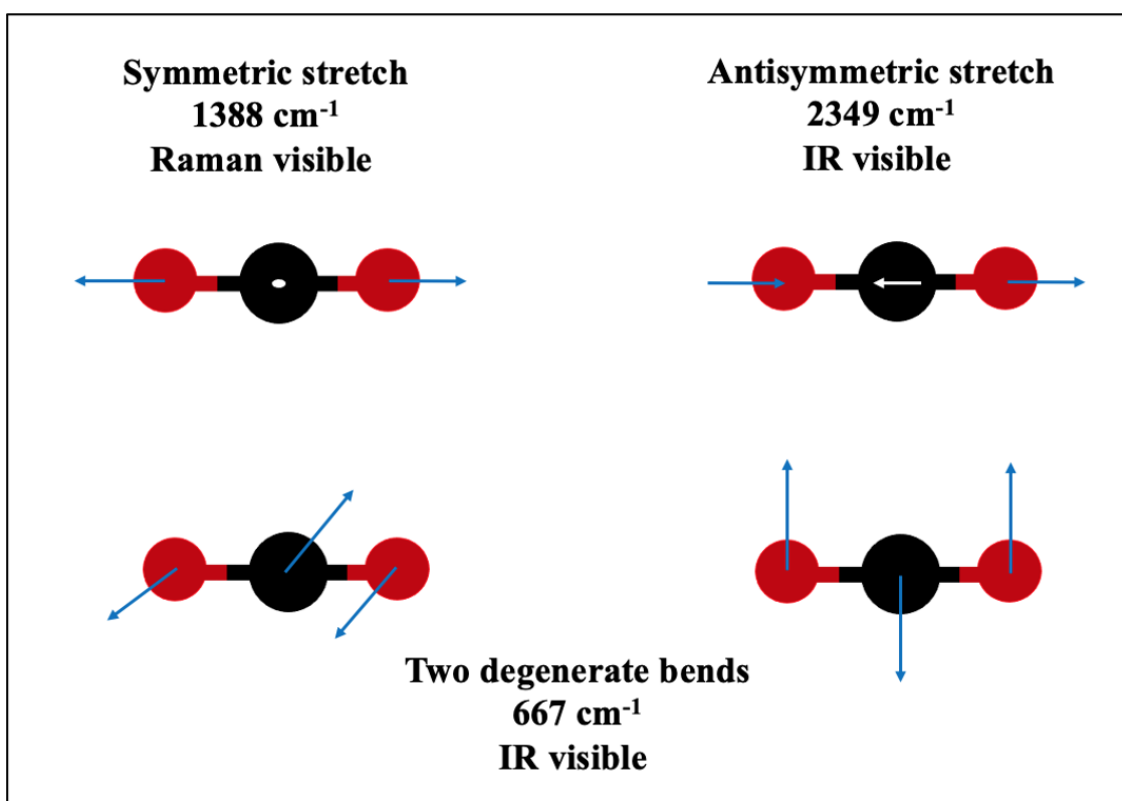


**Figure 1.3** – The CO<sub>2</sub> vibrational modes with wavenumbers of the fundamental transitions (cm<sup>-1</sup>).

The selection rules briefly state that strong IR transitions are permitted to occur only when the vibrational quantum number varies by one, for example  $\Delta v = \pm 1$  (fundamental transition). This condition implies that strong fundamental transitions absorption bands of IR occur at the initial frequency ( $\nu_0$ ). Most of these fall within the Mid-infrared (MIR) region, ranging from 250-4000 cm<sup>-1</sup> (40 - 2.5  $\mu\text{m}$ ). This region is called the fundamental region. This selection rule is relaxed because of anharmonicity, hence at higher frequency, weaker overtone transitions at  $\Delta v = \pm 2, 3, 4$  and so forth and combination bands, where different modes are changing, can be observed. The overtone transition bands are usually weak compared to fundamental bands. The Near-infrared (NIR) region ranges from 4000 cm<sup>-1</sup> to 14,000 cm<sup>-1</sup> (2500-700 nm) where overtone and combination transition bands are observed.

### 1.1.4 Rotational Fine Structure

Vibrational transitions often involve rotational changes as well which gives rise to rotational fine structure (ro-vibrational transitions). Using a high-resolution instrument for obtaining gas-phase IR absorption spectra, this fine structure inside the absorption band can be observed. For example, Fig 1.4 shows the absorption band for linear CO, showing two branches with narrow lines on either side of the middle of the fundamental frequency of the vibration. The structure occurs because of the simultaneous transition between various rotational states within the vibrational states. Rotational state separation is much smaller than for vibrational states, usually for light molecules only a few  $\text{cm}^{-1}$  and fewer for heavier species. This energy difference is so small that many of the higher rotational states at 298 K have a significant thermal population.

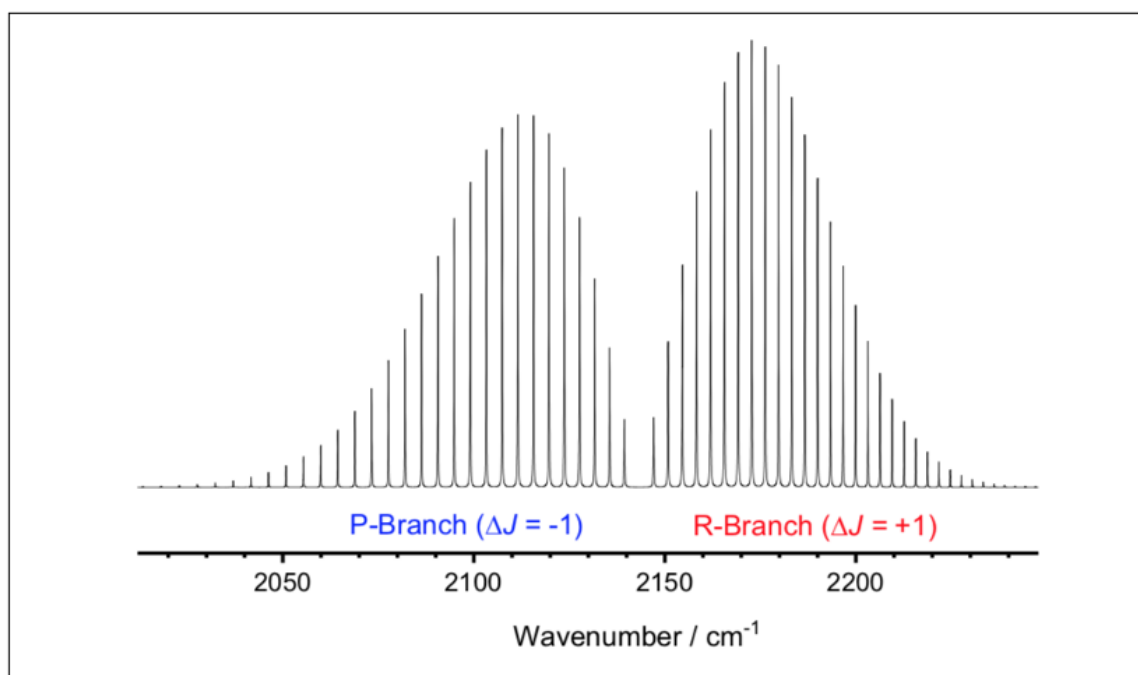


**Figure 1.4** – HITRAN 2012 database of simulation of the high-resolution carbon monoxide (CO) fundamental absorption band. The two rotational branches have  $\Delta J$  equal to -1 or +1, called the *P*-branch and *R*-branch, respectively.<sup>6</sup>

Molecular rotation is quantised.  $J$  is the rotational quantum number for a rotational state and  $F(J)$  is its term value. The term value (energy expressed as wavenumbers in  $\text{cm}^{-1}$ ) is given by:

$$F_v(J) = B_v J(J + 1), \quad J = 0, 1, 2, \dots \quad (7)$$

where  $F_v(J)$  indicates the rotational term value for the rotational quantum numbers within a vibration with  $v$  quantum number.  $B_v$  is the rotational constant and  $J$  refers to the rotational quantum number. The rotational state spacing increases as  $J$  increases.

According to the electronic dipole selection rules, a vibrational band has changes for rotation that occur only at  $\Delta J = \pm 1$ . In addition,  $\Delta J = 0$  may occur where the molecule has non-zero electronic or vibrational angular momentum (*e.g.* radicals such as nitric oxide, NO). Above the ground state, a molecule usually has considerable thermal population of rotational states, except vibrational states. This results in a series of rotational lines roughly evenly distributed in two branches correlating to *R*-branch transitions ( $\Delta v = +1, \Delta J = +1$ ) to greater wavenumbers and *P*-branch transitions ( $\Delta v = +1, \Delta J = -1$ ) to smaller wavenumbers.  $P(n)$  and  $R(n)$  refer to the location and the rotational quantum number of the original state for the individual lines of each branch. For example, the  $P(1)$  line refers to a transition from  $J = 1$  to  $J = 0$ . The *Q*-branch is a third branch that can be observed for molecules where  $\Delta J = 0$  is also permitted. It occurs at the fundamental vibrational frequency and shows up as a narrow, often unresolvable band, different to the broad *P* and *R*-branches.

For Raman spectroscopy, the selection rules for rotation are  $\Delta J = +2, 0$  and  $-2$ .  $\Delta J = +2$  gives rise to *S*-branch transitions, and  $\Delta J = -2$  to *O*-branch transitions. Most prominent and characteristic for Raman vibrational bands, however, are sharp and dominant *Q*-branch features. Water transitions are characteristically different in IR and Raman spectroscopy. Water rovibrational lines are strong in IR absorption, often obscuring other molecules, whereas Raman spectroscopy is rather insensitive to water. This is one of the major reasons that Raman spectroscopy is often preferred in chemical analysis of aqueous samples.

## 1.2 Vibrational Spectroscopy Techniques for Gas Analysis

### 1.2.1 Fourier-Transform Infrared (FTIR) Spectroscopy

Investigations of chemical reaction kinetics, monitoring of chemical processes, identification of functional groups, compound characterisation and chemical analysis are some of the main uses of Fourier Transform Infrared Spectroscopy (FTIR).<sup>7</sup> Although gas-phase analysis is a rather specialized application, atmospheric monitoring, analysis of headspace and

more fundamental studies on the existence of intra- and intermolecular interactions of specific model systems have nevertheless found important and relevant applications for this technique.

The FTIR spectrometer outline is shown schematically in Figure 1.5. The Michelson interferometer used in the FTIR spectrometer produces an interference pattern on the detector, which after a Fourier transformation, shows the spectral distribution of a light source, instead of depending on a dispersive element.<sup>8</sup> It boosts the quantity of light on the detector compared to a dispersive monochromator. The FTIR spectrometer relies on the interference of two IR beams which are combined on the detector and create constructive or destructive interference depending on the path difference of the Michelson interferometer. The Michelson interferometer consists of a set of retro-reflecting mirror cubes and an IR-transparent salt beam splitter, usually made from KBr, which is used to separate and recombine the two IR beams. The combined beam can be used for absorption measurements by passing it through a sample, similar to traditional absorption spectrometers. One of the retroreflecting mirror cubes is moved back and forth during measurements in order to change the difference in pathlength between the two split beams over time. Depending on the wavelength of the incident light, constructive or destructive interference will occur with the mirror movement, resulting in a complicated interference pattern on the detector (interferogram).

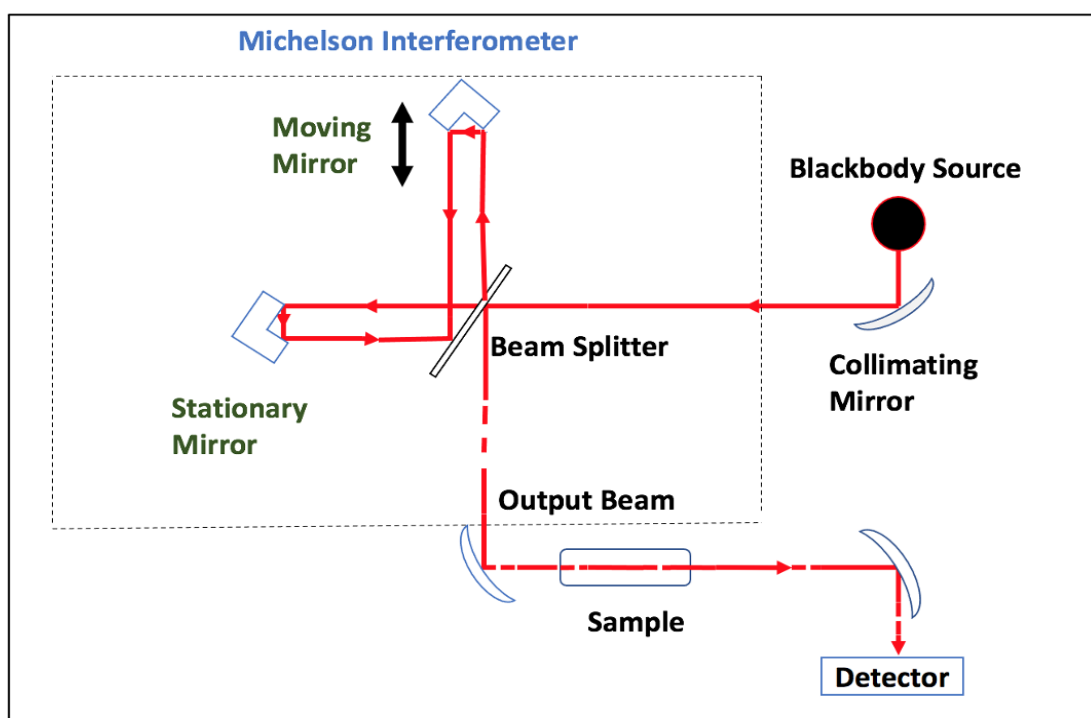


**Figure 1.5** – Outline of FTIR Spectrometer

As the displacement of the mirror is varied, the phase-matching conditions are fulfilled by distinct wavelengths. All wavelengths combine constructively only at zero path difference (ZPD). The raw FTIR data is reported as an interferogram to a computer, which is an intensity plot against mirror displacement at the detector as a function of time. The time dependent interferogram contains intensity and wavelength information in a cosine form. A mathematical Fourier transformation restores the intensity and wavelength content of the single beam, resulting in a FTIR spectrum.

In essence, the interferogram can be considered as a sum of cosine functions, with each function correlating to a single point in the 'natural' frequency domain continuum. FTIR spectroscopy provides various benefits over conventional dispersive equipment. Although the Fourier method of transformation seems complicated at first the most significant benefit is the multiplexing of wavelengths (the advantage of Fellgett), improved light efficiency since no slit is needed (the advantage of Jaquinot) and very strong wavenumber precision and stability (the advantage of Conne).<sup>9</sup> The first two benefits arise since the detector receives more light than in a dispersive instrument. This is in particular important in the MIR region. In this region, the detectors used are significantly less sensitive compared to the photodiodes used in the NIR, visible and UV regions. In a dispersive monochromator, a comparatively narrow range of wavelengths can be measured in one shot in the NIR and visible range if fitted with a CCD camera as detector. The resolution usually deteriorates in a monochromator, if for a broader wavelength range a lower resolution grating is chosen. FTIR spectroscopy does not suffer from the disadvantages of using a monochromator as it calculates all the wavelengths within the light source at once.

### **1.2.2 Multipass Cells**

The relatively low density of the gas phase compared to the condensed and solid phases is a significant challenge faced by all types of gas analysis with the sample at atmospheric pressure or below. For spot sampling (e.g. for atmospheric studies), preconcentration techniques using chemical or cryogenic traps may be used, but this is inadequate for monitoring rapidly changing processes that occur in closed systems. Increasing the sample pathlength is the most effective way of achieving higher sensitivities with optical techniques. This can be seen by the Beer-Lambert-Bouguer law which describes light absorption in a sample,

$$I = I_0 e^{-\sigma[C]l} \quad (8)$$

where  $I_0$  is the initial light intensity,  $I$  is the final intensity after absorption in the medium,  $\sigma$  is the absorption cross-section,  $[C]$  is the analyte's concentration and  $l$  is absorption pathlength or the sample depth. Using the natural or decadic logarithm, the absorbance  $A$  is derived as shown in Equation 9 and 10:

$$A_e = \ln \left( \frac{I}{I_0} \right) = \sigma[C]l \quad (9)$$

$$A_{10} = \varepsilon[C]l = \lg \left( \frac{I}{I_0} \right) \quad (10)$$

Note that  $A_e$  in equation (9) and  $A_{10}$  in equation (10) are different. For gas-phase applications, the natural logarithm form and  $A_e$  is utilised in most high-resolution gas-phase databases, using absorption cross-sections  $\sigma$  based on the equation of the natural logarithm. The absorbance at the peak of a specific band can be a straightforward way to evaluate the sample's concentration. However, peak heights are affected by pressure broadening effects and therefore the intensity of peaks of gas-phase samples in IR absorption spectroscopy is highly dependent on the overall sample pressure. It is therefore more accurate to use the integrated absorbance of a chosen line or band for gaseous samples since this is independent of total pressure (Equation 11):

$$\int_a^b A d\tilde{\nu} = [C]l \int_a^b \sigma d\tilde{\nu} \quad (11)$$

The  $a$  and  $b$  are the initial and final wavenumber of the line or band to be integrated. The other variables are previously defined. In the IR spectra of small molecules, many of the integrated rovibrational line absorption coefficients are listed in databases and are considered to be highly accurate, as detailed knowledge of their spectrum is particularly important for atmospheric studies.

Increasing the sample pathlength  $l$  is one of the strategies to increase the sensitivity of absorption measurements. Multiple pass cells which use two or more mirrors in a sample cell

to reflect the IR beam back and forth allow increasing sensitivity while retaining a sample volume as small as possible to avoid dilution effects. The White cell introduced originally by White in 1942 is the most widely used multipass design for FTIR spectroscopy.<sup>10</sup> The basic configuration of the four-pass White gas cell is shown in Figure 1.6. A pathlength of tens of metres can be accomplished with only a few tens of centimetres in base length resulting in a compact sample volume, in a proper alignment. In the literature, maximum pathlengths reported are over 100 m, but complex mirror arrangements usually occur in these systems.<sup>11</sup>

The three concave mirrors according to a V-shape configuration inside a sealed enclosure is the simplest White cells design as shown in Fig 1.6. The steering mirrors in the basic configuration are typically applied to divert the IR beam into and out of the measurement cell. Usually, it is recommended to seal the concave mirrors A to C inside the device, since it greatly eliminates the losses of transmission that can be suffered by several passes via the windows of the cell. Between the two upper concave mirrors (A and C) and the lower mirror (B), known as the field mirror, the beam is reflected back and forth after entering the cell. All three mirrors are spaced at twice the focal length and have the same radius of curvature or focal length. In this way, the divergent IR beam of the blackbody IR source is repeatedly refocused to keep the beam together. The number of passes is determined by the angle of mirrors A and C relative to the incoming and exiting beam.

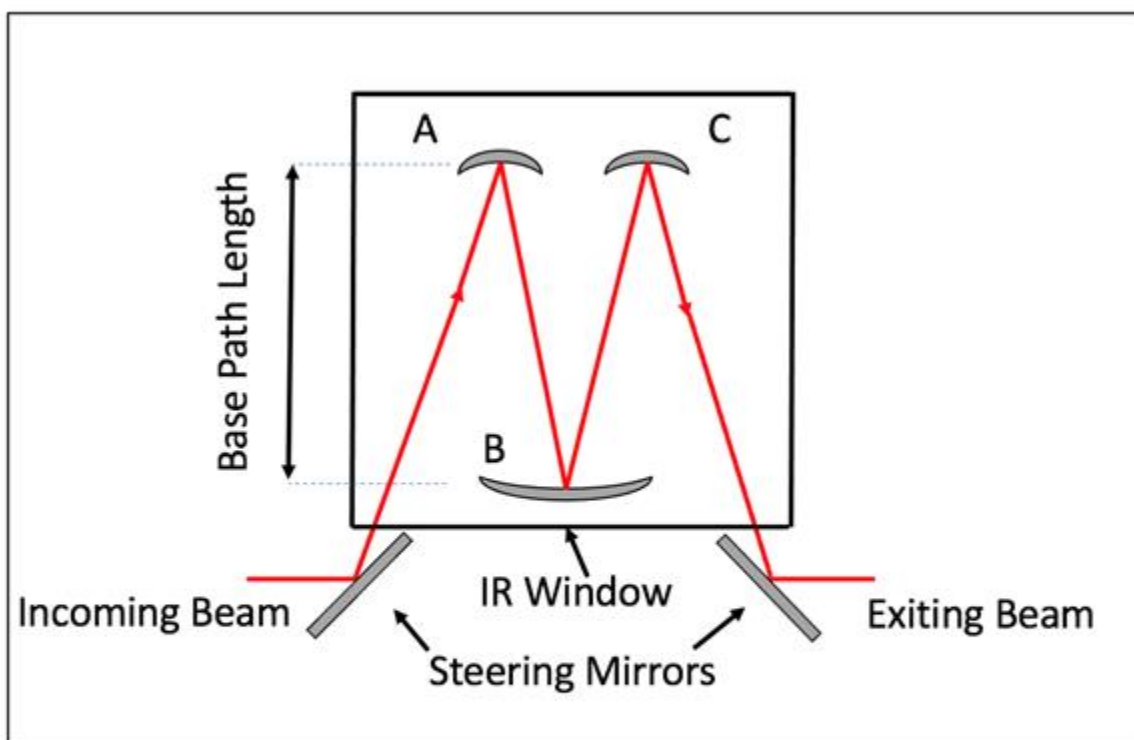


**Figure 1.6** – The simple four-pass White gas cell configuration. Three concave mirrors of the same focal length are part of the cell (labelled as A, B and C). The red colour solid lines display an idealised ray of light. The image of the input aperture is always carried to image on the lower field mirror due to the arrangement of the mirror foci (refocusing).

The second most frequently used multipass design is the Herriott cell.<sup>12</sup> This multipass cell consists of concave mirrors arranged to form a linear cell of similar focal lengths, as seen in Figure 1.7. In one of the mirrors, a small hole is cut, and the input beam is injected into an angle at the optical axis of the cell. The light is then continually reflected back and forth between the two mirrors before emerging into a second hole cut into one of the two mirrors, depending on the angle they hit with the concave mirrors. Alternatively, at a different angle to the input beam, the output beam can escape through the input hole. By changing the separation of the two mirrors, the reflection pattern and the number of passes can be varied. Note that in this design the concave mirrors are not refocusing the beam but steer them in a particular pattern. Since there is no refocusing, the Herriott design is more suited to collimated laser beams than for the diverging blackbody IR source of as FTIR instrument. For effective coupling into the cavity, this design requires the use of low numerical aperture beams, even though the Herriott cell design appears to be optically simpler than the White cell. This makes it impractical to be used with FTIR spectrometers in which the beam diameter is very wide and

divergent. The Herriott cell is better suited for laser-based absorption experiments, which ensures that the light beam can be proficiently coupled into the cell.

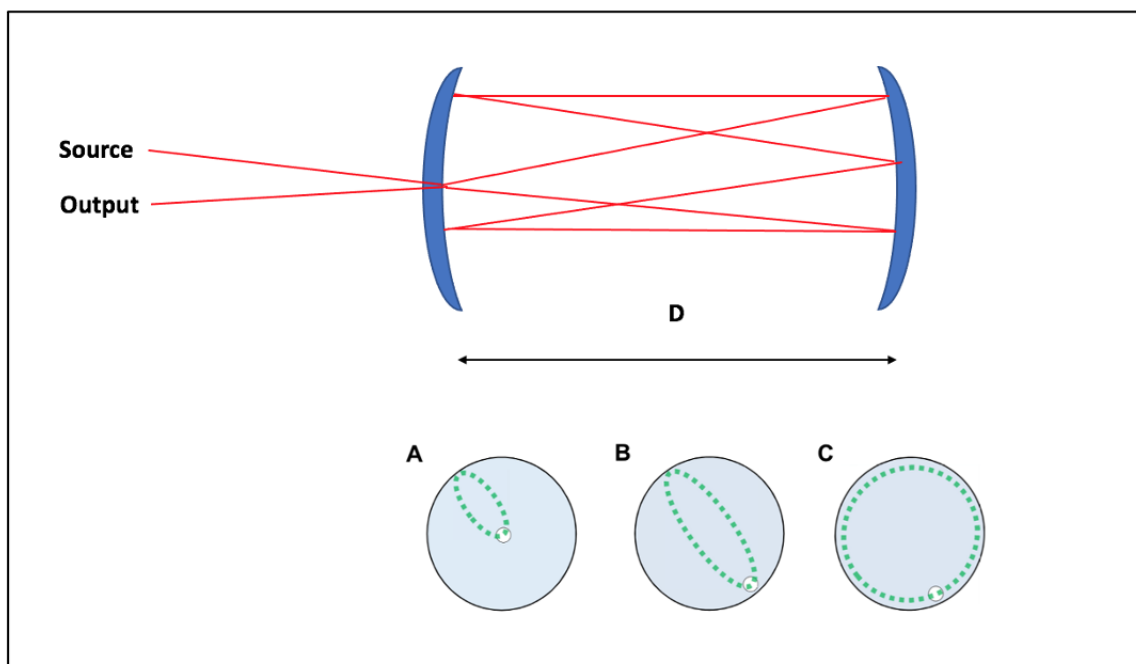


**Figure 1.7** – Top image: Two opposite concave mirrors, usually the first mirror cut with a hole with one or more apertures to allow beam injection (basic design of Herriott cell). Bottom image: scheme of the reflections on the side of the input mirror of a Herriott cell. Reflection patterns are seen for multiple mirror arrangements where the output and the reference hole are the same. A shows the injection hole located in the middle of the mirror. The mirror is used more conveniently by positioning the injection hole at the mirror's side B and C represent different mirror orientations that can finally achieve reflections of the circular arrangement, thus increasing the number of passes.

### 1.2.3 Approach of Cavity Ring-Down Spectroscopy (CRDS)

The White cell and the Herriott cell are both multipass cells where the beams are in a zigzag pattern reflecting back and forth between mirrors. In a different approach, resonant optical cavities are used to achieve long pathlengths, where beams are reflected into each other. The most commonly used method of resonant cavity enhanced spectroscopy is Cavity Ring-Down Spectroscopy (CRDS). Its development followed a fortunate discovery made in 1980 by Herbelin *et al.* when developing a new technique for analysing high reflectivity mirror coatings based on how long a light pulse can be retained in an optical cavity formed by mirrors.<sup>13</sup> They discovered the lifetime of light stored inside the cavity is varied based on the local air quality

after turning off the pumping laser source. The lifetime of light stored inside the cavity significantly reduced with higher concentrations of absorbing pollutants (presumably NO<sub>2</sub>). Anderson *et al.* and Crawford *et al.* developed and improved this approach, while they were still prominently involved in calculating the reflectivity of the high-performance mirrors of the cavity.<sup>14,15</sup> O'Keefe and Deacon identified the first application of high-finesse cavity decay measurements for spectroscopic applications, specifically to detect the relatively weak magnetic dipole transition in O<sub>2</sub>, demonstrating the utilisation of the method for the detection of weakly absorbing bands.<sup>16</sup> CRDS has since become one of the most sensitive optical detection methods for gaseous species, used for the study of molecular jet expansion clusters<sup>17</sup>, calculation of weak overtone and combination band transitions<sup>18,19</sup> and studies of short-lived radical species created during photolysis<sup>20</sup> and combustion processes.<sup>21</sup> CRDS was also used for ambient trace gas monitoring,<sup>22,23</sup> isotopic tracer studies<sup>24</sup> and breath analysis<sup>25</sup> in fundamental and applied chemical physics.

In CRDS, a laser, either pulsed or continuous wave (CW), is inserted directly into a high finesse cavity created by two or sometimes three high reflectivity mirrors (typically  $R > 99.98\%$ ). Inside the cavity, the laser beam is reflected back and forth several thousand times as the losses by the mirrors are very minimal. Significant intensity will stay inside the cavity for tens or even hundreds of microseconds even if the light source is shut off or removed.

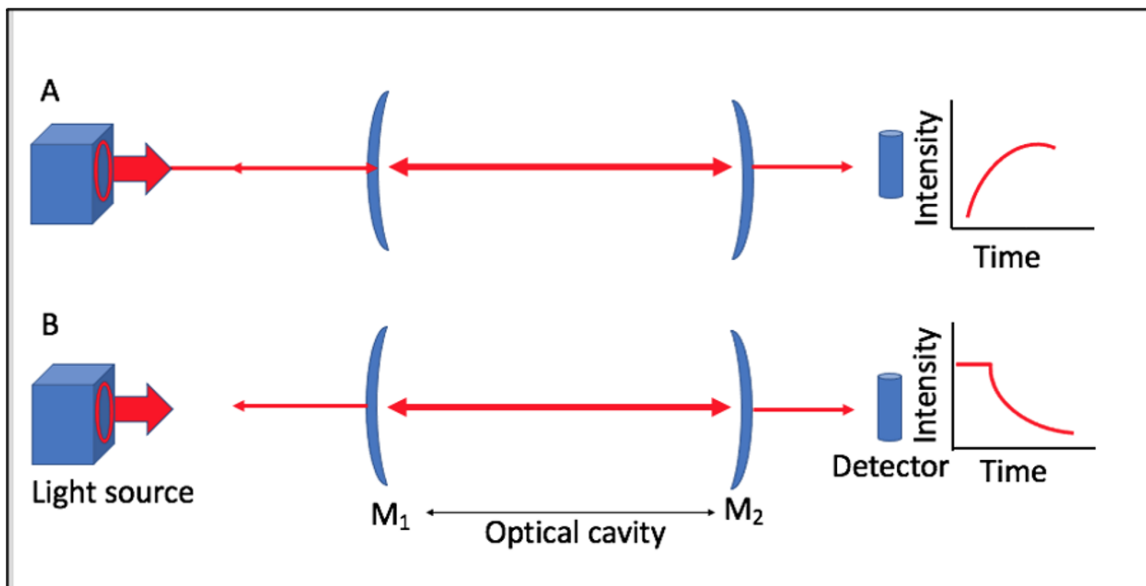


**Figure 1.8** – **A** is a schematic diagram of CRDS in a cavity of two mirrors. Fig. 1.8 shows a scheme of how CRDS works. When the light source is on, light will couple continuously into the cavity and the light intensity inside the cavity rises until reaching a steady state between the optical pumping and mirror and absorption losses. **B** shows the situation where the intensity of light inside the cavity decreases exponentially as the pumping light is removed and the light intensity escapes through the mirrors and by absorption. The identification of analyte concentration can be calculated by comparing the exponential lifetimes in the presence and absence of an absorbing analyte.

In CW CRDS schemes, light is continually injected into the cavity until it hits a steady state in which the amount of light lost in the cavity equals the light injected. The laser source is then immediately turned off at this stage either using an acousto-optic modulator or a Pockels cell. The resulting decay of light leaving the cavity can be determined by a photodiode located outside the cavity, opposite to the laser source. Except for that cavity injection happens over the length of the pulse, pulsed CRDS schemes are similar, resulting in decay of light intensity exiting the cavity after the laser pulse has finished.

The absorption species concentration can be obtained by comparing the decay rate when an absorbing analyte exists between the two mirrors and the decay rate of the empty cavity. An exponential decay (Equation 12) describes the light intensity leaving the cavity after the laser is switched off.

$$I = I_0 \exp\left(\frac{-t}{\tau}\right) \quad (12)$$

where the initial light intensity is  $I_0$  (leaving the cavity at the decay's early stage) and  $\tau$  is the ring-down time (influenced by the various losses inside the cavity). The reciprocal of  $\tau$  is the decay rate. If the two mirrors are in an enclosure with no absorbing species for a simple linear cavity, the ring downtime can be written as:

$$\tau_0 = \frac{l}{c(1-R)+X} \quad (13)$$

where  $l$  denotes the cavity length,  $c$  is the speed of light in a vacuum,  $X$  is added for any other intensity losses for example due to scattering and  $R$  is the mirror reflectivity. The presence of absorbing species leads to a shorter ring down time due to the additional absorption losses which are shown in Equation 14

$$\tau = \frac{l}{c(1-R+\sigma[C]l)+X} \quad (14)$$

where  $[C]$  is the concentration of analyte and  $\sigma$  is the absorption cross-section. Equation 15 is derived from the comparison of Equations 13 and 14,

$$\sigma[C] = \frac{1}{c\tau} - \frac{1}{c\tau_0} \quad (15)$$

All terms are as previously described. The procedure is insensitive to fluctuations in initial intensity inside the cavity, since CRDS depends on calculating ring-down times instead of any peak intensity. It is especially advantageous when the cavity is injected with highly variable output sources, particularly pulsed lasers, which, due to its broad spectral tuning range, are nonetheless useful for certain applications. This is a major benefit among other cavity-enhanced approaches and direct absorption spectroscopy that rely on measuring intensity as a function of wavelength instead of an intensity decay. Application examples of CRDS include measuring fundamentally weak absorption bands (prohibited transitions) or to evaluate lower gaseous species concentrations (trace detection). The CRDS technique can be utilised for the detection of weak absorption properties, well below the detection threshold of standard absorption measurements.

## 1.2.4 Cavity Enhanced Absorption Spectroscopy (CEAS) and Related Approaches

Even though in gas sensing applications CRDS is the most frequently used cavity enhanced spectroscopy, high finesse cavities are also used for other spectroscopic techniques, to produce either extreme enhancement of pathlength or intracavity power build up. Integrated Cavity Output Spectroscopy (ICOS) is a somewhat simplified version of CRDS since the light intensity emitted *via* the cavity during resonance is measured as a wavelength's function, instead of a decay measured in the case of CRDS.<sup>23</sup> The ICOS technique is also known as Cavity Enhanced Absorption Spectroscopy (CEAS). The enhancement of the pathlength provided by resonant cavities of up to several kilometres is necessary to observe directly absorption bands that are extremely weak. From the perspective of data collection and processing, ICOS is much easier to be implemented than CRDS because it relies on a straightforward measurement of the light emitted during resonance which can be stable for minutes. Moreover, there is no high time resolution or critical ring-down synchronisation required compared to CRDS where standard ring-down times are of the order of microseconds. In order to achieve a standard absorption spectrum, the fitting of an exponential function adds an extra data analysis stage to CRDS; ICOS merely gathers data intensity which can be utilised with little to no data processing to plot normal single beam spectra. However, while CRDS is immune to fluctuations in source intensity, the integrated signal in ICOS is strongly dependent on the intensity of light entering the cavity. Thus, ICOS is more suitable for constant output power light sources such as CW diode lasers.

CW diode lasers have a small footprint, low power consumption, a wide range of supported wavelengths from near-UV to MIR, low cost and good laser wavelength tuning capability, making it suitable for gas sensing and cavity-enhanced laser spectroscopy. The tuning of laser wavelength is through temperature variations or feedback from an optical element like a diffraction grating. The wide tunability of diode lasers is often extremely useful as it enables scanning over the range of a vibrational band's fine rotational structure in gas sensing applications. It also ensures that when shifts in the environment like temperature changes cause the cavity falling out of resonance with the laser, the laser wavelength can be readjusted very quickly. Techniques to keep the laser wavelength resonant with the cavity length include the locking Pound-Drever-Hall (PDH) technique, an electronic locking technique used to keep the diode laser to resonate with the cavity to increase its up-time, or

optical feedback.<sup>26</sup> For efficient implementation of ICOS in high finesse cavity-enhanced schemes, some kind of locking technique is necessary.

In cavity enhanced schemes, the laser beam is most often aligned along the optical axis. Off-axis alignment is an alternative approach similar to the Herriot multipass design; here, the beam is injected into the cavity at a substantial angle to the optical axis. This method is optically more stable compared to ICOS systems where the beam is coupled along the optical axis in just the simple Gaussian (TEM<sub>00</sub>) mode.<sup>27</sup> Although the off-axis approach has a reduced pathlength, resonance stability is gained as an advantage. Pathlengths in off-axis cavity enhancement are still much higher than those achieved in classical multipass cells. ICOS and CRDS with on- and off-axis technologies have now been commercialised, with the additional reliability and stability of off-axis compared to on-axis methods becoming especially desirable to ensure stable and accurate field measurement operation. There are various different approaches to cavity enhancement in addition to CRDS and ICOS, like the use of optical cavities in photoacoustic spectroscopy and Raman spectroscopy (see next section).<sup>28,29</sup> More details can be found in recent comprehensive reviews.<sup>30,31</sup>

### **1.2.5 Raman Spectroscopy**

Adolf Smekal first predicted the inelastic scattering of light by matter in 1923<sup>31</sup>. V. Raman and his student, K.S. Krishnan, first demonstrated the phenomenon in liquids experimentally in 1928. After that, Grigory Landsberg and his partner Leonid Mandelstam independently observed it in crystalline samples in 1934.<sup>32</sup> Somewhat controversially in the discovery of this effect, Raman is the only one who was awarded the 1930 Nobel Prize in Physics for the study. Raman spectroscopy is a complementary analysis method in addition to IR absorption. Although the principle of probing vibrational and rotational molecular level is similar as in IR, the underlying theory, selection rules and experimental implementation are different from IR absorption techniques.

A NIR, visible or UV laser is used in Raman spectroscopy to illuminate the sample of interest, and the scattered light is gathered and either passed through an FTIR-analogous interferometer or dispersed in a conventional grating spectrometer before being detected using a photomultiplier tube, camera or photodiode. By far the majority of photons is scattered inelastically with no energy changes, this is known as Rayleigh scattering. This is detected at the same wavelength as the laser source, which is spectroscopically a narrow band

source. In addition to Rayleigh scattering, there are also exceptionally weak bands on each side of the excitation frequency owing to Raman (elastic) scattering. In this case, energy is transferred from the scattered photon to excite the molecule into a higher energy level, known as Stokes shift, or energy is transferred from vibrationally excited states of the non-negligible thermal population to lower energy levels (anti-Stokes shift). The Stokes emission emerges from the transfer of energy to the molecules and it is thus redshifted as the scattered photon has lower energy than the light of excitation (as shown in Fig 1.9). Likewise, for anti-Stokes emission the photon energy is higher, and the emission wavelength is blue shifted because it obtains energy from a low-lying vibrational state. This is shown schematically in the energy diagram of Fig 1.9.

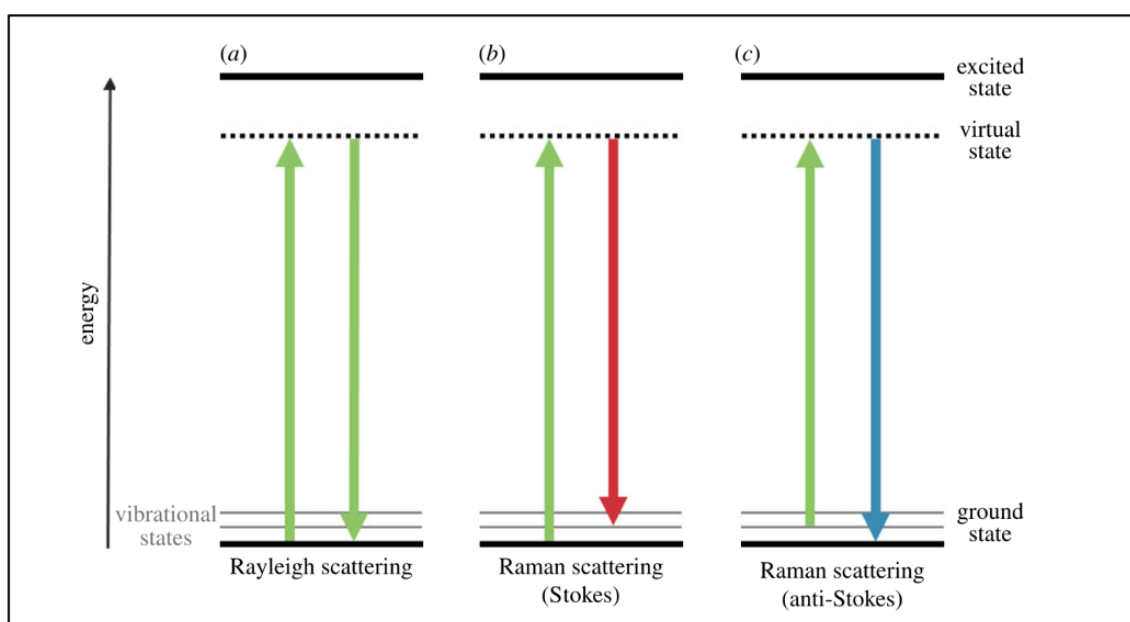


**Figure 1. 9-** A schematic diagram of Raman scattering processes involved in Raman spectra.

Unlike direct absorption, Raman scattering is a two-photon mechanism that happens in a very short-lived virtual state ( $\tau < \text{fs}$ ), which is essentially an electronic state or series of electronic states leading to rapid interaction. This differs from fluorescence, where there is a brief yet observable lifetime of the excited state, typically in nanoseconds. Energy conservation in fluorescence demands that the fluorophore of interest must be excited according to  $\Delta E = h\nu$ . This is different in Raman scattering where the transition to the virtual state is so short lived that  $\Delta E = h\nu$  does not apply strictly, or rather, the energy level of the virtual state is significantly

broadened due to lifetime broadening according to the Heisenberg energy time uncertainty. The Heisenberg energy time uncertainty states that  $\Delta E \Delta t \geq \frac{h}{4\pi}$  where  $h$  is plank's constant. That means, if the lifetime  $\Delta t$  of an excited state is short-lived, according to the Heisenberg uncertainty the energy of the excited state is broadened,  $\Delta E$ .  $\Delta E \Delta t$  is related to  $\Delta x \Delta p$  (the more common formulation of the Heisenberg uncertainty principle in terms of position/momentum uncertainty) which can be seen by the relation  $E = \frac{p^2}{2m}$  and  $p = mv = m\frac{\Delta x}{\Delta t}$ . As a consequence, the Raman excitation laser can be any monochromatic wavelength since it does not need to hit a resonance. Raman spectra are scattered intensity plotted against Raman shift or the shift of the wavenumber from the wavenumber of excitation. As in Raman transitions comparable initial and final vibrational states are involved as in IR absorption, vibrational spectra are obtained, with distinct vibrational information. The Raman shift and IR absorption wavenumber of any given band should be identical, if the transition is both Raman and IR allowed.

Raman spectroscopy is controlled by a range of selection rules, as is direct IR absorption. The selection rule corresponding to shifts in rotational energy levels that exist alongside vibrational transitions has been addressed in the case of Raman scattering (namely that  $\Delta J = 0, \pm 2$ ). There must be a change in polarizability associated with the vibrational mode for any given vibrational transition to be Raman permitted. The selection rules of IR and Raman are mutually exclusive for centrosymmetric molecules like  $N_2$ ,  $H_2$ ,  $CO_2$ ,  $O_2$  and  $HCCH$ . For most non-centrosymmetric molecules (e.g.  $H_2O$ ,  $HCl$ ,  $N_2O$ ,  $CO$ ), all vibrational modes result in transitions that are allowed in the Raman and IR spectra, although with different relative intensities. Detection of homonuclear diatomic molecules is one of the most relevant abilities of Raman spectroscopy in gas sensing, which is not possible by IR absorption. Other relevant applications of Raman spectroscopy include monitoring of hydrogen isotopomers emitted from nuclear fuels, the biological fixation of nitrogen and control of industrial processes using  $H_2$  as a reducing agent. Raman spectroscopy is much less sensitive to water vapour, whereas in IR absorption, water bands often dominate spectra and obscure weaker components. The optics and detectors used are typically more affordable and available than their counterparts in the MIR region, as typical excitation and detection wavelengths of Raman spectroscopy are in the visible and NIR regions.

Raman spectroscopy can capture an entire spectrum with several components without scanning, unlike diode laser techniques. A significant technological drawback of cavity-enhanced absorption systems and laser-based multipass techniques is that utilising a single diode laser does not exceed spectral bandwidths above a few hundred  $\text{cm}^{-1}$ . Multiple diodes are needed to achieve a wide scanning range, raising the cost of the device. There is no tuning requirement needed for Raman spectroscopy except for only one single monochromatic laser with perfect wavelength stability. Very suitable lasers for Raman applications are solid-state rare-earth-doped lasers. Commonly, lasers with neodymium-doped yttrium vanadate (Nd:YVO<sub>4</sub>) or yttrium aluminium (Nd:YAG or Nd: YAlO<sub>4</sub>), are employed, both at their fundamental wavelength (1064 nm), or frequency doubled (532 nm).

Although the exceptionally high selectivity of direct IR absorption is preserved by Raman spectroscopy, an inherent limitation of the Raman effect is its relatively low sensitivity. In addition to high-performance long pass filters which block Rayleigh scattering light with excellent excitation light rejection, sensitive cooled detectors or photomultipliers are commonly needed to acquire spectra. Shifting spontaneous Raman scattering to a more efficient approach such as resonant Raman or stimulated Raman spectroscopy can improve the Raman signal. In resonant Raman spectroscopy the excitation wavelength is chosen to be close to an electronic transition of the molecule of interest which greatly enhances Raman cross sections. In stimulated Raman spectroscopy a second laser is used at the scattered wavelength. These methods improve sensitivity compared to spontaneous Raman spectroscopy. A recent development is Surface Enhanced Raman Spectroscopy (SERS), which allows the detection of analytes with highest sensitivity.<sup>33</sup> In SERS, adsorption of analytes on a roughened or nanostructured noble metal surface occurs, and enhancement of the Raman effect is commonly observed by chemical and/or electric field enhancement by surface plasmon resonance effects.<sup>34</sup> Although the sensitivity obtained from SERS is tremendous, it is necessary to adsorb analytes to the metal surface chemically or physically. Different surface affinities of substrates may lead to surface pollution or poisoning. SERS is not specifically suitable for quantitative real-time monitoring processes since sampling is required and SERS substrates need refreshing, especially if there are high-affinity analytes in the system for traditional metal substrates (e.g. amines, thiols, phosphines).

Fiber-Enhanced Raman Spectroscopy (FERS) is a newly developed method in which a hollow-core photonic crystal fibre (HC-PCF) filled with the gaseous analyte traps the excitation

light.<sup>35,36</sup> Instead of being isotropically scattered, the resulting Raman scattered light is also confined inside the fibre and guided towards the detector, which ensures a much higher proportion of the light captured relative to conventional optics. Limits of detection below 20 ppmv for multiple gases have been reported using this method and 2 W 532 nm excitation.<sup>36</sup> FERS has also been applied successfully in breath analysis. In common with other Raman techniques, FERS has also the ability to identify H<sub>2</sub> (an essential metabolite and product of strict and optional anaerobes).<sup>35</sup>

Using an extremely powerful laser excitation source (many W CW solid state lasers) is the easiest way to improve the sensitivity of Raman spectroscopy since the number of scattered photons in Raman increases with the number of scattering events. Raman scattering is proportional to the scattered light frequency  $\nu^4$  to the power of four, so it is inversely proportional to the  $\lambda^{-4}$  of the scattered light wavelength, so the sensitivity should improve by moving to shorter wavelength excitation.<sup>37</sup> While fluorescence is a major problem for most applications of Raman with moving to shorter wavelength, in gas phase it is less problematic which means that shorter wavelength sources can be used with a comparatively small risk that the Raman signals will be drowned out by background fluorescence.

For Raman gas analysis, multipass and cavity enhancement schemes were reported where the long effective pathlengths allow more Raman scattering events and hence increasing Raman scattered intensity. Pioneered by the Hippler group, it has been demonstrated how resonant cavities similar to those utilized in CRDS can be used in cavity enhanced Raman spectroscopy (CERS) to achieve a significant improvement in Raman scattering.<sup>38-40</sup> This is an approach explored in this thesis for trace gas detection and will be introduced in more detail in the experimental chapters.

### **1.3 *Escherichia coli*: A Model Bacterium**

Spectroscopic techniques are well suited for chemical analysis. The topic of this thesis is the development and characterisation of advanced spectroscopic techniques and their application to monitor metabolism products of biological samples. This section gives an introduction to key metabolic modes of *Escherichia coli* (*E. coli*), which is a model bacterium for microbiological studies.

### 1.3.1 The metabolic modes of *Escherichia coli*

Figure 1.10 shows the cellular structure of *E. coli* with important structural features. *E. coli* is a Gram-negative facultative anaerobe which has the shape of long rods of approximately 1  $\mu\text{m}$  in length. Many strains are motile, possessing several flagella that help drive cells towards nutritional sources (chemotaxis). The single circular chromosome found in the bacterium is approximately 4.6 Mbp (Mega base pair) in length.

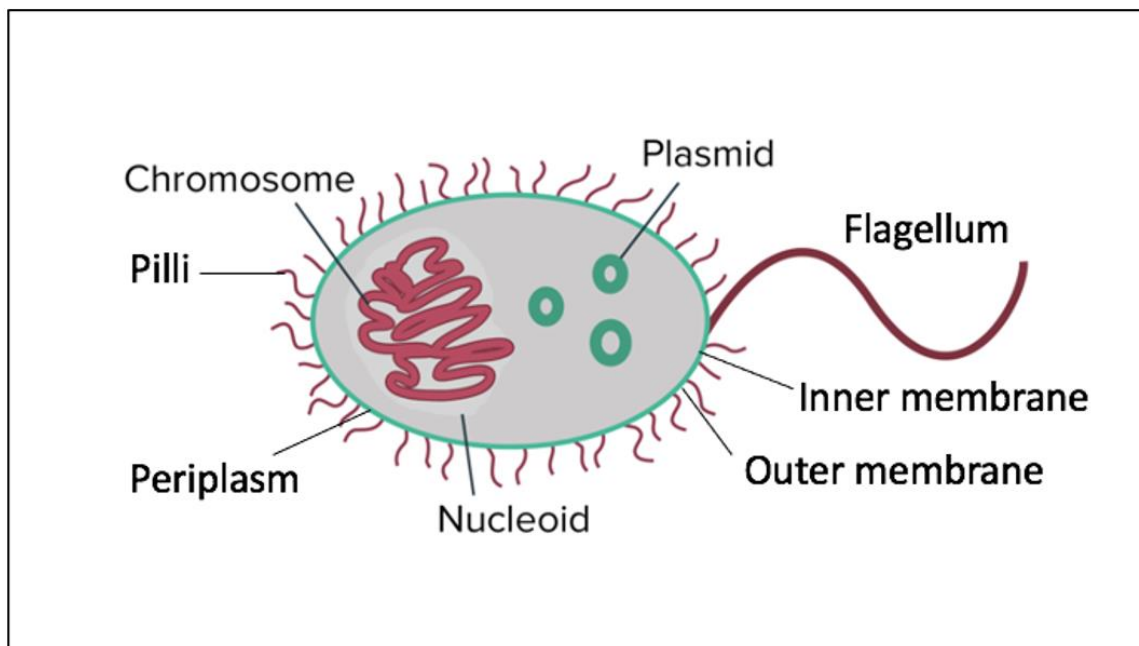


**Figure 1.10** – The cellular structure of *E. coli*

Similar to other Gram-negative bacteria, there are two lipid membranes in *E. coli*: the outer and inner membranes. The outer membrane capsulates the whole volume of the cell. The inner membrane separates the cell into an outer volume, the periplasmic compartment and the inner cytoplasmic compartment. To generate energy and promote growth *E. coli* may use various metabolic pathways. In terms of the mechanism of ATP synthesis and redox considerations, these pathways vary profoundly. The metabolic flexibility of *E. coli* suggests that the bacterium is well suited to guarantee the survival and reproduction of an effective host in the gastrointestinal tract.<sup>41</sup> In 2009, Slonczewski and Foster reported that certain pathogenic strains, such as uropathogenic *E. coli* (UPECs) could survive in other tissues and locations.<sup>42</sup> *E. coli* can grow on a relatively small range of low molecular mass compounds at low concentrations, often only briefly available. There are three metabolic modes open to *E. coli*

by way of adaptation. They are aerobic respiration, anaerobic respiration and fermentation (summarised in Figure 1.11).

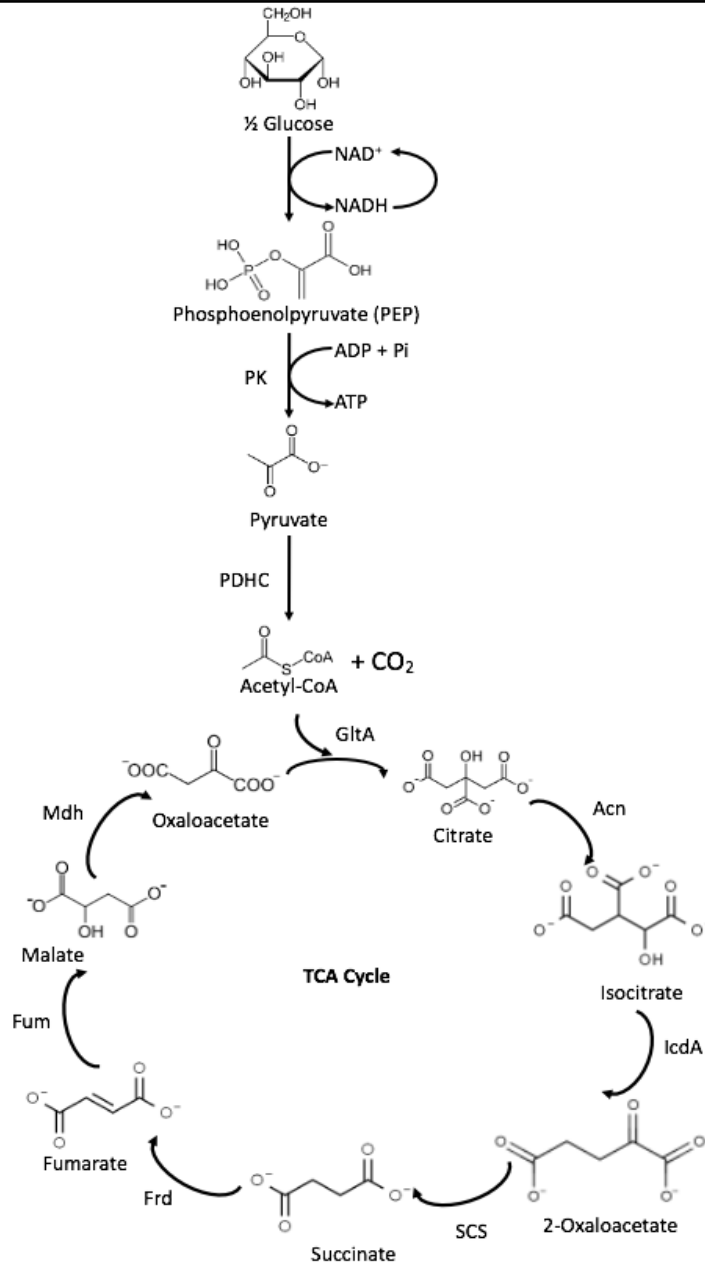
Oxido-reduction systems that need one or more terminal electron acceptors with a higher redox potential than the donor can retain the redox energy given by substrate oxidation. The four-electron reduction of oxygen to water is dominant among these electron acceptor reactions when molecular oxygen is available. Maximum energy is produced under aerobic conditions when pyruvate is oxidised into carbon dioxide through the citric acid cycle. The equivalent reduction induced enters the electron transport chain, ending with the reduction of oxygen to water. This form of metabolism offers the best potential energy yield (up to 38 ATPs per mole of glucose).<sup>43</sup>

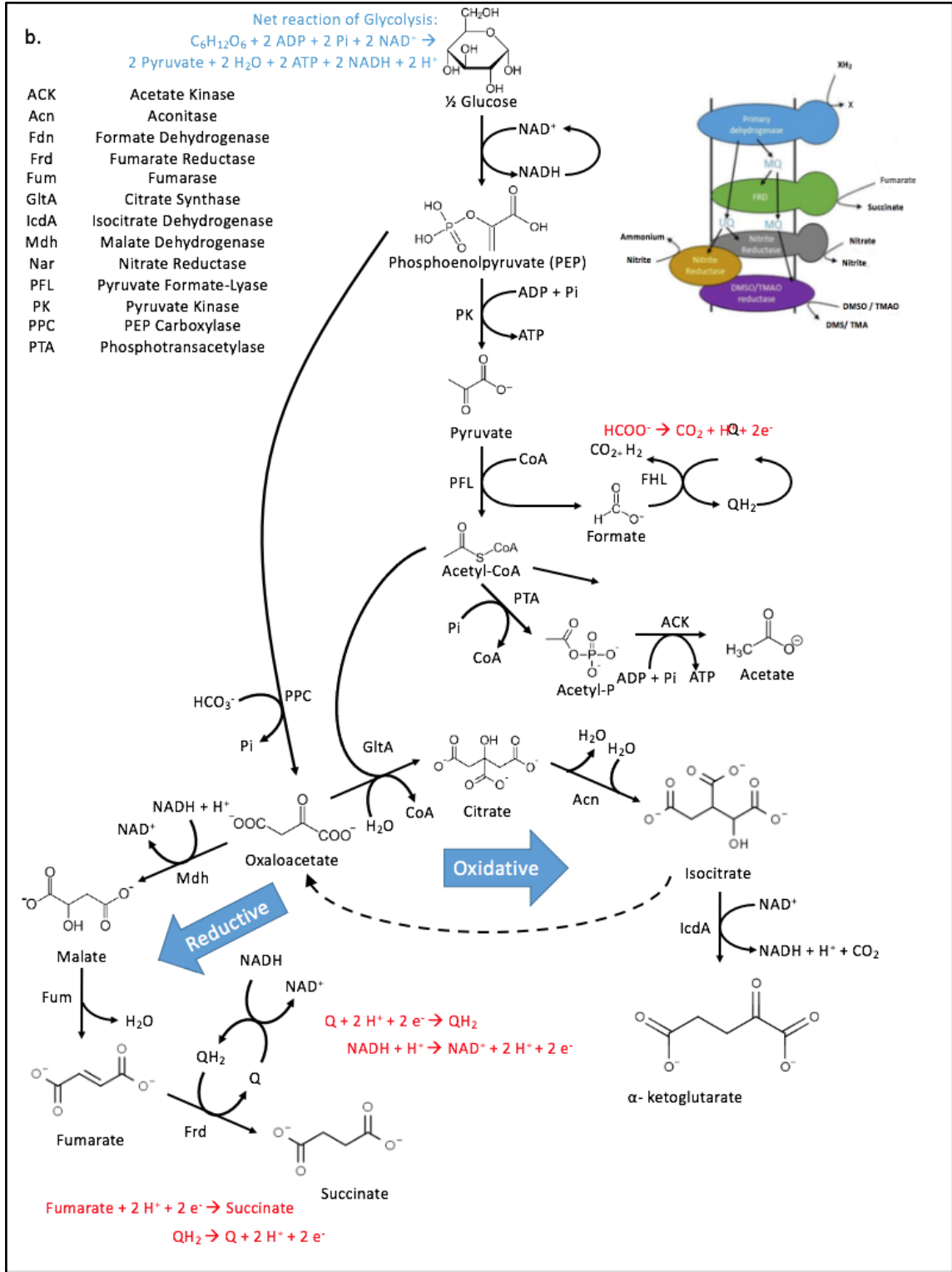
Under normal aerobic conditions of more than ~20 mbar, oxygen can diffuse quickly into the cytoplasm. However, availability of lower than 2 to 5 mbar of oxygen is restricting and different pathways with alternative electron acceptors are applied. There are a variety of alternative electron acceptors that *E. coli* can use including trimethylamine-N-oxide (TMAO), fumarate and nitrate.<sup>42,44,45</sup> The energy yield is much smaller under anaerobic respiratory conditions (4 ATP + 8[H] per mole of glucose), due to the loop of citric acid being non-cyclic and thereby contributing to the substrate's incomplete oxidation<sup>46</sup> (Figure 1.11b). To use different alternative electron acceptors needs adaptation which includes the synthesis of a variety of co-enzymes and co-factors that are necessary for anaerobic respiration and suppression of any genes involved in oxygen metabolism, to use different alternative electron acceptors.

*E. coli* can use one of many transport chains of anaerobic electrons that use trimethylamine oxide (TMAO), fumarate, dimethyl sulfoxide (DMSO), nitrate or nitrite as the terminal electron acceptor, although under aerobic conditions O<sub>2</sub> is favourite to be used as the terminal electron acceptor.<sup>45</sup> The expression of these alternative chains is closely regulated by a variety of regulatory proteins, such as ArcA and FNR (fumarate and nitrate reduction), which inhibit several regulatory proteins from being expressed in the presence and absence of O<sub>2</sub>. To help in the transition from aerobic to anaerobic conditions, a number of isoenzymes of the anaerobic terminal reductases are expressed predominantly by *E. coli*, this means that the cells under aerobic conditions can have a small amount of anaerobic respiratory and dehydrogenase, even though at much lower levels than the aerobically repressed enzymes. This suggests that to take advantage of changes in environmental conditions, a limited amount of enzyme would

still be present, potentially allowing the bacterium to adapt quickly through aerobic and anaerobic environments. The expression of the different protein components of the electron transport chain is generally regulated in such a way that only a limited number of dehydrogenase/reductase pairs are energetically feasible and co-expressed. Although any degree of 'mixing and matching' occurs under anaerobic conditions of the different reductases and dehydrogenases, expression of the several multiprotein complexes of the electron transport chain is regulated with only a few numbers of reductase pairs/energetically feasible dehydrogenase are ever co-expressed. The quinone/quinol used often varies depending on the electron transport chain. Ubiquinone (UQ) is used for aerobic electron transport chains and the NADH/nitrate pairs. However, menaquinone (MK) and demethylmenaquinone (DMK) are used in other anaerobic pathways as electron transfer agents.

a.





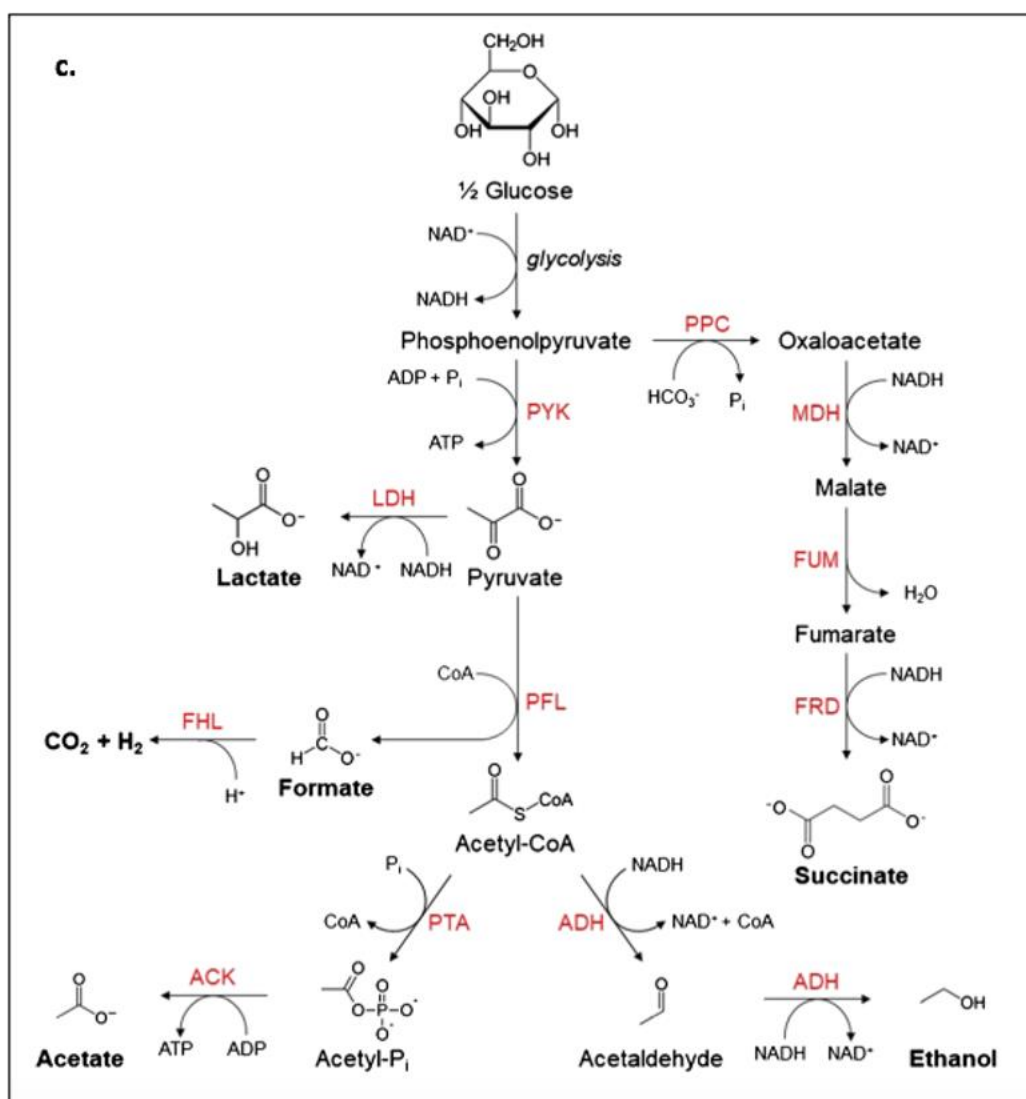


**Figure 1.11:** Three metabolic modes of *E. coli* denoted as: (a) aerobic respiration, (b) anaerobic respiration and (c) fermentation.<sup>47</sup>

The third metabolic mode that is adopted by *E. coli* is fermentation when neither oxygen nor any substitute exogenous electron acceptors are available. Utilising carbon and energy sources by this metabolic mode can generate more reduced products (Figure 1.11c). Phosphorylation of the substrate level is utilized to conserve energy, producing even less energy than other metabolic modes (3 ATP per glucose mole). During fermentation, *E. coli* produces several different end products which are known as a mixed acid fermentation. By producing various quantities of end products, redox is balanced during fermentation; these

include lactate, acetate, ethanol, CO<sub>2</sub>, H<sub>2</sub> and succinate. Each relative amount depends on both the environmental factors and the fermented carbohydrates.<sup>48</sup> This demonstrates the need of monitoring a variety and range of different metabolites to follow, characterise and gain more insight into metabolic pathways, which represents a challenge for analytical chemistry and spectroscopy.

## **1.4 Aim and Thesis Structure**

The aim of the projects presented in this thesis is to characterise and describe advanced vibrational spectroscopic techniques for chemical analysis, and their applications in the biosciences and biotechnology.

The structure of this thesis is as the following:

### **Chapter 1**

This chapter aims to give a brief introduction of vibrational spectroscopy, the relevant theory and IR and Raman spectroscopy principles and selection rules behind molecular rotational and vibrational spectroscopic techniques.

### **Chapter 2**

The aims of this chapter are to describe the construction and characterisation of a home-built multiple pass absorption White cell for gas phase FTIR spectroscopy. The preliminary measurements of C<sub>2</sub>H<sub>2</sub> allowed determination of the 2.0 m pathlength of the cell.

### **Chapter 3**

The aims of this chapter are to describe a newly home-built Cavity Enhanced Raman Spectroscopy (CERS) set-up with an optical feedback CW diode laser for gas phase analysis. The construction and characterisation of this set-up has been described to monitor N<sub>2</sub> and O<sub>2</sub> from ambient air to demonstrate the potential application and fundamental studies of these molecules in the later chapters.

## **Chapter 4**

This chapter aims to describe the detection of volatile species emitted by bananas as an application of CERS combined with long-path FTIR spectroscopy. The metabolic behaviour of bananas transitioning from aerobic respiration to anaerobic fermentation was investigated. CERS was used to monitor oxygen consumption and depletion, which cannot be achieved by FTIR spectroscopy. Volatile products were monitored by FTIR spectroscopy, including ethylene, acetaldehyde, ethyl acetate and ethanol.

## **Chapter 5**

This chapter aims to investigate TMAO reduction by wild-type *E. coli* using a combined set-up of long-path FTIR, liquid phase Raman and CERS. TMAO reduction was investigated under anaerobic and aerobic conditions and in the presence and absence of exogenous formate-d. The spectroscopic methods used together elucidated key differences in the metabolic activities, particularly in H<sub>2</sub> production.

## **Chapter 6**

Finally, this chapter offers a final conclusion and the scope for future work using these analytical spectroscopic tools.



## **Chapter 2- Long Path Multiple Pass White Cell Construction and Characterisation for FTIR Spectroscopy**

### **Abstract**

The effective use of FTIR spectroscopy for trace gas analysis requires a long absorption pathlength but without significantly increasing the sample volume. In order to obtain extremely long pathlengths in a comparatively small volume, multipass cells are employed that utilize reflective optics to pass the beam many times inside a relatively small sample volume. The construction and characterisation of a home-built White cell is described in detail in this chapter. A maximum of 28 passes with a 10 cm base length estimated to correspond to a 2.8 m total folded pathlength was achieved with the set-up as determined by the cw alignment laser. Less passes (in steps of 4) can be achieved depending on the angle of the light beam entering the cell. In the following applications in chapters 4 and 5, we use this set-up to continuously monitor volatile production by bananas and TMA.H<sup>+</sup> in bacterial culture samples, respectively. One banana volatile is the ripening hormone ethylene, hence acetylene was chosen as the calibration gas to determine the pathlength of the White cell in this chapter. As it is a simple, linear molecule, acetylene is ideal for the White cell pathlength determination, confirming the actual pathlength of the cell to be 2.0 m.

## 2.1 Introduction

### 2.1.1 Obtaining High Sensitivity with FTIR Spectroscopy

Some commercial accessories are designed specifically for FTIR spectrometers of condensed phase measurements, such as surface reflectance measurements, transmission through thin films, absorption by solid suspensions, solution phase measurements and attenuated total reflections. Most commercial FTIR instruments are only provided with simple single pass cells with IR transmissive windows for gas phase measurements which only allow detection of high concentrations of gases, for example the abundant CO<sub>2</sub> in the headspace of biological samples.

Multipass optical cells are an important accessory in laser spectroscopy, providing the long optical pathlengths required for studying weak absorption features of trace gases. They can be used in monitoring weak absorption features of molecules in spectral regions where convenient laser sources are available or in broadband FTIR spectroscopy.<sup>49</sup> Quantitative infrared absorption spectroscopy is based on the relationship between optical pathlength, light intensity and gas concentration as given by the Beer-Lambert-Bouguer law,

$$A = \ln \left( \frac{I_0}{I} \right) = \sigma [C] l$$

where  $I_0$  is the initial light intensity,  $I$  is the final intensity after absorption in the medium,  $\sigma$  is the absorption cross-section,  $[C]$  is the analyte's concentration and  $l$  is absorption pathlength or the sample depth.

As shown in the above equation, detection sensitivity can be improved by increasing the optical pathlength as absorbance scales linearly with it. Two types of gas cells are in common use to increase the pathlength in spectroscopic systems. A White cell utilizes three spherical mirrors to give a conjugate system while a Herriot cell utilizes two spherical parallel mirrors.<sup>50</sup> In the White cell design the distance between the spherical mirrors is the same as the curvature radius so that the spots are distributed up and down symmetrically. Thus, a long optical path is obtained by the number of reflections that is limited by the mirror size.<sup>51</sup> It is essential to select large-sized mirrors with large focal lengths to obtain very long optical paths. Due to the confocal arrangement of the mirrors in a White cell, the optical beam is refocused from the entrance after each reflection from the rear mirror. This makes a White cell

particularly useful for the divergent blackbody source in FTIR. A Herriott cell, described briefly in chapter 1, does not have this advantage and is thus more suitable for convergent laser beams.

In the White cell design the number of passes is dependent upon the angle of the incoming beam and the incident angle of the two upper mirrors.<sup>52</sup> The total number of passes is in multiples of four; each cycle of four passes contains the beam passing from the field mirror to one of the two upper mirrors before being reflected again to the field mirror (the entrance mirror). Before passing back to the field mirror this beam is then reflected to the second of the two angled mirrors (or in the case of the final pass passing through the exit aperture).

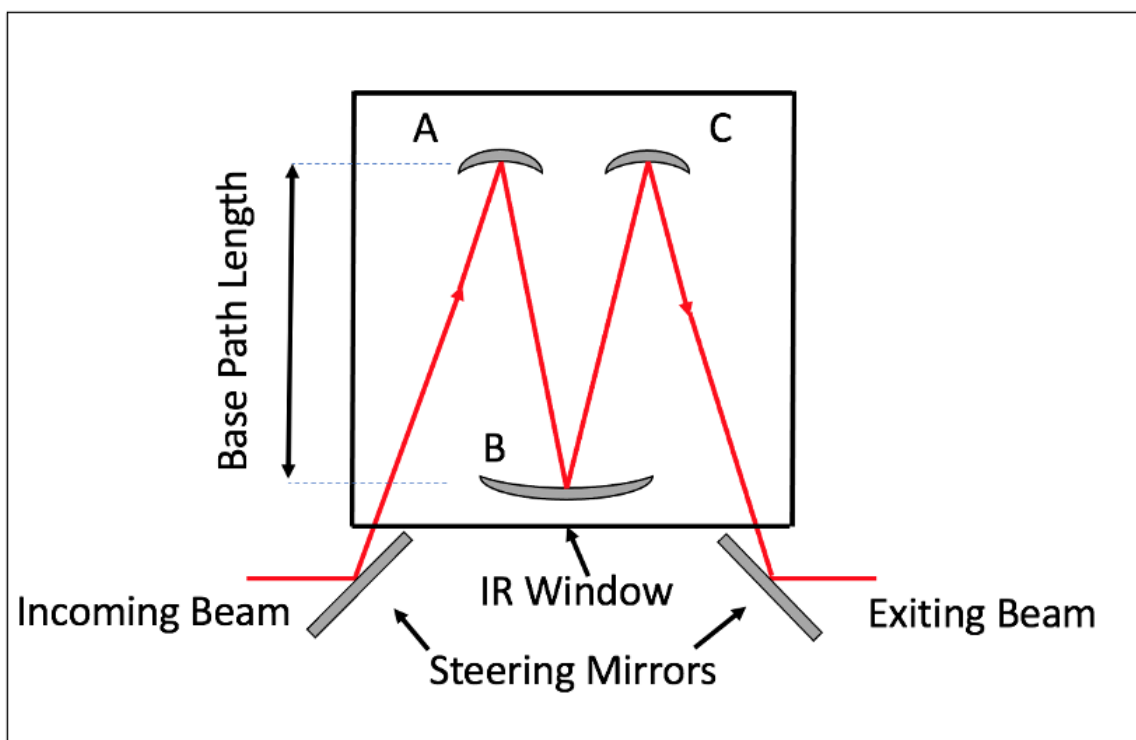


**Figure 2.1.** The simple four-pass White gas cell configuration. Three concave mirrors of the same focal length are part of the cell (labelled as A, B and C) A and C are the rear mirror while B, the field mirror. The red colour solid lines display an idealised ray of light. The image of the input aperture is always carried to image on the lower field mirror due to the arrangement of the mirror foci (refocusing).

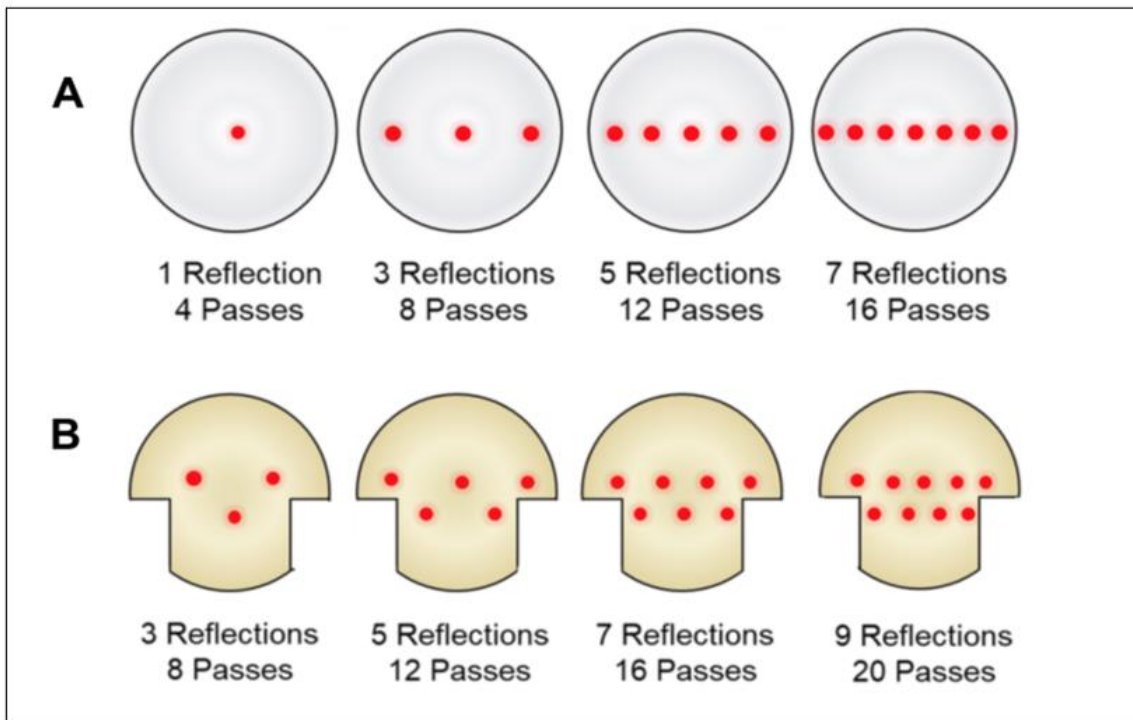


**Figure 2.2.** Number and configuration of reflections spots on the field mirror with only one row (A) or two rows (B) of the White cell. The total number of passes in both cases is equal to the  $2(N + 1)$  where  $N$  is the number of visible reflections formed on the field mirror.

The Fig (2.2) shows the visible spots formed on the field mirror by the reflected beam as the number of passes increases. Note that as the outermost spots move further to the edges of the field mirror, the number of passes increases. The maximum number of passes is limited by the total number of separate images that can be mounted along the diameter of the field mirror. The most used design uses a mushroom-shaped field mirror and depends on the incoming beam entering the cavity a little further from the field mirror to produce two rows of images (Fig.2.2 B). This design utilizes the mirror surface more efficiently, allowing it to accommodate a greater number of passes without increasing the diameter of the mirror. By using a low power visible cw alignment laser with high coherence such as a Helium-Neon (HeNe) laser, the number of passes can be obtained by visualising these reflections; the total number of passes is equal to  $2(N+1)$  where  $N$  is the number of spots formed on the surface of the field mirror.

In this chapter, direct IR absorption spectroscopy utilizing a commercial FTIR spectrometer is combined with a home built White cell to demonstrate a sensitive and attainable system. The pathlength of the constructed White cell is measured and performance is

characterised by using acetylene gas (C<sub>2</sub>H<sub>2</sub>). Due to being a linear, simple and light molecule, acetylene is an ideal test molecule and calibration gas for determining the White cell pathlength.

### **2.1.3 Aims**

Long absorption pathlengths are required to measure trace gas species, for example in the headspace of biological samples. A new home-built White Cell is constructed from commercially available optical components and characterised as described in this chapter. Using the new White cell, measurements of acetylene which is a molecule similar to the ripening hormone ethylene produced by bananas provide a first demonstration of the utility of gas phase FTIR for online monitoring of volatiles produced by bananas, for example.

## 2.2 Experimental

### 2.2.1 White Cell Components and Assembly

The White cell was made mainly by using commercially available components. Two gold coated concave mirrors (CM750-065-M01,  $f = 56.25$  mm,  $\text{Ø} = 75$  mm) were purchased from Thorlabs. The mirrors were then cut in shape by our departmental glass blower, Daniel Jackson. One mirror is T-shaped or mushroom shaped to give the field mirror, it was made from a mirror with two wedges cut out. Another mirror was cut in half along the diameter to give the two refocusing rear mirrors. The mirrors were placed inside a glass tube, also made by our glass blower, of around 10 cm length supplied with two Teflon taps to allow good control of continuous gas flow. A 632.8 nm HeNe laser (Milles Griot 05 STP 903, 1 mW output) was used for the alignment of the mirrors inside the glass tube. In order to achieve the optimum number of passes the angle of the two refocusing mirrors were adjusted while avoiding clipping the beam on the entrance or exit apertures. The mirrors were placed onto support mounts and guiding rods using black wax for preliminary fixture during laser alignment. After alignment, the mirrors were permanently attached by epoxy resin to the glass tube and the guiding rods and mounts were removed once the position of the mirrors had been finalised. After the mirrors were attached to the glass tube, the tube was sealed by Al disks, also by using epoxy resin. The front Al disk has two openings adjacent to the field mirror to allow the IR beam to pass into and out of the measurement cell. These openings were sealed by IR transparent KBr windows. In order to check for leaks in the system, the cell was placed under vacuum after assembly and sealing. No leaks were confirmed by evacuating the cell down to low pressures below  $10^{-3}$  mbar, which would be maintained over a prolonged period of time. The assembly procedure with the gas support mounts and the alignment procedure are summarised in Fig 2.3 and Fig 2.4 below.

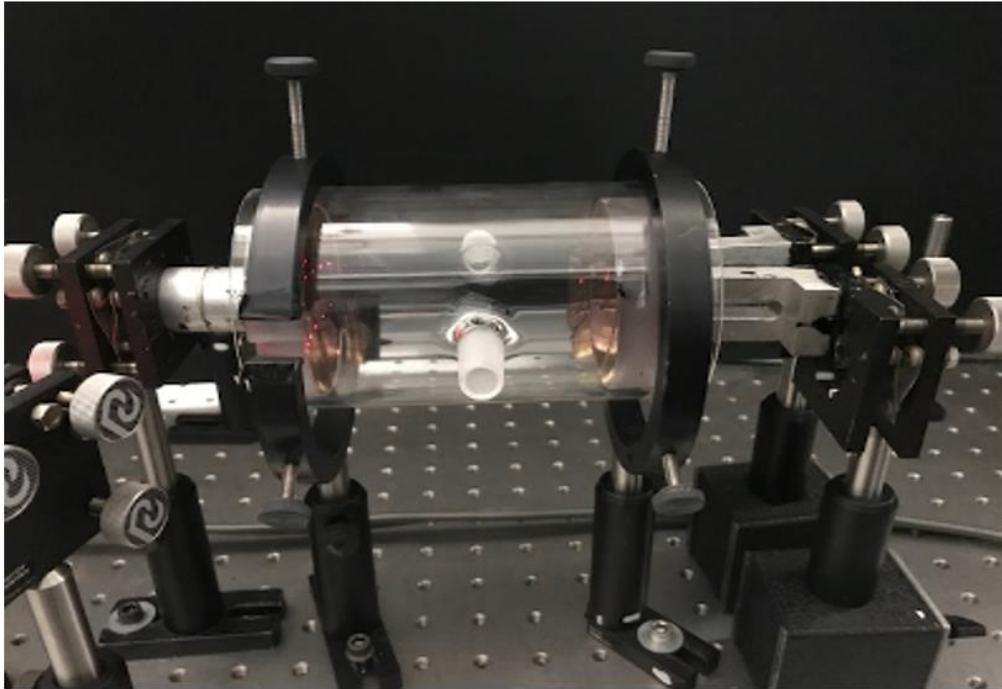


**Figure 2.3.** White cell with preliminary alignment inside the glass tube with the mirrors on support mounts.

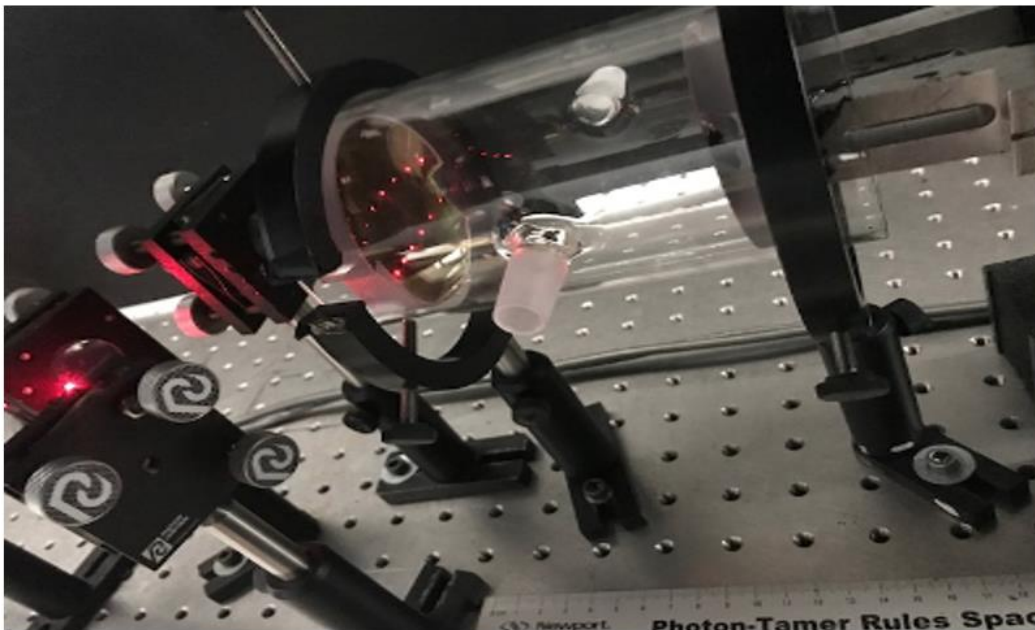


**Figure 2.4.** Two rows of images formed on the surface of the T-shaped (mushroom shaped) mirror during the preliminary alignment inside the glass tube. The laser beam enters from the wedge of the T-shaped mirror and is reflected between the mirrors.

The number of passes can be identified by counting the number of dots formed on the surface of the T-shaped mirror and multiplying it by two. According to the spot count using

the alignment laser, the maximum number of passes achieved in the home built White cell was 28 which predicts a pathlength of 2.8 m due to the base length of 10 cm. This pathlength had to be confirmed with the cell coupled to the FTIR instrument, using a calibration gas. After alignment of the White cell, resistive heating wire was wound around the exterior of the cell and the cell was wrapped with Al foil to allow heating it to *ca.* 45 °C which prevents water condensation inside the cell in biological experiments.

### **2.2.2 White Cell Connected to FTIR Using Transfer Optics**

Figure 2.5 shows the layout of the FTIR Bruker Alpha instrument used. The FTIR spectrometer relies on the interference of two IR beams which are combined on the detector to create constructive or destructive interference depending on the path length difference of the Michelson interferometer. The Michelson interferometer consists of a set of retro-reflecting mirror cubes and an IR-transparent salt beam splitter, usually made from KBr, which is used to separate and recombine the two IR beams to interrogate the sample. The combined beam can be used for absorption measurements by passing it through a sample. One of the retroreflecting mirror cubes is moved back and forth during measurements in order to change the difference in pathlength between the two split beams over time. Depending on the wavelength of the incident light, constructive or destructive interference will occur with the mirror movement, resulting in a complicated interference pattern on the detector (interferogram). After a mathematical Fourier transformation of the interferogram, a spectrum is obtained.

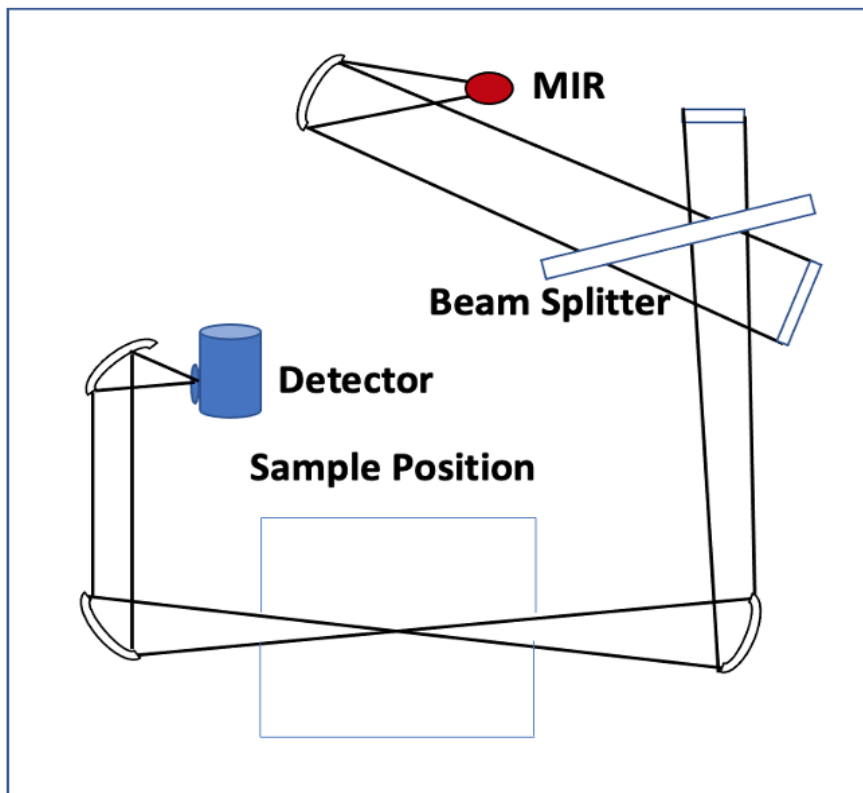


**Figure 2.5.** The scheme layout of the FTIR Bruker Alpha instrument.

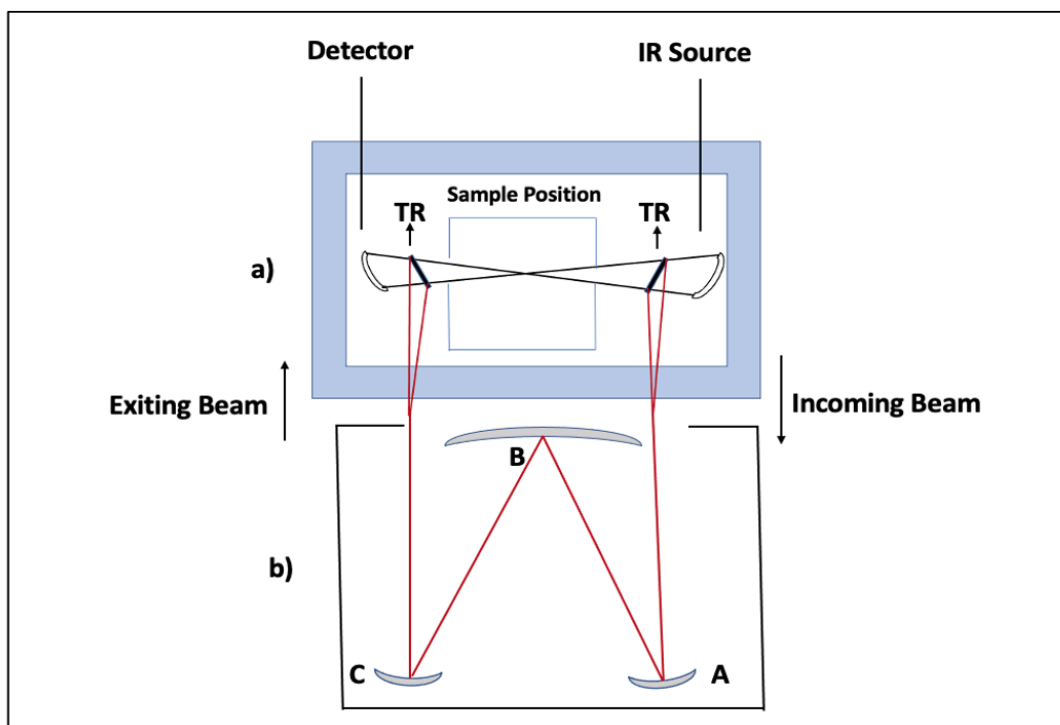


**Figure 2.6.** The scheme shows the sample compartment of the FTIR Bruker Alpha instrument in addition to transfer optics (TR) inside it to connect the FTIR with the White cell.

Fig. 2.6.a) shows a set of two gold coated mirrors labelled as (TR) transfer optics, located inside the sample compartment of the FTIR Bruker Alpha instrument. The light is emitted from the IR source of the FTIR Bruker Alpha spectrometer, the beam transferred from FTIR by TR into the White cell. The cell is placed such that the entrance aperture and exit aperture of the cell are at the position where IR beam is focused

The three concave mirrors according to a V-shape configuration inside a sealed enclosure is shown in Fig 2.6.b) The steering mirrors (transfer optics, TR) in the basic configuration are applied to divert the IR beam into and out of the sample compartment of the FTIR instrument. Between the two upper concave mirrors (A and C) and the lower mirror (B), known as the field mirror, the beam is reflected back and forth after entering the cell. All three mirrors are spaced at twice the focal length and have the same radius of curvature and focal length. The light exits the cell and is directed by the transfer optics into the detector. Fig. 2.7 shows a photograph of this set up.

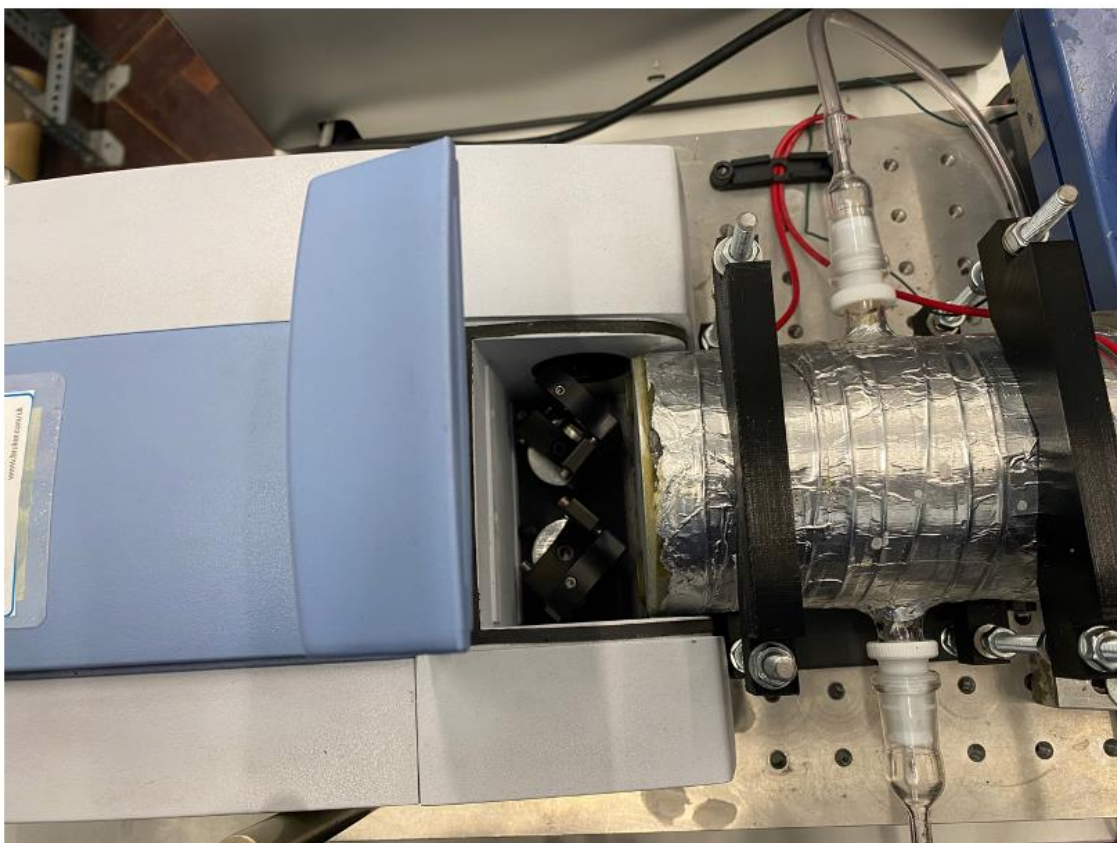


**Figure 2.7.** The FTIR Bruker Alpha spectrometer connected to the White cell by transfer optics.

### 2.2.3 Determination of Pathlength

Known pressures of acetylene  $C_2H_2$  were introduced into the cell by using a gas handling line (see Fig 2.8) to determine the White cell pathlength. The gas handling line has Teflon Young's style greaseless taps and pressure gauges. A Pirani pressure gauge was used to read low base pressures around  $10^{-3}$  mbar while a capacitance pressure gauge was used to monitor higher pressures up to 1 bar. It is necessary to evacuate the system before transferring the  $C_2H_2$ . In order to evacuate the system completely, the gas handling line has an oil diffusion pump backed by a roughing pump. A liquid nitrogen cold trap is utilized to avoid impurities gases reaching the pumps and oil vapor reaching the sample.



**Figure 2.8.** Gas handling line used to purify  $C_2H_2$  and introduce it with a defined pressure into the White Cell for pathlength determination.

A rubber balloon was used to collect  $C_2H_2$  from an acetylene cylinder (BOC, 98.5%), (A in Fig 2.8) and then connected to the gas handling line. A defined pressure of  $C_2H_2$  was then transferred from the rubber balloon to an attached glass balloon (C) as shown in figure 2.9 below.

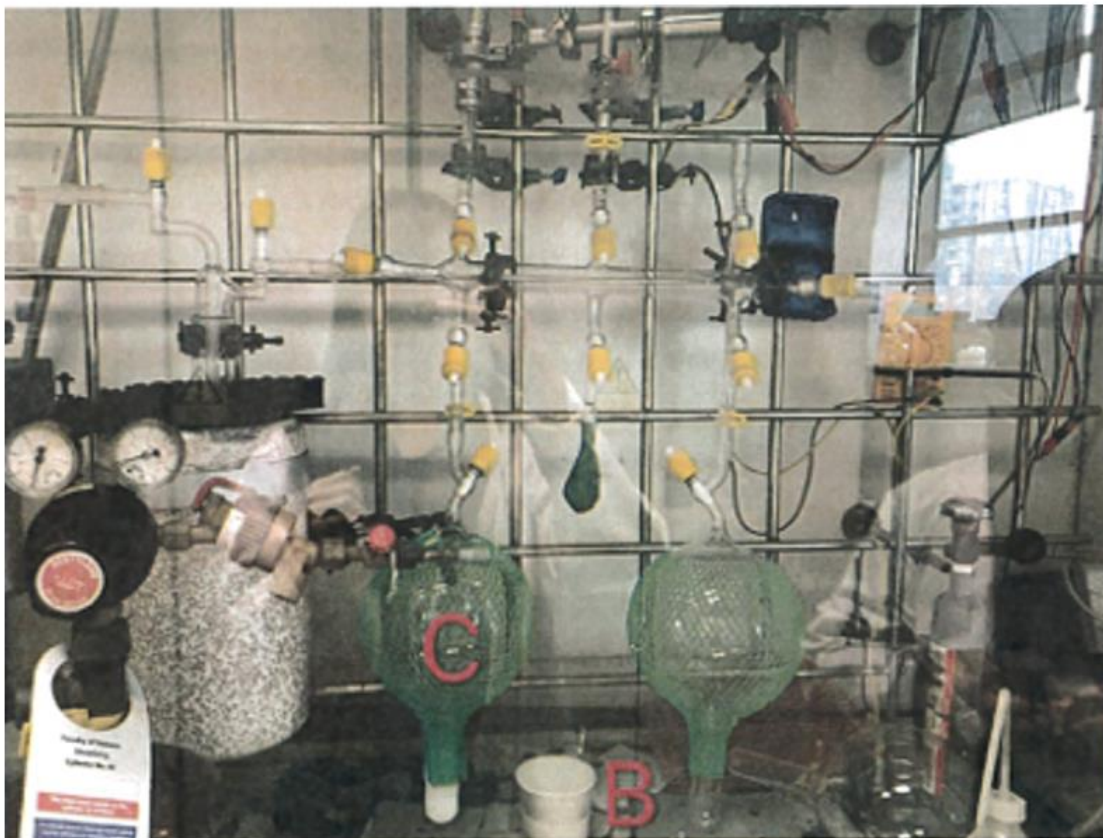


**Figure 2.9.** Liquid nitrogen used to allow freeze pump thaw purification to remove any non-condensable gases under glass balloons (C) containing  $C_2H_2$  and cryogenic transfer of gases.

$C_2H_2$  was purified by condensing into an evacuated cold trap cooled with liquid  $N_2$ . After sufficient  $C_2H_2$  has been condensed,  $C_2H_2$  is transferred back into the evacuated glass balloon (B) at a measured, defined pressure. The glass balloon is supplied with a Youngs tap that allows the glass balloon to be isolated from the rest of the system, and a cold finger which is utilized for purification to remove any non-condensable gases by using freeze pump thaw cycles of the glass balloon containing  $C_2H_2$ .

A controlled pressure of purified  $C_2H_2$  was then finally transferred from the glass balloon filled with acetylene (B) and introduced into the evacuated White cell (Figs 2.10 and 2.11). A background spectrum was recorded before FTIR sample spectra measurements (Bruker Alpha FTIR at  $0.8\text{ cm}^{-1}$  resolution).



**Figure 2.10.** Experimental setup used to transfer  $C_2H_2$  into the White Cell for pathlength determination.



**Figure 2.11.** The commercial FTIR spectrometer attached to the home built White cell.

The experimental absorbance spectra were calculated as  $\ln(I_{\text{Background}}/I_{\text{Sample}})$  and were compared with reference database spectra obtained by using absorption cross sections from the HITRAN 2016 database<sup>6</sup> for C<sub>2</sub>H<sub>2</sub> convoluted with Lorentz broadening to simulate the 0.8 cm<sup>-1</sup> instrumental resolution of the Bruker Alpha FTIR. Experimental absorption spectra were compared with a simulated spectrum based on the HITRAN 2016 absorption cross sections and assuming a certain pathlength (for example 2.8 m) of the White cell in order to identify the true pathlength. If the experimental spectrum showed good agreement with simulated spectra using the HITRAN 2016 absorption cross section, this would prove the validity of the approach and confirm the 2.8 m pathlength estimated before by counting the alignment laser spots.

## 2.3 Results and Discussion

### 2.3.1 Visible Alignment and Construction of the White Cell

Due to surface plasmon resonance bands, gold mirrors have a relatively weak reflectivity in the visible region. In the MIR region its reflectivity is excellent, however, with about 98 % reflectivity over the majority of the fundamental region. Therefore, gold mirrors are a good choice for the FTIR White cell. Aside from reflection losses, the total number of passes was limited by the number of images that can be fit along the diameter of the field mirror. In order to have an optimum of total number of passes and sensitivity, two-inch diameter gold mirrors were used.

KBr was selected for IR windows as it shows excellent transmission from 400 to 4000 cm<sup>-1</sup>. Its transmission is cut off at lower wavenumbers meaning that some low wavenumber vibrational modes are lost. Most small molecules have their absorption bands in the fundamental region at relatively high wavenumbers, with a typical stretching mode above 1500 cm<sup>-1</sup>. Other salt windows were less suitable for *in situ* headspace measurements of bacterial cultures where the water vapour concentration is close to saturation, because they are usually hygroscopic. CaF<sub>2</sub> is less hygroscopic but its transmission cuts below 1000 cm<sup>-1</sup>. KBr is a good choice if water condensation can be avoided. Thermal resistive heating wire was wrapped around the White cell to prevent condensation on the gold mirrors and KBr windows by heating to about 45 °C.

A red HeNe (636 nm) alignment laser was placed collinear with the IR beam. By counting the total number of spots on the field mirror the number of passes in the aligned White

cell could be estimated. In figure 2.4 above, there are 13 spots, corresponding to 28 passes through the cell volume. Since the space between mirrors is 10 cm, this led to an estimated total folded pathlength of 2.8 m. This pathlength had to be confirmed by a calibration gas ( $C_2H_2$ ).

### 2.3.2 Pathlength Determination with $C_2H_2$

By visualising the beam path with a visible laser, the total number of passes was easily obtained, while the actual pathlength was somewhat difficult to obtain directly. To a good first estimation, the pathlength was determined by multiplying the mirror separation with the number of passes. However, this method did not account for the fact that the beam was always somewhat angled with respect to the optical axis of the cell so that it took a slightly longer path. At either side of the field mirror as the beam entered and exited the cell the beam also travelled through an additional 2 - 3 cm of sample volume. Although visible laser alignment was helpful for precisely mounting the mirrors, the diameter of the IR beam was much larger than the HeNe alignment laser upon entering the White cell, which indicated that the spot of the IR beam formed on the field mirror was expected to be larger. Some of the light that had travelled a shorter number of passes may have leaked through the field mirror exit aperture. It was therefore important to confirm the pathlength by actual FTIR measurements of a calibration gas. As described before in 2.2.3, it is possible to purify and introduce a known pressure of gases which are IR active into the White cell by utilizing a simple Schlenk gas handling line system supplied with accurate pressure gauges.

Since  $C_2H_2$  acts as conventional ripening agent similar to ethylene hormone for bananas and encourages ripening process and was to be monitored in one of the applications described later, it was also chosen as the calibration gas to determine the pathlength of the White cell. In addition,  $C_2H_2$  was used because it was easily condensable by utilizing liquid nitrogen (boiling/sublimation point 189 K, melting point 192.3 K) which allowed purification by freeze-pump-thaw cycles. Due to being a linear, small and light molecule with distinct absorption features, it is an ideal test molecule for White cell pathlength determination.

64.6 mbar partial pressure of  $C_2H_2$  was transferred into a glass balloon made up to a total pressure of 964 mbar with nitrogen, giving 6.7 %  $C_2H_2$  in the mixture. 58.8 mbar of the acetylene-nitrogen mixture was then transferred to a second glass balloon and diluted with

nitrogen to a total pressure of 938 mbar, now having 0.42% C<sub>2</sub>H<sub>2</sub>. Then this diluted mixture in the glass balloon was connected to the evacuated White cell. When the glass balloon was opened, 720 mbar of the total pressure was recorded in the White cell. The FTIR absorbance spectrum of the C<sub>2</sub>H<sub>2</sub>-N<sub>2</sub> mixture is shown in figure 2.12. It shows the absorptions of C<sub>2</sub>H<sub>2</sub> because N<sub>2</sub> is not IR active according to IR selection rules.

Similar to other linear molecules, C<sub>2</sub>H<sub>2</sub> has a well-defined characteristic vibrational band structure. C<sub>2</sub>H<sub>2</sub> is a centrosymmetric molecule meaning that not all of the fundamental transitions are IR active.<sup>53</sup> The total number of fundamental normal modes of vibration of C<sub>2</sub>H<sub>2</sub> is 7. There are three singly degenerate stretching modes ( $\nu_1, \nu_2, \nu_3$ ) and two doubly degenerate bending modes ( $\nu_4, \nu_5$ ). Only two fundamental vibrational modes,  $\nu_3$  and  $\nu_5$ , are IR active because they produce a net change in the electric dipole moment of C<sub>2</sub>H<sub>2</sub> and hence give rise to IR absorption. The two fundamental IR active vibrational bands  $\nu_3$  and  $\nu_5$  have band origins at  $\sim 3300\text{ cm}^{-1}$  and  $730\text{ cm}^{-1}$ , respectively. In addition, C<sub>2</sub>H<sub>2</sub> also has IR active combination and overtone bands.

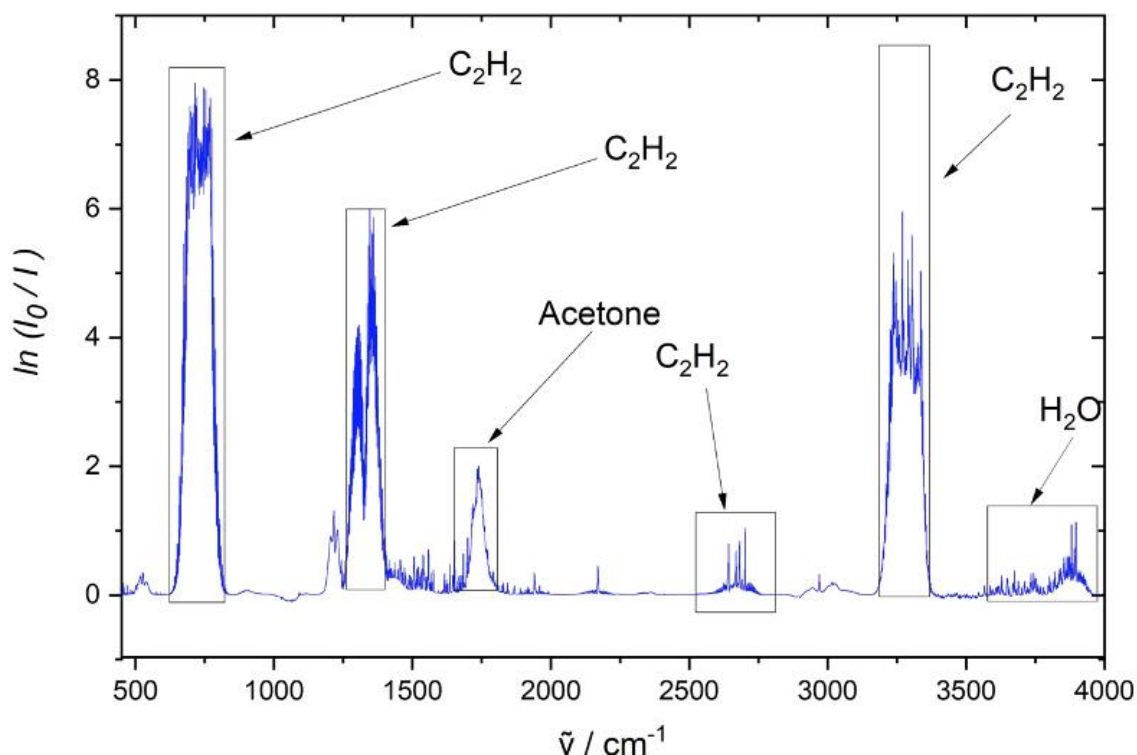


**Figure 2.12.** Absorbance spectrum of measurement of 3.03 mbar acetylene.

A single FTIR absorption measurement with a known pressure of  $C_2H_2$  was recorded at room temperature. The experimental FTIR absorption spectrum of 3.03 mbar  $C_2H_2$  in the figure 2.12 above shows the IR active bands. The band in the  $3294.8 \sim 3300 \text{ cm}^{-1}$  region is attributed to the fundamental  $\nu_3$  in anharmonic resonance with the combination  $\nu_2 + \nu_4 + \nu_5$ .<sup>54</sup> The  $729.1 \text{ cm}^{-1}$  feature is the IR active  $\nu_5$ , asymmetric C–H bending vibration.<sup>55</sup> The  $1300 \text{ cm}^{-1}$  feature is attributed to the  $\nu_4 + \nu_5$  combination band arising from the C–H bending. The  $2701.5 \text{ cm}^{-1}$  features are attributed to the  $\nu_2 + \nu_5$  combination band.<sup>53</sup>

$C_2H_2$  gas is supplied mixed in liquid acetone for safe storage and usage. A  $C_2H_2$  pressure cylinder therefore also contains traces of acetone which are difficult to remove by freeze-pump-thaw cycles. Therefore, traces of acetone impurities can be seen around  $1700 \text{ cm}^{-1}$ . There are also traces of water vapour apparent in  $3500\text{--}4000 \text{ cm}^{-1}$ , likely to be due to outgassing of the White cell.

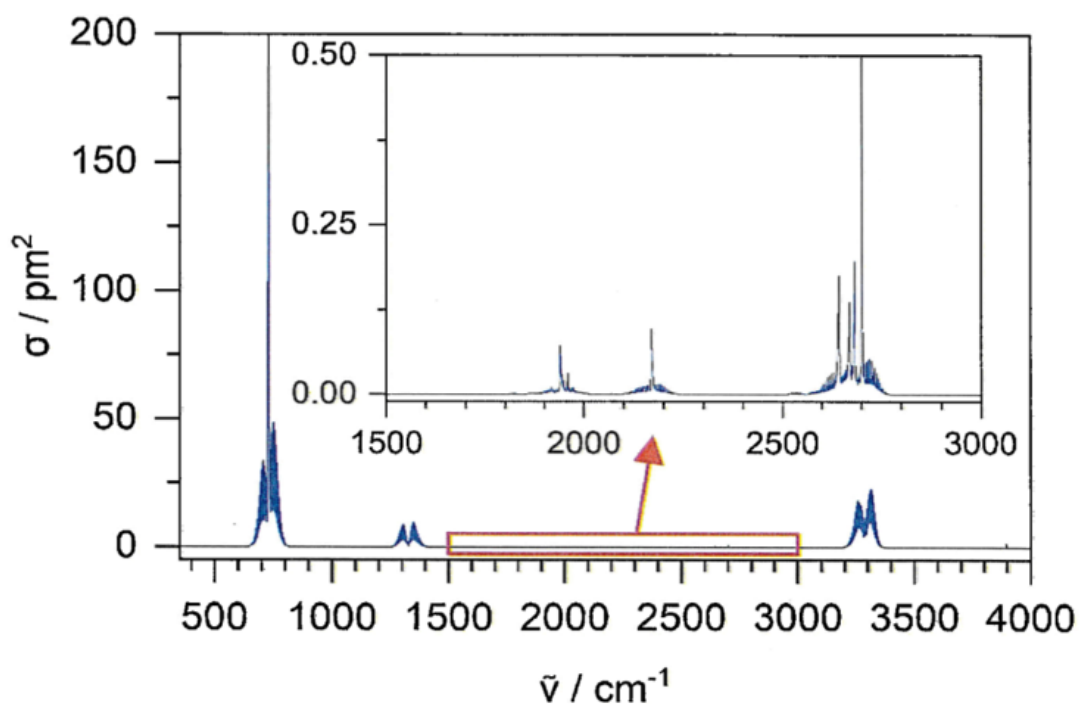


**Figure 2.13.** Absorbance cross sections of  $C_2H_2$  as a function of wavenumber.

The experimental absorption spectra were compared with simulated spectra from a reference database obtained by using absorption cross sections from the HITRAN 2016 database<sup>6</sup> as shown in Fig. 2.13 for C<sub>2</sub>H<sub>2</sub> convoluted with Lorentz broadening to simulate the 0.8 cm<sup>-1</sup> instrumental resolution of the Bruker Alpha FTIR. Experimental absorption spectra were compared at first with a simulated spectrum assuming 2.8 m pathlength of the White cell based on the alignment laser in order to confirm the true pathlength. A simulated spectrum corresponding to 2.8 m was found to not be a good match. Instead, as shown in Fig 2.14, a simulated spectrum corresponding to 2.0 m was a good match indicating that 2.0 m was the true folded pathlength of the White cell based on the calibration gas C<sub>2</sub>H<sub>2</sub>.

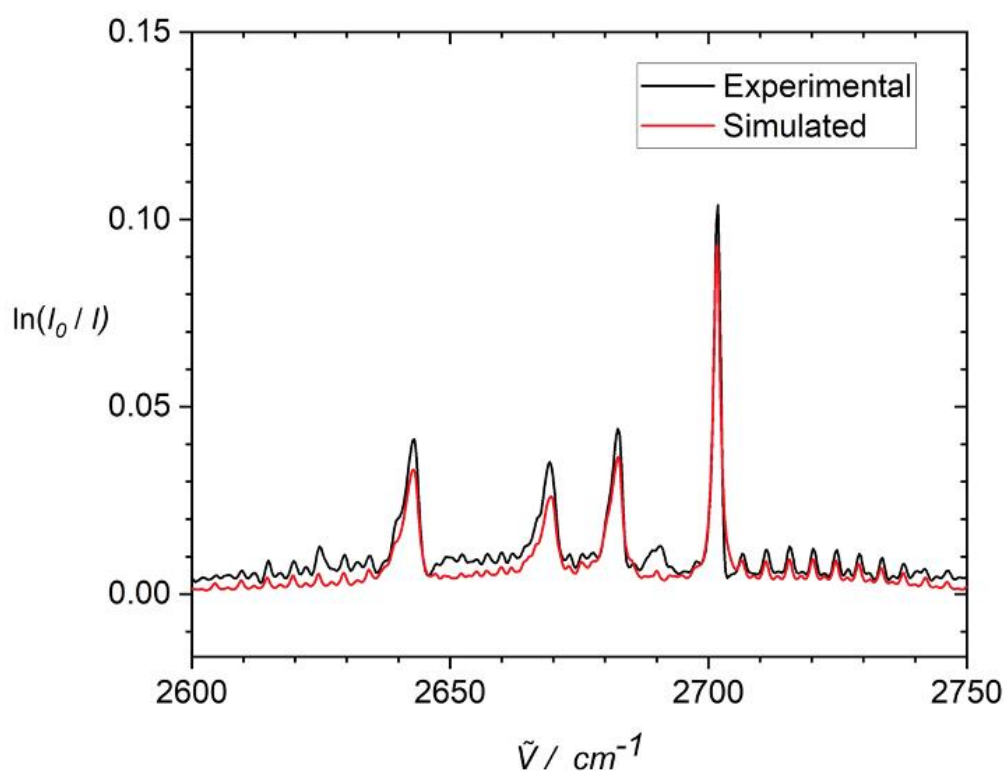


**Figure 2.14.** Experimental and simulated absorbances for C<sub>2</sub>H<sub>2</sub> to confirm the pathlength is approximately 2.0 m.

## 2.4 Conclusion and Future Work

A multiple pass, 2.0 m pathlength White cell was constructed, aligned and characterised successfully utilizing  $C_2H_2$ . Experimental absorption spectra were compared with a simulated spectrum based on the HITRAN 2016 absorption cross sections. The experimental spectrum showed good agreement with spectra simulated which proved the 2.0 m pathlength of the White cell.

This chapter only shows the preliminary measurement of  $C_2H_2$  for pathlength determination of the White cell using a commercial gas phase FTIR spectrometer. Clearly this assay holds a great deal of promise as a helpful tool for exploring many ranges of analytical applications. The ability for measuring many gas species online without sampling is important and has advantages over other sensitive gas phase assays. This assay can be utilized for monitoring banana respiration as a further application of the White cell set-up with FTIR, an application that is described in detail in chapter 4. The detection of TMA,  $NH_3$  for monitoring bacteria metabolism as further applications of the White cell are described in chapter 5.



## Chapter 3 - Constructing and Characterising A Cavity Enhanced Raman Spectroscopy Set-up

### Abstract

A new cw diode laser cavity enhanced Raman spectroscopy (CERS) set-up with optical feedback for measurement of gas phase species has been constructed successfully and used to record the Raman spectra of N<sub>2</sub> and O<sub>2</sub> from ambient air to demonstrate its potential for applications and fundamental studies. With 170 mW of 637 nm single mode diode laser excitation and 30 s integration time, noise equivalent detection limits ( $1\sigma$ ) of 1.71 mbar for N<sub>2</sub> and 0.53 mbar for O<sub>2</sub> at 1 atm were achieved. This result indicates that the CERS set-up is suitable to detect O<sub>2</sub> and other homonuclear diatomic molecules at low level. A relevant analytical application of CERS for monitoring the depletion of O<sub>2</sub> in biological aerobic respiration experiments will be discussed in the following chapters. The newly constructed set-up is small, compact and portable, and thus ideal for analytical applications.

### 3.1 Introduction

Development of advanced technologies for spectroscopic gas sensing is a challenging research subject. Infrared absorption-based approaches, such as direct infrared absorption spectroscopy<sup>56</sup>, photoacoustic spectroscopy<sup>57,58</sup> or cavity ring-down spectroscopy<sup>59,60</sup>, are among the most sensitive used techniques. Due to IR selection rules, the aforementioned methods have difficulty detecting diatomic homonuclear molecules. A variety of areas, including biology, infectious disease detection<sup>61</sup> and electrical equipment fault diagnosis<sup>62</sup> depend on monitoring gases like H<sub>2</sub>, N<sub>2</sub>, and O<sub>2</sub>. Furthermore, the sensing of gas mixtures can necessitate the use of multiple lasers and detectors as different gases need different wavelengths. As a result, infrared absorption-based gas detection systems have many drawbacks.

Among the various alternative sensing techniques, Raman spectroscopy<sup>63,64</sup> is a powerful method. In 1923, Adolf Smekal predicted Raman scattering first theoretically, and five years later, C. V. Raman discovered it experimentally.<sup>65</sup> Raman scattering is based on the principle where an incident photon excites a molecule which is in a vibrational, rotational or

rotational-vibrational state known as the initial state to a higher intermediate level, usually higher electronic states (virtual states or real states), and then returns the molecules to a lower, final state and emits a photon. Rayleigh scattering occurs when the final state is identical to the initial state and the frequency of emitted and the incident photon is equal to each other. Stokes Raman scattering or anti-Stokes Raman scattering applies if the emitted photon is shifted to a lower or higher frequency, if the final state is higher or lower than the initial state, respectively. Anti-Stokes Raman scattering can occur if the molecule is already in an excited state. Hence, according to the Boltzmann distribution, Stokes Raman scattering intensity is usually much greater than anti-Stokes Raman scattering, since at room temperature nearly all molecules stay at the vibrational ground state. As a consequence, sensing of molecules usually only measures Stokes Raman scattering.

In Raman spectroscopy, most gases can be identified except for monoatomic gases. As a benefit of Raman selection rules, Raman is not very sensitive to water, unlike IR spectroscopy. In a gas mixture, a single-wavelength laser can detect all Raman-active species in the mixture. Since the detected samples do not need extensive preparation, for instance, water removal, it can save significant time and cost. In assessing a gas-sensing technique, the limit of detection (LOD) is an important metric to be considered. Unfortunately, it is challenging to analyse trace gases using Raman spectroscopy since it has relatively low Raman scattering cross-sections. This is the reason why Raman spectroscopy is most often applied to liquid and solids which have a high density.

The key to expanding and improving the application of Raman gas sensing is to increase the scattering intensity of trace gases. Trace gas scattering intensity and LOD can be enhanced by increasing the power of the laser source, extending the scattering collection range and increasing the integration time. This will improve the scattering intensity and LOD of Raman spectroscopy during gas sensing. In addition, use of better grating diffraction efficiency of the monochromator and use of a higher quantum efficiency detector such as a photomultiplier tube (PMT) or charge-coupled device (CCD) also help to improve sensitivity. A high-power laser source necessitates costly devices and has laser safety issues and increasing the scattering length usually requires a gas cell that is too long and involves collection optics. Grating diffraction efficiency and quantum efficiency of detectors have a limited scope for improvement. Therefore, more recent effective techniques, such as fiber enhancement or cavity-enhancement, will significantly enhance scattering intensity and LOD.

One recent study discusses the use of fiber enhanced Raman spectroscopy (FERS) with Hollow-Core photonic crystal fibers (HC-PCF) to analyse a variety of climate relevant atmospheric gases that allow for a reliable quantification of CH<sub>4</sub>, CO<sub>2</sub>, N<sub>2</sub>O alongside N<sub>2</sub> and O<sub>2</sub> in one measurement.<sup>66,67</sup> HC-PCF is a new type of fiber that enhances light-analyte interaction along long optical pathlengths, including for very small sample volumes in a hollow core. It works when a powerful laser source is applied; by a microscope objective the laser source is coupled to a length of hollow optical crystal fiber (HC-PCF). Along the fiber the gaseous analyte is flowed. A power monitor allows the measurement of the total power transmitted over the fiber. The back scattered Raman light is passed back *via* the objective and by a beam splitter where the excitation light is reflected. To eliminate remaining excitation light, an edge filter is used before Raman light is coupled into a dispersive spectrometer with a CCD detector.<sup>66,67</sup> Improved analytical sensitivity was reached at a sub-part per million limits of detection that include a high dynamic range of 6 orders of magnitude, within a second of time measurement. A Raman fibre set-up that can detect in the visible range allows for a combination of advantages: high power lasers with excellent beam quality are available, availability of compact, high-quality gratings, detectors with high quantum efficiency and low noise, mirrors, filters, and microscope objectives. A Nd:YAG laser at 532.3 nm and a higher laser power of 2 W at 20 bar sample pressure was used in previous studies. The sensitivities for individual gases scale with their corresponding absolute scattering cross-section, which is particularly high for methane.<sup>66,67</sup> To demonstrate the high sensitivity, methane was analysed at an atmospheric concentration of 2 ppm, with signal-to-noise ratio (SNR) of 28 and LOD of 0.22 ppm. The low limit of detection (LOD) values proved that fiber-enhanced Raman gas spectroscopy is capable for use as a technique to simultaneously quantify the relevant gases CH<sub>4</sub>, CO<sub>2</sub>, N<sub>2</sub>O, N<sub>2</sub> and O<sub>2</sub>.

In an alternative approach, Fabry-Pe'rot cavities, multiple-pass cavities, microcavities and laser cavities are only a few of the cavity-enhanced developments that have been utilised in cavity-enhanced Raman spectroscopy (CERS) for gas sensing. The LOD is influenced by several additional parameters such as the efficiency of the laser source and detector, thus evaluating a cavity-enhanced technology based only on LOD as a metric is not sufficient. These cavity enhancement techniques have one similarity, which is the intracavity laser power which is increased by constructive optical interference. This is the basis of cavity-enhanced technologies in Raman spectroscopy, since Raman scattering increases with laser power.

The propagation of two or more coherent light waves along the same direction gives rise to a phenomenon called optical interference. The optical interference between waves of the same frequency can be constructive or destructive interference (Fig. 3.1). Constructive interference is also known as resonance. Fig. 3.1 shows two waves of the same frequency which interact optically. Different interference occurs depending on the phase difference between the waves in multiples of  $\pi$ . If the phase difference is an even multiple of  $\pi$ , the interference is constructive, if it is odd, then the interference is destructive. The resulting wave generated by destructive interference has a smaller amplitude than the individual amplitudes. If destructive interference occurs between two waves of equal magnitude, the resulting wave's amplitude is equal to zero. Each of the individual amplitudes is weaker than the amplitude of the resulting wave in a constructive interference, which leads to an increase of light intensity that could be useful for enhancing Raman spectroscopy.

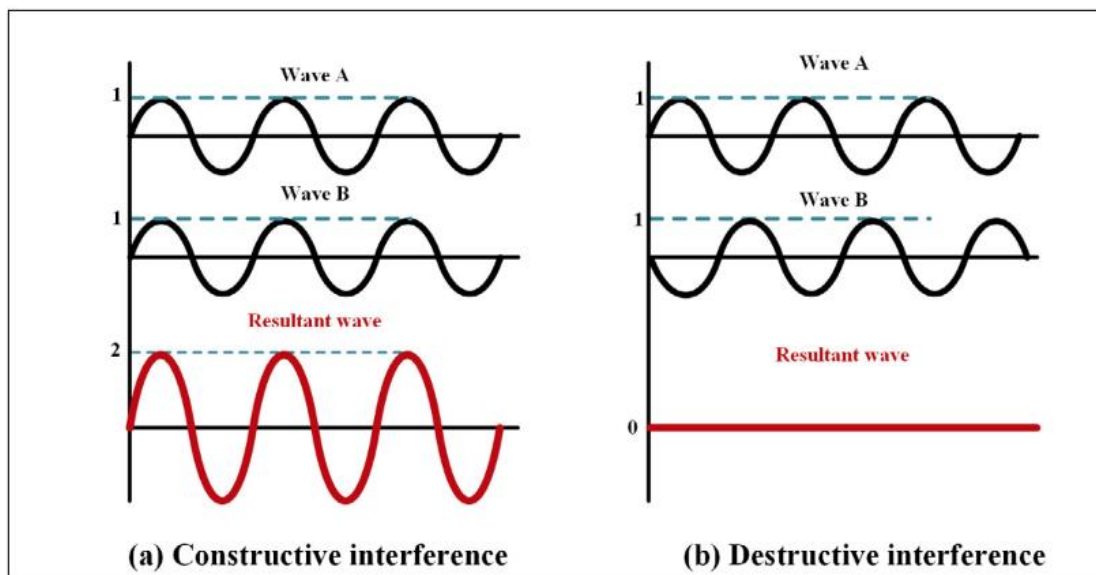


**Figure 3.1.** Two waves of the same frequency interact optically where different interference occurs depending on the phase difference between the waves in multiples of  $\pi$ .<sup>68</sup>

In 1899, the Fabry-Pérot cavity was invented and established as a very effective interferometer for optical applications.<sup>69</sup> Figure 3.2 demonstrates the simple configuration of the linear Fabry-Pérot cavity which is made up of two high-reflectivity mirrors set in parallel where at least one of the mirrors should be a concave mirror. Having one or both mirrors concave prevents beams from escaping the cavity and makes the cavity move optically stable and easier to align.

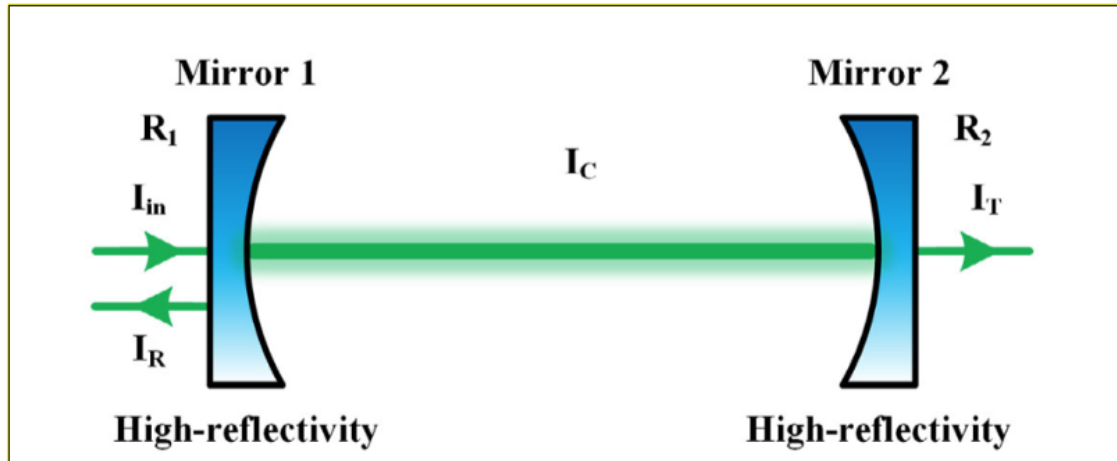


**Figure 3.2.** The basic configuration of a linear Fabry-Pérot cavity.  $I_{in}$  and  $I_T$  represents the laser input and laser output power of the cavity, respectively.  $I_R$  denotes the intensity of the laser beam directly reflected from the first cavity mirror. The intracavity laser power is  $I_C$ .<sup>68</sup>

Multi-beam interference significantly increases laser power inside a Fabry-Pérot cavity in resonance. As a result, to increase the intensity of Raman scattering, a linear Fabry-Pérot cavity is an ideal optical arrangement. In order for a resonance or constructive interference to occur, the cavity length must be a multiple of the laser wavelength. However, since the cavity length cannot be kept stable for an extended period, maintaining the resonance condition is difficult. The cavity length can be readily influenced by mechanical vibrations or changes in temperature. Therefore, a frequency-locking system that preserves the resonance is needed.

The use of a frequency-locking system is particularly important for diode lasers which often have fluctuating output if not stabilised. This then allows the use of laser diodes as a low-cost light source. One of the frequency-locking option techniques is an Optical Feedback Frequency Lock (OFFFL). The optical injection locking phenomenon in semiconductor lasers allows OFFFL. In a brief, the concept of optical injection locking describes a master laser which is the laser source from a single-mode laser that emits radiation and is injected into a slave laser (another laser source), with the master laser's frequency and phase characteristics replicated by the slave laser. In this concept, the laser source is the slave laser in OFFFL, while the Fabry-Pérot cavity serves as both the standard frequency and the master laser. The following is a summary of the OFFFL principle: Firstly, the Fabry-Pérot cavity with a high fineness is injected by laser radiation from the laser source (diode laser). If the laser radiation has a frequency corresponding to a cavity resonance frequency, a resonance builds up and exits the cavity. Secondly, the cavity then emits a laser beam which is now in resonance with the injecting laser

source. Thirdly, the master laser (cavity) which has now a laser output that is precisely at a resonance frequency is copied to the slave laser (laser source) using optical injection locking. In this way, due to interference, a large power build up in the cavity occurs. Note that the laser beam transmitted directly from the first entry mirror of the two-mirror cavity would also be fed back to the laser source. This feedback is unwanted since the reflected light has not passed the cavity and has therefore not the correct resonance frequency. If the directly reflecting beam cannot be removed, unwanted locking can take place. The trick of successful OFFL is to find a way to have feedback from the cavity output while blocking the directly reflected laser beam. Not all lasers are susceptible to OFFL. The laser source in OFFL is most often a semiconductor laser<sup>70,71</sup>, for example, a quantum cascade laser or laser diode.

Optical isolators are one of the methods applied to block the directly reflected beam. This approach was developed in previous research conducted by Hippler *et al.*, using a Fabry-Pérot cavity with OFFL for the gas sensor to implement CERS.<sup>72</sup> Figure 3.3 illustrates the previous experimental set-up of the Fabry-Pérot cavity with OFFL used in CERS.<sup>38</sup> Two high-reflectivity mirrors (SM) are separated by 35 cm to create the Fabry-Pérot cavity. The cavity is placed in a vacuum-tight glass enclosure with external windows. Typically, 10 mW linearly polarized laser radiation at approximately 635 nm is provided by a single-mode laser diode. An aspheric lens (L) collimates the laser beam, an anamorphic prism pair (AP) converts the elliptical laser spot into a circular, and a spatial filter (SF) uniformizes the laser beam intensity distribution. The laser is coupled into the cavity by using a mode matching focusing lens (ML). Two Faraday isolators (FI) protect the diode from the directly reflected beam from the entry mirror of the cavity. The laser output from the Fabry-Pérot cavity is returned for optical feedback into the laser diode (LD) *via* the first isolator's exiting polarizing beam-splitting cube. A rotating polarizer (rPol) controls the intensity of feedback light injection. For efficient feedback, the returned light must have the same phase than the emitting diode. This phase matching is achieved by adjusting the mirror (PM) mounted on a piezoelectric transducer (PZT). The Raman scattered light and laser radiation from the cavity are separated by a dichroic mirror (DM). After the dichroic mirror, the Raman-scattered light is focussed into a fibre and passed to the monochromator and CCD detector. The gain factor of laser power has been measured as 833, meaning if a laser power of 3 mW is added to the cavity, resulting in approximately 2.5 W inside the cavity.<sup>38,73</sup> This apparatus has a LOD of 50, 100, 140 and 1000 ppm for CH<sub>4</sub>, H<sub>2</sub>S, H<sub>2</sub> and N<sub>2</sub>, respectively, with a 30s integration time.<sup>38</sup>

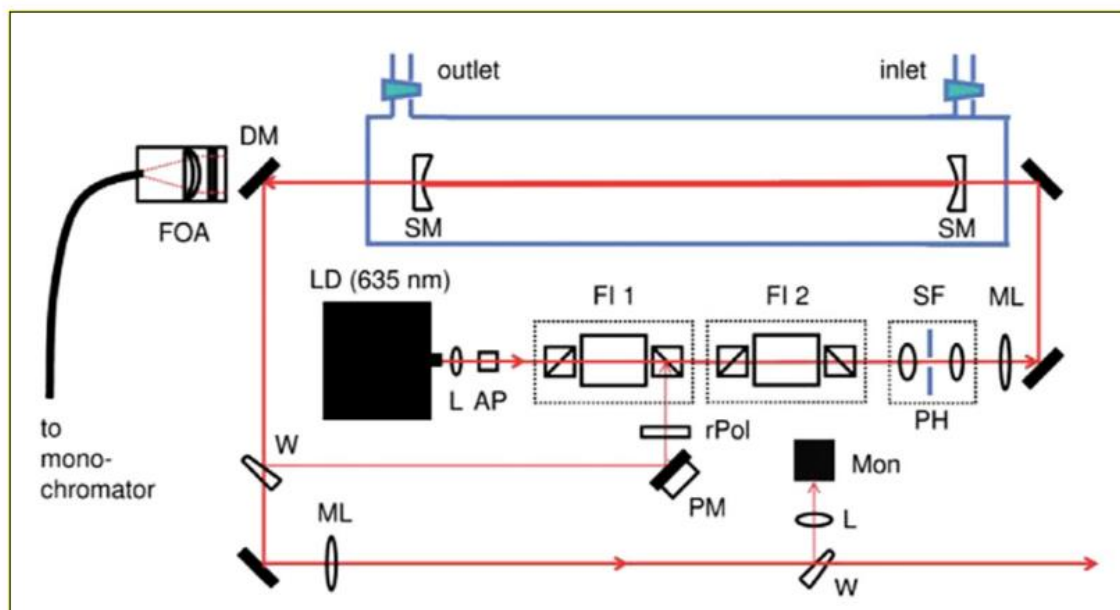


**Figure 3.3.** Optical isolators in the set-up of the Fabry-Pérot cavity with OFFFL in CERS.<sup>38</sup>

In previous research conducted in 2018 by Sandfort *et al.*,<sup>74</sup> a Fabry-Pérot cavity was utilized with a Pound–Drever–Hall frequency stabilisation of the laser frequency to the cavity resonance (PDH framework) for multi-gas sensing through CERS for food chain management. This is an alternative approach to OFFFL. As a light source, a 780.2 nm external-cavity diode laser was employed. Two concave mirrors separated by 38 mm provided the enhancing cavity. The mirrors have a radius of curvature of 0.5 m and a reflectivity higher than 99.85 %. Intracavity laser output exceeded 2.46 W with 2.9 mW incident power, resulting in a laser power gain factor of around 850. This instrument had LODs of 1412, 317, 261 and 3540 ppm for O<sub>2</sub>, CO<sub>2</sub>, C<sub>2</sub>H<sub>4</sub> and N<sub>2</sub>, respectively, using a 30-second integration time.<sup>68</sup>

### 3.1.2 Aims

In order to detect biologically relevant homonuclear diatomic molecules in the gas phase such as N<sub>2</sub> and O<sub>2</sub>, cavity enhanced Raman spectroscopy (CERS) is required. Some commercial optical components have been used for the construction and characterisation of such a new set-up. CERS has been employed for the detection of O<sub>2</sub> and N<sub>2</sub> from ambient air at 1 atm to demonstrate the utility of CERS for gas phase spectroscopy. It was beneficial to make this set-up portable, compact and smaller so that it could be used in many applications

such as detection of O<sub>2</sub> consumption by banana aerobic respiration, or monitoring the metabolism (O<sub>2</sub> consumption, CO<sub>2</sub> production) of microbes under different conditions. These applications will be introduced in detail in the two following chapters.

## 3.2 Experimental

### 3.2.1 Cavity Enhanced Raman Spectroscopy with Optical Feedback

A new CERS set-up has been constructed. The system relies on optical locking of a low power diode laser (Hitachi HL63133DG, 170 mW, 637 nm, LD) to an optical cavity which is composed of two concave high reflectivity mirrors (SM, Newport SuperMirrors, 583 – 633 nm,  $R > 0.9998$ , 1 m radius of curvature). The power build-up within this optical cavity can be used to enhance Raman scattering of gases between the mirrors in the closed system. CERS is well suited to detect homonuclear diatomic molecules that are IR inactive. The set-up is based on previous CERS experiments constructed in Dr. Hippler's group,<sup>73</sup> but has some important modifications as described below. Fig. 3.4 shows a scheme of the set up, and Fig. 3.5 shows a photograph.

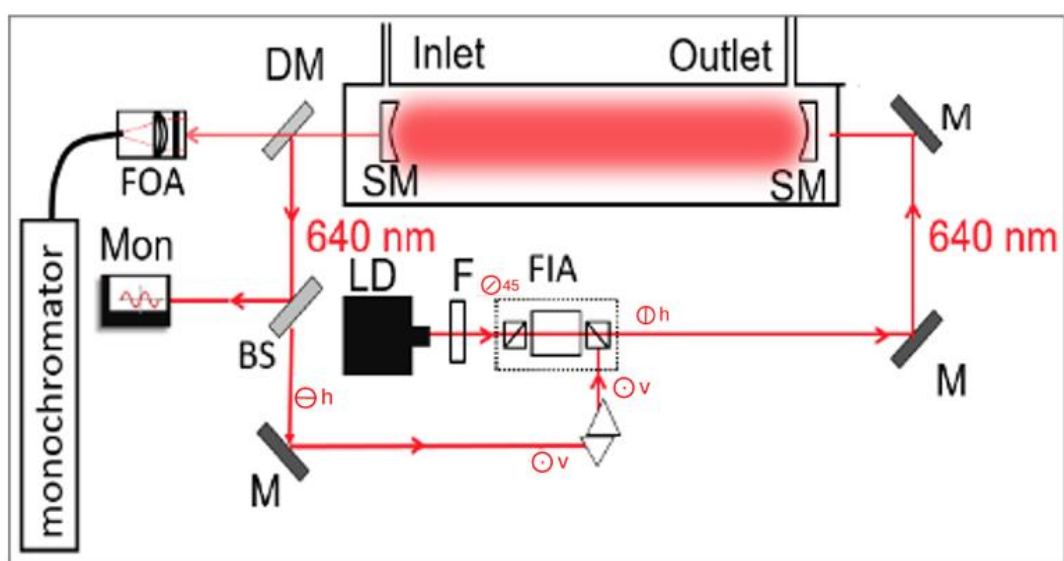


**Figure 3.4.** Scheme of the CERS setup. BS- beam splitter, DM- dichroic mirror, F- short pass filter, FIA- Faraday isolator assembly, FOA- fiber optic assembly, LD- laser diode, M- mirrors, Mon- monitor photodiode, SM- super mirrors.

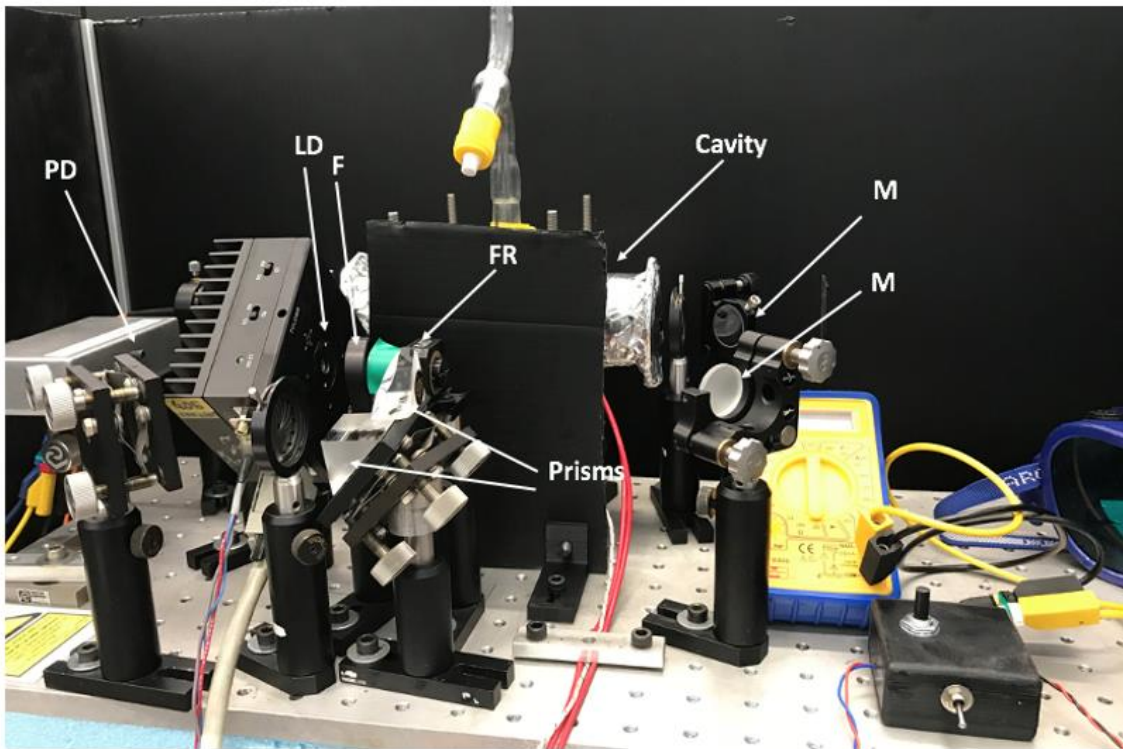


**Figure 3.5.** Front view of the CERS set-up.

To maintain stable operating conditions, the laser diode (LD) is mounted inside a temperature-controlled laser diode mount (Thorlabs TCLDM9) controlled by a temperature controller (Thorlabs TED200C) rotated by  $45^\circ$  relative to the laser table to allow the linearly polarized light to enter the Faraday isolator assembly (FIA). After the LD, the laser output passes through a short pass filter (Thorlabs Optics LMR1/M) attached to the laser mount which works as a clean-up filter for the laser in order to get rid of spurious weak emission bands at longer wavelengths that could contaminate the Raman light.

The cavity for the experiment is linear which means that the ingoing beam strikes normal to the back face of the entry mirror. This results in a direct unwanted backward reflection along the path of the incoming beam that could severely damage or destabilize the laser diode. The Faraday isolator assembly is used to prevent unwanted back reflections from the first supermirror into the diode. It consisted of one Faraday rotator and two polarizing beam splitting cubes which allowed transmission of the outgoing beam but rejected the direct back reflection light. To steer the incoming laser light into the optical cavity, a pair of 1-inch mirrors are utilized. A dichroic mirror, DM, (Semrock RazorEdge LPD01-633RS-25) is mounted after

the cavity to allow separation of the leftover excitation light from Raman signals exiting the cavity.

The optical cavity is placed inside a tight glass enclosure which has a 1000 mbar diaphragm gauge attached (PG, Edwards model D35736000) and which is connected via a tap to a vacuum pump to evacuate air and other gases inside the system. In order to prevent water condensation on the windows and the internal optics, a resistive heating wire is wrapped around the cell to heat the cell to 40 – 50° C. An optical cage system (Thorlabs) is used to hold the SM in place, to be locked securely and rigidly in the glass enclosure through custom Teflon mounting rings connecting the cage system with the enclosure.

The Raman light was coupled into a glass fiber and then passed to the monochromator (Shamrock, SR-163). The monochromator has a focal length of 163 mm and is equipped with a 1200 lines/mm grating blazed at 500 nm. The camera of the monochromator (Andor, DU420A-BV) was cooled to – 60 °C by a thermoelectric cooler to reduce electric noise. Effective slit width is given by the 105 µm core diameter fiber. The leftover excitation light was diverted back *via* the dichroic beam splitter to the diode for optical feedback. By using a glass wedge a small part of the laser was diverted to a photodiode to monitor the excitation light intensity. After each mirror, there was an iris which helped to adjust the path of the laser light. For recording Raman spectra, the Andor Solis programme was used to control the monochromator and the camera. For recording spectra, the exposure (integration) time was 30 s. A background spectrum was recorded before the start of measurements, and the background was then subtracted from each Raman spectrum.

Cavity resonances are not very stable, leading to fluctuation in Raman intensity which impacts all bands equally, so by using a suitable internal standard, the signal can be normalised. This is done by using the peak of the N<sub>2</sub> Q-branch (2329 cm<sup>-1</sup>), because the amount of N<sub>2</sub> remains constant inside the system for all planned experiments because N<sub>2</sub> is typically biologically inert for *E. coli* and bananas. Other important gaseous analytes that have been monitored using CERS are O<sub>2</sub> (1556 cm<sup>-1</sup>), CO<sub>2</sub> (1285 cm<sup>-1</sup> and 1388 cm<sup>-1</sup>) and water vapour (3653 cm<sup>-1</sup>).

Through the polarizing beam splitting cube 2 of FIA, a portion of the laser light is diverted back to the laser diode for optical feedback to lock the laser to the optical cavity. By using optical prisms, the linear polarisation of light was rotated by 90° to match the

polarisations of diode laser and feedback light. Before the first polarizing beam splitting cube 1, the laser light was linearly polarized at  $45^\circ$  to the optical bench. Polarizing beam splitting cube 1 allows these components to pass. The Faraday rotator rotates the plane of polarization of the light by  $-45^\circ$ , so that afterward, the light is passed through polarizer cube 2 horizontally polarized with respect to the bench ( $0^\circ$ ). The light coming out of the optical cavity will also be mainly horizontally polarized, however this would make it unsuitable for optical feedback because polarizing beam splitting cube 2 of FIA will only reflect vertically polarized light back to the laser diode in the return path. So, it is necessary to rotate the plane of polarization of light. This is done by a pair of optical prisms, the first diverting the beam by  $90^\circ$  up vertically from the bench and then the second diverting it horizontally. The polarization was thus changed from horizontal into vertical. By polarizing beam splitting cube 2, the light can then pass through the Faraday rotator, where it will be rotated optically by  $-45^\circ$  leading to  $+45^\circ$  polarisation, which can enter the polarizer cube 1 for optical feedback. These optical prisms are important if the system utilizes just one Faraday rotator.

### **3.2.2 Laser Alignment**

After installing all the optical components on the breadboard, the laser had to be aligned to the cavity and the cavity had to be aligned so that the mirrors are exactly parallel. Laser alignment is a specialised skill that requires careful adjustment of mirrors to find the optimum alignment. The mirrors needed to be aligned with the laser by changing the alignment of both controls (horizontal and vertical) of the mirrors simultaneously, one mirror was changed slowly while the other was changed backwards and forwards more rapidly until the best alignment was found. To align the laser to the centre of the optical cavity, an alignment tool with a centre hole was used. After focussing the laser beam to the centre of the cavity, the resonances inside the cavity were monitored in real-time by observing the light intensity coming out as monitored by the photodiode.

The next stage of alignment was to make sure the existing excitation laser light from the cavity super mirror, SM, is a circular and sharp spot corresponding to a pure TEM<sub>0,0</sub> Gaussian mode. This was done by using a piece of white paper and observing the pattern of cavity light on the paper after the cavity. The alignment was adjusted by using the two screws of the controls of the mirrors and an Allen key. The beam was directed to the centre of both mirrors and an alignment iris by adjustment of the mirror's screws.

For optical feedback, the leftover excitation light from the second cavity mirror SM was coupled back to the laser diode (LD). This alignment is helped by the fact that there is some weak light from the diode which is rejected by the second polarising beam splitting cube. This cube is also the back door for returning light as feedback. The rejected light is moving from the second cube to the exit cavity mirror, at exactly the same path as the feedback beam. For an initial alignment, the feedback light from the cavity is traced on the rejected beam path. First resonances are then already seen on the monitor photodiode. Optimum fine adjustment of the feedback path is then made by making these resonances as strong and persistent as possible.

For optimizing Raman signal on the monochromator, a rough alignment was achieved by monitoring the intensity of laser light by eye from SM mirror that was coupled *via* a glass fibre to the monochromator. N<sub>2</sub> in ambient air is used for the alignment of Raman light into the fibre, so in order to optimize the Raman signals, the N<sub>2</sub> peak on the monochromator was monitored while optimising the position of the lens focussing Raman light into the fibre. As the feedback strengthened, resonances in the cavity would build up and N<sub>2</sub> Raman signals increase.

### **3.3 Results and Discussion**

#### **3.3.1 Nitrogen and Air**

To investigate the suitability of the cavity enhanced Raman spectroscopy (CERS) set-up for trace gas detection, firstly the Stokes lines of N<sub>2</sub> and O<sub>2</sub> from ambient air inside the unenclosed cavity were observed. The cavity was unsealed for recording initial air measurements to allow easy access to realign the cavity mirrors and tune the cavity before recording a spectrum. After optimum alignment, the cavity was sealed with external glass windows to give a closed system for monitoring O<sub>2</sub> consumption in aerobic respiration experiments, for example.

Vacuum tightness of the closed system was tested and confirmed. The following conditions, acquisition settings and components for the set-up to record Raman spectra of ambient air have been used. The diode laser current was set at 140 mA, temperature at 20.19 °C, and a sawtooth modulation of the diode current was applied at a frequency of 2 kHz and amplitude at 0.09 vp-p. By this modulation, resonances are found automatically which are then enforced by optical feedback. Raman shift ( $\Delta\tilde{\nu}$ ) peak positions are 2329 cm<sup>-1</sup> for N<sub>2</sub> and 1550

$\text{cm}^{-1}$  for  $\text{O}_2$  and are observed in ambient air. For both homonuclear diatomic molecules, the peak observed was the  $Q$ -branch of the fundamental stretching vibration in-between their unresolved  $O$ - and  $S$ - branches.

To characterise the performance of this new CERS set-up, the Raman spectrum of ambient air is shown in Figure 3.6, recorded with the Shamrock SR-163 imaging spectrograph that was connected to a CCD camera with an exposure time of 30 s. A Gaussian curve was fitted to both  $Q$ -branches giving a full width at half maximum (FWHM) of  $24 \text{ cm}^{-1}$  for  $\text{N}_2$  and  $25 \text{ cm}^{-1}$  for  $\text{O}_2$ . This value was limited by the instrumental resolution of the monochromator. As shown in Fig. 3.6, the  $\text{O}_2$  peak was stronger than expected given that ambient air has about 20 %  $\text{O}_2$  and 80 %  $\text{N}_2$ , and given that Raman scattering cross sections are similar. This was probably due to the monochromator grating which was blazed at 500 nm and therefore more efficient at the  $\text{O}_2$  position. In analytical spectroscopy the signal to noise ratio is very important. Detection limits for CERS were determined by analysing the noise limit. The standard deviation ( $\sigma$ ) of the background noise level that can be detected by the monochromator defines the sensitivity of this technique. It has been determined to be 3 counts per second. A limit of detection ( $3\sigma$ ) in ambient air (210 mbar  $\text{O}_2$  and 790 mbar  $\text{N}_2$ ) was therefore calculated as 5.13 mbar for  $\text{N}_2$  and 1.56 mbar for  $\text{O}_2$  at 30 s integration time. These results show that the set-up can detect  $\text{O}_2$  to low levels which is ideal for monitoring the depletion of  $\text{O}_2$  in aerobic respiration experiments, as discussed in later chapters.

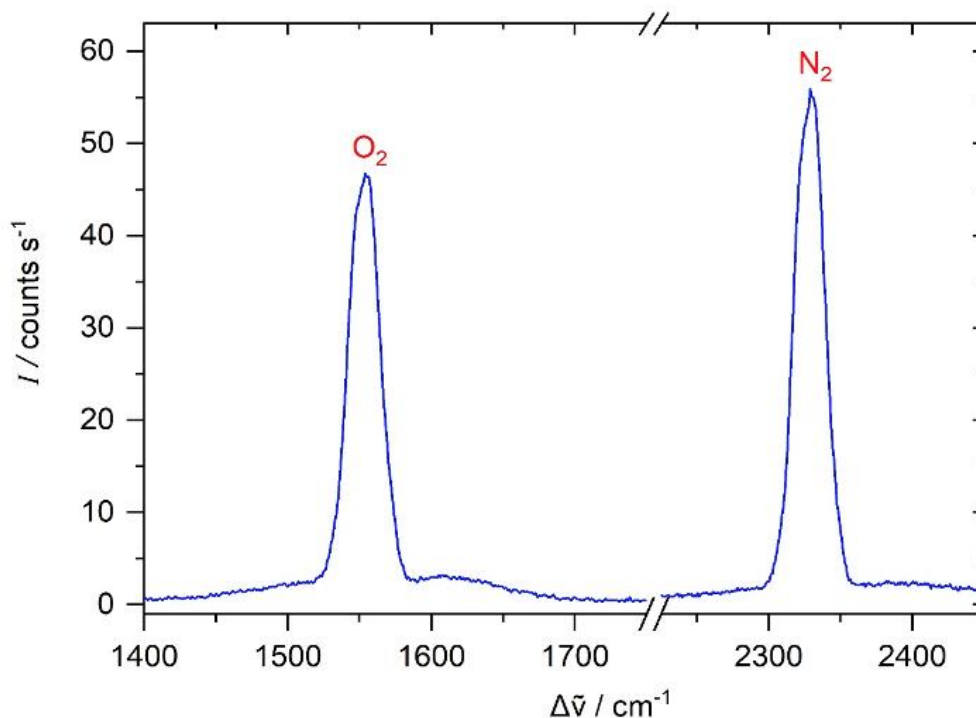


**Figure 3.6.** CERS Raman spectrum of 210 mbar O<sub>2</sub> and 790 mbar N<sub>2</sub> in ambient air, recorded using a Shamrock SR-163 monochromator equipped with an Andor DU420A-BV camera. Both O<sub>2</sub> and N<sub>2</sub> have a strong Q-branch in-between their unresolved O- and S- branches.

### 3.4 Conclusions and Future Works

A new CERS set-up with an optical feedback cw-diode laser at 636 nm excitation has been successfully constructed, aligned and characterised by observing Raman signals of N<sub>2</sub> and O<sub>2</sub> from ambient lab air. A practical application of this technique is to detect homonuclear diatomic gases such as N<sub>2</sub>, O<sub>2</sub> and H<sub>2</sub> which cannot be observed by IR spectroscopy due to selection rules. With this cavity noise equivalent detection limits ( $1\sigma$ ) of 1.71 mbar for N<sub>2</sub> and 0.53 mbar for O<sub>2</sub> at 1 atm total pressure are achieved. Dr. Hippler used a previously a different CERS set-up for multicomponent analysis of natural gas mixtures including H<sub>2</sub>, N<sub>2</sub>, CO<sub>2</sub> and alkanes with low power diode lasers at 636.2 nm.<sup>2,73</sup> The newly constructed set-up is smaller and portable, and still has similar good performance.

Since various gaseous pollutants exist at different concentrations in the atmosphere, monitoring these gases is a scientific and technical challenge that requires sensitive techniques

like CERS. CERS can be used to complement FTIR spectroscopic techniques by detecting gases with unfavourable selection rules. CERS has a wide range of uses and is particularly valuable in biochemistry and biology to monitor the uptake and production of gases and volatiles in fruit ripening and bacterial metabolism, as introduced in the following two chapters.



## **Chapter 4 - Long-Path FTIR and CERS Analysis of Volatiles Produced by Bananas During Respiration and Fermentation**

### **Abstract**

To demonstrate the potential of the analytical set-ups described and characterised in the two previous chapters for biotechnological applications, headspace gases from the metabolism of bananas in a closed system have been monitored. FTIR and CERS both offer non-contact, non-intrusive, *in situ* monitoring without sampling. Monitoring of trace gas levels is very important for applications in biochemistry and biotechnology. For instance, oxygen and carbon dioxide are important gases to be monitored online in bioreactors. O<sub>2</sub> availability is a key parameter for aerobic respiration as well as in anaerobic systems. Real-time, *in situ* gas detection can also give mechanistic insights into metabolic activity. To demonstrate the strength of each technique, CERS monitored O<sub>2</sub> consumption by bananas while FTIR monitored the volatiles produced during aerobic respiration and anaerobic fermentation. By recording simultaneous measurements of O<sub>2</sub> consumption and CO<sub>2</sub> production, the different phases of banana respiration and fermentation were identified. Time-dependent concentrations of ethylene, ethanol, ethyl acetate and acetaldehyde from aerobic respiration and anaerobic fermentation have been obtained. The metabolic changes in the production of volatiles during the respiration and fermentation of bananas was followed with changes noticeably during the different phases of respiration and fermentation. This shows how CERS and White cell FTIR have the potential to be cost-effective, highly specific analytical tools in biochemistry and biotechnology, complementing and superseding existing more conventional techniques.

## 4.1 Introduction

### 4.1.1 Overview of Fruit Ripening

Being rich in nutrients such as organic acids, vitamins and sugars, fruits are nutritious sources of food for human beings and are high value, commercial products. Botanically, fruits are a diverse group that consists of highly complex texture, flavours, aromas and colours ranging from dry to fleshy fruits. Nuts and grains are examples of dry fruits, and bananas and peaches are examples of fleshy fruits.<sup>75</sup> Fruit ripening is a mixture of anabolic and catabolic mechanisms that involve a series of molecular, biochemical and physiological changes. The synthesis of new flavours and pigments is conducted through the various biochemical transitions. Ripening allows the mature plant organ to be even more attractive in terms of taste and appearance to enable seed dispersion. Growth, maturation and senescence are the main stages in fruit development. Each of these phases vary depending on the fruit or commodity. The enlargement of tissue during rapid and substantial cell division defines the growth stage. The maturation stage refers to the process that inevitably leads to ripening of fruits. The final senescence is a degenerative mechanism that is followed by increasing anabolic synthesis and activating catabolic activities.<sup>76</sup> The enhanced anabolic and catabolic behaviours correlate with sub-sequential of death tissues and macromolecular breakdown. Different biochemical and physiological changes vary across various organisms however, where colour changes, loss of firmness, altered sugar metabolism, development of aroma and elevated risk to pathogenic infections are the most significant differences.

Fruit ripening is closely related to the production of the volatile ethylene, a phytohormone that can initiate ripening and cell death (senescence). According to the regulatory mechanism of fruit ripening, fruits are classified into two groups, climacteric and non-climacteric fruits.<sup>77</sup> Table 4.1 illustrates the division of the groups. An effective respiratory peak with a high-level of ethylene biosynthesis exists as the ripening progress continues in climacteric fruits. In non-climacteric fruits, the respiratory rate is almost unchanged or displays a gradual decline before senescence occurs, with no or little rise in ethylene production.<sup>78,79</sup> Climacteric fruits are considered as ethylene-based fruits which can ripen after the harvest, sometimes with the aid of exogenous ethylene. In contrast, non-climacteric fruits only ripen if they are still connected with the parent plant.<sup>44</sup>

Climacteric fruits	Nonclimacteric fruits
Apple	Cashew
Apricot	Cherry
Avocado	Cucumber
Banana	Grape
Blueberry	Grapefruit
Durian	Lemon
Guava	Lime
Kiwifruit	Litchi
Mango	Mandarin
Papaya	Melon
Passion fruit	Orange
Peach	Pineapple
Pear	Pomegranate
Persimmon	Rambutan
Plum	Raspberry
Sapodilla	Strawberry
Tomato	Watermelon

**Table 4.1.** Classification of climacteric and non-climacteric fruits.<sup>80</sup>

#### 4.1.2 Major Factors Affecting Ripening of Climacteric Fruits

Differential gene expression is responsible for ripening, which is affected by phytohormones and environmental factors. The gaseous alkene ethylene is the most significant of the many phytohormones that control fruit ripening. It is essential for the emergence and development of ripening in all climacteric fruits, including bananas.<sup>81</sup> The production of ethylene starts triggering a signal cascade that affects the function of multiple genes involved in the ripening process.

### 4.1.3 Ethylene Biosynthesis

In the late 1970s, Yang and his colleagues discovered the main ethylene biosynthesis pathway.<sup>82</sup> The overall precursor of ethylene is the amino acid methionine. S-adenosylmethionine synthase (SAM synthase) converts methionine and ATP to the intermediate S-adenosylmethionine (SAM).<sup>83,84</sup> The enzymes 1-amino-cyclopropane-1-carboxylic acid (ACC) synthase (ACC-S) and ACC oxidase are active in the subsequent ethylene synthesis pathway (ACC-O). The rate-limiting step in the ethylene biosynthesis is the conversion of SAM to ACC by the enzyme ACC-S.<sup>82</sup> Oxygen is necessary for the conversion of ACC to ethylene. Figure 4.1 shows an overview of the metabolic pathway for ethylene biosynthesis in plants.<sup>84</sup>

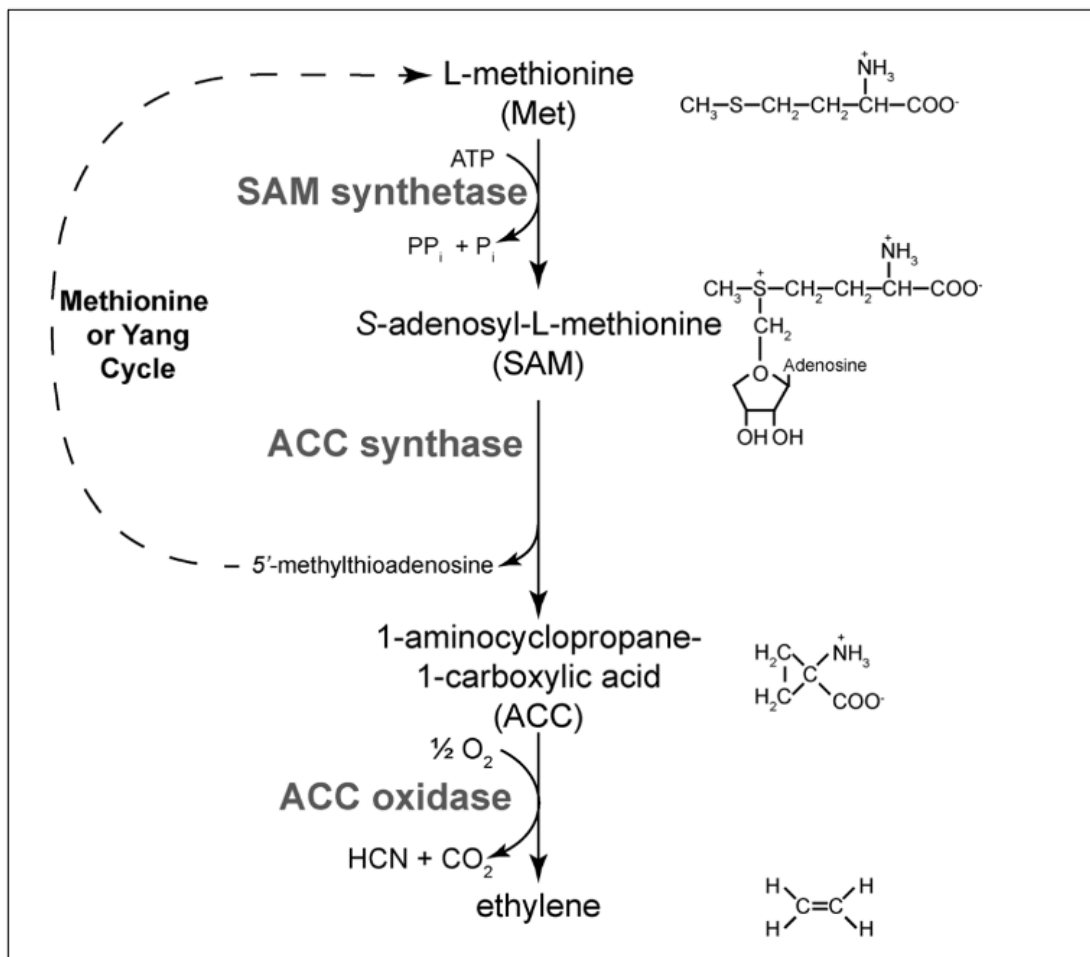


**Figure 4.1.** Metabolic pathway of ethylene biosynthesis in plants.<sup>85</sup>

#### 4.1.4 Ethylene Signalling Pathway

Arabidopsis has been used as a model plant in many previous studies to investigate the ethylene signalling pathway. It is also a model plant for many genetic and molecular studies, including the discovery of the ETR1 (Ethylene receptor). Ethylene receptors are located in the endoplasmic reticulum membrane. Membrane proteins found in bacteria, algae, and plants are identical to these. The ethylene receptor ETR1 was the first to be discovered. Hua *et al.* discovered in 1998 the ERS1 ethylene receptor gene (Ethylene sensor).<sup>86</sup> These enzymes (ETR1 and ERS1) respond differently to applied exogenous ethylene. During the production and ripening process, the ETR1 response is ethylene-independent, while ERS1 is ethylene dependent, and developmentally regulated and tissue-specific. Ethylene starts its activity by binding to membrane-bound receptors, inducing a difference in the binding protein. The message that ethylene is bound to a receptor is communicated through various molecules, activating a signal transduction pathway that leads to the expression of genes and subsequent physiological responses.<sup>87</sup> The receptors are negative regulators, and Constitutive Triple Response (CTR1) is activated in the absence of ethylene. The CTR1 suppresses ethylene response through the deactivation of Ethylene Insensitive 2 (EIN2). It triggers a transcriptional cascade involving Ethylene Insensitive 3 (EIN3)/Ethylene Insensitive 3 like 1 (EIL1) as the primary transcription factor, followed by Ethylene Response Factor (ERFs), thus regulates genes involved in ripening.

Ethylene receptors are made up of two proteins: a sensor that auto-phosphorylates an internal histidine residue in response to signals (*e.g.*, environmental), and a regulator that stimulates the downstream portion after receiving a phosphate from the histidine residue on its aspartate residue.<sup>88</sup>

#### 4.1.5 Respiratory Biochemistry (Respiration in Plants)

Respiration is a critical mechanism in all living cells that allows energy to be released by breaking down carbon compounds and creating carbon skeletons, which are needed for conservation and synthetic reactions after harvest. Living cells of plants constantly respire, using accumulated supplies and oxygen (O<sub>2</sub>) from the atmosphere while releasing carbon dioxide (CO<sub>2</sub>). Respiration is an essential aspect of the metabolic processes taking place in live processed products.<sup>81</sup> The main difference between processed plant products and live products is the loss of respiration. The term "respiration" refers to a sequence of oxidation-reduction

reactions in which several substrates inside the cells are oxidized to carbon dioxide using oxygen from the atmosphere which is consumed and products are excreted as gases. The complete oxidation of glucose can be summarised as follows:



Energy, carbon dioxide and water obtained from this reaction are needed for essential cellular processes. Although some of the energy produced during the respiration of harvested crops is lost as heat (46%), a significant amount remains in chemical forms by the cells which can be utilised for these critical processes.

Free glucose is the chemical substance involved in the initial oxidative step in most situations, however, carbohydrates are not usually stored in the plant in the form of free glucose. Starch is a glucose polymer that is the primary storage of carbohydrates in a plant. It can be converted into glucose or glucose-1-phosphate by enzymes like amylases, maltase and phosphorylase, respectively. Some foods contain a lot of sucrose, which can be hydrolysed into glucose and fructose by the enzyme invertase or converted to UDP-glucose and then glucose-1-phosphate by sucrose synthase. Interconversion of sucrose and starch also occurs in several plant tissues.<sup>81</sup>

Figure 4.2 illustrates a simplified scheme for the initial conversions of storage carbohydrates. Starch and sucrose are converted to glucose and fructose, which are oxidized to other respiratory substrates. Degradation of starch and sucrose is generating the 6-carbon sugars glucose and fructose, which are then oxidized *via* glycolysis. The phosphorylation reactions of glucose and fructose, as well as some of the enzymes involved, are shown in Fig. 4.2. Uridine diphosphoglucose (UDP)-glucose is a crucial nucleotide sugar involved in cell wall synthesis, starch/sucrose interconversions, and other essential carbohydrate interconversions.

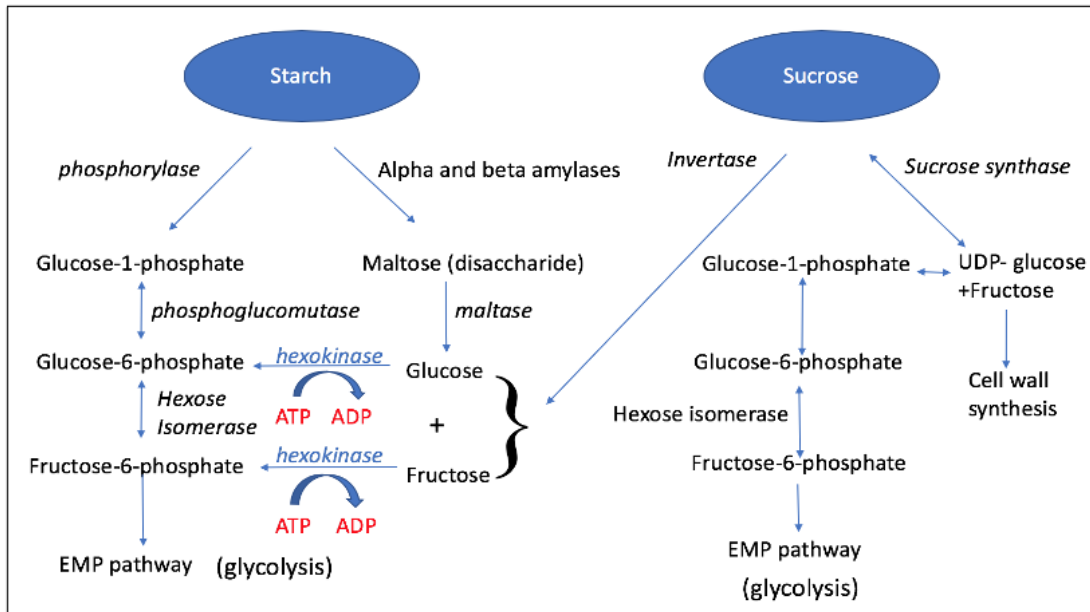


**Figure 4.2:** Simplified scheme for the initial conversions of the storage carbohydrates.

In the respiratory oxidation of sugar or starch, three overlapping pathways are involved in a sequence of steps. Glycolysis is the first step, in which sugar is broken down into pyruvic acid, a three-carbon compound. This pathway can act without oxygen. It is located in the cytoplasm. The tricarboxylic acid (TCA) or Krebs cycle, takes place in the mitochondria and transforms pyruvic acid to carbon dioxide, it is the second pathway. The TCA pathway needs oxygen as well as some organic acids to proceed even though they do not react directly in these steps. The electron transport mechanism, which is located in the inner membrane of the mitochondria, converts hydrogen atoms (reducing power) from organic acids in the tricarboxylic acid cycle and form 3-phosphoglyceraldehyde (third pathway). The electrons travel through a series of oxidation-reduction steps before joining with oxygen to form water. Chemical energy is converted in the form of adenosine triphosphate (ATP) as the energy is utilised to pump protons through a proton channel. ATP is then used to power a variety of energy-intensive reactions within the cell.

Anaerobic conditions can arise during the postharvest handling of plant materials, posing a significant problem.<sup>89</sup> Under anaerobic conditions, pyruvic acid can no longer move through the tricarboxylic acid cycle if the oxygen concentration within the tissue declines below a threshold level which is around 2%. Under anaerobic conditions, pyruvic acid is converted to either lactate or ethanol by fermentation, which can build up to levels toxic to the

plant. In eatable products, short-term exposure to anaerobic conditions often results in the development of off-flavours. The off-flavours can be removed when returning to aerobic environments, however, depending on the tissue and the duration of low oxygen exposure.

If anaerobic conditions arise in the extracted tissue due to limited oxygen entry or inadequate supply in the environment surrounding the product, the tricarboxylic acid cycle does not allow the pyruvic acid to enter the cycle to be oxidised. The failure to join the cycle is caused by a lack of oxidised flavin adenine dinucleotide (FAD) and NAD, both of which are necessary for the cycle to continue. Pyruvic acid builds up at this stage, this usually creates CO<sub>2</sub> and acetaldehyde from the decarboxylated processes which is then converted to ethanol. Lactic acid may also be produced as pyruvate is reduced. Lactic acid and alcohol accumulate in the tissues.

NADH supplies the energy needed for both reactions, the oxidation of 3-phosphoglyceraldehyde and the previous pathway. The simplified reaction mechanism is displayed in the following equation:



where P<sub>i</sub> is inorganic phosphate, ATP is adenosine triphosphate, ADP is adenosine diphosphate. Two ATP molecules are needed to generate ethanol from glucose, but four are produced from each free glucose molecule, producing a net yield of two ATPs in the anaerobic fermentation. This represents a quarter of the energy yield extracted from the glycolytic pathway when adequate oxygen supply is available, and only 1/16 of the energy yield obtained when glucose is completely oxidized in the glycolysis and aerobic tricarboxylic acid cycle. Under aerobic conditions, one glucose molecule produces 32 ATP equivalents, while under anaerobic conditions, a glucose molecule produces only 2 ATP equivalents. Although anaerobiosis has negative implications for living tissue in terms of the depletion of accumulated reserves and the aggregation of unwanted substances, it is the base of fermentation, an important biochemical process in biotechnology.

#### 4.1.6 Aroma of Fruits

Aroma is a term used to describe the odour of the fruit. The overwhelming amount of analytical flavour studies have concentrated on the volatile constituents because the aroma is crucial to flavour perception. The volatiles found in most fruits are made up of a diverse range of chemical compounds. Lactones, ketones, aldehydes, acids, alcohols, acetals, esters, phenols, thiols, ethers, hydrocarbons, and heterocyclic oxygen compounds are the most relevant examples among them.<sup>90,91</sup>

Typically, volatiles in fruits are found in trace quantities that are less than 100 ppm. (100 parts in million parts, per volume) Examples of the concentration of volatiles found in banana, cucumber and strawberry are 12-18 ppm, 17 ppm and 5-10 ppm, respectively.<sup>92,93</sup> Even though there are many volatiles that can contribute to fruit taste, only a few of them are responsible for the aroma.

The majority of flavour compounds are generated as the fruit ripens. A number of differences in biochemistry and physiology reactions are involved in this process. All processes in fruit ripening, such as softening, hydrolysis of storage material, flavour, climacteric respiration and changes in pigmentation, are generally activated and initiated by ethylene, although it is produced only in a small trace amount during a short period of ripening. According to previous studies,<sup>94</sup> increased membrane permeability in response to ethylene may cause increased respiration levels and correlate to precursors produced for flavour compounds.

Fruit aroma is produced naturally by metabolic pathways that produce the flavour compounds. Fatty acid, amino acid and carbohydrate conversions are the main metabolic pathways.<sup>95</sup> The first two pathways are the primary contributors to banana flavour biogenesis. Alcohols, ketones, aldehydes, esters and phenol esters are examples of volatile compounds produced by ripening bananas. Typically, up to 70% of the volatiles is accounted for by esters.

Off-flavour grows in fresh fruits and vegetables either under low concentration of O<sub>2</sub> or high CO<sub>2</sub> environment. It is believed to be caused by the aggregation of fermentation products such as acetaldehyde, ethanol, ethyl acetate, and perhaps other volatiles.<sup>87</sup> The ethanol content of fruits has a logarithmic association with alcoholic off-flavour. It is the most significant damaging impact of fruit exposure to low O<sub>2</sub> levels.

#### **4.1.7 Banana**

The banana (botanical name *Musa spp*) is among the world's most commonly grown and eaten fruit crops. It is thought to be one of the first fruit crops to be grown at the start of humanity. Native fruits to Southeast Asia are bananas, and bananas are now grown in over 130 countries around the world in tropical and subtropical climates.<sup>80</sup> After rice, wheat, and maize, it is the world's fourth most important food crop. Bananas are cultivated worldwide in 5.6 million hectares at a yield of about 114 million metric tons per year. Around half of the overall banana production is eaten cooked, referred to as plantains, with the remainder being dessert varieties. In terms of banana production, Brazil, India, and the Philippines are the top three countries.

The peel and pulp are the two primary ingredients of the banana. Several layers of hypodermal parenchyma are deeply embedded with vascular bundles, chloroplasts containing chlorophyll, latex vessels and other pigments throughout the peel. Due to the vast number of starch grains in mature and unripe tissues (typically 20-23% in fresh pulp), the composition of banana pulp varies and is difficult to establish.<sup>96</sup> A comparatively high portion of peel in banana fruit is accounted for by about 80, 40, and 30 % of the fresh weight of juvenile, mature, and ripe fruits, respectively, which is one distinguishing feature of bananas.

#### **4.1.8 Anaerobic Respiration and its Products**

Once plants are subjected to anoxic environments, their carbohydrate metabolism changes from oxidative to fermentative metabolism.<sup>97</sup> At first, deactivation of pyruvate decarboxylase (PDC) occurs and then the lactate dehydrogenase (LDH) is triggered. This leads to lactate aggregation and the pH reduces. Pyruvate decarboxylase and alcohol dehydrogenase (ADH) is initiated at this stage. PDC produces acetaldehyde, and ADH reduces acetaldehyde into ethanol. The acetaldehyde needs to be directly removed after its production process as this compound is highly toxic.<sup>98</sup> As a consequence, ADH is essential in preventing cell toxification. The pH of the cell is stabilised when ethanolic fermentation happens, and plants can survive.

Acetaldehyde is a plant metabolite that exists in small quantities in nature. For instance, banana has about 5 mg/100 g fresh weight, while apples contain 0.5 mg/100 g fresh weight.

Acetaldehyde concentrations increase dramatically when anaerobic fermentation or senescence processes are involved. Acetaldehyde is considered to be more cytotoxic than ethanol.<sup>98</sup>

Ethanol is present in nature, either in a free form or in an esterified state. In the plants it can be abundant, but in germinating seeds, fruits and root tips, it exists only in trace quantities. The reduction of acetaldehyde in the presence of NADH produces ethanol under an anaerobiosis reaction. Therefore, ethanol production is caused by a rise of acetaldehyde concentration. The acetaldehyde:ethanol ratio is frequently of the order of 1:100.<sup>99</sup> Ethanol is the most abundant of the alcohols found in the banana pulp. Through the reaction of alcohol acyl CoA transferase, it can convert into aroma esters, acetate and butyrate.<sup>100</sup> Esterase is an enzyme that catalyzes the AAT (alcohol acetyltransferase) reverse reaction related to the production of esters in microorganisms and fruits.<sup>101,102</sup> The presence of ethanol that anaerobically forms in pulp banana can cause a significant decrease in the production of ethyl acetate. The production of ethyl acetate increases in anaerobic conditions as acetaldehyde in bananas are produced from acetyl CoA.

#### **4.1.9 Methodology for Investigating the Production of Volatiles in Fruits**

One of the most significant characteristics of foods in evaluating market approval is flavour. Analysis of volatile flavours has been performed in the past using several approaches. Powerful analytical techniques are essential to the development of quality assurance during the product processing, storage, or production stages, especially in the fruit-producing or fruit-processing industry. Gas chromatography (GC) or gas chromatography/mass spectrometry (GC/MS) is widely used to evaluate volatiles extraction. Almost every fruit volatile can be detected using these techniques due to their high sensitivity and wide detection range. Several sample preparation approaches can be used based on the process of sample selection. Thermal desorption of Solid Phase Micro Extraction (SPME) fibres in temperature-programmable injection ports, thermal desorption of collection tubes, liquid injection and cold on-column injection of headspace samples are some of these options.<sup>103</sup> Although the latter technique needs specialist tools, the use of collection tubing has a range of benefits, including versatility in collection volumes and remote sampling. Hence, it leads in general to good analysis accuracy.

Solid Phase Micro Extraction (SPME) is one of the technologies used for food flavour analysis<sup>104</sup>, for example for melons, grapes and bananas.<sup>105</sup> SPME involves the use of a fiber that is inserted into a hollow needle of a syringe. The fiber, for example a fused silica fiber coated with an absorbent or stationary phase, acts as a sponge to extract a sample and concentrate the organic analytes on its surface so that they can be transferred to a heated GC injector. While in the injector, the analytes are thermally absorbed from the fiber and transferred to the GC column for analysis.<sup>106,107</sup> This SPME method becomes more commonly used as a volatile sampling method for fruit volatile analysis due to the lack of extraction solvents, its speed and sensitivity. It can detect volatiles in parts per billion (ppb) concentrations. However, SPME can only provide a semi-quantitative analysis of volatiles due to the matrix impacts, low repeatability, problems with calibration and site competitiveness on the adsorbent fibre.

The study of volatiles in bananas to monitor the degree of maturity is often conducted by using a headspace solid-phase microextraction (HS-SPME) approach. Over the past few decades, HS-SPME is the most common technique used to investigate the aroma profile of fruits. In HS-SPME, the fiber is inserted directly into the headspace of the vial to extract the sample. After some appropriate time, the analytes in the solution phase diffuse into the headspace, and the fiber is exposed to the headspace. The fiber is then withdrawn from the headspace of the vial and transferred to a GC for analysis, after a suitable time.<sup>106,107</sup> This method is also generally utilised for flavour analysis in food samples owing to its simplicity, speed and reliability. As a disadvantage, the method is sample matrix dependent.

Spectroscopy is an alternative technique for qualitative and quantitative analysis of headspace compounds. Spectroscopy has many benefits over other approaches since it allows non-contact detection, it can simultaneously measure several components and has high sensitivity and selectivity. Infrared spectroscopy has been used to measure volatiles released from rotting fruits in recent years.<sup>108</sup> However, it was discovered that measuring volatiles at very low concentrations is difficult using traditional infrared spectroscopy. Increasing the optical pathlength is a possibility explored in this thesis to enhance infrared spectroscopy sensitivity. The identification of several compounds such as esters and alcohols produced during the degradation of grapes and strawberries has been completed using this method<sup>108</sup> to establish a model for classifying the different rotting stages.<sup>108</sup> Infrared spectroscopy with a

long optical path has also been used to analyse compounds volatilised from Chinese wine and vinegar, and a system has been established for wine and vinegar species detection.<sup>108</sup>

#### **4.1.10 Aims**

The detection of volatile species released by bananas is described in this chapter as an application of CERS combined with long-path FTIR spectroscopy. Using these approaches, aerobic respiration and anaerobic fermentation by banana metabolism has been monitored and characterised. CERS is essential to monitor aerobic respiration of bananas because it can monitor oxygen levels in the headspace. Volatile products of banana metabolism can be monitored in the headspace by FTIR spectroscopy including, ethylene, acetaldehyde, ethyl acetate and ethanol. According to selection rules, homonuclear diatomic molecules such as O<sub>2</sub>, N<sub>2</sub> and H<sub>2</sub> are only Raman active because they have a symmetric stretching vibration. Continuous measurements of O<sub>2</sub> consumption by bananas can only be obtained utilizing CERS. CERS can also monitor CO<sub>2</sub> production effectively, since FTIR with a White cell tends to be too sensitive to the abundant and strong IR absorber CO<sub>2</sub> and easily saturates. The aim of this chapter is a demonstration of the home-built CERS and White cell instruments as powerful analytical tools in biotechnology, with a relevant application monitoring the transition from aerobic respiration to anaerobic fermentation in banana.

## 4.2 Experimental Details

A brief outline of the experimental apparatus used to monitor banana respiration is presented here. The set-up is based on a combined FTIR and Raman set-up, used for monitoring banana metabolism in a closed system. Both White cell FTIR and CERS have been described in more detail in the previous chapters.

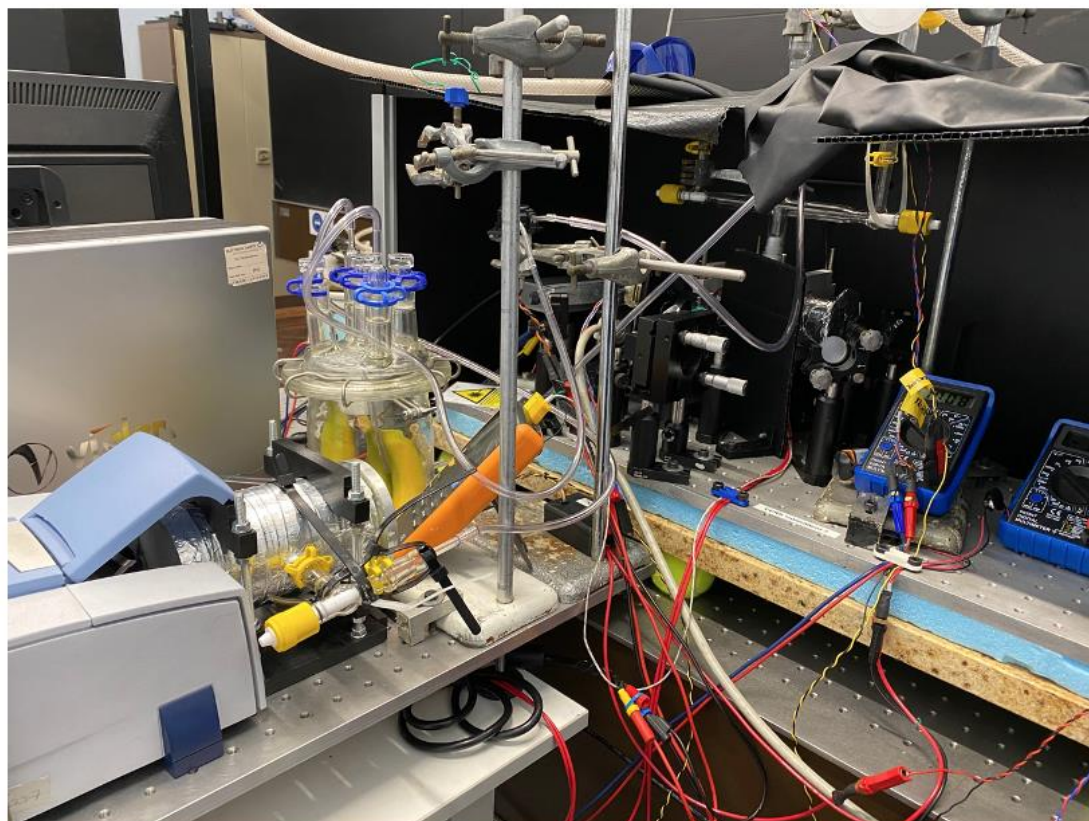


**Figure 4.3.** Photo of the experimental set-up. About 3 bananas (origin Ghana, Volta River Estates, Co-op, Fairtrade Small Bananas) were placed in a respiration chamber where volatiles emitted from bananas in the headspace are cycled using a peristaltic pump in a closed system. The volatiles are cycled for gas phase FTIR measurements in a long path White cell and to a cell with CERS.

The set-up consists of a respiration chamber containing bananas, initially under 1 atm of lab air. The headspace is cycled in a closed, airtight system by a peristaltic pump (3 L/h) to a White cell for FTIR measurements and to a CERS cell for Raman measurements. A photo of the set-up is shown in Fig. 4.3. The total headspace volume containing the respiration chamber and the two cells is about 2.4 L.

## 4.2.1 FTIR Measurements

Production of ethylene, CO<sub>2</sub>, acetaldehyde, ethyl acetate and ethanol in the closed system were monitored by FTIR spectroscopy (Bruker Alpha) with a home-built White cell attached, taking recordings every 300 s continuously at a spectral resolution of 0.8 cm<sup>-1</sup>. The home-written kinetics program uses the Bruker OPUS software to record FTIR spectra automatically and continuously. Trace quantities of volatiles produced were determined using the FTIR instrument with a multiple pass long path absorption White cell (home built) as described in chapter 2. The White cell has 20 passes at a base length of 10 cm, giving a total pathlength of 2.0 m. The temperature of the White cell was kept at 45° C using heating wire to prevent water condensation. The spectral range of the instrument is from 350 cm<sup>-1</sup> to 7000 cm<sup>-1</sup>. Ethylene, CO<sub>2</sub>, acetaldehyde, ethyl acetate and ethanol partial pressures were detected by FTIR spectroscopy using reference spectra and applying the Beer-Lambert law. Absorbance spectra were calculated as  $\lg(I_{background}/I_{sample})$ , using the decadic logarithm.

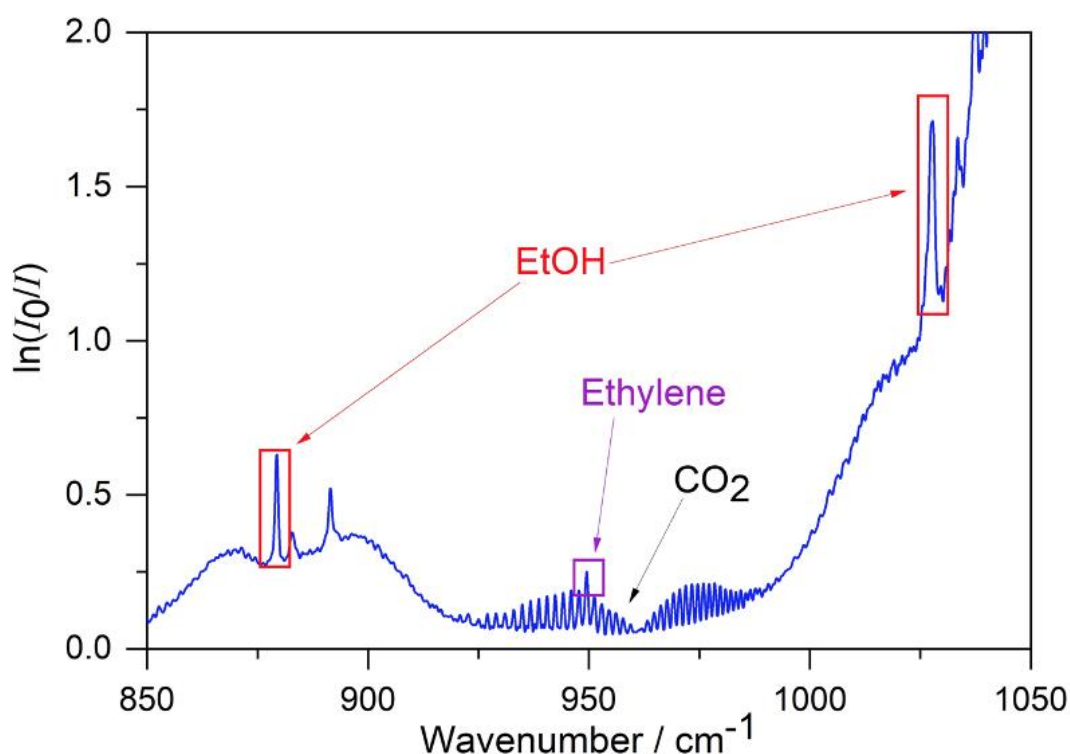


**Figure 4.4.** An absorption spectrum of the  $\nu_{10}$  and  $\nu_4$  C-O stretching vibration bands of EtOH showing molecular absorption as a function of wavenumber. The regions of the bands integrated in experimental spectra to determine  $p$  (EtOH) are indicated in a red box.

Fig. 4.4. shows a typical experimental FTIR spectrum obtained of the headspace in banana respiration. Apart from CO<sub>2</sub> in the 4905-5033 cm<sup>-1</sup> overtone region (see Fig. 4.5 below), absorption bands of compounds are in general overlapping and a multicomponent fit of several reference spectra is required to get partial pressures of individual components. This procedure is explained in the Results and Discussions section below.

## 4.2.2 CERS Measurements

The O<sub>2</sub> consumption was analysed by using gas phase Raman spectroscopy using the home-built cavity enhanced Raman spectroscopy (CERS) set-up described in the previous chapter 3. Briefly, the cw-red Raman excitation light source is a 637 nm, 170 mw diode laser (Hitachi HL63133DG). For recording Raman spectra, Andor Solis imaging and spectrograph software controlled the Shamrock SR-163 monochromator and the CCD camera cooled to -60 °C. For recording spectra, the exposure time was 30 s. To evacuate the CERS cell, a vacuum pump was connected to the system and a background spectrum was recorded at the start of the experiment. To fill the system with laboratory air, a gas inlet valve was opened. Then the respiration chamber containing the bananas was connected where a peristaltic pump was cycling the headspace through the White cell and the CERS cell in a closed loop. When the air inlet valve was closed, the set-up was now a closed system to be ready for continuous Raman and FTIR measurements. The kinetic acquisition mode in the Andor Solis software was used to record Raman spectra every 200 s. A microprocessor programmed by Arduino worked in synchronisation with the 200 s interval of the kinetics acquisition mode. Switching on and off of the laser diode in synchronisation with the measurements was controlled by the Arduino microprocessor. In addition, the laboratory temperature and the total partial pressure inside the closed system of the CERS set-up as measured by a capacitance pressure gauge have been recorded by the Arduino microprocessor.

Cavity resonances are not very stable, leading to fluctuation in Raman intensity which impacts all bands equally, so by using a suitable internal standard, the signal can be normalised. This is done by using the peak of N<sub>2</sub> *Q*-branch stretching vibration (2329 cm<sup>-1</sup>), because the amount of N<sub>2</sub> remains constant inside the system since the bananas do not produce or consume N<sub>2</sub>. Gaseous analytes that have been monitored by CERS are the *Q*-branch of the stretching vibration of the O<sub>2</sub> (1556 cm<sup>-1</sup>) and the Fermi resonance pair of CO<sub>2</sub> (1285 cm<sup>-1</sup> and 1388 cm<sup>-1</sup>).

To determine the partial pressure of O<sub>2</sub> and the partial pressure of CO<sub>2</sub>, integrals of the peak areas of the CO<sub>2</sub> and O<sub>2</sub> were divided by the peak area of the N<sub>2</sub> for normalisation and corrected for the different Raman cross sections of N<sub>2</sub>, CO<sub>2</sub> and O<sub>2</sub>.<sup>2</sup> This procedure results in a value that indicates the O<sub>2</sub> and CO<sub>2</sub> fraction compared to N<sub>2</sub>. The amount of partial pressure of N<sub>2</sub> remains constant inside the closed system at 790 mbar as N<sub>2</sub> is not used in the metabolism of banana respiration. The partial pressures of O<sub>2</sub> or CO<sub>2</sub> are determined by multiplying the fraction of O<sub>2</sub> or CO<sub>2</sub> compared to N<sub>2</sub> against 790 mbar, the abundance of N<sub>2</sub> in 1 atm lab air.

## **4.3 Results and Discussion**

### **4.3.1 Gas Phase FTIR Spectroscopy with White Cell for Ethylene, CO<sub>2</sub>, Acetaldehyde, Ethyl acetate and Ethanol Analysis**

All FTIR spectra were recorded utilizing the 2.0 m White cell over the spectral range of 350 to 7000 cm<sup>-1</sup> with a spectral resolution of 0.8 cm<sup>-1</sup> to determine gas phase species from the banana's metabolism. CO<sub>2</sub> is one of the most indicative compounds of the banana's metabolism. The main CO<sub>2</sub> absorption bands cannot be utilized for its quantification by FTIR spectroscopy because of saturation even at ambient levels. The Fermi resonance triad and associated hot bands in the 5000 cm<sup>-1</sup> overtone regions were used to quantify the partial pressure of CO<sub>2</sub>. This region was found to be very convenient because it does not suffer from interferences with other bands. To generate the reference absorption spectrum with a known  $p$  (CO<sub>2</sub>), absorption cross sections for CO<sub>2</sub> were retrieved from the HITRAN database<sup>6</sup> and broadened by the instrumental 0.8 cm<sup>-1</sup> resolution with a self-written computer programme. The integral of the Fermi resonance triad and associated hot bands of CO<sub>2</sub> (4905 – 5033 cm<sup>-1</sup>) was used to get partial pressures  $p$  (CO<sub>2</sub>), as shown in figure 4.5 below. By comparing the integral in the reference spectrum from the HITRAN database with the experimental FTIR spectrum, the partial pressure of the CO<sub>2</sub> of the headspace above bananas metabolism was obtained.

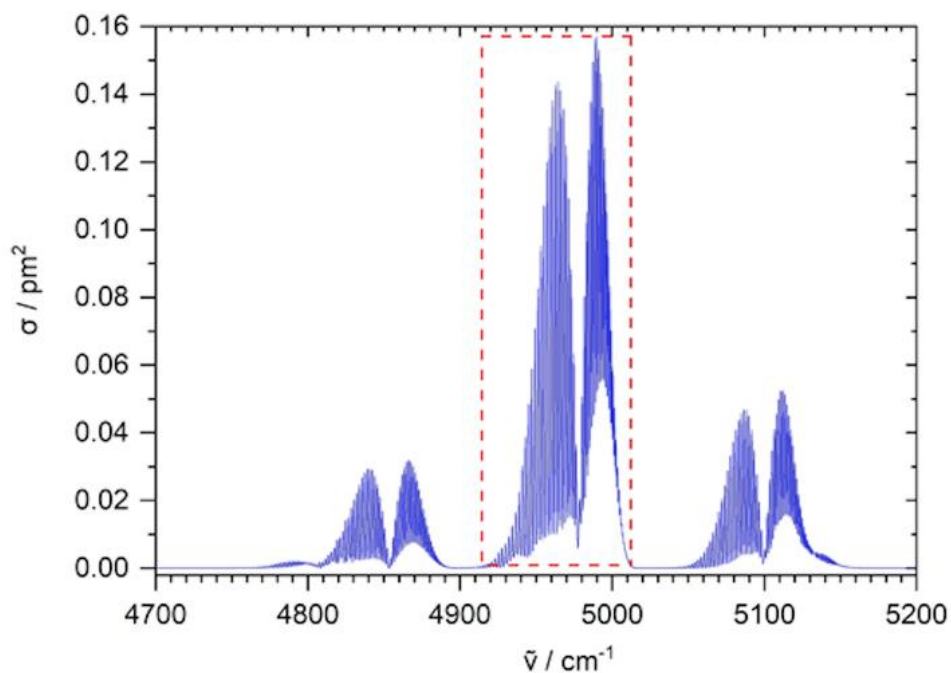


**Figure 4.5.** Stimulated absorption spectrum of the Fermi resonance triad and associated hot bands showing molecular absorption cross-sections as a function of wavenumber. The data is convoluted with Gaussian broadening to simulate the  $0.8 \text{ cm}^{-1}$  instrumental resolution of the Bruker Alpha FTIR. The red dashed box indicates the region of the band integrated in experimental spectra to determine  $p(\text{CO}_2)$ .

Further products of banana metabolism can be determined in the headspaces above banana respiration by FTIR spectroscopy, in particular ethylene, acetaldehyde, ethyl acetate and ethanol. Ethylene plays an essential role in the ripening of fruits by regulating a set of ripening associated processes, as discussed in the Introduction. Ethylene is essential in the production of volatiles of bananas. The characteristic spectral signature of ethylene is the CH-bending vibration  $\nu_7$  at  $949.44 \text{ cm}^{-1}$  on top of  $\text{CO}_2$  absorptions (see Fig. 4.6), so there is an overlap between  $\text{CO}_2$  features and ethylene features. Experimental FTIR spectra in the region  $930\text{-}960 \text{ cm}^{-1}$  were simultaneously fitted to the sum of an ethylene reference spectrum (PNNL database)<sup>109</sup> and  $\text{CO}_2$  reference spectrum (HITRAN database)<sup>6</sup> and a linear baseline (see Fig. 4.6). The multipliers of the reference spectra were then converted into partial pressures. The partial pressure of ethylene was then used. The partial pressure of  $\text{CO}_2$  was not used further, because the integration of the  $\text{CO}_2$  overtone gives more accurate  $p(\text{CO}_2)$  values.

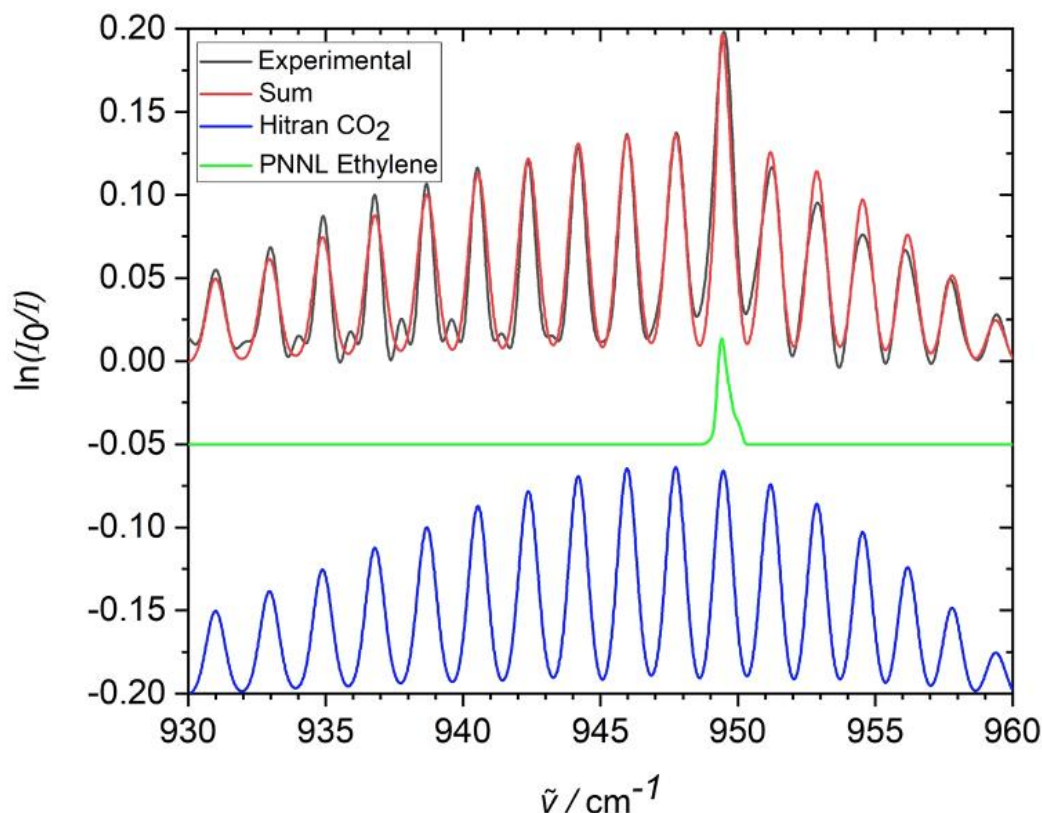


**Figure 4.6.** FTIR absorbance spectrum of banana headspace with fitted PNNL and HITRAN model spectra. In black is the experimental spectrum, the PNNL model spectrum of ethylene is in green, the HITRAN model spectrum of CO<sub>2</sub> in blue, and the sum of both models shown in red.

Ethanol is the major compound produced by bananas in the fermentation steps. Ethanol has characteristic spectral features in the  $\nu_{10}$  and  $\nu_4$  C-O stretching vibration bands in the regions at 879.36 and 1027.75  $\text{cm}^{-1}$ , respectively. A simple integration of spectral signatures in these regions worked because these regions were free from overlapping with any features of other significant band interferences. In a fitting procedure, the 879.36 and 1027.75  $\text{cm}^{-1}$  regions were fitted to the ethanol PNNL reference<sup>109</sup> spectrum (1 ppm) and a linear baseline (see figure 4.7 below). The multiplier of the reference spectrum was then converted into partial pressures of ethanol.

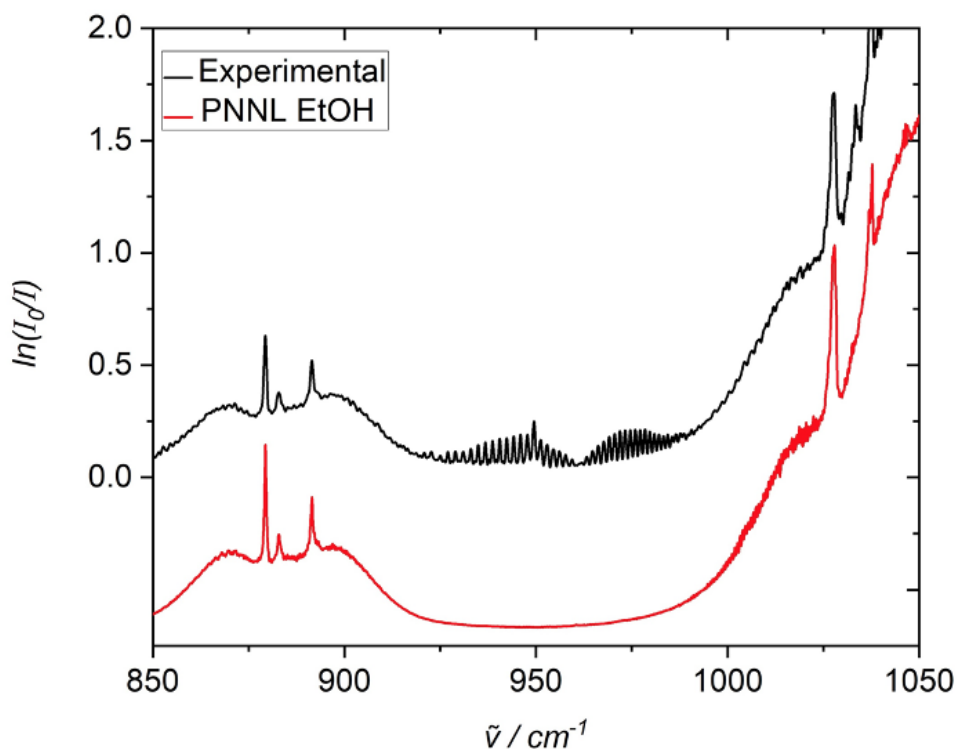


**Figure 4.7.** FTIR absorbance spectrum of banana headspace with fitted PNNL model spectrum. In black is the experimental EtOH spectrum and the PNNL model spectrum of EtOH is shown in red. Around 950  $\text{cm}^{-1}$  are additional  $\text{CO}_2$  and ethylene features as discussed before.

Acetaldehyde is generated in fruit from pyruvate by the pyruvate decarboxylase enzyme (PDC). The two immediate products generated from acetaldehyde are ethanol by the alcohol dehydrogenase enzyme (ADH) and acetyl coenzyme A (CoA) by the aldehyde dehydrogenase enzyme (ALDH). In a fitting procedure, the 2715.3  $\text{cm}^{-1}$  region of an experimental FTIR spectrum was fitted to the acetaldehyde PNNL<sup>109</sup> reference spectra (1 ppm) and a linear baseline (see Fig. 4.8). This region contains very characteristic IR peaks of acetaldehyde in the wing of other absorption bands, but it is easily distinguished from other features. The multiplier of the fitted reference spectrum was then converted into partial pressure of acetaldehyde.

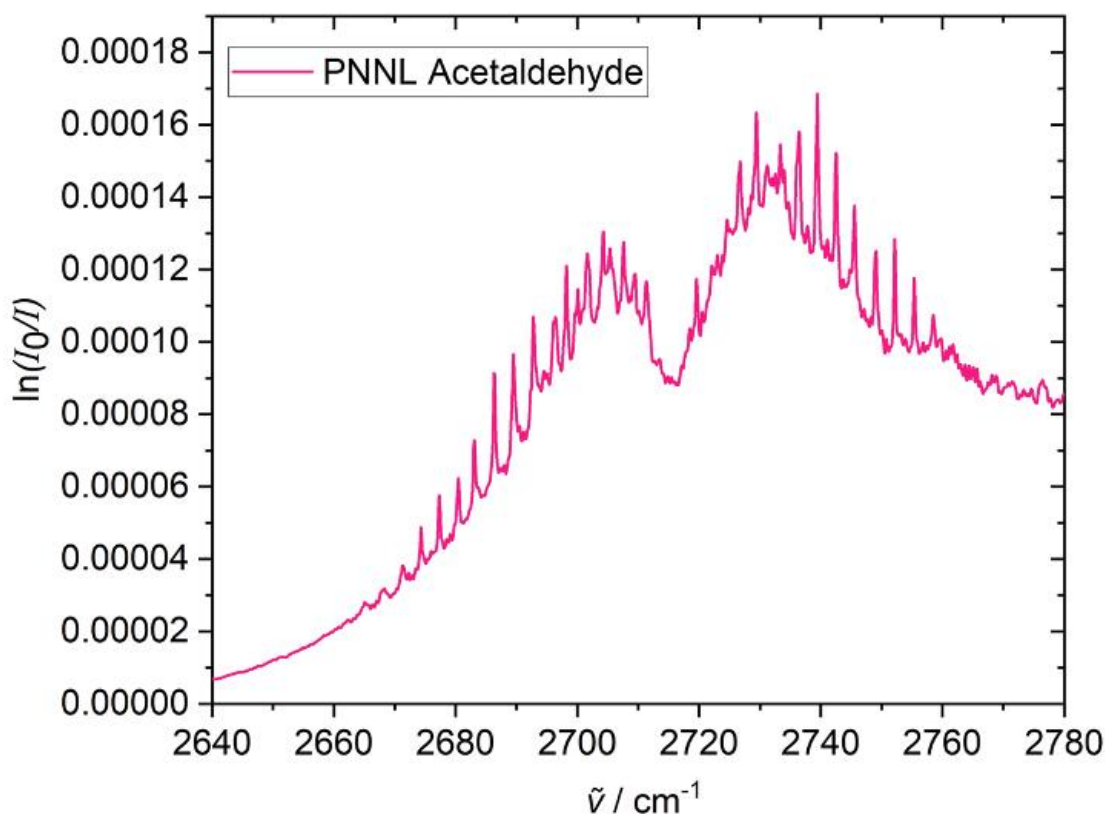


**Figure 4.8.** The PNNL model spectrum of acetaldehyde.

Esters form the most abundant compounds in the volatile profile of bananas, the most abundant one is ethyl acetate. Ester volatiles are produced mainly by the reaction between alcohols and acetyl-CoA *via* esterification. Acetyl CoA is the precursor for long ester chains. The 849 and 929  $\text{cm}^{-1}$  regions have very weak absorption bands of ethyl acetate (see Fig. 4.9), but these features are outside from interferences with other bands. Therefore, the weak absorption bands shown in figure 4.9 were suitable for ethyl acetate analysis. The C-O stretching vibration band near 849 and 929  $\text{cm}^{-1}$  can be analysed to determine the partial pressure of ethyl acetate after comparison with the PNNL model spectrum (1 ppm). The 849 and 929  $\text{cm}^{-1}$  regions of an experimental spectrum were fitted to the ethyl acetate PNNL<sup>109</sup> reference spectrum and a linear baseline. The multiplier of the reference spectrum was then converted into partial pressure of ethyl acetate.

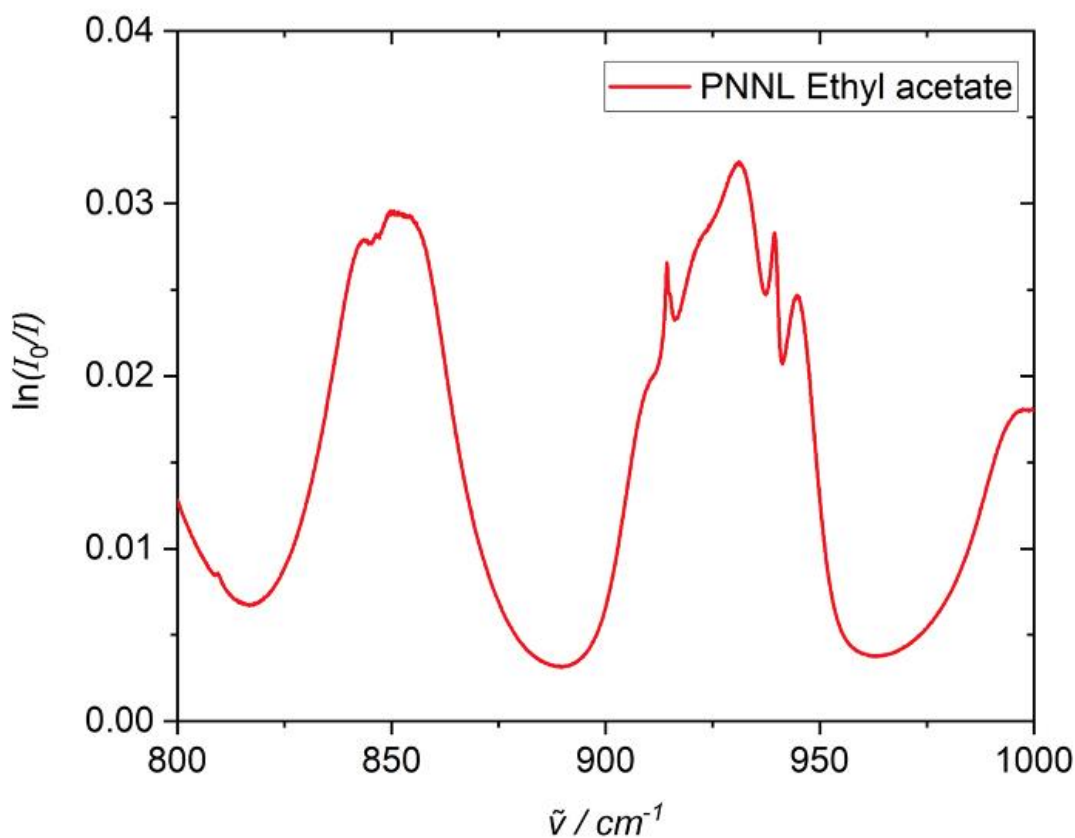


**Figure 4.9.** The PNNL model spectrum of ethyl acetate.

### 4.3.2. Spectroscopic Analysis of Volatiles Produced by Banana

The spectroscopic techniques described above, FTIR spectroscopy with a White cell and CERS, have been applied to monitor the headspace in the respiration chamber which has been filled with 3 fresh bananas in a closed system over 30 h. The origin of all bananas used in this experiment came from Volta River Estates in Ghana as shown on the label in Fig. 4.10.

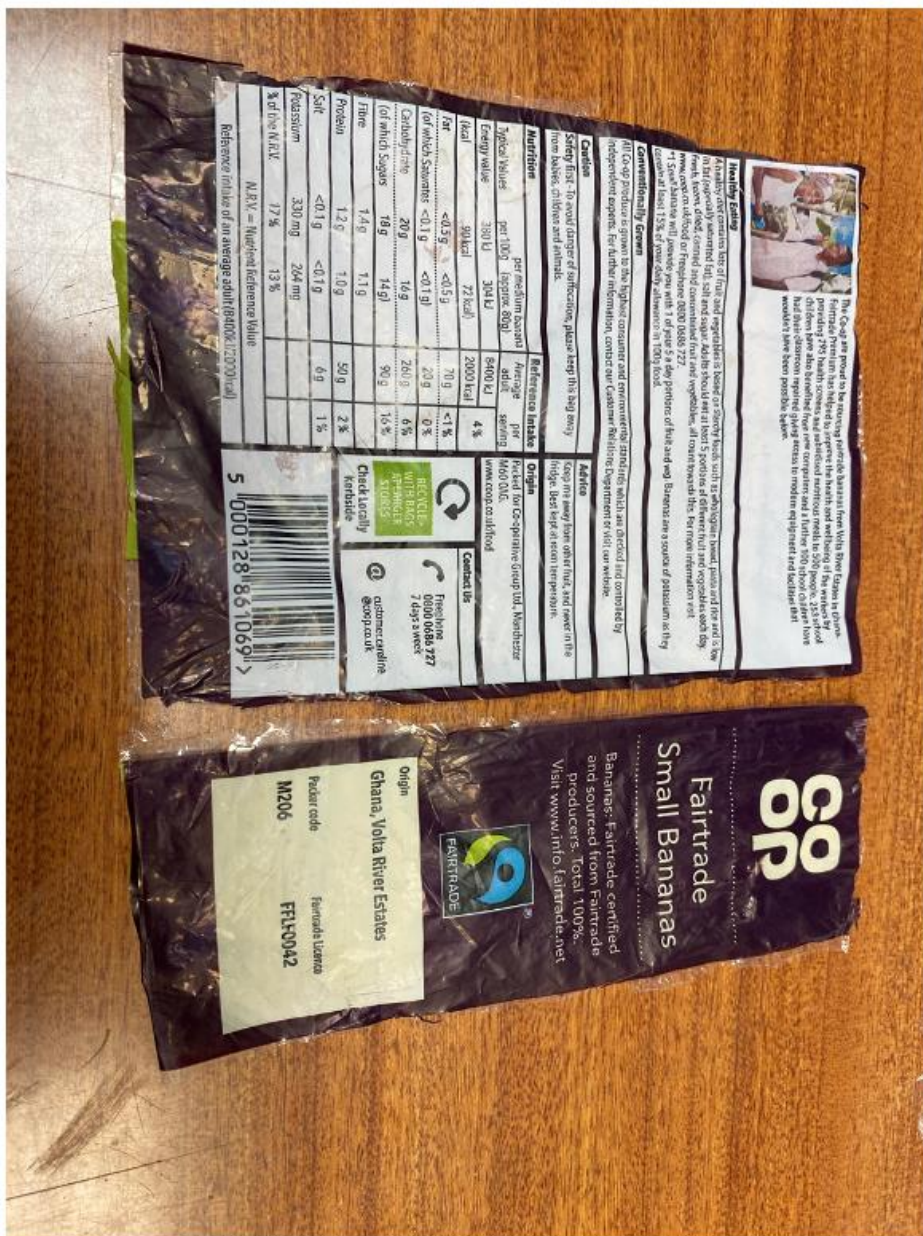


**Figure 4.10.** The label of bananas used in this experiment.

They were bought from a CO-OP supermarket. At the beginning and at the end of the experiment, the weight of three bananas were measured to be 317.604 g and 315.299 g respectively. The following picture (Fig 4.11) shows the changes in peel colour of three bananas at the beginning and at the end of the experiment.



**Figure 4.11.** The photo shows the changes in peel colour of bananas at the beginning and at the end of the experiment. The colour of the banana peel changed from green to yellow during 30 h, which indicates that bananas were fully ripened.

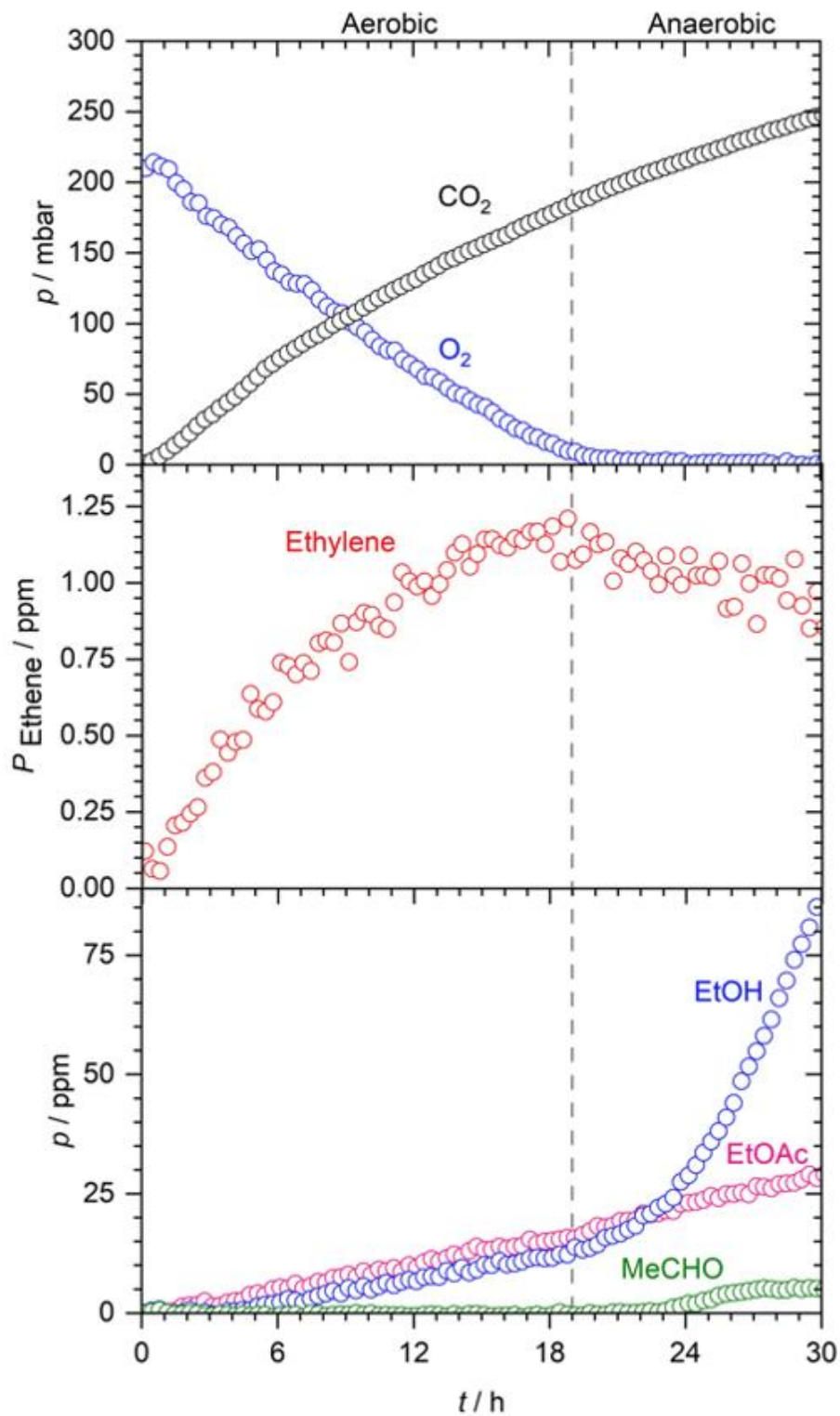


**Figure 4.12.** Time dependent partial pressures of volatiles production by banana respiration, as determined by FTIR White cell and CERS headspace measurements in a closed system.

Fig. 4.12. shows time dependent partial pressures of volatiles and metabolites in the headspace in a closed respiration chamber over 30 h, as determined by FTIR White cell and CERS. Fig. 4.12. is a representative example. Several repeats show similar behaviour. The upper plot in Fig. 4.12. shows the time dependent partial pressures of O<sub>2</sub> and CO<sub>2</sub> from CERS. Two different phases are apparent, aerobic respiration and anaerobic fermentation, separated by the dotted line in Fig. 4.12. During the first 19 h of aerobic respiration of bananas, O<sub>2</sub> was consumed while CO<sub>2</sub> was produced in an approximate 1:1 ratio. After 19 h, O<sub>2</sub> was exhausted and bananas were in anaerobic fermentation. CO<sub>2</sub> was further increasing to about 250 mbar at 30 h, the end of the experiment. The middle plot of Fig. 4.12. shows the time dependent partial pressure of ethylene from the FTIR measurement. The bottom plot of Fig. 4.12. shows the time dependent partial pressures of ethanol, ethyl acetate and acetaldehyde obtained from the FTIR measurements.

The production of ethylene for the ripening yellow bananas was increasing rapidly during aerobic respiration. The peak in the ethylene production was at the end of aerobic respiration and reached a value of 1.25 ppm at 19 h. Ethylene production increases with respiration. After 19 h anaerobic fermentation started, after O<sub>2</sub> was depleted. The ethylene production ended, because O<sub>2</sub> is necessary for the conversion of ACC to ethylene in the biosynthesis pathway according to the Yang cycle (see Introduction). Therefore, ethylene stays approximately constant in the anaerobic phase, it even seems to slightly decrease.

Under anaerobic conditions, bananas have been reported to produce fermentation products, including ethanol and ethyl acetate. High levels of ethanol in the peel and pulp in ripe bananas can be attributed to ethanol production during the later stages of ripening. In our experiment, during aerobic respiration only low ethanol concentrations were observed, slightly rising to about 10 ppm in the headspace. After 19 h higher levels of ethanol accumulate in the anaerobic fermentation phase, to about over 100 ppm at the end of the experiment.<sup>110</sup> High levels of ethanol are observed when banana fruit becomes over-ripe. The main volatile esters group produced in this experiment was ethyl acetate. As the level of ethanol was increasing, a large amount of acetyl CoA was utilized to produce ethyl acetate.<sup>111</sup> Under anaerobic fermentation, the banana produced a considerable amount of ethyl acetate of about 25 ppm in the headspaces at the end of experiment. As a consequence of the production of significant amounts of ethanol and ethyl acetate, “off-flavour” developed, which explains the smell of alcohol in banana fruit at the over-ripe stage where they become inedible. At different stages

of ripening in banana fruit, volatile compounds exhibit significant variations, as can be seen in Fig. 4.12.

Acetaldehyde production as a precursor of ethanol was not detectable during aerobic respiration (Fig. 4.12). During the anaerobic phase, after 24 h it started to increase giving a peak value of 6 ppm at 28 h and then it stays approximately constant, presumably in a steady state of production and simultaneous consumption because acetaldehyde is known to be a precursor of many other metabolites. According to a previous study,<sup>112</sup> ethanol and acetaldehyde in the tissue of the plant are converted to acetyl CoA, which is the precursor for other metabolites such as acetate esters. Optical spectroscopy can detect only a limited number of compounds, mainly smaller molecules. Fortunately, this captures the most important volatiles in the metabolism of bananas.

Up to 350 different compounds of banana volatiles have been reported using GC and MS equipment, with varying concentrations depending on sampling and separation methods.<sup>95</sup> Differences in methodology yield different results for the composition of ripening banana volatiles.<sup>95</sup> Several external factors can also affect volatiles production, such as the temperature during fruit storage.<sup>113</sup> Therefore, a more reproducible condition for studying volatiles of banana is maintaining banana at constant temperature, for example at 20° C. In the temperature range between 20-35° C, the banana volatiles production is exponential and at about 25° C, the maximum volatiles production occurred according to a previous study.<sup>113</sup>

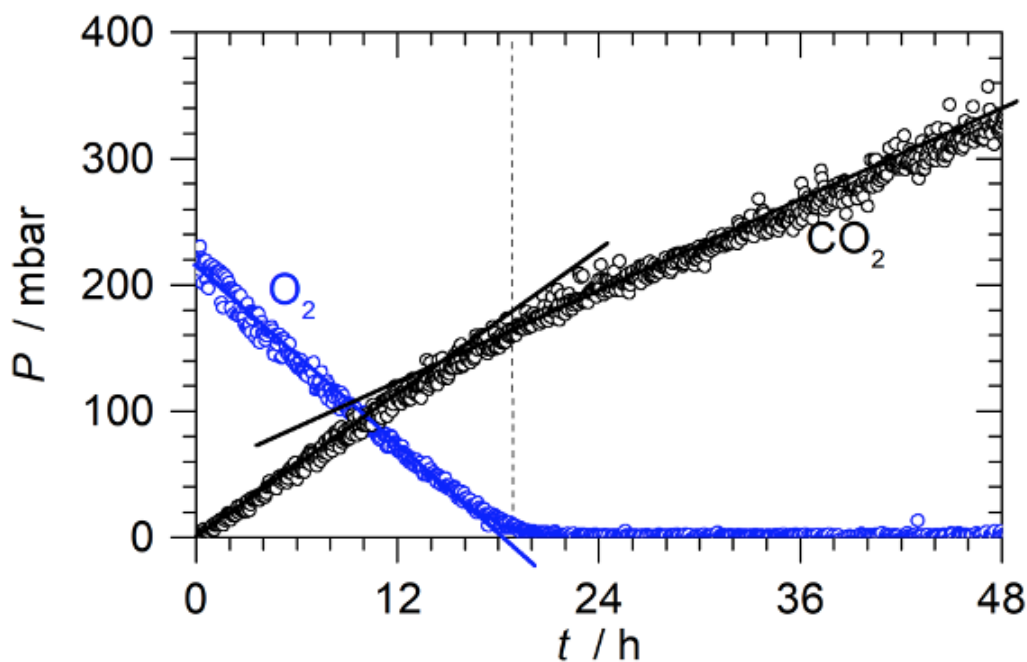


**Figure 4.13.** Second example of a banana experiment where  $\text{CO}_2$  and  $\text{O}_2$  are monitored by CERS. The blue curve shows the partial pressure of  $\text{O}_2$  consumption and the black curve shows the partial pressure of  $\text{CO}_2$  production of banana respiration as a function of time.

The main advantage of CERS is the ability to monitor the transition from aerobic to anaerobic conditions. Fig. 4.13 above shows the ability of CERS to monitor the  $\text{O}_2$  consumption and  $\text{CO}_2$  production of banana respiration. During aerobic metabolism, bananas convert starch which is a glucose polymer (the primary storage carbohydrate in a plant) into 6-carbon sugars, glucose and fructose, which are then oxidized *via* glycolysis into  $\text{CO}_2$ , with typically one unit of  $\text{CO}_2$  produced per unit  $\text{O}_2$  consumed in a 1:1 ratio. The plot shows the time-dependent partial pressure of the  $\text{CO}_2$  and  $\text{O}_2$  for a second experiment monitoring the headspace above the banana in a closed system (Fig. 4.13). These measurements were made using CERS using three bananas (origin Ghana, Volta River Estates, CO-OP, Fairtrade Small Bananas). The experiment was observed for 48 hours. The level of  $\text{CO}_2$  that bananas produce increases and  $\text{O}_2$  decreases during this time in an approximate 1:1 ratio. At the end of the aerobic phase around 19 h, the initial 210 mbar  $\text{O}_2$  were consumed and converted to about 160 mbar  $\text{CO}_2$ . In the anaerobic phase,  $\text{CO}_2$  was increasing further to over 350 mbar.

In summary, CERS and White cell FTIR enabled successfully monitoring the different behaviour of the metabolism of bananas in a closed system. The approach is suitable for monitoring aerobic and anaerobic phases because CERS can monitor  $\text{O}_2$  consumption and  $\text{CO}_2$

production at the same time. CERS will be very useful in the biosciences to monitor metabolites which are difficult to detect with other methods, in particular homonuclear diatomic gases such as O<sub>2</sub>, H<sub>2</sub> and N<sub>2</sub>. The distinct feature of CERS over long-path FTIR spectroscopy is the capability for the detection of homonuclear diatomic gases as IR techniques cannot monitor these gases due to selection rules. The advantage of FTIR is that it can detect a wide range of other relevant molecules at high sensitivity.

## 4.4 Conclusions and Future Works

An experimental set-up for continuous monitoring of banana respiration and fermentation by using headspace FTIR spectroscopy combined with CERS has been proven to be a valuable tool for determining the volatile species released from bananas. The FTIR spectra analysis provides partial pressures of ethylene, CO<sub>2</sub>, acetaldehyde, ethyl acetate and ethanol using calibrations by reference spectra or using the Beer-Lambert-Bouguer law. CERS provides partial pressures of O<sub>2</sub> and CO<sub>2</sub>. FTIR and CERS complement each other. Both spectroscopies are required to obtain a more complete set of measurements. In contrast to standard analytical methods such as GC or MS, the techniques mentioned above are non-invasive and offer concentrations in real time without sampling. In comparison to more expensive techniques such as GC and MS spectroscopy, they are cost-efficient alternative techniques to study banana respiration and fermentation. These techniques have been applied to study volatiles production of bananas in a closed system. Different volatiles of banana respiration have been characterised and observed.

CERS and long path FTIR spectroscopy have the potential to serve as two complementary tools in biochemistry and biotechnology, alongside more established techniques such as GC and MS. Long path FTIR spectroscopy is ideal to detect trace gases at low concentration (ppm) due to its extreme sensitivity. Only CERS can detect homonuclear diatomic molecules according to selection rules governing Raman and IR spectroscopy. An example of an application where CERS detection is required for detection of trace gases is the investigation into aerobic respiration and anaerobic fermentation of bananas. O<sub>2</sub> consumption cannot be measured by long path FTIR spectroscopy which would make the study of the transition of aerobic to anaerobic conditions in bananas impossible. These results highlight that it is essential to monitor O<sub>2</sub> and also CO<sub>2</sub> and other gases simultaneously, and only the

combination of CERS and FTIR makes this possible. Only the combination of CERS and long-path absorption FTIR as optical spectroscopies provides a more complete picture of the metabolism of banana in an analytical technique which does not require sampling, is contactless, *in situ* and provides real-time data. This combination of spectroscopic techniques has many potential applications in biochemistry and biotechnology to study the metabolism of plants, fruits and microbes. A final application example will be provided in the next chapter where TMAO metabolism of *E. coli* is studied by CERS and White cell FTIR spectroscopy.



## **Chapter 5- Advanced Analytical Techniques for Monitoring the Effect of O<sub>2</sub> and Exogenous Deuterated Formate on Trimethylamine-N-Oxide Reduction and H<sub>2</sub> Production by *E. coli***

### **Abstract**

Trimethylamine-N-oxide (TMAO) reduction by *E. coli* cultures in a closed system was studied using a combination of the analytical spectroscopic techniques of long-path FTIR, liquid phase Raman spectroscopy and Cavity Enhanced Raman Spectroscopy (CERS). Spectral signatures and fitting procedures for quantitative analysis are described in detail. Time-dependent concentrations of TMAO, acetate, formate, phosphates and glucose were obtained using liquid phase Raman spectroscopy. Noise equivalent (1  $\sigma$ ) detection limits of 1.8 mM TMAO, 2.6 mM acetate, 1.5 mM formate and 1.9 mM of glucose were determined. By using a modified Henderson-Hasselbalch equation, the concentrations of phosphate anions could be utilized to obtain the pH *in situ*. The partial pressures of CO<sub>2</sub> and ethanol were determined by long-path FTIR spectroscopy, and of O<sub>2</sub> and H<sub>2</sub> by CERS. By using Henry's law the pressure can be converted into concentrations in solution. TMA and ammonia concentrations were determined by a second gas phase FTIR instrument with a noise equivalent (1  $\sigma$ ) detection limit of 0.2 mM TMA.

TMAO reduction was studied under different growth conditions, including anaerobic, aerobic and in the presence of exogenous deuterated formate (formate-d). By isotopically labelling exogenous formate-d it could be spectroscopically distinguished from unlabelled endogenous formate. Differences in physiology and H<sub>2</sub> production by formate hydrogen lyase (FHL) are discussed. Under aerobic conditions, H<sub>2</sub> production is not observed because FHL is repressed by O<sub>2</sub>. Under anaerobic conditions with TMAO, H<sub>2</sub> was only observed after TMAO is depleted, because TMAO suppresses FHL activity. This suppression was overcome by high levels of exogenous formate-d, where we observe H<sub>2</sub> production even in the presence of TMAO. Our measurements of H<sub>2</sub> and formate support a previous enzymatic study which observed that FHL activity in *E. coli* is suppressed by TMAO due to drainage of the inducer formate. The work described in this chapter was done in collaboration with fellow PhD student George D. Metcalfe and represents a joint effort.

## 5.1 Introduction

### 5.1.1 The Metabolic Hierarchy of *E. coli* and its Regulation

*Escherichia coli* (*E. coli*) is a gram-negative, facultative anaerobe and a model bacterium for microbiological studies. In *E. coli*, aerobic respiration typically takes precedence over anaerobic respiration and fermentation.<sup>114,115</sup> The concerted activity of transcription factors (TFs) maintains this order.<sup>115</sup> Thus *E. coli* has the potential to maximize ATP yield under a variety of redox conditions due to this inherent metabolic flexibility. *E. coli* has the ability to switch metabolic modes depending on a variety of redox-responsive regulatory mechanisms that work together to ensure optimal adaptation.<sup>45</sup> The adaptability comes at a cost even though *E. coli* can survive in a variety of redox conditions; each of the metabolic systems must have a genetic and enzymatic "tool kit" provided by the bacterium. The *E. coli* central metabolic pathways are influenced by the supply of O<sub>2</sub>, the growth substrate, and the presence of any alternative electron acceptors. For example, the production of nitrate reductase and fumarate reductase enzymes is repressed in the presence of O<sub>2</sub>, which is energetically the preferred electron acceptor.<sup>45</sup> For electron transport-coupled oxidative phosphorylation, *E. coli* can respire with O<sub>2</sub> or anaerobically with a variety of terminal electron acceptors, see table (5.1).<sup>45,116</sup> In order of decreasing potential energy, key alternative electron acceptors are nitrate, nitrite, dimethyl sulfoxide (DMSO), Trimethylamine-N-oxide (TMAO), and fumarate.<sup>45</sup> This hierarchy reflects the relative amounts of energy that these metabolic modes can conserve, with oxygen supply serving as the primary signal that determines the use of metabolic modes. Gene expression is mediated and altered by the key regulators involved in the aerobic/anaerobic pathways which sustains this metabolic hierarchy in *E. coli*. Of the common alternative terminal electron acceptors, the redox pair of TMAO/TMA is the second least preferred in terms of energy used by *E. coli*. Typically, the use of electron acceptors follows the amount of energy that is potentially available to produce the most cellular energy (see above). However, TMAO is an exception to this general rule because it is reduced simultaneously alongside O<sub>2</sub> and other electron acceptors.<sup>117</sup>

<b><u>Redox Couple</u></b>	<b><u>Reduction potential (<math>E_0'</math>) (V)</u></b>
O <sub>2</sub> / H <sub>2</sub> O	+ 0.82
NO <sub>3</sub> <sup>-</sup> / NO <sub>2</sub> <sup>-</sup>	+ 0.42
NO <sub>2</sub> <sup>-</sup> / NH <sub>4</sub> <sup>+</sup>	+ 0.36
DMSO / DMS	+ 0.16
TMAO / TMA	+ 0.13
Fumarate / Succinate	+ 0.03

**Table 5.1.** Redox pair energetics of terminal electron acceptors used by *E. coli*.

### 5.1.2 TMAO Respiration by Bacteria

In the human body about 95% of the bacterial genes, about 3.6 million genes, are found in the large intestine. More than 1000 different species colonize the human intestine.<sup>118</sup> There is significant interindividual variability in the composition of the gut microbiota, which is thought to have a role in maintaining health and disease progression. Many functions have been assigned to the microbiome such as development of the immune system, storage of fats, synthesis of vitamins, digestion of sugars and regulation of angiogenesis. Over the past decade, next generation sequencing has developed rapidly, that has had a significant effect in the field. A number of factors such as diet can be affected by the microbiome. Therefore, the gut microbiota modulation by diet to obtain a healthy status is a major research topic.<sup>119,120</sup>

In humans recent evidence indicates that a high concentration of TMAO in blood plasma is linked to an increased risk of cardiovascular disease. TMAO and TMA (Trimethylamine) are mainly excreted by humans in urine, sweat and by breathing.<sup>121</sup> The concentration of TMAO in human blood plasma in healthy individuals is within 3 mmol/L, and this increases in patients with renal failure to 40 mmol/L.<sup>122</sup> Gut bacteria are the main source of TMAO in the blood and dietary TMAO reduction by enteric bacteria for example *E. coli*, is

a potential contributing factor, as the produced TMA enters the bloodstream and is oxidized in the liver and in the gut to produce TMAO.

The amine oxide TMAO is a natural metabolite in many living organisms. In anaerobic metabolism, TMAO can act as an alternative electron acceptor for numerous bacteria. The bacteria which can reduce TMAO to trimethylamine (TMA) inhabit three major conditions, marine, animal intestines and brackish ponds. TMAO reduction can promote oxidative phosphorylation in the absence of O<sub>2</sub> for the Enterobacteriaceae which includes *E. coli*.<sup>123</sup> TMAO is also an essential nutrient for some marine bacteria.<sup>124</sup> TMAO is reduced to foul-smelling TMA (Fig. 5.1). The biochemistry and genetics of *E. coli*'s use of TMAO as an alternative electron acceptor in respiration has been investigated intensively in recent research.<sup>125-127</sup> Research into marine-fish spoilage began in the last century, showing that TMA is created by reducing TMAO, which is naturally present in fish.<sup>123</sup> Characterisation of TMAO reductases and the other elements of the TMAO respiratory transport chain have been extensively studied,<sup>127</sup> however not as much as other electron acceptors such as nitrate respiration.

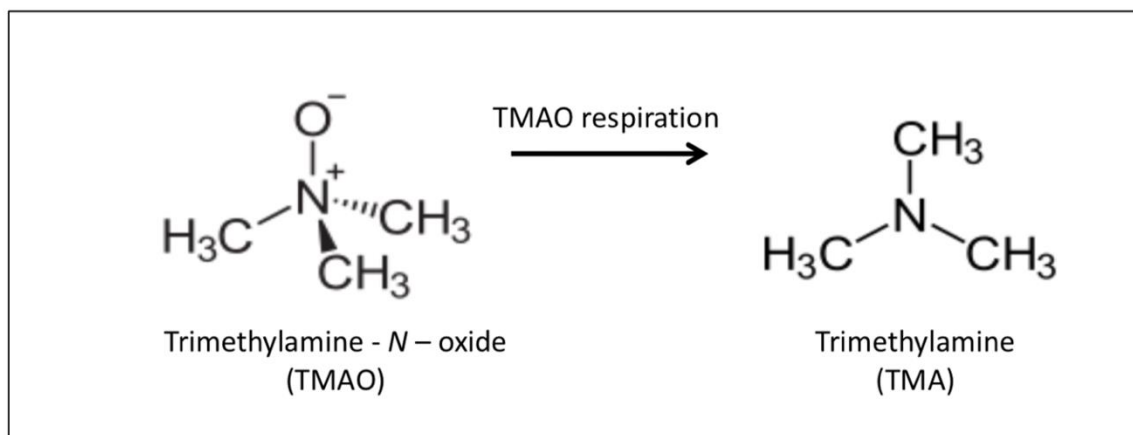


**Figure 5.1.** The reduction of TMAO to TMA.

### 5.1.3 TMAO Reductase

*E. coli* express two TMAO reductases: the *torCAD* operon is induced in the presence of TMAO via the TorS/TorT/TorR regulatory system while the *torZY* operon codes for a second TMAO reductase that has a weak degree of constitutive expression and is not induced

by TMAO.<sup>128</sup> Under both aerobic and anaerobic growth conditions, the presence of TMAO is required for expression of the *torCAD* operon.

*torCAD* expression is regulated by a two-component mechanism involving three proteins: TorT, S, and R. In order to generate a sensory complex that sufficiently transmits the signal (TMAO) through the cytoplasmic membrane to induce the change of behaviour of the regulator TorR, a periplasmic TMAO-binding protein (TorT) binds to the membrane protein TorS.<sup>129</sup> When the TorS protein is stimulated, it phosphorylates the regulator TorR, which then stimulates *torCAD* transcription.<sup>130</sup> TorS functions as a TorR-P phosphatase if TMAO is unavailable, thus preventing TMAO reductase from being formed.<sup>131</sup> TorA, a subunit of the TMAO reductase, is found in the periplasm and has a molybdopyranopterin cofactor. The membrane-associated pentaheme cytochrome TorC transfers electrons from reduced quinones (menaquinol and dimethylmenaquinol) to TorA.<sup>132</sup> TorD is a membrane *b*-type cytochrome involved in the electron transfer pathway of the reduction of TMAO. Therefore, TMAO reduction may be linked to numerous dehydrogenases that reduce the quinone pool, to conserve energy chemiosmotically. The TMAO respiratory pathway is shown schematically in Fig. 5.2. TMAO respiration has been reported to happen in the presence of the preferred terminal electron acceptor O<sub>2</sub>, unlike other alternative terminal electron acceptors utilised by *E. coli*.<sup>117</sup> The advantage of the cell for reducing TMAO in the presence of O<sub>2</sub> is not understood. Even in the presence of O<sub>2</sub> *E. coli* will excrete acetate (overflow metabolism) when glucose is available in excess, possibly because of an imbalance in uptake of glucose and the capacity of the Krebs cycle to metabolize acetyl CoA. As acetate accumulates, the pH of the medium decreases. Eventually acetate accumulation inhibits growth. TMA being a basic compound, reduction of TMAO to TMA can help mitigate some of the acidification from the acetate production that happens in aerobic conditions.<sup>117</sup>

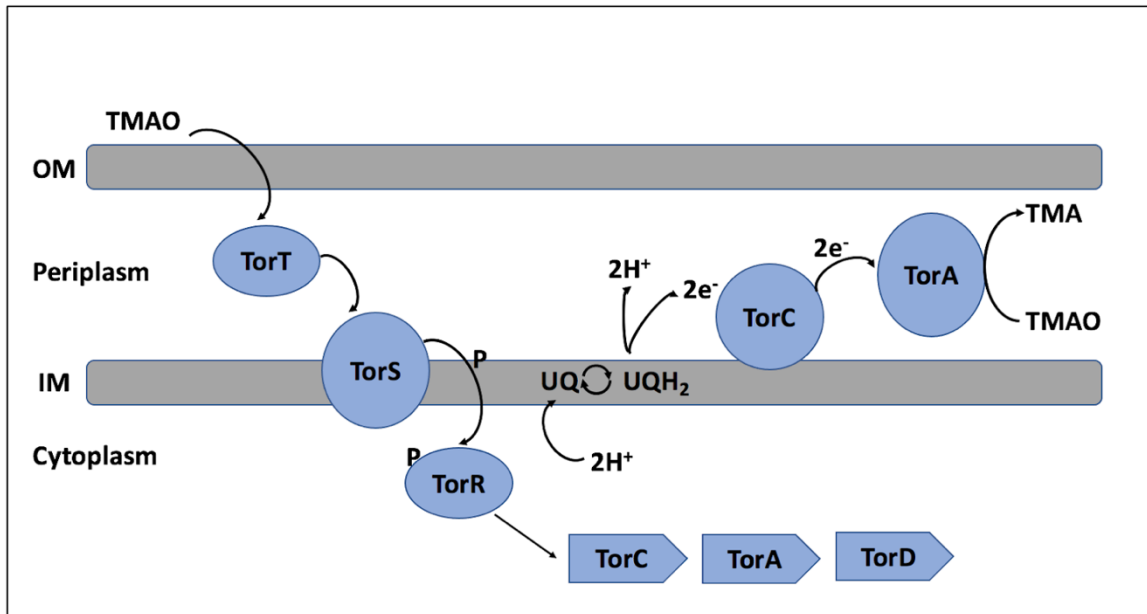


**Figure 5.2.** The TMAO respiration Tor pathway and the genes regulated by the Tor three component system **TorT**, **TorS** and **TorR**. **UQ**, ubiquinone, **UQH<sub>2</sub>**, ubiquinol, **IM**, inner membrane, **OM**, outer membrane.

## 5.1.4 Formate and H<sub>2</sub> Production

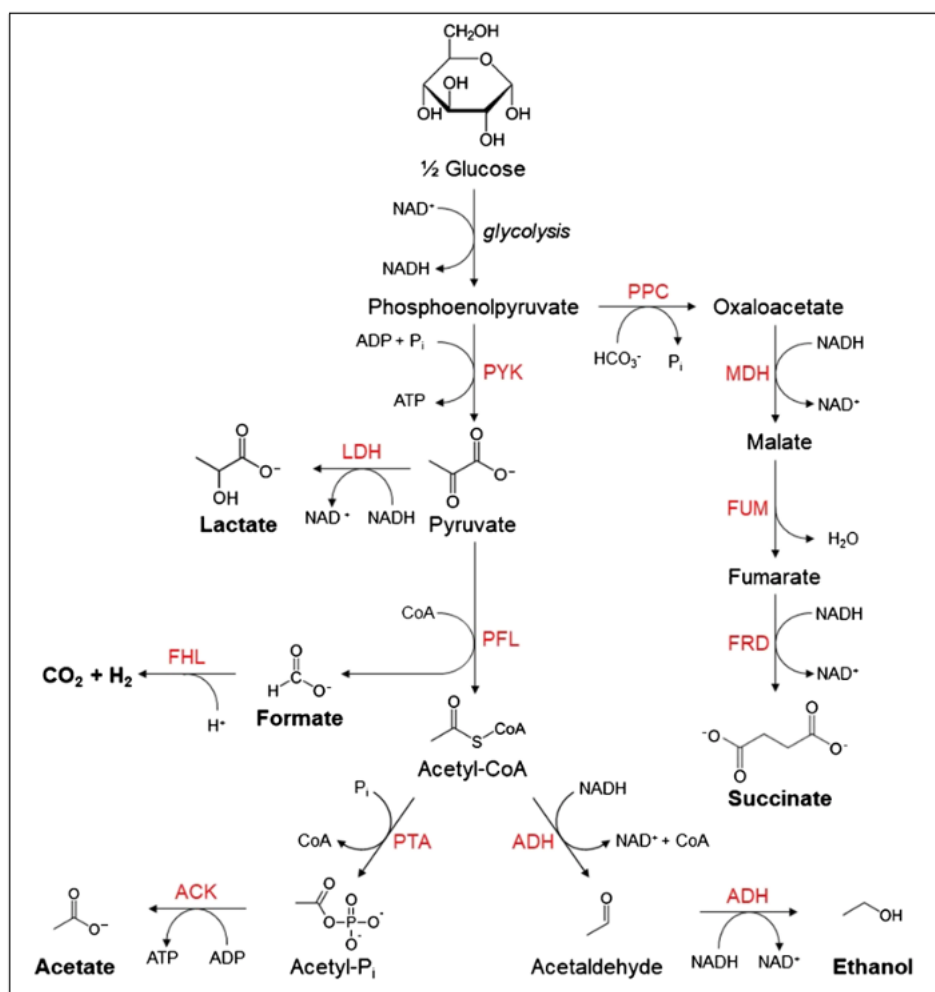


**Figure 5.3.** Fermentation pathways of *E. coli* supplemented with glucose. The enzymes are shown on red: **ACK**, acetate kinase; **ADH**, alcohol dehydrogenase; **FHL**, formate hydrogenlyase; **FRD**, fumarate reductase; **LDH**, lactate dehydrogenase; **MDH**, malate dehydrogenase; **PFL**, pyruvate formate lyase; **PPC**, phosphoenolpyruvate carboxylase; **PTA**, phosphotransacetylase; **PYK**, pyruvate kinase.<sup>47</sup>

Formate is one of the physiological sources of electrons for TMAO reduction and is produced anaerobically by fermentative pathways that are summarised in Fig. 5.3. Pyruvate is the end product of glycolysis. Under anaerobic conditions, pyruvate can be cleaved into formate and acetyl-CoA by pyruvate formate lyase (PFL). Acetyl-CoA can then be further metabolised to generate two different fermentative products, either acetate *via* acetyl~P (to generate ATP) or ethanol *via* acetaldehyde (for removing reducing equivalents).<sup>133</sup> Formate metabolism can proceed in one of two distinct pathways depending on the availability of electron acceptors. Formate can undergo oxidation to CO<sub>2</sub> by membrane-bound respiratory formate dehydrogenases. Alternatively, *E. coli* catalyses the disproportionation of formate to

H<sub>2</sub> and CO<sub>2</sub> by the membrane-associated enzyme complex formate hydrogen lyase (FHL).<sup>134</sup> FHL is composed of five subunits, notably a hydrogenase (Hyd-3) and a formate dehydrogenase.<sup>134</sup> FHL is repressed by O<sub>2</sub> and nitrate; however, high formate concentrations can partially reverse the repression by nitrate, but not by O<sub>2</sub>.<sup>135</sup> FHL induction requires a sufficient amount of intracellular formate.<sup>136</sup> Although TMAO does not repress FHL, a recent study noted that TMAO respiration had an inhibiting effect on FHL expression. Formate metabolism linked to TMAO reduction likely prevents sufficient build-up of endogenous formate, suppressing FHL. One important aim of this chapter is to re-investigate TMAO respiration in the presence and absence of exogenous formate-d using advanced analytical techniques.

### **5.1.5 Analytical Techniques for Determining TMAO and TMA**

Precise and effective analytical methods play a crucial role in studying cell biochemistry and pathway elucidation.<sup>47</sup> Mass spectrometry (MS) and chromatographic techniques such as gas chromatography (GC) are the most used methods to identify and quantify a wide range of metabolites.<sup>137</sup> Based on previous research, chromatography techniques such as ion-exchange chromatography can be applied to detect extracted TMAO from marine fish tissues.<sup>138</sup> GC/MS is often used to estimate the concentration of TMAO indirectly.<sup>139</sup> It necessitates TMA derivatisation and reduction, which takes time. Because of the need for sampling and chemical reactions, these techniques are not readily accessible for rapid and online analysis.<sup>140</sup> In the reduction of TMAO to TMA, High-Performance Liquid Chromatography<sup>141</sup> and GC techniques are also commonly used for determination of volatile amines.<sup>142,143</sup> The main benefits of chromatographic techniques are their high efficiency, precision and ability to determine several compounds simultaneously. Unfortunately, the chromatographic approaches have certain inherent flaws, especially in detecting low-molecular-mass amines which is due to the high-water solubility and volatility of these compounds. As a further disadvantage, there is a need for costly specialised equipment and skilled technical personnel.

In a novel method for simultaneous quantitative analysis, TMA and its detoxification metabolite TMAO in plasma and urine were simultaneously determined by an ultrahigh performance liquid chromatography-tandem mass spectrometry technique.<sup>144</sup> The detection limits ranged from 0.08 to 0.12 µmol/L. The accuracy, precision, and recovery of the system

were outstanding. The assay has a fast run time and quick sample analysis, making it ideal for high-throughput research or routine clinical application.<sup>145</sup> This technique, however, is complicated and expensive, and it requires sampling and calibration.

High resolution <sup>1</sup>H-NMR spectroscopy is ideal for detecting a wide variety of endogenous low molecular weight metabolites in living organisms. This method is rapid and provides a lot of structural and quantitative data, allowing for simultaneous analysis of several metabolites.<sup>146</sup> Other metabolomic approaches, such as chromatography and MS procedures, do not have these benefits of NMR spectroscopy. It is a more comprehensive detection system that can be utilised to precisely identify and measure metabolites in real-time, even *in vivo*. The non-destructive aspect of NMR, as well as the ability to test biological samples directly, in a comparatively short period, is most attractive. As a further benefit of NMR, quantification is simple for most molecules, since most detectable metabolites may be quantified using a single internal standard, without requiring individual calibration curves. As disadvantage, NMR equipment is bulky and expensive with high maintenance costs.<sup>147</sup>

In 1945 Dyer *et al.* stated that the most popular approach for TMA analysis was the reaction of TMA with picric acid in benzene or toluene to produce a yellow-coloured complex which can be analysed by colorimetry.<sup>148</sup> It is, however, a time-consuming approach that uses toxic and explosive reagents. In 1974 Castell *et al.* suggested a different colorimetric assay for the quantitative analysis of DMA and TMA.<sup>149</sup> This assay is a modified method of Dyer's colorimetric assay for determination of TMA using a picrate salt instead of picric acid.

Electrochemical sensors are commonly used to monitor pH and trace ion species. These sensors are vulnerable to cross-interference between other chemical species, changes in the solution behaviour and long-term drift. The risk of contamination of continuous cultures in microbiological studies is increased as a consequence of physical contact between the electrode and cell culture. Hence, the electrodes need to be stable towards sterilisation.

In medicine, Fourier Transform Infrared (FTIR) spectroscopy is a rapidly expanding area that has been used to diagnose a wide variety of diseases and samples.<sup>150</sup> It is an excellent tool for analysing biological samples in several respects due to being quantitative and being able to deliver a lot of detail in a single spectrum. Moreover, owing to the growing advancement in technologies in both hardware and software, high-quality IR spectra can be generated and interpreted without extensive technical experience or preparation. Based on the on-line measurement of vapour phases, FTIR spectrometry is an excellent method for the

quantitative identification of volatile or semi-volatile compounds.<sup>151</sup> FTIR is also used to identify volatile substances produced when liquids are injected directly into a reactor<sup>152</sup> or during a chemical reaction. FTIR has also been used to monitor the consistency of fish products, utilising IR methodologies to determine volatiles like TMA.<sup>152</sup>

Spectroscopic techniques can be conveniently used for observing bioprocesses *in situ* and online without sampling required. Vibrational spectroscopic techniques, such as Raman and FTIR spectroscopy, demonstrate high specificity for diverse molecules. These are due to the spectral band character that makes them very useful for metabolic studies. Moreover, isotopologues and isotopomers can be differentiated by vibrational spectroscopies, permitting online monitoring in isotope labelling analysis.<sup>153</sup> Great sensitivities are found in the condensed phase, and concentrations can be derived by applying the Beer-Lambert law or utilizing calibrations. Headspace gas measurement frequently suffers from low sensitivity, hence special improvement techniques such as long-path absorption of FTIR spectroscopy White cells<sup>153</sup> or Cavity Enhanced Raman Spectroscopy (CERS)<sup>154</sup> are required. Henry's Law can then be used to convert the partial pressure in the headspace into concentrations in the solution.<sup>153,155</sup> Although FTIR spectroscopy is found in some bioprocess monitoring, its application to monitor metabolites at low concentrations is constrained by the broad absorption profile of liquid water across much of the region where the strong and most distinctive absorption bands are found. The lack of an expanded hydrogen bonding network in the gas phase gives rise to limited water absorption for certain spectral regions. Molecules with absorption bands out of these regions can be easily detected even in the presence of high-water vapour levels. Raman spectroscopy is more applicable to direct liquid phase analysis since it is insensitive to water molecules. In complex media such as Lysogeny Broth (LB), the components cause fluorescence which makes identification of weak Raman light difficult. By switching to longer excitation wavelengths or using media free of strongly fluorescent materials, fluorescence can be avoided, and liquid Raman spectroscopy can be successfully used. Raman-based techniques are needed to detect the presence of compounds that are not IR active, for example N<sub>2</sub>. Here, cavity-enhanced Raman spectroscopy (CERS) techniques are most relevant as methods used for gas analysis, owing to the substantial improvement in Raman scattered light achieved using a resonant optical cavity.<sup>156</sup> Quantum Cascade Laser (QCL) absorption spectroscopy is also used to detect gaseous molecules.<sup>157</sup> Even though this technique is sensitive, it has a limited tuning range since typically it can only tune over a single IR absorption band and has limited dynamic range due to band saturation effects.

The use of a combination of online liquid phase Raman, CERS and gas-phase FTIR White cell spectroscopy has recently been reported by the Hippler group for continuous online monitoring of *E. coli* metabolism.<sup>47</sup> This combination of techniques has been used here for the detection of different metabolites such as TMAO, TMA, NH<sub>3</sub>, ethanol, CO<sub>2</sub>, glucose, formate, acetate, phosphate ions and pH in the TMAO respiration of *E. coli*.

### 5.1.6 Aims

Over the past decade, TMAO and TMA have received increased attention due to their potential association with cardiovascular diseases. By gut microbiota, TMAO is metabolised into TMA which, in turn, is oxidized back into TMAO by hepatic flavin monooxygenases. Hence, liver flavin monooxygenase activity, diet and gut microbiota composition determine TMAO levels in plasma.<sup>158</sup> A number of animal-based foods including red meat, eggs, and dairy products are considered potential sources of TMAO. This has led to an expanded interest in studying the impact of a diet high in dietary methylamines on the formation of TMAO. These studies require analytical techniques for simultaneous determination of TMAO and related metabolites; not just in biological samples, but also in foods.<sup>158</sup> *E. coli* is a physiological source of TMAO reduction to TMA in the gut and thus is an ideal model for studying TMAO reduction in various metabolic environments.

In this chapter, long-path FTIR, liquid phase Raman and CERS analytical spectroscopic techniques are used to monitor metabolites during TMAO respiration by *E. coli* cultures. TMAO respiration under different aerobic and anaerobic conditions are compared.

FTIR spectroscopy can be used to monitor the products of bacterial metabolism in the headspaces above *E. coli* cultures, including CO<sub>2</sub> and ethanol. With liquid Raman spectroscopy time-dependent concentrations of TMAO, acetate, formate and glucose can be obtained. The growth of *E. coli* in minimal medium M9 with added glucose and TMAO will permit detection of changes in physiology during the growth cycle.

According to selection rules, homonuclear diatomic molecules such as O<sub>2</sub>, N<sub>2</sub> and H<sub>2</sub> are only Raman active because they have a symmetric stretching vibration. The continuous measurements of O<sub>2</sub> consumption and H<sub>2</sub> production by *E. coli* can only be obtained utilizing CERS. One of the main aims of the present study is to investigate H<sub>2</sub> production during TMAO

reduction under different conditions, aerobic, anaerobic and anaerobic with additional exogenous formate-d. H<sub>2</sub> production in the presence of exogenous formate is particularly relevant because in a previous study by Abaido *et al.* in 1997,<sup>159</sup> it was found that growth of *E. coli* on TMAO and exogenous formate greatly stimulated the expression of FHL which disproportionates formate to H<sub>2</sub> and CO<sub>2</sub>. In the previous study, however, only enzyme activity was measured, not the production of H<sub>2</sub>. In the present study, we want to supplement this work by measuring H<sub>2</sub> directly.

## 5.2 Experimental Details

### 5.2.1 Experimental Set-up

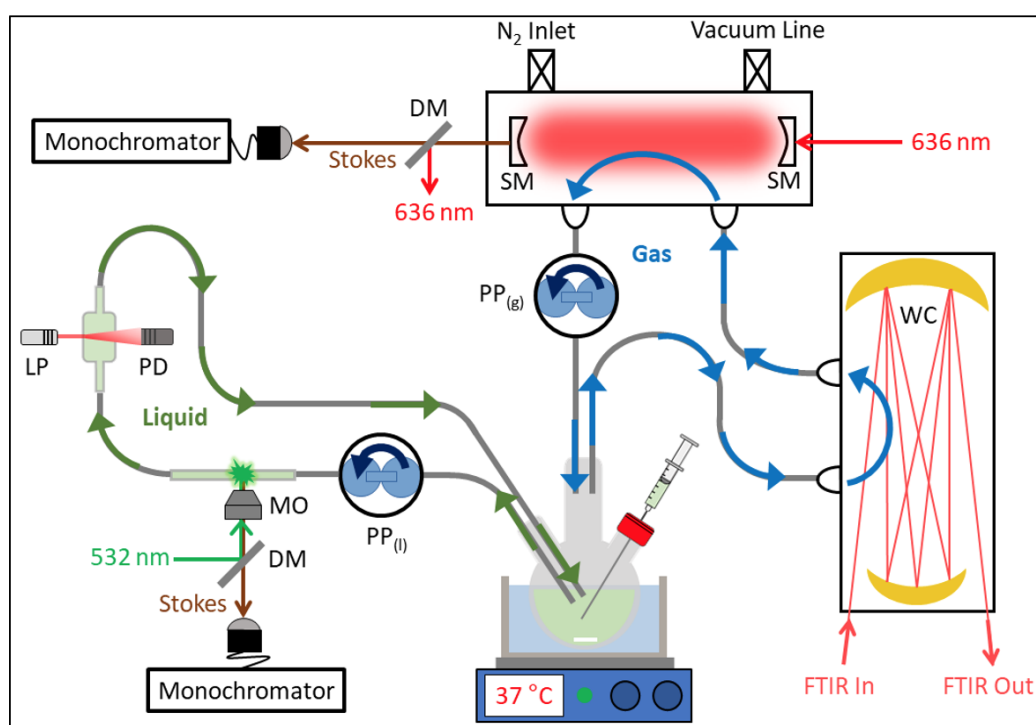


**Figure 5.4.** Schematic diagram of the experimental set-up for spectroscopic analysis of bacterial respiration. DM, dichroic mirror; LP, laser pointer; MO, microscope objective; PD, photodiode; PP(g), gas-phase peristaltic pump; PP(l), liquid-phase peristaltic pump; WC, White cell; SM, super mirrors. (Figure prepared by George D Metcalfe)

A brief outline of the experimental apparatus used to monitor TMAO respiration by *E. coli* is presented here. Some additional details can be found in recent publications of the Hippler group.<sup>47</sup> The experimental apparatus is based on a combined FTIR and Raman set-up, used for monitoring bacterial batch cultures in a closed system (see Fig. 5.4). 250 mL of an *E. coli* suspension, held at 37 °C, was rapidly stirred inside a 3-neck custom flask from which both

the suspension and headspace gas were cycled by peristaltic pumps (4.5 L/h). From one neck the suspension was cycled for *in situ* OD<sub>600</sub> (optical density at 600 nm in a 1 cm cuvette) and liquid Raman measurements. The headspace (1425 mL volume) was cycled from another neck for gas phase FTIR measurements with long path White cell and CERS. A third neck was supplied with a silicone rubber septum for reagent addition or sampling of the bacterial culture. There are another two ports connected to the CERS cell which led to vacuum and nitrogen lines, used to purge the system of O<sub>2</sub>, to give anaerobic growth conditions when necessary.

*E. coli* (strain K-12 MG1655) was transferred from the glycerol stock of bacteria (stored at - 80 °C) and streaked on agar plates with LB medium. To allow the growth of distinct single colonies, plates were kept overnight at 37 °C. Before each measurement, 50 mL of sterile LB medium was inoculated with a single *E. coli* colony in a sealed centrifuge tube and incubated anaerobically for 16 h (37 °C, 200 rpm incubator) to grow to a typical OD<sub>600</sub> of 1.2. From this starter culture, 20 mL was centrifuged and resuspended into 250 mL of sterile fresh M9 minimal growth medium in a round bottom flask, giving a typical starting OD<sub>600</sub> of 0.1. The M9 medium prepared had the following composition:

- 48 mM Sodium phosphate dibasic
- 30 mM Glucose
- 20 mM TMAO
- 22 mM Potassium phosphate monobasic
- 18 mM Ammonium chloride
- 8.5 mM Sodium chloride
- 1 mM Magnesium sulphate
- 1 mM Thiamine hydrochloride
- 300 µM Calcium chloride
- 134 µM Tetrasodium EDTA
- 56.6 µM Boric acid
- 31 µM Iron (III) chloride
- 9 µM Nickel chloride hexahydrate
- 6.2 µM Zinc chloride
- 4 µM Biotin
- 4 µM Sodium selenite
- 3.2 µM Sodium molybdate dihydrate
- 2.7 µM Cobalt (II) chloride hexahydrate

- 1.3  $\mu\text{M}$  Manganese (II) chloride tetrahydrate
- 0.2  $\mu\text{M}$  Copper (II) sulphate

The flask was kept at constant temperature at 37 °C using a heated water bath under rapid stirring to allow efficient gas transfer from suspension to the headspace. 0.6 mL samples of the bacterial culture were taken every 40 min during experiments to determine ammonia and TMA concentrations (see below). The bacterial suspension was centrifuged, washed and dried at the end of experiment to record the dry biomass (typically around 200 mg).

## 5.2.2 Spectroscopic Monitoring of TMAO Respiratory Growth

### 5.2.2.1 White Cell FTIR Spectroscopy Analysis for CO<sub>2</sub> and Ethanol

The production of ethanol and CO<sub>2</sub> was monitored by gas-phase FTIR spectroscopy, with recordings taken every 5 minutes for 128 accumulations. A Mattson Research Series FTIR instrument (0.4  $\text{cm}^{-1}$  spectral resolution, no apodization, liquid N<sub>2</sub>-cooled MCT detector) was used in conjunction with a bespoke multiple-pass absorption White cell fitted with CaF<sub>2</sub> windows and 2-in. (50.4 mm) gold mirrors (made previously by T.W. Smith).<sup>160</sup> The White cell had a base length of 20 cm with 20-40 passes, providing a total pathlength of 4-8 m; the pathlength was set to 6 m in the present experiment. To prevent water condensation on the windows, the White cell was heated to approximately 45 °C using heating tape. The FTIR instrument covered a spectral range from 1000 to 7000  $\text{cm}^{-1}$ , limited at lower wavenumbers by the CaF<sub>2</sub> windows and at higher wavenumbers by the Globar light source. By utilizing the Beer-Lambert-Bouguer law and reference spectra, the partial pressures of CO<sub>2</sub> and ethanol were determined. By using Henry's law, partial pressures were then converted into concentrations in solution. As estimated from an ideal gas law calculation, about 10.0 % of total amount of CO<sub>2</sub> and 99.7% of total ethanol will be in solution, the remainder being in the gas phase.

The partial pressure of CO<sub>2</sub> was determined by integrating the  $\nu_1+2\nu_2+\nu_3$  band (4920-5015  $\text{cm}^{-1}$ ,  $\nu_0 = 4978 \text{ cm}^{-1}$ ) of the Fermi resonance triad and comparing the integral with the 1 ppm reference spectrum from the PNNL database<sup>109</sup> (see Fig. 5.5). PNNL reference spectra were scaled to an absorption pathlength of 6 m which is the folded path-length of the White cell used, since data from the database is given corresponding to 1 ppm-m of a species. The Fermi resonance triad used to quantify the partial pressure of CO<sub>2</sub> is convenient, because this overtone/combination band region does not suffer from interference by other bands.

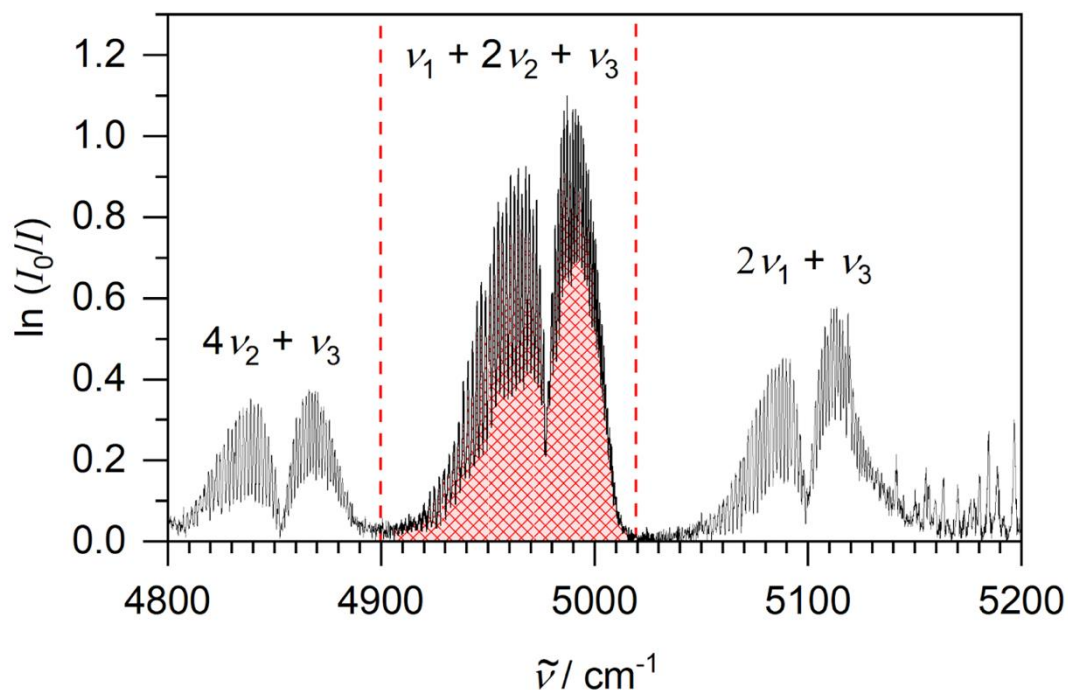


**Figure 5.5.** Experimental FTIR absorption spectrum of the Fermi resonance triad of  $\text{CO}_2$  showing molecular absorption as a function of wavenumber. The region of the band integrated in experimental spectra to determine  $p(\text{CO}_2)$  is indicated in a red dashed box.

Ethanol is another metabolite of bacterial metabolism which was identified in the headspace above bacterial suspensions by the FTIR technique. Ethanol is an essential bioprocess end product in the fermentation pathway (Fig. 5.3). Fig. 5.6 shows the PNNL reference spectrum of ethanol.<sup>109</sup> Fig. 5.7 shows that in an experimental spectrum at the C–H stretching range of  $2800 - 3050 \text{ cm}^{-1}$ , the ethanol spectral features are clearly visible. Since the ethanol spectrum overlaps with rotationally resolved water lines at higher wavenumbers, a simple integration of spectral features does not work in this situation. In this case, the sum of ethanol and water PNNL reference spectra are fitted to the experimental spectrum in the range of  $2800 - 3050 \text{ cm}^{-1}$ , as demonstrated in Fig. 5.7.

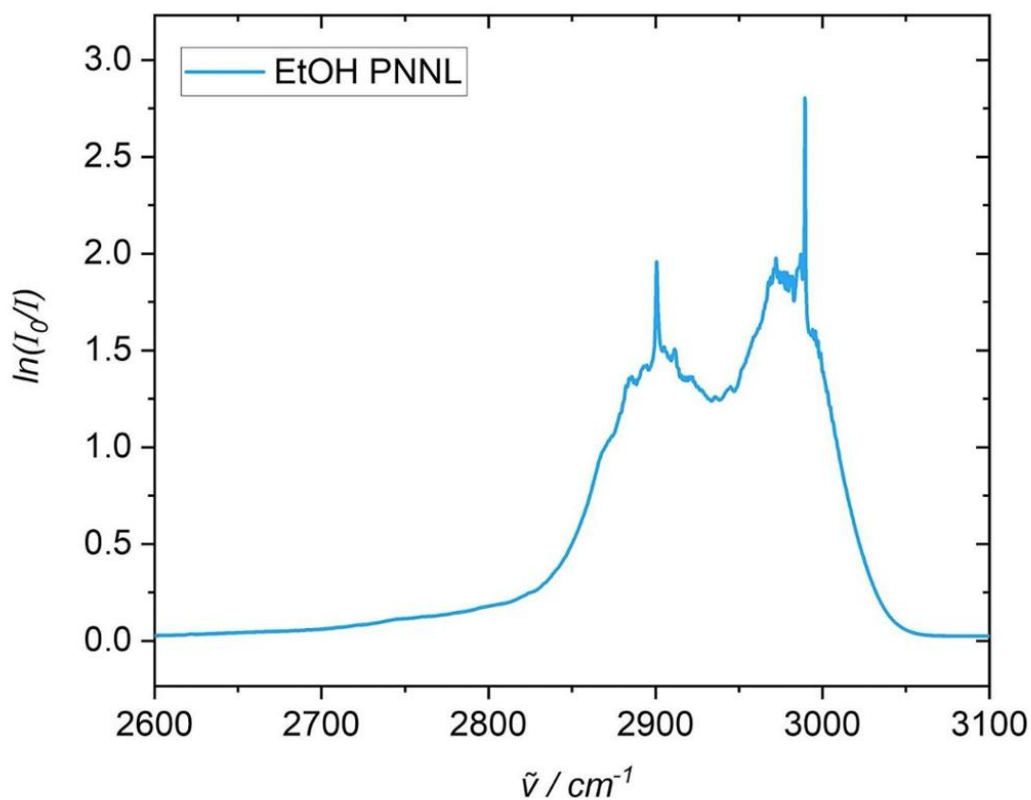


**Figure 5.6.** The PNNL reference spectrum of ethanol.<sup>109</sup>

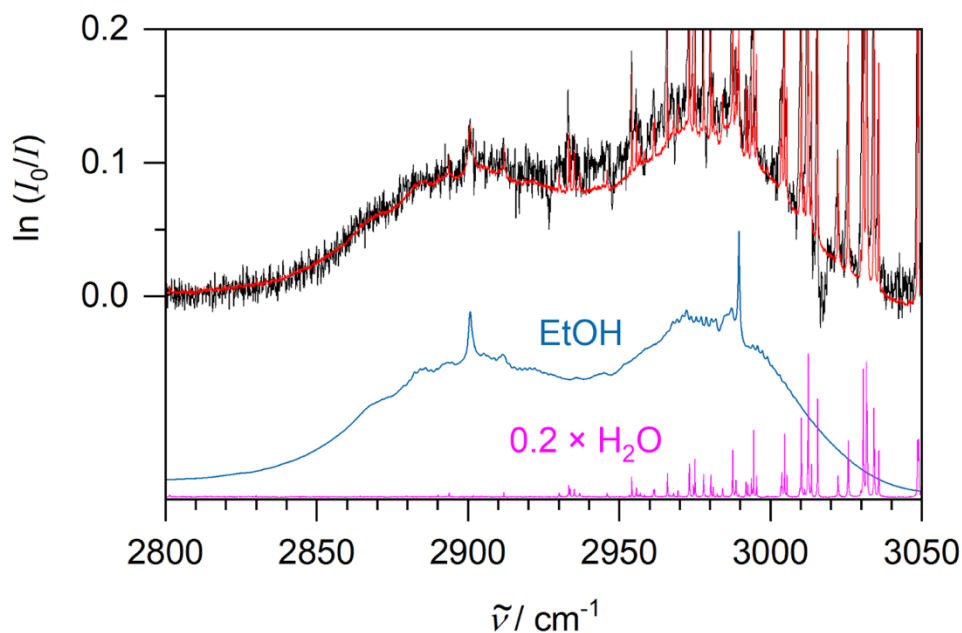


**Figure 5.7.** The experimental bands of overlapping water and ethanol (63 ppm) features are shown in black, the reference spectrum of water in pink, the reference spectrum of ethanol in blue, and the sum of both models matching the experimental spectrum in red. Due to the intense water lines the model spectrum of water is divided by a factor of five to make it clearer.

Henry's law describes the equilibrium between headspace gases and dissolved gases,

$$c = k_H p$$

where  $c$  represents the concentration (molarity) of a dissolved gas in the solution,  $k_H$  is the Henry's law constant for the gas at a constant temperature and the partial pressure of the gas in the headspace above the solution is  $p$ . Monitoring  $p$  and utilizing Henry's law gives insight into the total amount of gas in the headspace and solution in closed system. Henry's law can be utilised to calculate the molarity of a dissolved gas from its partial pressure. It will help to estimate the molar concentrations of ethanol and CO<sub>2</sub> present in the bacterial suspension from the FTIR measurements in the headspace.<sup>161,162</sup> The Henry's Law constants of CO<sub>2</sub> and ethanol in aqueous solutions at 37°C are 0.026 mM mbar<sup>-1</sup> and 82 mM mbar<sup>-1</sup>, respectively.<sup>163</sup> The standard deviation for ethanol partial pressure from a statistical analysis of the spectral baseline as conducted by our fitting routine correspond to 0.26 μbar, which can be used as an approximation for the noise equivalent (1σ) detection limit. According to Henry's constant, this detection limit equates to 22 μM of ethanol in solution. CO<sub>2</sub> is partially soluble in water. It will produce carbonic acid once it is dissolved owing to the reaction of a small proportion of the CO<sub>2</sub> with water, thus depending on the pH carbonic acid will be in equilibrium with bicarbonate and carbonate ions. It is estimated that carbonic acid and carbonates absorb less than 1 % of dissolved CO<sub>2</sub> under our conditions, which is negligible to a first approximation. The *in situ* and online FTIR identification allows for continuous and responsive testing without sampling, which is a significant benefit for monitoring bioprocesses.

### **5.2.2.2 Liquid Raman Spectroscopy for Phosphates, Formate, Acetate, Glucose and TMAO Analysis**

The bacterial suspension was cycled by a peristaltic pump PP(1) (4.5 L/h) from the custom flask to a sealed borosilicate tube with a 1 cm glass cuvette, before returning the suspension to the flask. For measuring the OD<sub>600</sub> *in situ*, a 650 nm laser pointer beam was scattered by the bacterial suspension through the 1 cm glass cuvette. The transmitted intensity was measured by a photodiode and calibrated with start and end OD values that were obtained externally with an UV-Vis spectrometer. Typically, the OD<sub>600</sub> of the bacterial suspension was between 1.0-1.2 in the stationary phase at the end of an experiment. A home-built liquid phase Raman spectrometer was used for analysing the bacterial suspension flowing through the sealed borosilicate tube. In summary, a green 20 mW cw laser (Lasos, GL3dT) at 532.2 nm

was turned by  $90^\circ$  using a small mirror (DM) and coupled into a microscope objective (MO) which focuses the beam to the suspension inside the glass tube. Back scattered Raman light was collimated by the same microscope objective, passed through the dichroic mirror DM, and focussed by a lens into a glass fibre for transmission to the monochromator (Shamrock SR-750-A) equipped with a CCD camera (Andor i-DusDU420A-OE, cooled to  $-80^\circ\text{C}$ ) and a  $1200\text{ mm}^{-1}$  grating blazed at  $750\text{ nm}$ . The grating offered a  $880\text{ cm}^{-1}$  spectral range between  $830$  to  $1710\text{ cm}^{-1}$  at a resolution of about  $0.8\text{ cm}^{-1}$ . Position of Raman peaks was estimated to be  $\pm 3\text{ cm}^{-1}$  accurate after wavenumber calibration. Raman spectra were taken every 5 min with 30 s integration time and 10 accumulations. The Raman intensities were normalised by using the water bending vibration at  $1630\text{ cm}^{-1}$ . The normalisation is important for biological samples that become turbid over time. The water peak was fitted by a Gaussian contour with an FWHM of  $80\text{ cm}^{-1}$  and a centre at  $1630\text{ cm}^{-1}$  in the normalisation. Since water concentrations stay constant during the course of an experiment, this water region must be similar in all Raman spectra and can therefore be used for normalisation. Reference Raman spectra of  $0.1\text{ M}$  of ammonium acetate, potassium formate, glucose, TMAO,  $\text{K}_2\text{HPO}_4$  and  $\text{KH}_2\text{PO}_4$  solutions were recorded for calibration and comparison purposes.<sup>164</sup>

The analytical efficiency of liquid Raman spectroscopy in biological samples is limited by two major factors. First, as the cell density rises, this will lead to the increasing of the turbidity of the solution, thus reducing the Raman signal intensity. Turbidity has a major impact on sensitivity and, most specifically, calibration. This problem is addressed by the water normalisation. Second, in Raman spectroscopy there is often interference by fluorescence, which can obscure Raman signals. In our biological experiments fluorescence was not a problem since the medium used was M9, a minimal medium which is colourless and non-fluorescent, as well as most metabolites being non-fluorescent at the  $532\text{ nm}$  excitation wavelength. However, using coloured growth media like LB, this has been seen before to be a limiting factor.<sup>109</sup> Fluorescence can often be reduced by switching to a longer wavelength Raman excitation, such as red or near-infrared lasers.

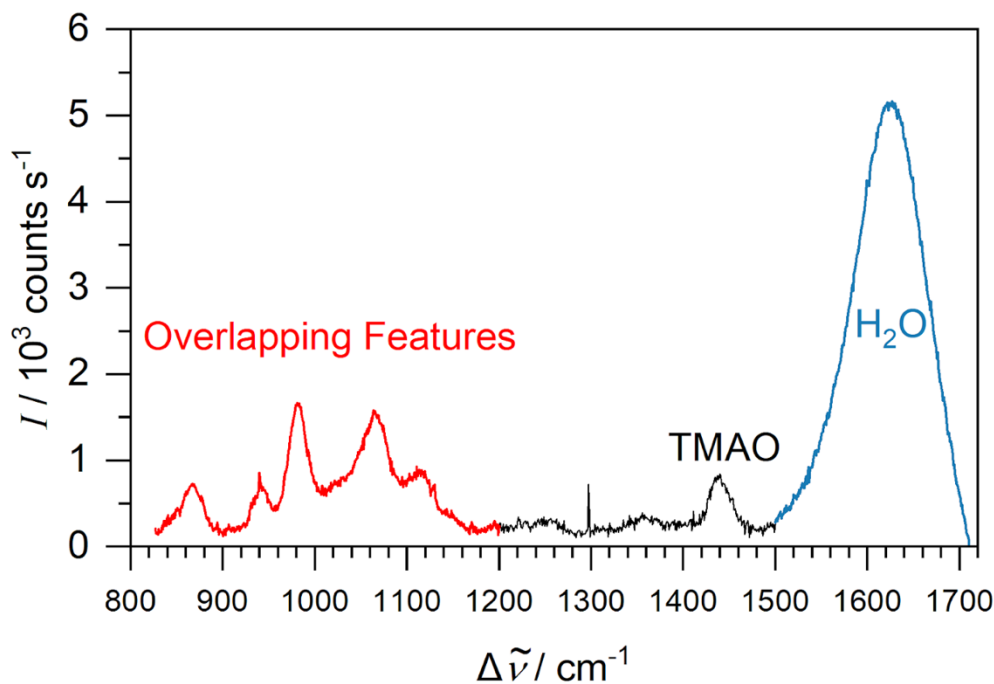


**Figure 5.8.** Experimental Raman spectrum of M9 medium supplemented with 30 mM glucose and 20 mM TMAO. In blue, the water bending vibration band is shown, in red overlapping features of different compounds.

A typical experimental Raman spectrum of a bacterial suspension in the region of 830 – 1710  $\text{cm}^{-1}$  contains characteristic Raman peaks, as shown in Fig. 5.8. Bands are observed for TMAO (945 and 1465  $\text{cm}^{-1}$ ), water (1630  $\text{cm}^{-1}$ ),  $\text{HPO}_4^{2-}$  (989  $\text{cm}^{-1}$ ),  $\text{H}_2\text{PO}_4^-$  (1076  $\text{cm}^{-1}$ ) and glucose (960 and 1180  $\text{cm}^{-1}$ ).<sup>164</sup> The overlapped features of the spectrum in red colour are discussed in Fig.5.9, which shows the features in a typical experimental liquid Raman spectrum in the range of 830–1200  $\text{cm}^{-1}$  in more detail. It includes the peaks of phosphate ions ( $\text{H}_2\text{PO}_4^-$ ,  $\text{HPO}_4^{2-}$ ), TMAO and glucose in the bacterial suspension at the start of a typical experiment. Phosphates are part of M9 medium, as a buffer. Glucose is supplied as an energy source for the bacteria. TMAO is an electron acceptor compound. The experimental Raman spectra can in principle arise due to products and metabolites within the bacterial cells, or from the solution. Since the total volume of bacterial cells is much smaller than the liquid medium, the experimental spectra are mainly due to species in solution.

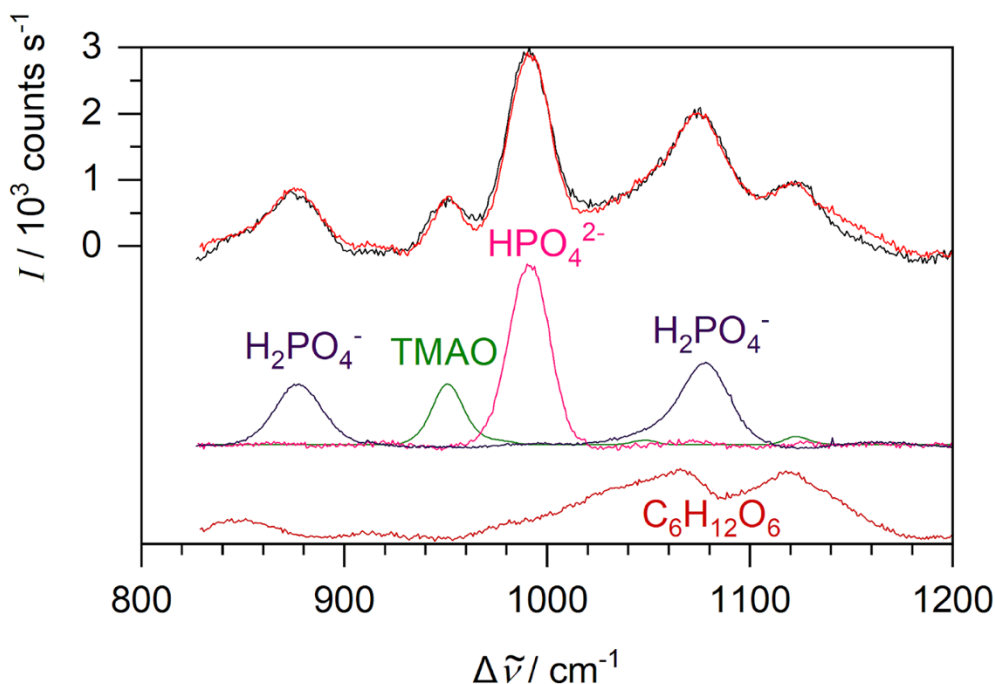


**Figure 5.9.** Raman experimental spectra of a bacterial suspension in M9 medium containing 20 mM TMAO, 30 mM glucose, 47 mM  $\text{HPO}_4^{2-}$  and 22 mM  $\text{H}_2\text{PO}_4^-$  at the start of a typical experiment.

As shown in Fig. 5.9, the experimental liquid Raman spectrum in the region of 830-1200  $\text{cm}^{-1}$  was fitted to the sum of the reference Raman spectra of pure compounds of known concentration (TMAO, phosphates and glucose) and a linear baseline.<sup>153</sup> The least-squares fit procedure has been implemented by a self-written computer program (Dr. Hippler). The multipliers of the reference spectra are then converted into concentration. The noise equivalent detection limit of this procedure can be estimated by recording a sequence of Raman spectra and analysing the noise level by observing the standard deviation value of the baseline. This noise equivalent ( $1\sigma$ ) detection limit for TMAO and glucose is about 1.8 mM and 1.9 mM at a total integration time of 5 min. The limits improve to 0.7 mM and 0.8 mM for TMAO and glucose, respectively when the integration period is averaged to 30 min. Note that the noise equivalent detection limit is defined as  $1\sigma$  (one standard deviation), but practical detection limits are often cited as  $3\sigma$  in literature.

The two phosphate anions represent a weak acid and its corresponding base at equilibrium around pH 7. The actual pH can therefore be determined spectroscopically *in situ* from the phosphate anion concentrations and a modified Henderson-Hasselbalch equation, as described by Hippler *et al.*<sup>165</sup> The phosphate buffer approximately maintains a constant pH by absorbing  $\text{H}^+$  by shifting  $\text{HPO}_4^{2-}$  to  $\text{H}_2\text{PO}_4^-$ . The change in concentration of the phosphate

anions therefore also allows the estimation of net  $[H^+]$ , the change of the net concentration of the sum of all acids (generating  $H^+$ ) minus the sum of all bases (removing  $H^+$ ) produced by bacterial activity.<sup>47</sup>

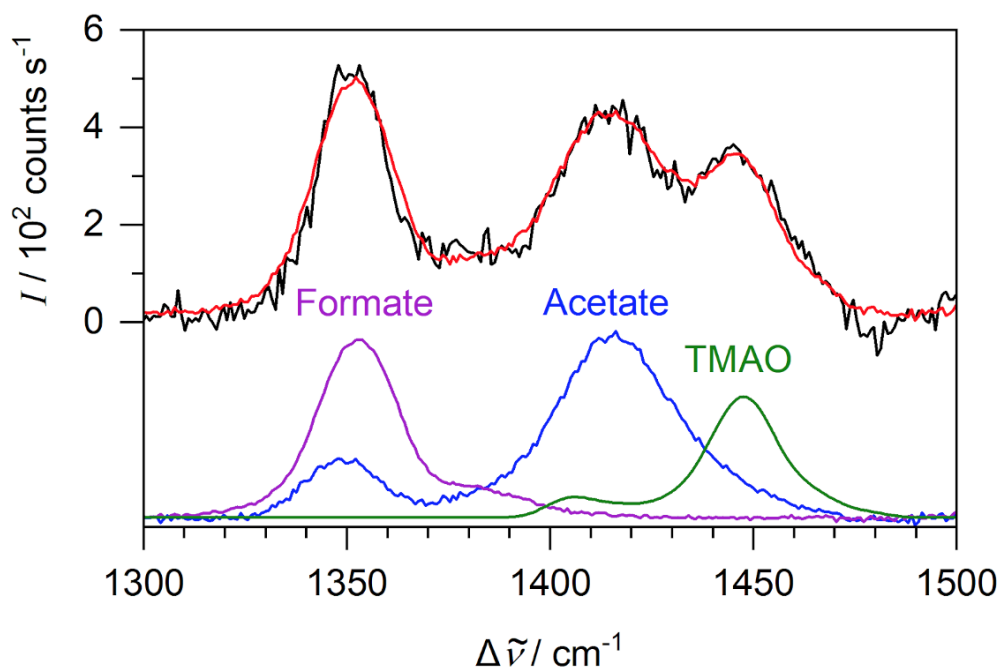


**Figure 5.10.** Experimental Raman spectrum of a bacterial suspension in M9 containing 10 mM TMAO, 10 mM formate and 20 mM acetate (in black). The sum of the references of the pure compounds (lower panel) is overlaid in red.

The concentrations of TMAO, acetate and formate were obtained by applying the least-squares fit procedure of a different region ( $1300\text{-}1500\text{ cm}^{-1}$ ), as shown in Fig. 5.10. The experimental Raman spectrum is fitted to the sum of the reference spectra of known concentrations (TMAO, acetate and formate) and a linear baseline. The multipliers of the model spectra were then converted into concentration. The noise equivalent detection limit of this procedure is again estimated by recording a sequence of Raman spectra and analysing the noise level by observing the standard deviation value of the baseline. This noise equivalent ( $1\sigma$ ) detection limit for formate and acetate is about 1.5 mM and 2.6 mM at an integration time of 5 min. The limits improve to 0.6 mM and 1.0 mM for formate and acetate, respectively when the integration period is averaged to 30 min.

During their metabolism, *E. coli* produces endogenous formate which is unlabelled (Fig. 5.3). Supplementing exogenous formate-d (Sigma 373842, 99% D) to bacterial

suspensions allows the distinction of endogenous and exogenous formate-d, because labelled formate-d and unlabelled formate have distinct shifted, separated Raman bands which can be distinguished in liquid Raman spectroscopy, as shown in Fig. 5.11. This allows the observation of formate produced and consumed by metabolic activity (endogenous formate), and exogenous formate being consumed.

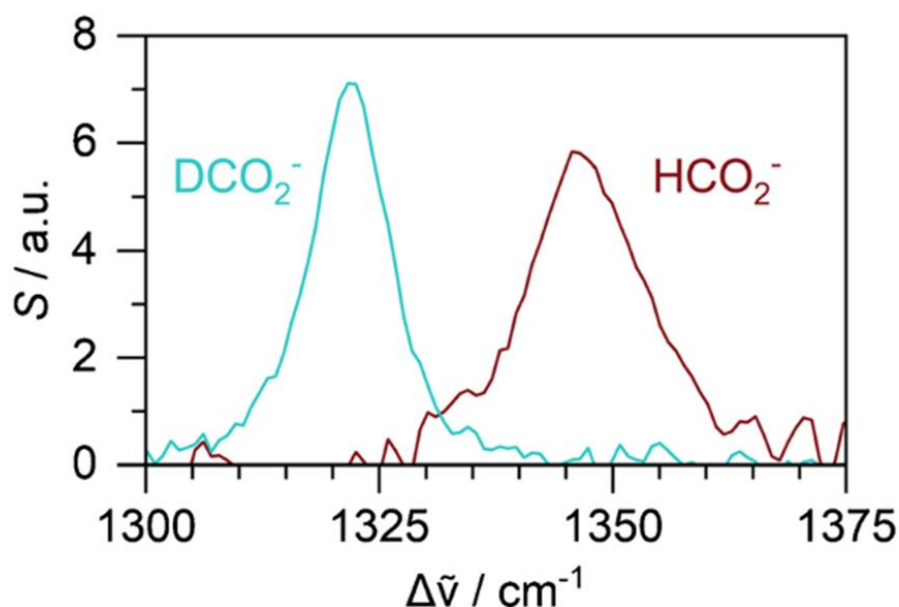


**Figure 5.11.** Liquid Raman spectra of 40 mM formate-d in blue and unlabelled formate solutions in red, demonstrating the spectral distinction of both compounds.<sup>47</sup>

### 5.2.2.3 FTIR Spectroscopy for TMA and NH<sub>3</sub> Analysis

TMA and ammonia NH<sub>3</sub> have very characteristic IR absorption bands which allow their identification and quantitative analysis. Under our acidic conditions in the bacterial suspension, however, these compounds exist in the protonated form which are not volatile. In chemistry the ammonium/ammonia equilibrium is well known, and the direction is controlled by the pH of the solution. Half of the ammonia will be un-ionized (NH<sub>3</sub>) and half will be ionized (NH<sub>4</sub><sup>+</sup>), when the pH is equal to the pK<sub>a</sub> = 9.25. 90% and 99% of the ammonia will be un-ionized at pH 10.25 and 11.25 respectively. With increasing pH, the volatility of the NH<sub>3</sub> increases; therefore, at high pH values it volatilizes freely from the solution. The same applies to TMAH<sup>+</sup> converting to volatile TMA (pK<sub>a</sub> = 9.87).<sup>117,166</sup> A typical pH of the M9 medium starts at 6.9 and ends in a typical experiment between 5.0 – 5.5 because of the excretion of organic acids.

Therefore, ammonia and TMA exist as  $\text{NH}_4^+$  and  $\text{TMAH}^+$  in the solution and need to be liberated as a gas in a sampling procedure. By taking samples from the suspension and adding appropriate amounts of a base (NaOH), the pH can be forced to around 11 which releases volatile TMA and  $\text{NH}_3$  which can then be analysed by FTIR spectroscopy.

Fig. 5.12 shows the measurement apparatus for determination of TMA and  $\text{NH}_3$  with a Bruker alpha FTIR spectrometer at  $0.8\text{ cm}^{-1}$  resolution. The spectra were recorded utilizing a multi-pass White cell equipped with KBr windows as described in chapter 2 of this thesis. In all culture samples, the  $\text{NH}_3$  and TMA concentrations were determined as described below.

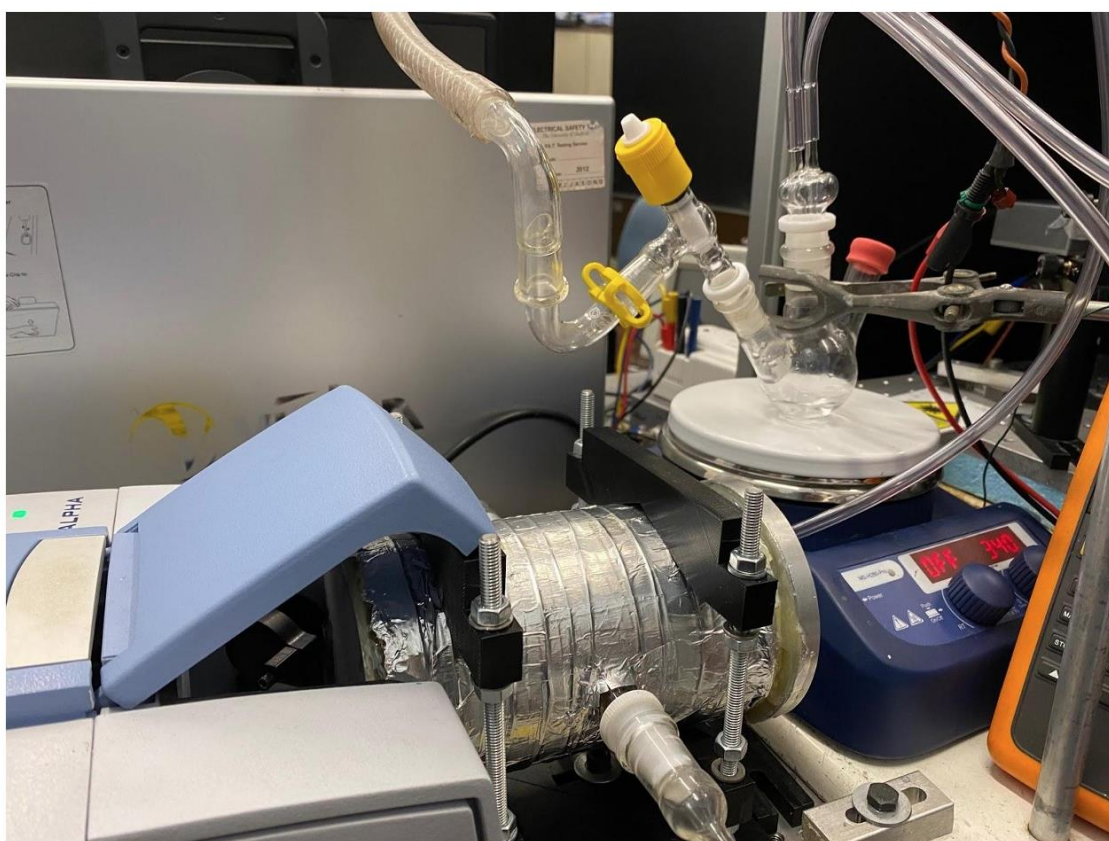


**Figure 5.12.** The experimental set-up for TMA and  $\text{NH}_3$  quantification with the Bruker alpha FTIR spectrometer and the home-built 2.0 m White cell.

The  $\text{NH}_3$  and TMA generated by the bacteria were measured after sampling. In brief, 0.6 mL samples of an *E. coli* suspension were taken every 40 min. The sample was then placed inside a 3-neck custom flask with stirring to allow continuous mixing. One neck led to the vacuum pump for purging the flask prior to measurements. The other neck was utilized to cycle the headspace above the sample with a peristaltic pump through the White cell for gas phase FTIR measurements. For  $\text{NH}_3$  and TMA liberation in the samples, 2 mL of NaOH (1M)

solution was pipetted into the flask to make the solution basic. This allows the conversion of ammonium in the liquid phase to be released as ammonia into the gas phase by changing the pH of the culture samples to pH around 11. This also applies to TMAH<sup>+</sup> converting it to volatile TMA. In the gas phase TMA and ammonia have absorption bands in the IR region that can be used to determine concentrations after a calibration. The concentrations of TMA and NH<sub>3</sub> in each sample were determined by taking recordings every 300 s continuously for 35 minutes before NH<sub>3</sub> and TMA signals peaked in the headspace. The OPUS software of the Bruker Alpha instrument was used to record FTIR spectra automatically.

Because the highest intensity absorption bands of TMA are between 2700 to 3030 cm<sup>-1</sup> and because this region is free from significant spectral interferences, this region was chosen for quantification of TMA. Fig. 5.13 shows the experimental FTIR spectrum of TMA with a fitted PNNL reference spectrum<sup>109</sup> in the spectral region of 2700 cm<sup>-1</sup> to 3030 cm<sup>-1</sup>. A home-written computer programme implements a least squares fit of the experimental FTIR spectrum in the region of 2700-3030 cm<sup>-1</sup> to the reference PNNL spectrum and a linear baseline. Using a calibration (see below), the concentration of TMA was then determined.

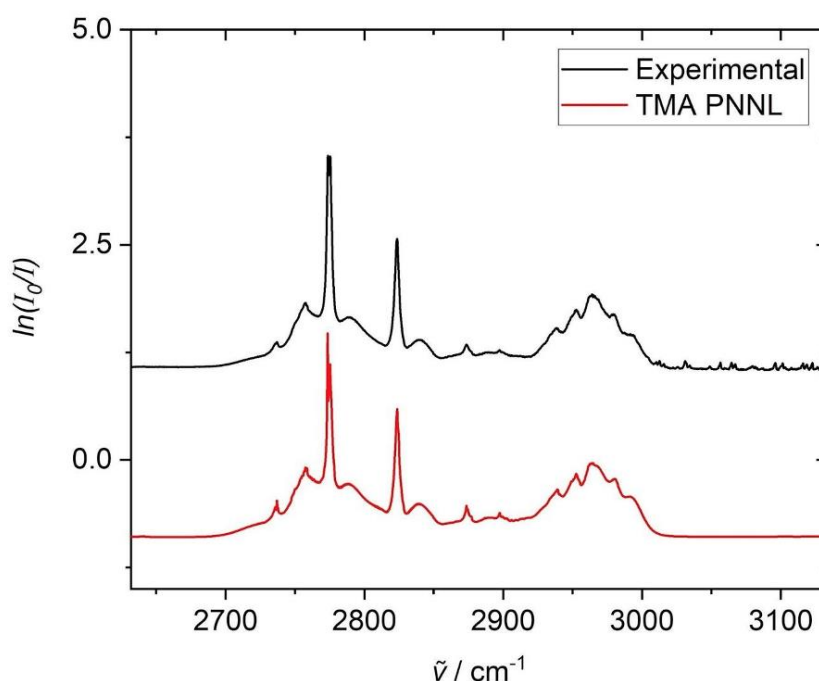


**Figure 5.13.** FTIR absorbance spectrum of TMA with fitted PNNL reference spectrum. In black is the experimental spectrum and the fitted PNNL reference spectrum is shown in red.

Figs 5.14 and 5.15 show the experimental FTIR spectrum of  $^{14}\text{NH}_3$  (black) and isotopically labelled  $^{15}\text{NH}_3$  (red) in the spectral region of  $900\text{ cm}^{-1}$  to  $1000\text{ cm}^{-1}$ . The region shows characteristic  $Q$ -branches of the  $\nu_2$  N-H wagging fundamental deformation vibration with a double peak centred around  $960\text{ cm}^{-1}$  for  $^{14}\text{NH}_3$ . This doubling of  $Q$ -branches is due to inversion doubling which is typical for triangular molecules like ammonia. Because the highest intensity absorption bands of ammonia are at  $966\text{ cm}^{-1}$  and since this band is free from significant spectral interference, it was chosen for quantification of  $^{14}\text{N}/^{15}\text{N}$  ammonia. The two isotopomers  $^{14}\text{NH}_3$  and  $^{15}\text{NH}_3$  can clearly be distinguished. A home-written computer programme calculated the least squares fit of the experimental spectrum of the FTIR spectrum in the region of  $955\text{--}970\text{ cm}^{-1}$  to the sum of scaled reference spectra of  $^{14}\text{NH}_3$  and  $^{15}\text{NH}_3$  and a linear baseline. Using a calibration (see below), the concentration of labelled and unlabelled ammonia was then determined.

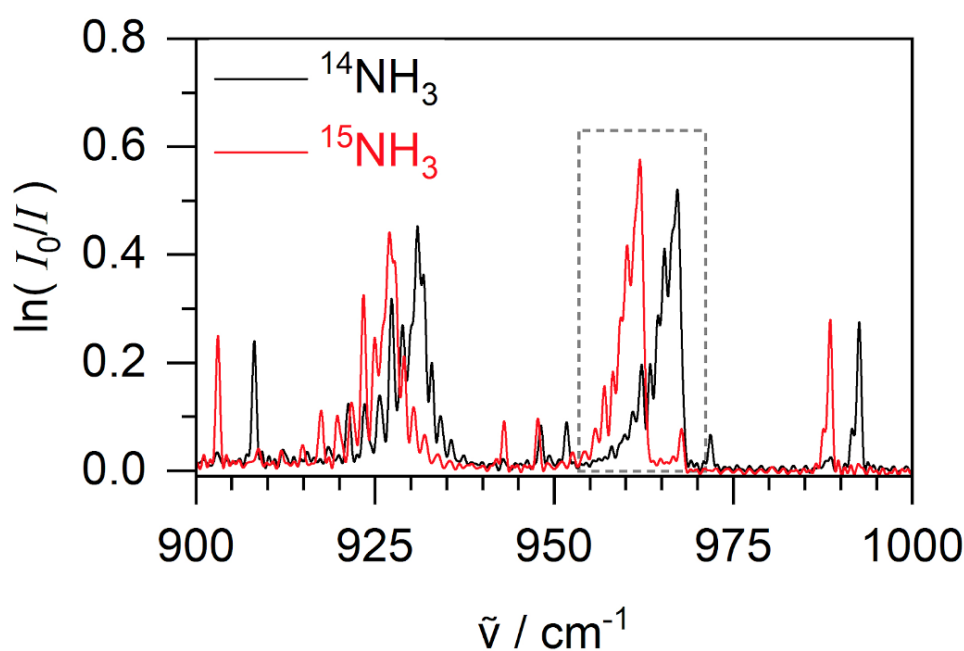


**Figure 5.14.** Experimental FTIR experimental spectra of  $^{14}\text{NH}_3$  (black) and  $^{15}\text{NH}_3$  (red) corresponding to  $20\text{ mM NH}_4^+$  in solution. The dashed line (grey) is the area of the  $\nu_2$   $Q$ -branch fitted for  $\text{NH}_3$  analysis of the two isotopomers.

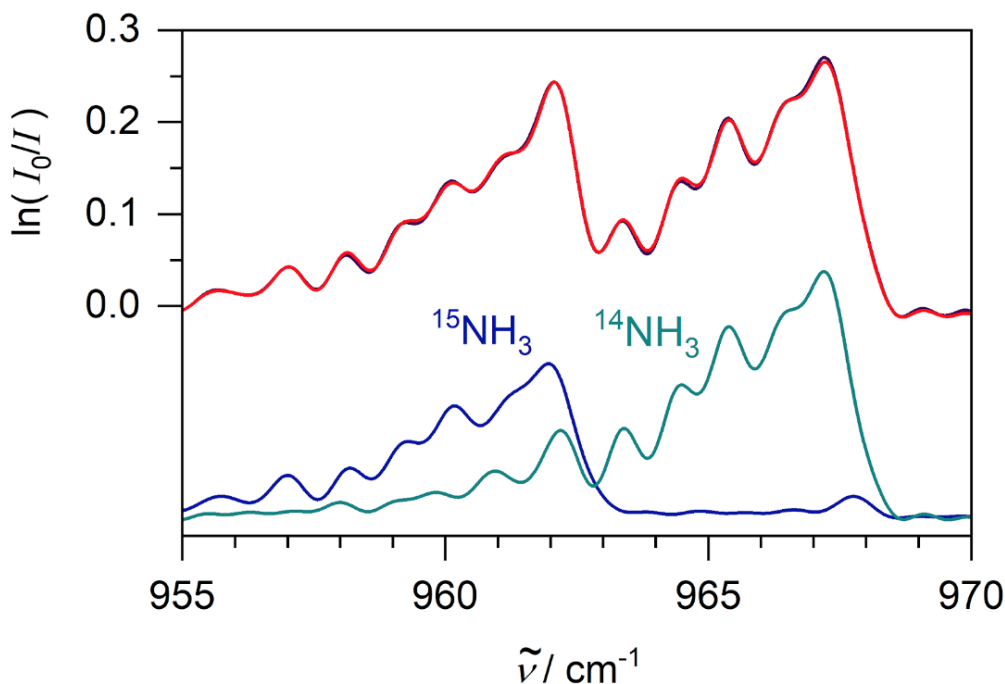


**Figure 5.15.** The experimental FTIR spectrum of a mixture of  $^{14}\text{NH}_3$  (12.5 mM) and  $^{15}\text{NH}_3$  (8.25 mM) in solution is shown in black. The sum of both fitted reference spectra (lower panel) of  $^{14}\text{NH}_3$  and  $^{15}\text{NH}_3$  is shown overlaid in red, demonstrating an almost perfect fit.

The concentrations of TMA,  $^{14}\text{NH}_3$  and  $^{15}\text{NH}_3$  were determined by gas phase FTIR spectroscopy. Since FTIR spectroscopy measures partial pressures, concentrations in the solution are obtained by a calibration. This is more accurate than just using Henry's law. In the calibration, 0.6 mL of the sample with known concentrations of ammonium salt was made basic with 2 mL of NaOH (1M) and measured as described before. FTIR spectra were fitted to reference spectra. The multipliers ( $x'$ ) of the reference spectra provide the y-axis of the calibration plots. The x-axis are the known concentrations. The calibration curves are shown in Figs 5.16 and 5.17. They showed good linearity and dynamic range. The 2.0 m White cell afforded trace gas detection of TMA with a noise equivalent ( $1\sigma$ ) detection limit corresponding to 0.2 mM in solution. The noise equivalent detection limit ( $1\sigma$ ) for ammonia was 0.13 mM ( $^{14}\text{NH}_3$ ) with a dynamic range up to 22.5 mM. As samples at the start contain 18 mM unlabelled  $^{14}\text{NH}_4^+$  as part of the M9 medium, this is a convenient range for the bacterial culture measurements. Due to the biomass synthesis, the concentration of  $^{14}\text{NH}_4^+$  in the medium will decrease during bacterial growth.

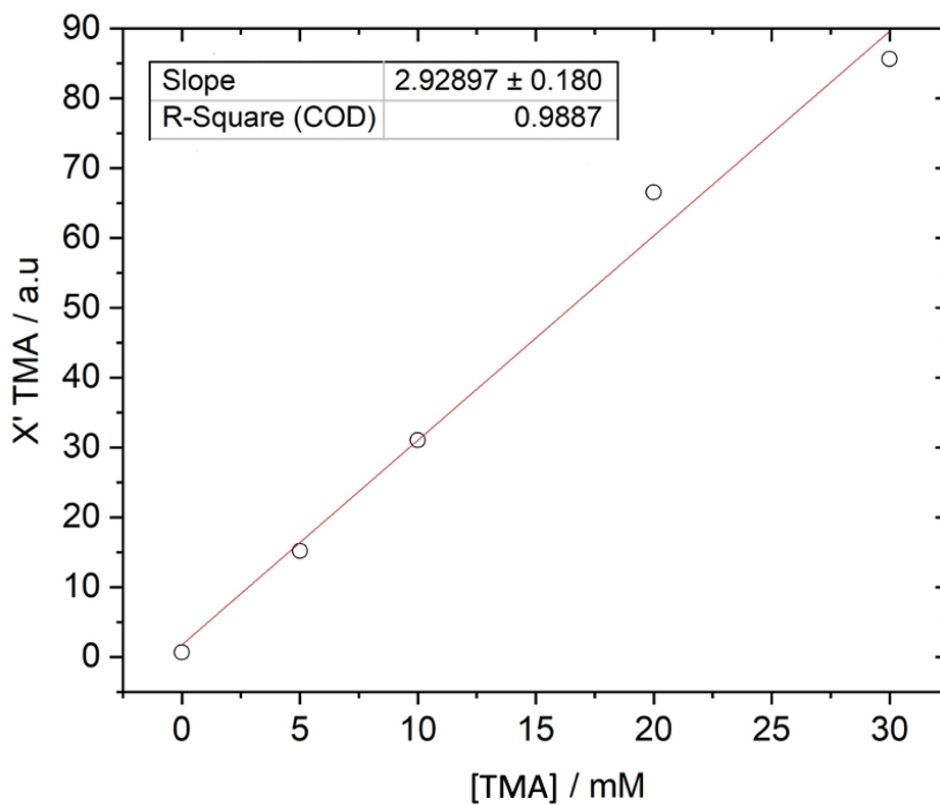


**Figure 5.16.** Calibration plot for TMA in solution.

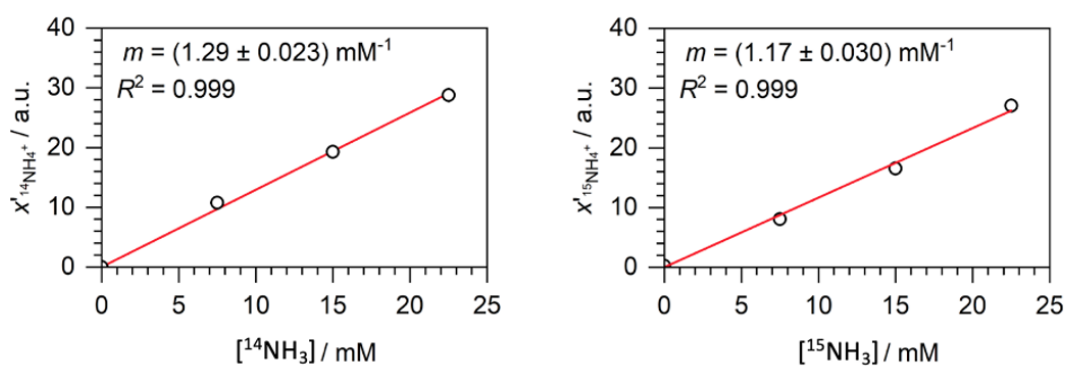


**Figure 5.17.** Calibration plots for  $^{14}\text{NH}_3$  and  $^{15}\text{NH}_3$  in solution.

### 5.2.2.4 CERS Measurements for H<sub>2</sub>, N<sub>2</sub>, CO<sub>2</sub> and O<sub>2</sub>

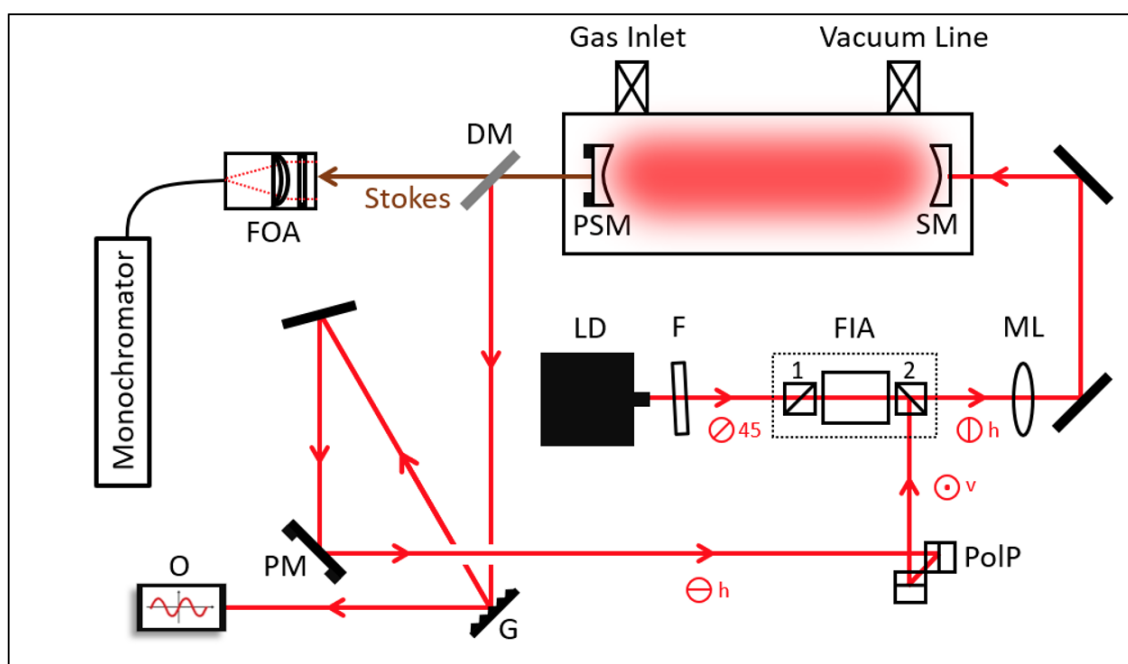


**Figure 5.18.** Experimental setup of CERS. LD- laser diode, F- filter, FIA- Faraday isolator assembly, ML- mode matching lens, SM- super mirrors, PSM- super mirror on a piezomount, DM- dichroic mirror, PM- piezomount of the mirror, FOA- fiber optic assembly, O- oscilloscope, G- grating, PoIP- pair of prisms for turning polarization plane of light. (Figure prepared by George D Metcalfe)

CERS was used for measurements of H<sub>2</sub>, N<sub>2</sub>, CO<sub>2</sub> and O<sub>2</sub> in the headspace above bacterial suspensions. This set-up was similar to the one that has been described before in detail in chapter 3, but several modifications were added (see Fig. 5.18). In summary, a 636.7 nm single mode cw laser diode (Opnext HL63133DG) provided up to 170 mW power. To facilitate single mode operation, however, the laser was operated at a reduced power of 40 mW. The diode laser was coupled by a short pass filter and a mode matching lens into the optical cavity which consisted of two highly reflective mirrors, SM, (Newport SuperMirrors,  $R > 99.99\%$ ). Unwanted back reflections from the first cavity mirror SM were prevented from reaching and damaging the laser diode by using the Faraday isolator assembly, FIA. The optical resonance builds up optical power within the cavity by up to 3 orders of magnitude if the wavelength of the laser matches the length of the cavity. Light confined inside the cavity reflects multiple times between the mirrors, PSM and SM. The resonances significantly increased the Raman signal as Raman signals scale linearly with laser power. A dichroic mirror DM was mounted

after the cavity to allow separation of laser light from Raman light. The Raman signal was coupled into a linear glass fibre bundle (7 x Ø105 µm) and transferred to the monochromator. Through the polarizing beam splitting cube 2 of FIA, a portion of the laser light was fed back to the laser diode for optical feedback to lock the laser to the optical cavity. There are additional elements in the feedback loop, a grating (G), piezo mounted mirror (PSM) and optical prisms (PoIP).

By using the optical prisms PoIP, the plan of polarization light in the feedback loop is modified. The laser light was linearly polarized at 45° before the first polarizing beam splitting cube 1 which allows this component to pass. The Faraday rotator rotates the plane of polarization of the light by -45°, so that afterwards, the light passes polarizer cube 2 since the light is now horizontally polarized with respect to the bench (0°). The light coming out of the optical cavity will also be mainly horizontally polarized, however this would make it unsuitable for optical feedback because polarizing beam splitting cube 2 of FIA will only reflect vertically polarized light back to the laser diode in the return path. It is therefore necessary to rotate the plane of polarization of light by 90° up vertically from the bench which is done by the optical prisms. By polarizing beam splitting cube 2, the returning light can then pass-through the Faraday rotator, where it will be rotated optically by -45° leading to +45° polarisation, which can pass the polarizer cube 1 for optical feedback of the diode.

Further additional elements of this set-up are the piezo actuator PM and grating G. The piezo is used to allow phase matching, to adjust the length of the feedback loop to multiples of the laser wavelength, this enhances the power build up inside the cavity to create detectable levels of scattered Raman light. The grating in the feed-back loop is used to make the wavelength more selective, to ensure single mode operation. More additional details of the CERS set-up were described by Hippler *et al.*<sup>47</sup>

Fig. 5.19 shows the O<sub>2</sub> and N<sub>2</sub> Raman lines utilized for the measurements. It is dominated by the Q-branch of the N<sub>2</sub> fundamental stretching vibration at 2329 cm<sup>-1</sup> and the Q-branch of the fundamental stretching vibration of O<sub>2</sub> at 1556 cm<sup>-1</sup> in 1 atm air. Fig. 5.20 shows Raman lines of a mixture of 140 mbar of CO<sub>2</sub> and 140 mbar H<sub>2</sub> as recorded during an anaerobic fermentation experiment. The spectrum is dominated by the Q-branches of the CO<sub>2</sub> ν<sub>1</sub>/2ν<sub>2</sub> Fermi resonance pair at 1285 cm<sup>-1</sup> and 1387 cm<sup>-1</sup> and pure rotational lines of H<sub>2</sub> at S<sub>0</sub> (1) 587 cm<sup>-1</sup>, S<sub>0</sub> (2) 814.4 cm<sup>-1</sup> and S<sub>0</sub> (3) 1034 cm<sup>-1</sup>.<sup>167</sup>

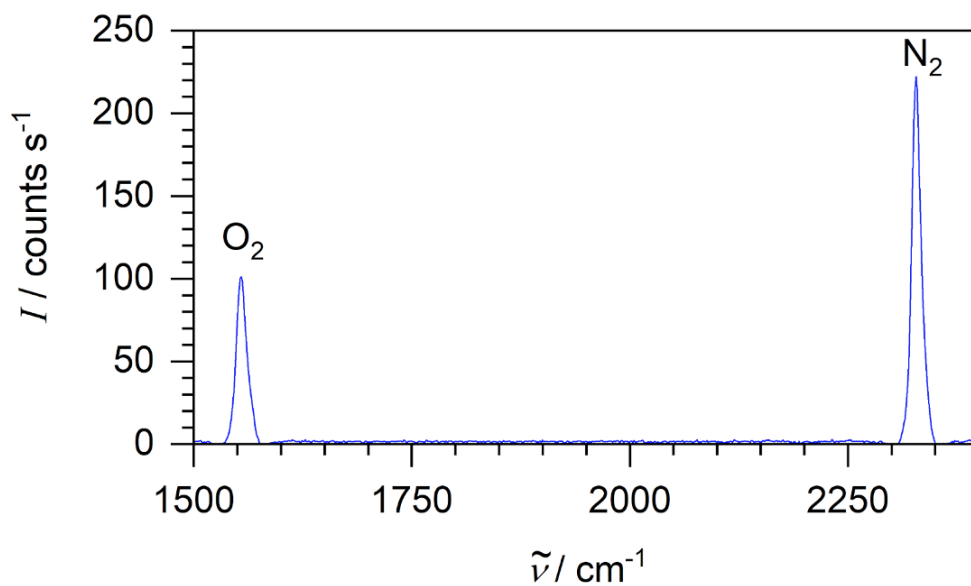


**Figure 5.19.** CERS Raman spectrum of  $O_2$  and  $N_2$  in 1 atm air. Both  $O_2$  and  $N_2$  have a strong  $Q$ -branch of their stretching vibration in-between their unresolved  $O$ - and  $S$ - branches.

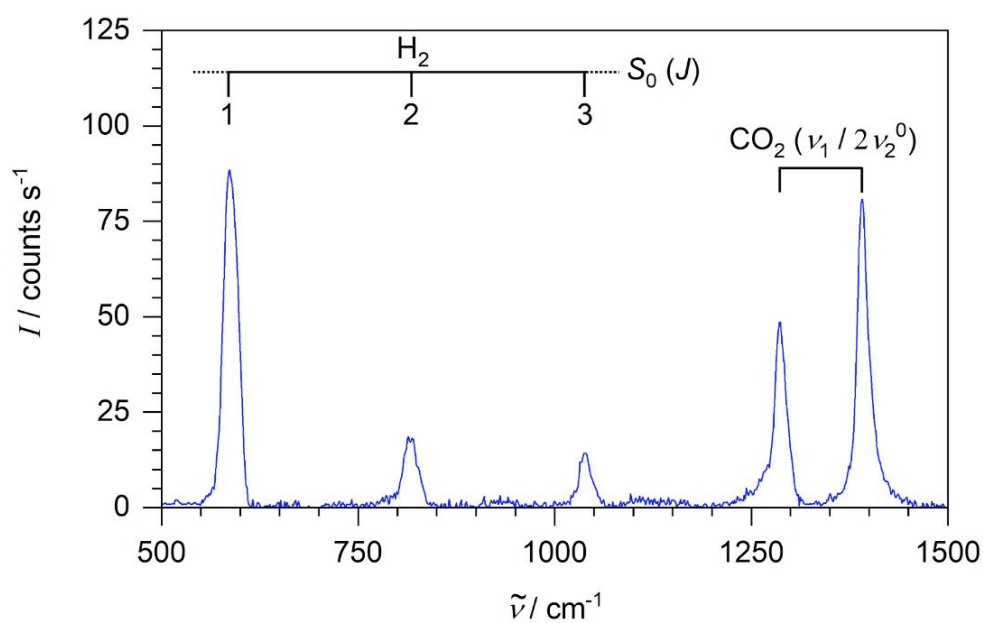


**Figure 5.20.** CERS Raman spectrum of 140 mbar  $H_2$  (rotational  $S$ - branch lines) and 140 mbar  $CO_2$  (Fermi resonance).

The N<sub>2</sub> peak of air can be used to normalize Raman signals in a closed system, since N<sub>2</sub> is not consumed or produced by *E. coli*. To obtain partial pressure of H<sub>2</sub> after a calibration, the S<sub>0</sub>(1) 587 cm<sup>-1</sup> area of the rotational line of H<sub>2</sub> was divided by the N<sub>2</sub> peak corresponding to 790 mbar in air. A calibration was constructed for H<sub>2</sub> using known partial pressures of H<sub>2</sub> gas, as shown in Fig 5.21. The calibration plot of H<sub>2</sub> showed good linearity. A similar method has been used with CO<sub>2</sub>; good linearity was also shown in the CO<sub>2</sub> calibration plot, Fig. 5.21.

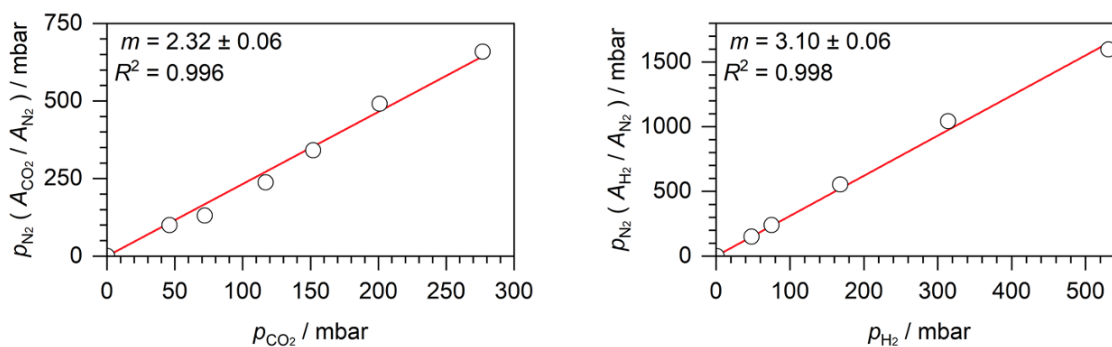


**Figure 5.21.** Calibration plots of CERS signals of CO<sub>2</sub> and H<sub>2</sub> (divided by N<sub>2</sub> as normalisation, see text)

## 5.3 Results and Discussion

### 5.3.1 Anaerobic TMAO Respiration

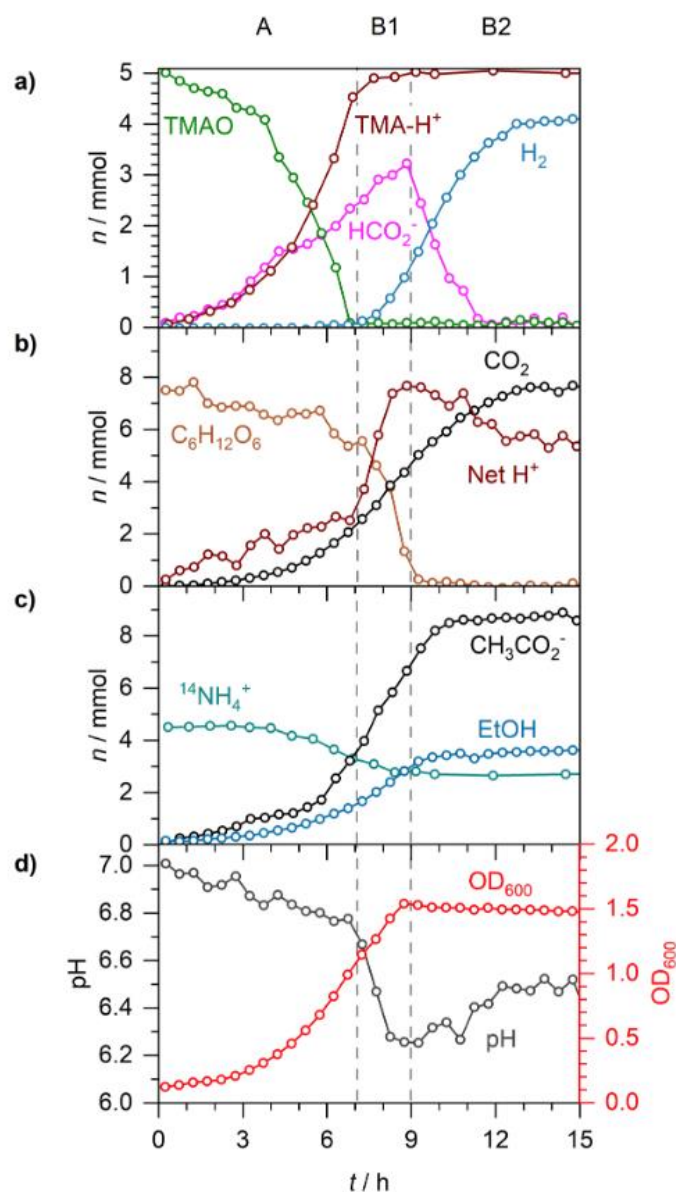


**Figure 5.22.** Anaerobic respiration of 20 mM TMAO by *E. coli* grown in M9 medium. Three distinct phases are observed: TMAO respiration (A), fermentation during exponential growth (B1) and fermentation after glucose depletion (B2). **a)** Time-dependent number of moles ( $n$ ) of TMAO, TMA-H<sup>+</sup>, formate and H<sub>2</sub>. **b)**  $n$  of CO<sub>2</sub>, glucose and net H<sup>+</sup>. **c)**  $n$  of acetate, ethanol and ammonium. **d)** Spectroscopically measured pH and OD<sub>600</sub>.

Anaerobic TMAO respiration was studied first for comparison with aerobic TMAO respiration and anaerobic TMAO respiration with added exogenous formate-d. Figure 5.22

displays the time-dependent number of moles ( $n$ ) of metabolites alongside pH and OD measurements for *E. coli* grown anaerobically in M9 medium supplemented with 20 mM TMAO and 30 mM glucose. Moles in solution were determined by multiplying concentrations (molarities) with the volume of the culture (0.25 L). Moles in the headspace were calculated by the ideal gas law and corrected for the dissolved percentage according to Henry's law. Experiments were repeated in triplicate and all repeats exhibited similar behaviour, Fig. 5.22 is a representative measurement selected from the three repeats. Fig. 5.23 shows the amount of variation associated with repeat measurements with averaged moles of TMAO and CO<sub>2</sub> for the three repeats, error bars were calculated by the standard deviation.

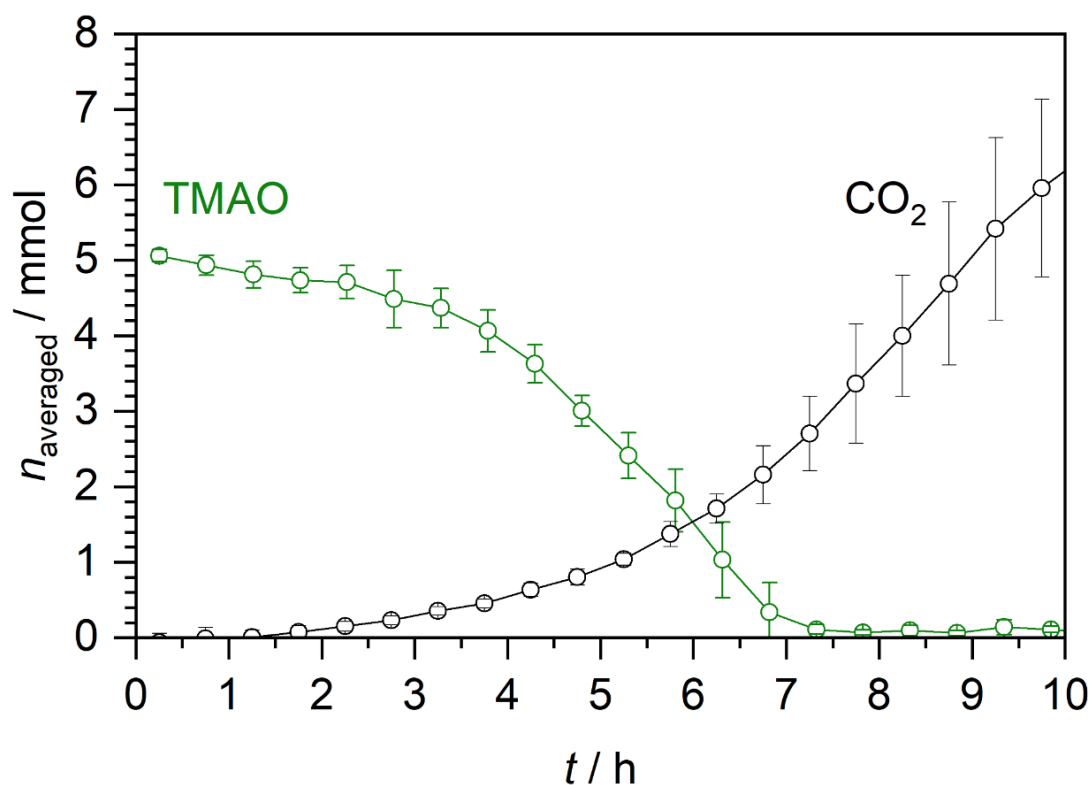


**Figure 5.23.** Averaged moles of TMAO and CO<sub>2</sub> during the three repeats of anaerobic respiration of *E. coli* grown in M9 medium supplemented with 20 mM TMAO.

Three distinct phases were apparent over the 13 h of *E. coli* growth curve labelled as **A**, **B1** and **B2** in Fig. 5.22. TMAO respiration occurred between 0 - 7 h, in phase **A**. When TMAO was depleted at 7 h, the bacteria switched to glucose fermentation between 7 - 13 h in phase **B**. Once the glucose was depleted in phase **B1**, accumulated formate was converted to H<sub>2</sub> and CO<sub>2</sub> (phase **B2**) after which no further signs of metabolic activity were observed. The

fermentation phase was divided into **B1** and **B2** at 9 h which was the point glucose was depleted triggering the end of exponential growth. The end of exponential growth is apparent in Fig. 5.22 as the OD peaks at 1.5 at 9 h. However, much more detailed information and insight is obtained by looking at the metabolite concentrations.

During the 7 h of phase **A**, all 5 mmol TMAO was reduced to protonated TMA, due to the acidic pH of the medium. The OD started at 0.1 and did not increase much for approximately 3 h and then increased significantly indicating exponential growth. The consumption of TMAO almost mirrored the growth curve. Formate produced by PFL in the cytoplasm was immediately excreted out of the cell by FocA.<sup>168</sup> 2.4 mmol formate was produced during **A**, but no H<sub>2</sub> production was observed. This suggested that formate oxidation by formate dehydrogenase-N was coupled to TMAO reduction by *torCAD* to generate PMF.<sup>169</sup> During **A**, due to biosynthesis during exponential growth, glucose and ammonium decreased by 2 mmol and 1 mmol, respectively. Glucose metabolism also produced 3.4 mmol acetate, 1.4 mmol ethanol and 2.3 mmol CO<sub>2</sub>, all of which mirrored the growth curve in their production. The 2.3 mmol CO<sub>2</sub> produced indicated that 2.3 mmol formate was oxidised likely by formate-dependent TMAO reduction. Under our growth conditions, it is expected that formate will serve as a physiological source of electrons for TMAO reduction.<sup>170</sup> Glycerol, succinate, pyruvate, lactate and H<sub>2</sub> can also serve as electron donors, but they are not present to any significant degree during **A**. The remaining 2.7 mmol TMAO was likely coupled to the oxidation of NADH generated during glycolysis. This likely means under our anaerobic conditions, TMAO reduction coupled in a ratio of almost 50:50 to the oxidation of formate and NADH. This is consistent with the work of Sakaguchi *et al.* who observed that among a series of electron donors, NADH followed by formate showed the highest activity for coupling to TMAO reduction in *E. coli*.<sup>170</sup>

By totalling CO<sub>2</sub> and excreted formate, 4.7 mmol formate must have been made during **A**. The observed 3.4 mmol acetate and 1.4 mmol ethanol (total 4.8 mmol) are in good agreement with the 4.7 mmol formate. Net H<sup>+</sup> is an estimate of the change of the net concentration of the sum of all excreted organic acids (generating H<sup>+</sup>) minus the sum of all bases (removing H<sup>+</sup>) produced, by analysing the balance of the phosphate anions of the phosphate buffer. Net H<sup>+</sup> increased to about 2 mmol consistent with the observed fall in the pH from 6.9 to 6.8. In balance, during phase **A**, there are 5 mmol of basic TMA-H<sup>+</sup> and 5.8 mmol of acidic acetate and formate excreted. The calculated resulting net H<sup>+</sup> of 1 mmol is less than the 2 mmol value obtained from the analysis of the phosphate buffer. This is probably due to

uncertainties in the measurement of phosphate anion concentrations. To obtain net  $H^+$ , two big numbers (phosphate anion concentrations) are subtracted to get one small number (net  $H^+$ ) which introduces noise and uncertainty.

In phase **B1**, the excretion of formate into the growth medium continued as glucose was still available to be metabolised. When glucose was depleted at 9 h and the  $OD_{600}$  peaked at 1.5, extracellular formate also peaked at 3.2 mmol. Formate was also disproportionated to  $CO_2$  and  $H_2$  by FHL in **B1**, starting when TMAO was depleted. This is consistent with the findings of Abaibou *et al.* who observed that when TMAO is present, despite the high amount of formate excretion, intracellular formate is too low to trigger expression of FHL due to coupling to TMAO reduction.<sup>159</sup> However, as soon as TMAO is depleted, FHL expression can occur. Excreted formate shows complicated kinetics due to formate being an intermediate. Below a pH of 6.8, FocA can re-import formate for disproportionation by FHL. In the present experiment, this cannot be directly observed as a decrease in formate in **B1**, due to the net excretion of formate. As discussed further in section 5.3.3, with the use of deuterated formate, formate import can be distinguished from formate excretion. Also during **B1**, a further 5.3 mmol acetate and 0.8 mmol formate are excreted causing the pH to decrease from 6.8 to 6.25. The pH decreased more in **B1** than **A** due to no further basic TMA production and more acids being produced in **B1**.

In the stationary phase **B2**, formate can no longer be generated due to glucose depletion. The 3.2 mmol extracellular formate was then reimported and consumed between 9 - 13 h, almost linearly. 3.0 mmol  $H_2$  and 3.2 mmol  $CO_2$  were observed to be produced during **B2**, in good agreement with the amount of formate reimported. Ammonium concentrations remained constant during **B2**, as no significant biosynthesis could occur without glucose, the carbon source for growth. In **B2**, the pH recovered to 6.5, as the acidic formate was reimported. This was also seen in the net  $H^+$  which decreased by roughly 3 mmol, in good agreement with the amount of reimported formate.

The dry biomass at the end of the experiment was typically around 200 mg. *E. coli* can be estimated to be 48% carbon (C) and 14% nitrogen (N).<sup>171</sup> This estimation has been confirmed by elemental analysis which showed that our *E. coli* had roughly 44 % for C and 12 % for N. It is therefore expected that the biomass contains about 8 mmol C and 2 mmol N. The 8 mmol C in the biomass originated from the 7.5 mmol glucose (containing 45 mmol C). 40 out of the 45 mmol C from glucose can be accounted for in the biomass (8 mmol C), 7.6 mmol

CO<sub>2</sub>, 8.7 mmol acetate (17.4 mmol C) and 3.5 mmol ethanol (7.0 mmol C) produced. The N in the biomass can be accounted for by the ammonium which dropped from 4.5 mmol to 2.7 mmol, as it is the only significant N source available in the growth medium.

### 5.3.2 Aerobic TMAO Respiration

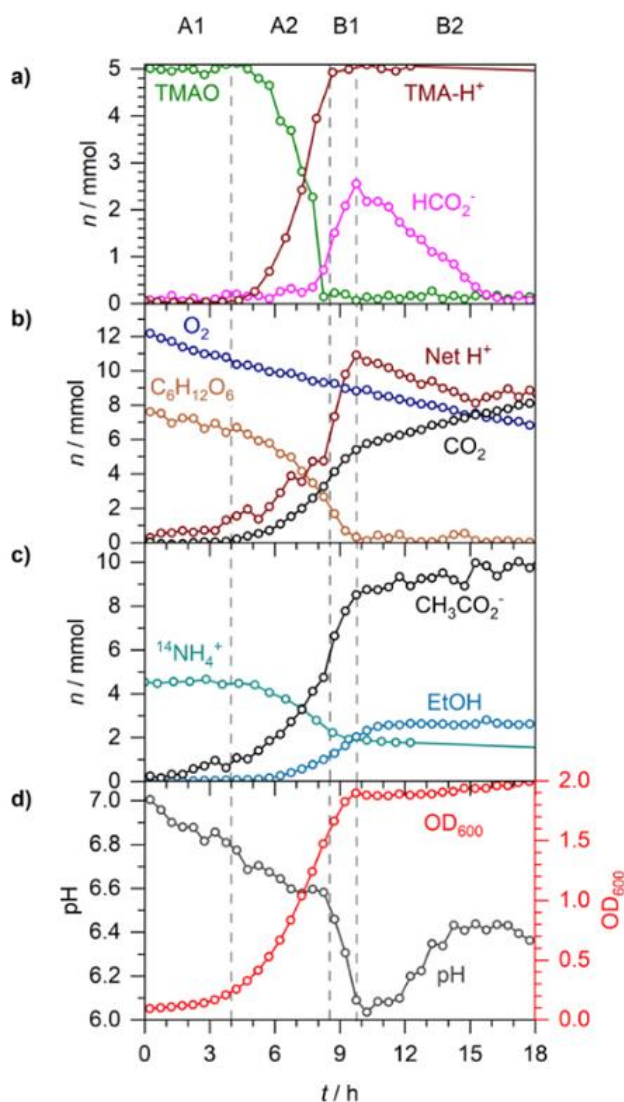


**Figure 5.24.** Aerobic respiration of 20 mM TMAO by *E.coli* grown in M9 medium. Four distinct phases are observed: lag in aerobic TMAO reduction (**A1**), TMAO reduction (**A2**), aerobic respiration during exponential growth (**B1**) and aerobic respiration after glucose depletion (**B2**). **a**) Time-dependent number of moles ( $n$ ) of TMAO, TMA- $H^+$  and formate. **b**)  $n$  of  $O_2$ ,  $CO_2$ , glucose and net  $H^+$ . **c**)  $n$  of acetate, ethanol and ammonium. **d**) Spectroscopically measured pH and  $OD_{600}$ .

Aerobic TMAO respiration was studied next to compare directly with anaerobic TMAO respiration (previous section). Using Henry's law, we estimate that the initial 210 mbar of  $O_2$  corresponds to 0.2 mM dissolved  $O_2$  in solution. *E. coli* typically uses electron acceptors in a hierarchical order which reflects the relative amounts of conserved energy. During aerobic growth most alternative respiratory systems are repressed, because  $O_2$  has the highest reduction potential. Nevertheless, TMAO is an exception to this rule. Under both aerobic and anaerobic

growth conditions, the expression of *torCAD* and the reduction of TMAO happens despite the comparatively low energy yield of the TMAO-TMA pair.<sup>117,172</sup> The reason why *E. coli* responds to and reduces TMAO under aerobic conditions is not completely understood at present. Although *torCAD* is transcribed at similar average levels for aerobic and anaerobic *E. coli* cultures, the behaviour among the cellular population is very different.<sup>117,172</sup> Cellular levels of *torCAD* transcription are relatively homogeneous in their distribution for anaerobic cultures, but aerobically the distribution is highly heterogeneous.<sup>172</sup> One hypothesis for why aerobic cultures reduce TMAO is that the production of basic TMA helps maintain stable growth conditions by resisting the acidification of the medium.<sup>117</sup> The variable level of TMAO reduction across all of the cells in the population may be to balance the cost of expressing different levels of the *torCAD* operon against the advantage of producing basic TMA for maximum benefit. Alternatively, the non-uniform level of *torCAD* expression may be due to a bet-hedging strategy in case the aerobic culture transitions to anaerobiosis. The cost of expressing *torCAD* aerobically would be balanced by the advantage of having pre-expressed *torCAD* in the absence of oxygen.<sup>172</sup>

In this section, we study aerobic respiration of *E. coli* in the presence of O<sub>2</sub> and TMAO as electron acceptors. A summary of our results is shown in Fig. 5.24. Four distinct phases were apparent over the 16 h of metabolic activity by *E. coli* labelled as **A1**, **A2**, **B1** and **B2** in Fig. 5.24: lag in aerobic TMAO reduction (**A1**), TMAO reduction (**A2**), aerobic respiration during exponential growth (**B1**) and aerobic respiration after glucose depletion (**B2**).

During both aerobic (this section) and anaerobic growth (previous section) TMAO is consumed, but with aerobic TMAO there is a distinct lag phase (phase **A1**). During **A1**, there is no detectable TMA produced for the first 4 h; in contrast with the anaerobic experiment where it is produced immediately, mirroring the growth curve. Metabolic activity does occur during **A1**. Despite the lag in TMAO reduction, the OD<sub>600</sub> rises slightly (as in the previous section) and O<sub>2</sub> is consumed. By 4 h, O<sub>2</sub> had decreased by 1.7 mmol but no significant CO<sub>2</sub> was produced. This likely was due to the bacteria transferred from the starter culture undergoing adjusting to the new growth environment (from LB to M9 medium) and generating energy in preparation of exponential growth by coupling O<sub>2</sub> reduction to NADH oxidation. The lag in aerobic TMAO reduction is consistent with the findings of Ansaldi *et al.* who found when comparing aerobic and anaerobic TMAO reduction, under aerobic conditions the expression of the *tor* operon was very low during early exponential growth.<sup>117</sup>

TMAO respiration occurred between 4 – 8.5 h, in phase **A2**. After the lag, TMAO is reduced almost linearly, at a similar rate to anaerobic TMAO reduction. This is consistent with *torCAD* transcription being at similar levels in aerobic and anaerobic environments containing TMAO. It is difficult to determine the amounts of electron donors coupling to TMAO aerobically as electron donors will also be used for oxidative phosphorylation. During **A2**, the pH decreased to 6.6 due to excretion of 7 mmol acetate, but no detectable amount of formate. 4 mmol CO<sub>2</sub> was produced that may have come from the oxidation of intracellular formate preventing significant build-up of the acidic species that would require excretion. Acetate was excreted in **A2**, as glucose uptake was likely exceeding aerobic respiratory capacity leading to overflow metabolism. Possibly the acidification of the medium and O<sub>2</sub> decreasing below 10 mmol may have prompted TMAO reduction to begin in **A2**. Glucose, ammonia, net H<sup>+</sup>, ethanol and OD<sub>600</sub> all showed similar trends to anaerobic conditions.

When all TMAO was reduced at 8.5 h, the bacteria continued to reduce O<sub>2</sub> and oxidised available carbon sources in phases **B1** and **B2**. **B1** and **B2** were divided at 10 h which was the point where glucose was depleted triggering the end of exponential growth. The end of exponential growth is apparent in Fig. 5.24 as the OD peaked at 1.9 and essentially plateaued afterwards. Aerobic growth typically yields a higher optical density than anaerobic growth.

In phase **B1**, the excretion of formate into the growth medium began as glucose was still available to be metabolised. This may suggest formate was always being produced during **A2** and was being immediately oxidised by coupling to TMAO reduction. In **B1**, without TMAO to couple to, the *E. coli* may simply be excreting formate to prevent cytoplasmic acidification. Extracellular formate peaked at 2.6 mmol at the transition from **B1** to **B2**. During **B1**, alongside formate excretion, the further 4.0 mmol acetate excreted caused the pH to decrease from 6.6 to 6.1. The pH decreased more in **B1** than **A** due to no basic TMA being produced to counterbalance the acids being produced.

In phase **B2**, formate can no longer be generated due to glucose depletion. The extracellular formate was then reimported and oxidised to CO<sub>2</sub> between 10 to 16 h, almost linearly. No H<sub>2</sub> production was observed in either **B1** or **B2** unlike anaerobic conditions after TMAO depletion. This was simply because FHL typically cannot be expressed in the presence of O<sub>2</sub>.<sup>136</sup> Ammonium concentrations remained constant during **B2**, as no significant biosynthesis could occur without glucose. In **B2**, the pH recovered to 6.5, as the acidic formate was oxidised to CO<sub>2</sub>. This was also seen in the net H<sup>+</sup> which decreased by roughly 2.6 mmol,

in good agreement with the amount of reimported formate. Outside the range displayed in Fig. 5.24, O<sub>2</sub> continued to decrease exponentially, even when oxidisable carbon sources were depleted and no further CO<sub>2</sub>, acetate or ethanol were produced. Most likely this was a starvation survival response from *E. coli* that can now only couple O<sub>2</sub> reduction to NADH oxidation.<sup>41</sup>

The 45 mmol C provided by the glucose can be mostly accounted for in the biomass (*ca.* 8 mmol), 7.6 mmol CO<sub>2</sub>, 10 mmol acetate (20 mmol C) and 3 mmol ethanol (6 mmol C) produced, totalling 41.6 mmol C. The 2 mmol N in the biomass can be accounted for by the ammonium which dropped from 4.5 mmol to 2.5 mmol.

### 5.3.3 Anaerobic 20 mM TMAO and 20 mM Formate-d

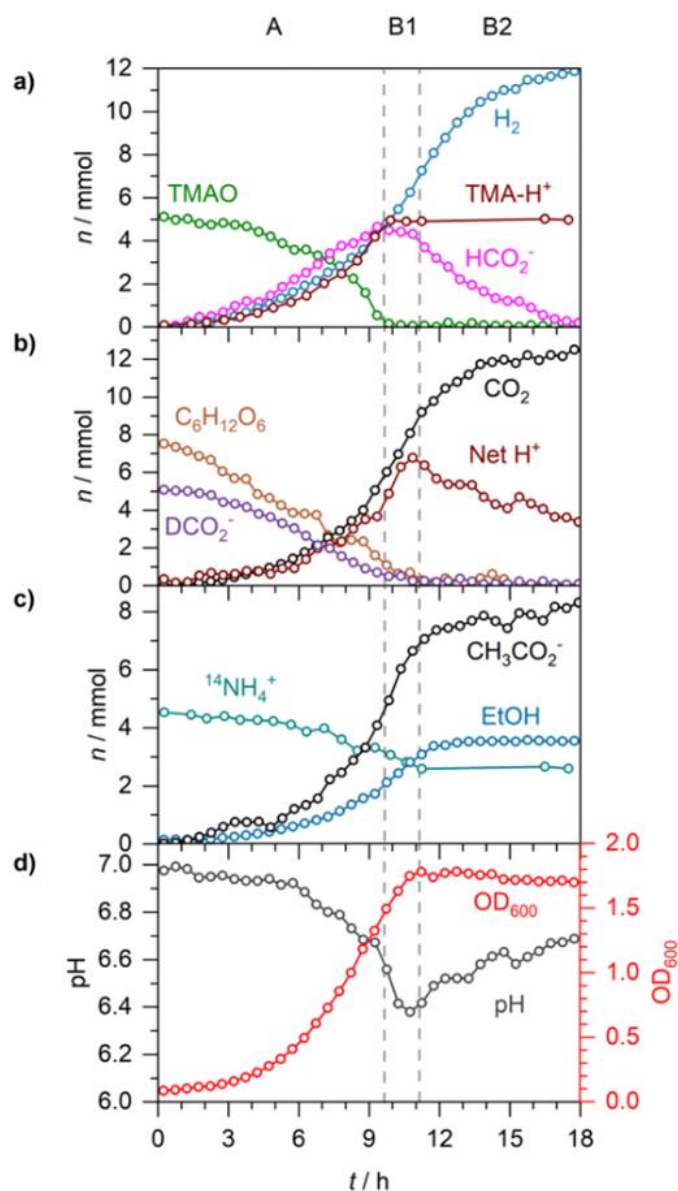


**Figure 5.25.** Anaerobic respiration of 20 mM TMAO by *E. coli* grown in M9 medium supplemented with 20 mM formate-d ( $\text{DCOO}^-$ ). Three distinct phases are observed: TMAO reduction (**A**), fermentation during exponential growth (**B1**) and fermentation after glucose depletion (**B2**). **a)** Time-dependent number of moles ( $n$ ) of TMAO, TMA- $\text{H}^+$ , formate and  $\text{H}_2$ . **b)**  $n$  of formate-d,  $\text{CO}_2$ , glucose and net  $\text{H}^+$ . **c)**  $n$  of acetate, ethanol and ammonium. **d)** Spectroscopically measured pH and  $\text{OD}_{600}$ .

In order to study TMAO respiration in the presence of exogenous formate, and to demonstrate how isotopic labelling the exogenous formate can distinguish import of exogenous against excretion and reimport of endogenous formate, 20 mM TMAO and 20 mM formate-d (D-labelled formate) were added to *E. coli* in the final experiment. The main findings are summarized in Fig. 5.25, showing time dependent pH,  $\text{OD}_{600}$  and metabolite measurements, as

monitored by using a set of different spectroscopic analysis techniques. Three distinct phases were apparent over the 15 h of metabolic activity by *E. coli* labelled as **A**, **B1** and **B2** in Fig. 5.25. TMAO respiration occurred between 0 – 9.5 h, in phase **A**. When TMAO was depleted at 9.5 h, the bacteria could only utilise fermentative pathways between 9.5 - 15 h in phase **B**, until all oxidisable carbon sources were depleted and no further signs of metabolic activity were observed. The fermentation phase was divided into **B1** and **B2** at 11 h which was the point at which glucose was depleted triggering the end of exponential growth. The end of exponential growth is apparent in Fig. 5.25 as the OD peaks at 1.7 at 11 h. However, again much more detailed information and insight was obtained by looking at the metabolite concentrations.

As in anaerobic TMAO respiration, the reduction of TMAO in the presence of exogenous formate-d also mirrored the growth curve. All 5 mmol TMAO was reduced to TMA at the end of phase **A**. As in the previous experiments, the production of CO<sub>2</sub>, acetate and ethanol all mirrored the OD<sub>600</sub> rise. The exogenous formate-d was imported and oxidised almost immediately, while unlabelled formate was produced and excreted. Formate oxidized to CO<sub>2</sub> and H<sub>2</sub> by FHL in 1: 1 stoichiometry,<sup>126</sup> as apparent by the 5.0 mmol H<sub>2</sub> formed in phase **A**. This likely suggests mainly NADH was coupling to TMAO reduction. For preventing cytoplasmic acidification, the formate and acetate were excreted by the cells, causing the extracellular pH to decrease from 6.9 to 6.6.

During phase **B1**, formate was reimported and oxidized. In phase **B1**, formate concentrations decreased and glucose was consumed. Additional CO<sub>2</sub> and H<sub>2</sub> were produced. The pH decreased from 6.6 to 6.4 due to acid excretion. The OD<sub>600</sub> peaked at 11 h and reached the maximum value of 1.7 at the end of the experiment. At 12 h, all glucose was depleted and the 4 mmol excreted formate started to decrease. In **B1**, a further 3.0 mmol acetate, 1.0 mmol ethanol, 3.0 mmol CO<sub>2</sub> and mmol 2.8 H<sub>2</sub> were produced. Ammonium concentration declined during exponential growth due to biosynthesis until 11 h. After 11 h it was approximately 3 mmol.

During phase **B2**, no glucose was left. No further rise in OD<sub>600</sub> was observed. Formate production declined in **B2** as no glucose was available. Further CO<sub>2</sub> was produced and reached the maximum value of 12 mmol at the end of phase **B2**. Ethanol production increased to a transient peak of 4 mmol at the beginning of phase **B2** and then stayed constant. The H<sub>2</sub> production reached the maximum value of 12 mmol at the end of the experiment.

As mentioned before in section 5.3.1, formate is produced from the cleavage of pyruvate by PFL. It is converted by FHL to H<sub>2</sub> and CO<sub>2</sub> in the absence of exogenous electron acceptors. According to a previous study by Abaido *et al.* in 1997,<sup>159</sup> growth of *E. coli* on TMAO and formate greatly stimulated the expression of FHL. In their work, however, they did not measure H<sub>2</sub> directly, they only measured enzyme activity. Our spectroscopic monitoring has been applied to measure the metabolites production in the presence of TMAO with formate. Without exogenous formate, it was observed that *E. coli* did not make H<sub>2</sub> anaerobically in the presence of TMAO, and H<sub>2</sub> production was only observed after the depletion of TMAO (see section 5.3.1. Fig. 5.22). This is in contrast to the present experiment where deuterated formate was added and H<sub>2</sub> production was observed from the start. The exogenous formate was consumed and imported immediately during TMAO reduction. This shows that H<sub>2</sub> production is suppressed by TMAO but overcome in the presence of exogenous formate-d, consistent with the finding of Abaibou *et al.*<sup>159</sup>

The 50 mmol C provided by the glucose (45 mmol C) and formate-d (5 mmol C) can be mostly accounted for in the biomass (*ca.* 8 mmol), 12.4 mmol CO<sub>2</sub>, 8.3 mmol acetate (16.6 mmol C) and 3.6 mmol ethanol (7.2 mmol C) produced, totalling 44.2 mmol C. The 2 mmol N in the biomass can be accounted for by the ammonium which dropped from 4.5 mmol to 2.5 mmol.

## 5.4 Conclusions and Future Work

An experimental set-up for continuous monitoring of bacterial respiration is introduced, characterised and applied. It consists of a combination of advanced analytical techniques, headspace FTIR spectroscopy with White cell, liquid phase Raman spectroscopy and CERS. These techniques have been applied to study the metabolic activity of *E. coli* with TMAO as alternative electron acceptors during aerobic and anaerobic respiration and in the presence of exogenous formate. The above-mentioned techniques have proven to be a valuable tool for determining the concentration of multi-component metabolites in real time. The spectroscopic techniques are described in detail, which spectral signatures are most suitable for analysis, and fitting procedures and data analysis for quantitative analysis are discussed.

The partial pressures of CO<sub>2</sub> and ethanol were monitored by FTIR spectroscopy and can be converted to concentration in the solution by using Henry's law. Many major metabolite

products were determined *in situ* utilizing liquid Raman spectroscopy with laser excitation at 532 nm. The concentrations of dissolved species such as TMAO, glucose, formate, acetate and phosphate buffer anions were provided by liquid-phase Raman spectroscopy. In addition, by using a modified Henderson- Hasselbalch equation, a direct spectroscopic determination of the pH was obtained by liquid Raman analysis from phosphate anions concentration. This method can be utilized to determine the pH in systems where traditional electrochemical pH sensors are unworkable or where contamination is an issue in bacterial cultures. One important feature of the liquid-phase Raman set-up is that it is truly non-contact, just light shining and collecting *via* the glass capillary where the bacterial suspension is flowing. This is in contrast to traditional Raman probes that have to be submerged in the solution, which have problems in preserving optical performance and sterile conditions. Further features of this technique are that it can be simply adjusted to accommodate monitoring additional components because the unique spectroscopic signatures offer high selectivity. Vibrational spectroscopy can be used to distinguish between isotopomers, a unique advantage not available to other techniques except MS. In addition, spectroscopic monitoring is a very cost-efficient alternative in comparison with more expensive and elaborate techniques such as GC and MS.

These methods have been applied for studying the respiration of *E. coli* under anaerobic conditions, aerobic conditions and anaerobic conditions with exogenous formate added. Formate-d labelling enables the distinction of the exogenous labelled formate from endogenous formate (formed by catabolism of unlabelled glucose) during anaerobic respiration of *E. coli*. Distinct phases of bacterial growth were monitored and characterised. The production of metabolites such as CO<sub>2</sub>, acetate and ethanol have been discussed. Most notably, in comparing the different conditions, there is a distinct lag phase in aerobic TMAO reduction compared to anaerobic reduction where no lag phase is observed. The lag in aerobic TMAO reduction is consistent with the findings of Ansaldi *et al.* who found when comparing aerobic and anaerobic TMAO reduction, under aerobic conditions the expression of the *tor* operon was very low during early exponential growth.<sup>117</sup> No excretion of formate was found during TMAO aerobic reduction, until TMAO was depleted. Very distinct differences in H<sub>2</sub> production were observed. Under aerobic conditions, no H<sub>2</sub> was produced, because FHL cannot be expressed in the presence of O<sub>2</sub>. Under anaerobic conditions, however, H<sub>2</sub> was produced: without exogenous formate, H<sub>2</sub> is produced only after TMAO depletion, whereas with exogenous formate, H<sub>2</sub> production is observed immediately. Formate-d exogenous formate was consumed and imported immediately during TMAO reduction. This shows that H<sub>2</sub> production was suppressed

by TMAO but overcome in the presence of exogenous formate, consistent with the finding of Abaibou *et al.*<sup>159</sup>

In future work, it is planned to expand the spectroscopic methods to observe various additional, different bacterial anaerobic pathways, specifically for studying the hierarchy and preference of different terminal electron acceptors by *E. coli*, including nitrate, nitrite, DMSO and fumarate and combinations of electron acceptors. The noise equivalent detection limits for TMAO and TMA detection by liquid phase Raman and FTIR were 1.8 mM and 0.2 mM, respectively. These techniques are sensitive enough to detect TMAO in blood plasma, which ranges from 3 to 40 mM so they could be used for medical diagnostics in future work. In conclusion, spectroscopic bioprocess monitoring has been shown to be a promising supplement or replacement for traditional sampling and monitoring methods such as monitoring the OD<sub>600</sub>.

## Chapter 6- Conclusions and Future Work

This thesis has discussed the construction, development and applications of several analytical spectroscopic set-ups. Firstly, a 2.0 m folded pathlength absorption White cell for long-path FTIR spectroscopy was constructed, aligned and characterized using C<sub>2</sub>H<sub>2</sub>. This set-up has served as a helpful tool for exploring many analytical applications. The set-up has the capability of simultaneously measuring different species, including CO<sub>2</sub>, acetaldehyde, ethanol, ethyl acetate, ethylene, ammonia and TMA.

Secondly, a CERS (cavity-enhanced Raman spectroscopy) set-up with an optical feedback cw diode laser was successfully constructed, aligned and characterised using N<sub>2</sub> and O<sub>2</sub> from ambient lab air. CERS can detect homonuclear diatomic gases such as N<sub>2</sub>, O<sub>2</sub> and H<sub>2</sub> which cannot be observed by IR spectroscopy due to selection rules, making it an excellent complementary technique to use alongside long-path FTIR. CERS is less sensitive to water vapour, which is a major benefit for measuring volatiles released from aqueous samples, such as with biological cultures. Unlike IR absorption techniques, CERS can measure all Raman active gas components simultaneously.

FTIR and CERS were used together to study the metabolism of bananas in a closed system during transition from aerobic respiration to anaerobic fermentation when O<sub>2</sub> was depleted. CERS allowed monitoring of O<sub>2</sub> while FTIR provided sensitive detection of many volatiles at low ppm concentrations, including CO<sub>2</sub>, acetaldehyde, ethanol, ethyl acetate and the ripening hormone ethylene. O<sub>2</sub> was observed to be consumed linearly by the bananas, implying zeroth order kinetics; however CO<sub>2</sub> was produced almost exponentially, even after O<sub>2</sub> was depleted. CO<sub>2</sub> was still produced anaerobically due to the metabolic shift from aerobically respiration to fermentation. The ripening hormone ethylene was only produced aerobically due to its production cycle (Yang) requiring O<sub>2</sub>. Ethanol, and its precursor acetaldehyde, are produced at greater rates anaerobically as bananas mainly ferment their cellulose and sugar reserves to ethanol. Ethyl acetate, one of the esters that gives bananas their distinctive aroma, was produced at the same rate both aerobically and anaerobically. Typically banana metabolism is monitored and investigated in a closed system, like what was used in this study, but with sampling for analysis by GC and/or MS. Although GC-MS offers detection of numerous more volatile alcohols and esters, the FTIR and CERS set-up could easily be used alongside conventional sampling techniques as it offers real-time *in situ* analysis, with O<sub>2</sub> data being particularly useful for pinpointing the transition point in the metabolic behaviour.

Chapter 4 has demonstrated how advanced spectroscopic experiments have great potential for monitoring applications in Biotechnology, or for process control in bioreactors. To build upon the insights on banana ripening as presented in chapter 4, a number of directions could be taken. First of all, it would be extremely important to obtain bananas from well defined sources and under well defined growth, harvesting and postharvest treatment conditions. This was not possible by buying from a supermarket, but could be possible in future work by seeking collaborations with banana growers in the relevant banana growing countries. It would be interesting to investigate in more detail the response of banana ripening to external addition of gases like CO<sub>2</sub>, ripening hormones like ethylene and acetylene, and the effect of removing oxygen from the headspace above bananas. It would also be interesting to use green bananas instead of ripening bananas to investigate the difference in both volatile productions.

A second FTIR and CERS set-up was combined with a liquid phase Raman spectroscopy set-up for analysing bacterial cultures. Liquid Raman spectroscopy could quantify TMAO, glucose, acetate, formate and the phosphate buffer (HPO<sub>4</sub><sup>2-</sup> and H<sub>2</sub>PO<sub>4</sub><sup>-</sup>) for studying TMAO reduction to TMA by *E. coli*. The concentrations of the phosphate buffer could be used to calculate the pH *in situ* using a modified Henderson-Hasselbalch equation, this is significant as it provides contactless pH measurements instead of using an invasive pH probe. Studying TMAO respiration is important due to the significant link between TMAO and TMA to cardiovascular diseases. Gut bacteria reduce TMAO to TMA where it is re-oxidised in blood plasma to TMAO; however, renal failure results in higher concentrations of TMAO in plasma up to 40 mM. The constructed FTIR White cell set-up was modified for analysing TMA and NH<sub>3</sub> content after basification of samples of bacterial cultures. This provided a noise equivalent detection limit of 0.2 mM, making it a potential instrument for medical diagnosis.

*E. coli* is a model gut organism and in studying its TMAO respiration metabolism it was found that anaerobically it would only undergo H<sub>2</sub> generation by FHL after TMAO depletion. TMAO is theorized to inhibit FHL expression by making formate unavailable to trigger expression. Our findings support this hypothesis as supplementation by exogenous deuterated formate overcame the inhibition allowing H<sub>2</sub> to be produced immediately. Exogenous deuterated formate could be distinguished from endogenous unlabelled formate in liquid Raman spectra thanks to the favourable isotope shift. Further insights to TMAO respiration were obtained aerobically where it was observed that despite aerobic respiration being more energetically favourable, TMAO respiration still occurs after an initial lag.

To build upon the insights of the work presented in chapter 5, a number of directions could be taken. It would be interesting to utilize other mixed electron acceptors such as DMSO, fumarate and succinate to investigate the different dynamic adaptive processes that *E. coli* uses in order to respond to the other electron acceptors. These alternative electron acceptors have Raman spectra, potentially enabling such studies. However, detection limits for our liquid Raman set-up have yet to be determined. The success of the results obtained with both CERS and long-path FTIR spectroscopy shows that they can be useful tools in medical diagnosis.

In conclusion, a combination of advanced spectroscopic techniques has been shown to have great potential for applied and fundamental studies in the biosciences and in biotechnology, for chemical analysis and to provide mechanistic insight into biochemical pathways.

## References

- 1 R. Yu and F. Javier García De Abajo, *Sci. Adv.*, 2020, **6**, 1–7.
- 2 M. Hippler, *Anal. Chem.*, 2015, **87**, 7803–7809.
- 3 K. Fuwa and V. Bert, *Anal. Chem.*, 1963, **35**, 942–946.
- 4 P. Atkins and D. Paula, *Physical chemistry*, 2006.
- 5 J. L. Jungnickel and J. W. Forbes, *Anal. Chem.*, 1963, **35**, 938–942.
- 6 I. E. Gordon, L. S. Rothman, C. Hill, R. V. Kochanov, Y. Tan, P. F. Bernath, M. Birk, V. Boudon, A. Campargue, K. V. Chance, B. J. Drouin, J. M. Flaud, R. R. Gamache, J. T. Hodges, D. Jacquemart, V. I. Perevalov, A. Perrin, K. P. Shine, M. A. H. Smith, J. Tennyson, G. C. Toon, H. Tran, V. G. Tyuterev, A. Barbe, A. G. Császár, V. M. Devi, T. Furtenbacher, J. J. Harrison, J. M. Hartmann, A. Jolly, T. J. Johnson, T. Karman, I. Kleiner, A. A. Kyuberis, J. Loos, O. M. Lyulin, S. T. Massie, S. N. Mikhailenko, N. Moazzen-Ahmadi, H. S. P. Müller, O. V. Naumenko, A. V. Nikitin, O. L. Polyansky, M. Rey, M. Rotger, S. W. Sharpe, K. Sung, E. Starikova, S. A. Tashkun, J. Vander Auwera, G. Wagner, J. Wilzewski, P. Wcisło, S. Yu and E. J. Zak, *J. Quant. Spectrosc. Radiat. Transf.*, 2017, **203**, 3–69.
- 7 R. M. Amir, F. M. Anjum, M. I. Khan, M. R. Khan, I. Pasha and M. Nadeem, *J. Food Sci. Technol.*, 2013, **50**, 1018–1023.
- 8 R. Kellner and G. Gidály, *Mikrochim. Acta*, 1981, **75**, 119–129.
- 9 W. D. Perkins, *Virginia Mil. Inst.*, 1987, **64**, 95.
- 10 J. U. White, *Opt Soc Am*, 1976, **66**, 411–416.
- 11 J. F. Doussin, R. Dominique and C. Patrick, *Appl. Opt.*, 1999, **38**, 4145–4150.
- 12 D. R. Herriott and H. J. Schulte, *Appl. Opt.*, 1965, **4**, 883–889.
- 13 J. M. Herbelin, J. A. McKay, M. A. Kwok, R. H. Ueunten, D. S. Urevig, D. J. Spencer and D. J. Benard, *Appl. Opt.*, 1980, **19**, 144–147.
- 14 D. Z. Anderson, J. C. Frisch and C. S. Masser, *Appl. Opt.*, 1984, **23**, 1238–1245.
- 15 K. Ferrière, *Astron. Astrophys.*, 2012, **540**, 1–21.
- 16 A. O’Keefe and D. A. G. Deacon, *Rev. Sci. Instrum.*, 1988, **59**, 2544–2551.
- 17 J. J. Scherer, J. B. Paul, C. P. Collier and R. J. Saykally, *J. Chem. Phys.*, 1995, **102**, 5190–5199.
- 18 A. A. Lukashvskaya, O. V. Naumenko, S. Kassi and A. Campargue, *J. Mol. Spectrosc.*, 2017, **338**, 91–96.

- 19 H. Wu, N. Stolarczyk, Q. H. Liu, C. F. Cheng, T. P. Hua, Y. R. Sun and S. M. Hu, *Opt. Express*, 2019, **27**, 37559.
- 20 T. K. Huang, B. J. Chen, K. C. Lin, L. Lin, B. J. Sun and A. H. H. Chang, *J. Phys. Chem. A*, 2017, **121**, 2888–2895.
- 21 J. L. Zhiyan Li, Renzhi Hu, Pinhua Xie, Hao Chen, Shengyang Wu, Fengyang Wang, Yihui Wang, Liuyi Ling and W. Liu, *Opt. Express*, 2018, **26**, 433–449.
- 22 M. Gaj, M. Beyer, P. Koeniger, H. Wanke, J. Hamutoko and T. Himmelsbach, *Hydrol. Earth Syst. Sci.*, 2016, **20**, 715–731.
- 23 E. R. Crosson, *Appl. Phys. B Lasers Opt.*, 2008, **92**, 403–408.
- 24 K. W. T. A. Daniel McCartt, Ted J. Ognibene and Graham Bench, *Anal. Chem.*, 2016, **88**, 8714–8719.
- 25 K. Stamy, O. Vaittinen, J. Jaakola, J. Guss, M. Metsl, G. Johanson and L. Halonen, *Biomarkers*, 2009, **14**, 285–291.
- 26 N. J. van Leeuwen, J. C. Diettrich and A. C. Wilson, *Appl. Opt.*, 2003, **42**, 3670–3677.
- 27 P. Maddaloni, G. Gagliardi, P. Malara and P. De Natale, *J. Opt. Soc. Am. B*, 2006, **23**, 1938–1945.
- 28 K. S. Rao and A. K. Chaudhary, *Appl. Spectrosc.*, 2017, **71**, 1481–1493.
- 29 A. Kachanov, S. Koulikov and F. K. Tittel, *Appl. Phys. B Lasers Opt.*, 2013, **110**, 47–56.
- 30 S. Maithani and M. Pradhan, *J. Chem. Sci.*, 2020, **132**, 1–19.
- 31 K. Zheng, C. Zheng, H. Zhang, J. Li, Z. Liu, Z. Chang, Y. Zhang, Y. Wang and F. K. Tittel, *IEEE Sens. J.*, 2021, **21**, 6830–6838.
- 32 C. V. Raman, *Indian J. Phys.*, 1928, **2**, 387–398.
- 33 M. Moskovits, *J. Raman Spectrosc.*, 2005, **36**, 485–496.
- 34 K. Wu, T. Li, M. S. Schmidt, T. Rindzevicius, A. Boisen and S. Ndoni, *Adv. Funct. Mater.*, 2018, **28**, 1–11.
- 35 S. Hanf, T. Bögözi, R. Keiner, T. Frosch and J. Popp, *Anal. Chem.*, 2015, **87**, 982–988.
- 36 S. Hanf, R. Keiner, D. Yan, J. Popp and T. Frosch, *Anal. Chem.*, 2014, **86**, 5278–5285.
- 37 A. C. Albrecht, *J. Chem. Phys.*, 1961, **34**, 1476–1484.
- 38 R. Salter, J. Chu and M. Hippler, *Analyst*, 2012, **137**, 4621–4868.
- 39 J. Thorstensen, K. H. Haugholt, A. Ferber, K. A. H. Bakke and J. Tschudi, *J. Eur. Opt. Soc.*, 2014, **9**, 14054–6.
- 40 S. ichi Zaitso and T. Imasaka, *Anal. Sci.*, 2014, **30**, 75–79.
- 41 W. J. Ingledeew and R. K. Poole, *Microbiol. Rev.*, 1984, **48**, 222–271.

- 42 V. R. Sutton, E. L. Mettert, H. Beinert and P. J. Kiley, *J. Bacteriol.*, 2004, **186**, 8018–8025.
- 43 E. Bueno, S. Mesa, E. J. Bedmar, D. J. Richardson and M. J. Delgado, *Antioxidants Redox Signal.*, 2012, **16**, 819–852.
- 44 G. Uden, S. Becker, J. Bongaerts, G. Holighaus, J. Schirawski and S. Six, *Arch. Microbiol.*, 1995, **164**, 81–90.
- 45 G. Uden and J. Bongaerts, *Biochim. Biophys. Acta - Bioenerg.*, 1997, **1320**, 217–234.
- 46 H. Cruz-Ramos, J. Crack, G. Wu, M. N. Hughes, C. Scott, A. J. Thomson, J. Green and R. K. Poole, *EMBO J.*, 2002, **21**, 3235–3244.
- 47 G. D. Metcalfe, T. W. Smith and M. Hippler, *Anal. Bioanal. Chem.*, 2020, **412**, 7307–7319.
- 48 S. Iuchi and E. C. C. Lin, *Mol. Microbiol.*, 1993, **9**, 9–15.
- 49 D. Das and A. C. Wilson, *Appl. Phys. B Lasers Opt.*, 2011, **103**, 749–754.
- 50 G. Zhong, Z. Ma, J. Wang, C. Zheng, Y. Zhang and Y. Wang, *Sensors*, 2020, **20**, 1266.
- 51 R. Kong, T. Sun, P. Liu and X. Zhou, *Appl. Opt.*, 2020, **59**, 1545–1552.
- 52 C. Robert, *Appl. Opt.*, 2007, **46**, 5408–5418.
- 53 E. F. Nasir and A. Farooq, *Appl. Phys. B Lasers Opt.*, 2015, **120**, 223–232.
- 54 T. Shimanouchi, *J. Phys. Chem. Ref. Data*, 1977, **6**, 993–1102.
- 55 R. E. Hachtouki and J. Vander Auwera, *J. Mol. Spectrosc.*, 2002, **216**, 355–362.
- 56 F. M. Hoffmann, *Surf. Sci. Rep.*, 1983, **3**, 107–192.
- 57 S. Manohar and D. Razansky, *Adv. Opt. Photonics*, 2016, **8**, 586–617.
- 58 A. Rosencwaig, *Rev. Sci. Instrum.*, 1977, **48**, 1133–1137.
- 59 G. Berden, R. Peeters and G. Meijer, *Rev. Phys. Chem.*, 2000, **19**, 565–607.
- 60 E. S. D. Romanini, A.A. Kachanov, N. Sadeghi, *Chem. Phys. Lett.*, 1997, **264**, 316–322.
- 61 D. E. Canfield, A. N. Glazer and P. G. Falkowski, *Science*, 2010, **330**, 192–196.
- 62 J. Dukarm, Z. Draper and T. Piotrowski, *Energies*, 2020, **13**, 6459.
- 63 T. Theophanides, *Infrared Spectrosc. Mater. Sci. Eng. Technol*, 2012, 2–10.
- 64 Z. Huang, H. Zeng, I. Hamzavi, D. I. McLean and H. Lui, *Opt. Lett.*, 2001, **26**, 1782–1784.
- 65 C. V Raman and K. S. Krishnan, *Nature*, 1928, 121, 501–502.
- 66 S. Hanf, R. Keiner, D. Yan, J. Popp and T. Frosch, *Anal. Chem.*, 2014, **86**, 5278–5285.
- 67 S. Hanf, T. Bögözi, R. Keiner, T. Frosch and J. Popp, *Anal. Chem.*, 2015, **87**, 982–988.
- 68 P. Wang, W. Chen, F. Wan, J. Wang and Jin Hu, *Appl. Spectrosc. Rev.*, 2020, **55**, 393–417.

- 69 J. M. Vaughan, *Handbook of the Fabry-Perot Interf.*, (Boca Rotan), 1970, 1–583.
- 70 R. Lang and K. Kobayashi, *IEEE J. Quantum Electron.*, 1980, **16**, 347–355.
- 71 R. Hui, A. D’Ottavi, A. Mecozzi and P. Spano, *IEEE J. Quantum Electron.*, 1991, **27**, 1688–1695.
- 72 H. Li and N. B. Abraham, *IEEE J. Quantum Electron.*, 1989, **25**, 1782–1793.
- 73 T. W. Smith and M. Hippler, *Anal. Chem.*, 2017, **89**, 2147–2154.
- 74 V. Sandfort, J. Goldschmidt, J. Wöllenstein and S. Palzer, *Sensors*, 2018, **18**, 1–16.
- 75 A. Parra-Coronado, G. Fischer and J. Camacho-Tamayo, *Agron. Colomb.*, 2018, **36**, 68–78.
- 76 D. Valero and M. Serrano, *Postharvest Biol. Technol. Preserv. Fruit Qual.*, 2010, **10**, 1–271.
- 77 A. Theologis, *Cell*, 1992, **70**, 181–184.
- 78 J. M. Lelièvre, L. Tichit, P. Dao, L. Fillion, Y. W. Nam, J. C. Pech and A. Latché, *Plant Mol. Biol.*, 1997, **33**, 847–855.
- 79 J. B. Biale, *Science*, 1964, **146**, 880–888.
- 80 S. D. T. Maduwanthi and R. A. U. J. Marapana, *Int. J. Food Sci*, 2019, **19**, 1–8.
- 81 Y. H. Hui, F. Chen and O. Martín-belloso, *Handbook of Fruit and Vegetable Flavors.*, Y. H. Hui, ed (Canada), 2010.
- 82 D. O. Adams and S. F. Yang, *Proc. Natl. Acad. Sci.*, 1979, **76**, 170–174.
- 83 S. F. Yang and N. E. Hoffman, *Annu. Rev. Plant Physiol.*, 1984, **35**, 155–189.
- 84 T. I. Zarembinski and A. Theologis, *Plant Mol. Biol.*, 1994, **26**, 1579–1597.
- 85 A. Bakshi, J. M. Shemansky, C. Chang and B. M. Binder, *J. Plant Growth Regul.*, 2015, **34**, 809–827.
- 86 J. Hua, H. Sakai, S. Nourizadeh, Q. G. Chen, A. B. Bleecker, J. R. Ecker and E. M. Meyerowitz, *Plant Cell*, 1998, **10**, 1321–1332.
- 87 S. E. Hajjar, R. Massantini, R. Botondi, P. Kefalas and F. Mencarelli, *Postharvest Biol. Technol.*, 2010, **58**, 36–41.
- 88 K. L. C. Wang, H. Li and J. R. Ecker, *Plant Cell*, 2002, **14**, 131–152.
- 89 A. John Wiley and L. Sons, *Handbook of Fruits and Fruit Processing*, N. K. Sinha, J. S. Sidhu, J. B. J. S. B. Wu, M. C. Pilar and M. G. da Silva, ed (UK, Oxford), 2007.
- 90 X. Zhu, Q. Li, J. Li, J. Luo, W. Chen and X. Li, *Molecules*, 2018, **23**, 1–17.
- 91 E. Pesis, *springer-Verlag Berlin Heideelberg*, 1996, **18**, 19–35.
- 92 J. B. Harborne, *Handbook of the Biochemistry of Fruits and their Products*, A. C. Hulme, ed. (London and New York), 1970.

- 93 W. Gou, L. Zhang, F. Chen, Z. Cui, Y. Zhao, P. Zheng, L. Tian, C. Zhang and L. Zhang, *Pakistan J. Bot.*, 2015, **47**, 2257–2262.
- 94 V. Paul, R. Pandey and G. C. Srivastava, *J. Food Sci. Technol.*, 2012, **49**, 1–21.
- 95 M. A. M. El Hadi, F. J. Zhang, F. F. Wu, Chun-Hua Zhou and J. Tao, *Molecules*, 2013, **18**, 8200–8229.
- 96 C. Brady, *Funct. Plant Biol.*, 1976, **3**, 163.
- 97 R. A. Kennedy, M. E. Rumpho, T. C. Fox, R. A. Kennedy, M. E. Rumpho and T. C. Fox, *Am. Soc. Plant Biol.*, 1992, **100**, 1–6.
- 98 M. Larsen and C. B. Watkins, *Postharvest Biol. Technol.*, 1995, **5**, 39–50.
- 99 J. C. Fidler, *J. Exp. Bot.*, 1968, **19**, 41–51.
- 100 H. Nimitkeatkai, Y. Ueda, K. Inamoto and M. Doi, *J. Japanese Soc. Hortic. Sci.*, 2006, **75**, 148–153.
- 101 B. Duffus and A. M. Macfod, *J. Inst. Brew.*, 1976, **82**, 170–174.
- 102 H. Suomalainen, *J. Inst. Brew.*, 1981, **87**, 296–300.
- 103 T. T. Liu and T. S. Yang, *J. Agric. Food Chem.*, 2002, **50**, 653–657.
- 104 J. Song and C. F. Forney, *Can. J. Plant Sci.*, 2008, **88**, 537–550.
- 105 J. Song, B. D. Gardner, J. F. Holland and R. M. Beaudry, *J. Agric. Food Chem.*, 1997, **45**, 1801–1807.
- 106 W. Wojnowski, T. Majchrzak, T. Dymerski, J. Gębicki and J. Namieśnik, *J. AOAC Int.*, 2017, **100**, 1599–1606.
- 107 K. Hiroyuki, L. Heather and P. Janusz, *J. Chromatogr. A*, 2000, **880**, 35–62.
- 108 L. Jiao, D. Dong, P. Han, X. Zhao and X. Du, *Anal. Methods*, 2017, **9**, 2458–2463.
- 109 S. W. Sharpe, T. J. Johnson, R. L. Sams, P. M. Chu, G. C. Rhoderick and P. A. Johnson, *Appl. Spectrosc.*, 2004, **58**, 1452–1461.
- 110 L. T. Bui, G. Novi, L. Lombardi, C. Iannuzzi, J. Rossi, A. Santaniello, A. Mensuali, F. Corbineau, B. Giuntoli, P. Perata, M. Zaffagnini and F. Licausi, *J. Exp. Bot.*, 2019, **70**, 1815–1827.
- 111 S. K. Wendakoon, Y. Imahor and M. Ishimaru, *J. Agric. Food Chem.*, 2004, **52**, 1615–1620.
- 112 S. Lurie and E. Pesis, *Postharvest Biol. Technol.*, 1992, **1**, 317–326.
- 113 H. Zhu, X. P. Li, R. C. Yuan, Y. F. Chen and W. X. Chen, *J. Hortic. Sci. Biotechnol.*, 2010, **85**, 283–288.
- 114 R. P. Gunsalus, *J. Bacteriol.*, 1992, **174**, 7069–7074.
- 115 G. Uden, S. Becker, J. Bongaerts, J. Schirawski and S. Six, *Antonie Van Leeuwenhoek*,

- 1994, **66**, 3–22.
- 116 M. Takagi Sawada and M. Ishimoto, *J. Biochem.*, 1981, **148**, 762–768.
- 117 M. Ansaldi, L. Théraulaz, C. Baraquet, G. Panis and V. Méjean, *Mol. Microbiol.*, 2007, **66**, 484–494.
- 118 J. Qin, R. Li, J. Raes, M. Arumugam, K. S. Burgdorf, C. Manichanh, T. Nielsen, N. Pons, F. Levenez, T. Yamada, D. R. Mende, J. Li, J. Xu, S. Li, D. Li, J. Cao, B. Wang, H. Liang, H. Zheng, Y. Xie, J. Tap, P. Lepage, M. Bertalan, J. M. Batto, T. Hansen, D. Le Paslier, A. Linneberg, H. B. Nielsen, E. Pelletier, P. Renault, T. Sicheritz-Ponten, K. Turner, H. Zhu, C. Yu, S. Li, M. Jian, Y. Zhou, Y. Li, X. Zhang, S. Li, N. Qin, H. Yang, J. Wang, S. Brunak, J. Doré, F. Guarner, K. Kristiansen, O. Pedersen, J. Parkhill, J. Weissenbach, P. Bork, S. D. Ehrlich, J. Wang, M. Antolin, F. Artiguenave, H. Blottiere, N. Borruel, T. Bruls, F. Casellas, C. Chervaux, A. Cultrone, C. Delorme, G. Denariatz, R. Dervyn, M. Forte, C. Friss, M. Van De Guchte, E. Guedon, F. Haimet, A. Jamet, C. Juste, G. Kaci, M. Kleerebezem, J. Knol, M. Kristensen, S. Layec, K. Le Roux, M. Leclerc, E. Maguin, R. Melo Minardi, R. Oozeer, M. Rescigno, N. Sanchez, S. Tims, T. Torrejon, E. Varela, W. De Vos, Y. Winogradsky and E. Zoetendal, *Nature*, 2010, **464**, 59–65.
- 119 B. A. Methé, K. E. Nelson, M. Pop, H. H. Creasy, M. G. Giglio, C. Huttenhower, D. Gevers, J. F. Petrosino, S. Abubucker, J. H. Badger, A. T. Chinwalla, A. M. Earl, M. G. Fitzgerald, R. S. Fulton, K. Hallsworth-Pepin, E. A. Lobos, R. Madupu, V. Magrini, J. C. Martin, M. Mitreva, D. M. Muzny, E. J. Sodergren, J. Versalovic, A. M. Wollam, K. C. Worley, J. R. Wortman, S. K. Young, Q. Zeng, K. M. Aagaard, O. O. Abolude, E. Allen-Vercoe, E. J. Alm, L. Alvarado, G. L. Andersen, S. Anderson, E. Appelbaum, H. M. Arachchi, G. Armitage, C. A. Arze, T. Ayvaz, C. C. Baker, L. Begg, T. Belachew, V. Bhonagiri, M. Bihan, M. J. Blaser, T. Bloom, V. R. Bonazzi, P. Brooks, G. A. Buck, C. J. Buhay, D. A. Busam, J. L. Campbell, S. R. Canon, B. L. Cantarel, P. S. Chain, I. M. A. Chen, L. Chen, S. Chhibba, K. Chu, D. M. Ciulla, J. C. Clemente, S. W. Clifton, S. Conlan, J. Crabtree, M. A. Cutting, N. J. Davidovics, C. C. Davis, T. Z. Desantis, C. Deal, K. D. Delehaunty, F. E. Dewhirst, E. Deych, Y. Ding, D. J. Dooling, S. P. Dugan, W. Michael Dunne, A. Scott Durkin, R. C. Edgar, R. L. Erlich, C. N. Farmer, R. M. Farrell, K. Faust, M. Feldgarden, V. M. Felix, S. Fisher, A. A. Fodor, L. Forney, L. Foster, V. Di Francesco, J. Friedman, D. C. Friedrich, C. C. Fronick, L. L. Fulton, H. Gao, N. Garcia, G. Giannoukos, C. Giblin, M. Y. Giovanni, J. M. Goldberg, J. Goll, A. Gonzalez, A. Griggs, S. Gujja, B. J. Haas, H. A. Hamilton, E. L. Harris, T. A. Hepburn,

- B. Herter, D. E. Hoffmann, M. E. Holder, C. Howarth, K. H. Huang, S. M. Huse, J. Izard, J. K. Jansson, H. Jiang, C. Jordan, V. Joshi, J. A. Katancik, W. A. Keitel, S. T. Kelley, C. Kells, S. Kinder-Haake, N. B. King, R. Knight, D. Knights, H. H. Kong, O. Koren, S. Koren, K. C. Kota, C. L. Kovar, N. C. Kyrpides, P. S. La Rosa, S. L. Lee, K. P. Lemon, N. Lennon, C. M. Lewis, L. Lewis, R. E. Ley, K. Li, K. Liolios, B. Liu, Y. Liu, C. C. Lo, C. A. Lozupone, R. Dwayne Lunsford, T. Madden, A. A. Mahurkar, P. J. Mannon, E. R. Mardis, V. M. Markowitz, K. Mavrommatis, J. M. McCorrison, D. McDonald, J. McEwen, A. L. McGuire, P. McInnes, T. Mehta, K. A. Mihindukulasuriya, J. R. Miller, P. J. Minx, I. Newsham, C. Nusbaum, M. O’Laughlin, J. Orvis, I. Pagani, K. Palaniappan, S. M. Patel, M. Pearson, J. Peterson, M. Podar, C. Pohl, K. S. Pollard, M. E. Priest, L. M. Proctor, X. Qin, J. Raes, J. Ravel, J. G. Reid, M. Rho, R. Rhodes, K. P. Riehle, M. C. Rivera, B. Rodriguez-Mueller, Y. H. Rogers, M. C. Ross, C. Russ, R. K. Sanka, P. Sankar, J. Fah Sathirapongsasuti, J. A. Schloss, P. D. Schloss, T. M. Schmidt, M. Scholz, L. Schriml, A. M. Schubert, N. Segata, J. A. Segre, W. D. Shannon, R. R. Sharp, T. J. Sharpton, N. Shenoy, N. U. Sheth, G. A. Simone, I. Singh, C. S. Smillie, J. D. Sobel, D. D. Sommer, P. Spicer, G. G. Sutton, S. M. Sykes, D. G. Tabbaa, M. Thiagarajan, C. M. Tomlinson, M. Torralba, T. J. Treangen, R. M. Truty, T. A. Vishnivetskaya, J. Walker, L. Wang, Z. Wang, D. V. Ward, W. Warren, M. A. Watson, C. Wellington, K. A. Wetterstrand, J. R. White, K. Wilczek-Boney, Y. Qing Wu, K. M. Wylie, T. Wylie, C. Yandava, L. Ye, Y. Ye, S. Yooseph, B. P. Youmans, L. Zhang, Y. Zhou, Y. Zhu, L. Zoloth, J. D. Zucker, B. W. Birren, R. A. Gibbs, S. K. Highlander, G. M. Weinstock, R. K. Wilson and O. White, *Nature*, 2012, **486**, 215–221.
- 120 V. D’Argenio and F. Salvatore, *Clin. Chim. Acta*, 2015, **451**, 97–102.
- 121 M. A. Bain, R. Faull, G. Fornasini, R. W. Milne and A. M. Evans, *Nephrol. Dial. Transplant.*, 2006, **21**, 1300–1304.
- 122 W. H. Tang, Z. Wang, B. S. Levison, R. A. Koeth, E. B. Britt, X. Fu, Y. Wu and S. L. Hazan, *N. Engl. J. Med.*, 2013, **368**, 1575–1584.
- 123 E. L. Barrett, *Annu. Rev. Microbiol.*, 1985, **39**, 131–149.
- 124 I. Lidbury, J. C. Murrell and Y. Chen, *Proc. Natl. Acad. Sci. U. S. A.*, 2014, **111**, 2710–2715.
- 125 M. T. Velasquez, A. Ramezani, A. Manal and D. S. Raj, *Toxins.*, 2016, **8**, 1–11.
- 126 M. M. Nakano and F. M. Hulett, *FEMS Microbiol. Lett.*, 1997, **157**, 1–7.
- 127 S. Gon, M. T. Giudici-Ortoni, V. Méjean and C. Iobbi-Nivol, *J. Biol. Chem.*, 2001, **276**, 11545–11551.

- 128 V. Méjean, C. Lobbi-Nivol, M. Lepelletier, G. Giordano, M. Chippaux and M. C. Pascal, *Mol. Microbiol.*, 1994, **11**, 1169–1179.
- 129 C. Baraquet, L. Théraulaz, M. Guiral, D. Lafitte, V. Méjean and C. Jourlin-Castelli, *J. Biol. Chem.*, 2006, **281**, 38189–38199.
- 130 G. Simon, V. Mejean, C. Jourlin, M. Chippaux and M. C. Pascal, *J. Bacteriol.*, 1994, **176**, 5601–5606.
- 131 M. Ansaldi, C. Jourlin-Castelli, M. Lepelletier, L. Théraulaz and V. Méjean, *J. Bacteriol.*, 2001, **183**, 2691–2695.
- 132 U. Wissenbach, D. Ternes and G. Unden, *Arch. Microbiol.*, 1992, **158**, 68–73.
- 133 V. Stewart, *Microbiol. Rev.*, 1988, **52**, 190–232.
- 134 R. G. Sawers, *Biochem. Soc. Trans.*, 2005, **33**, 42–46.
- 135 A. Pecher, F. Zinoni, C. Jatisatienr, R. Wirth, H. Hennecke and A. Böck, *Arch. Microbiol.*, 1983, **136**, 131–136.
- 136 R. Rossmann, G. Sawers and A. Böck, *Mol. Microbiol.*, 1991, **5**, 2807–2814.
- 137 N. M. Dixon and D. B. Kell, *J. Microbiol. Methods*, 1989, **10**, 155–176.
- 138 R. Charest and A. Dunn, *Anal. Biochem.*, 1984, **136**, 421–424.
- 139 A. D. Hatton and S. W. Gibb, *Anal. Chem.*, 1999, **71**, 4886–4891.
- 140 J. James and H. Zeisel, *Anal. Biochem.*, 1990, **187**, 234–239.
- 141 F. Özogul, K. D. A. Taylor, P. Quantick and Y. Özogul, *Int. J. Food Sci. Technol.*, 2002, **37**, 515–522.
- 142 M. T. Veciana-Nogues, M. S. Albala-Hurtado, M. Izquierdo-Pulido and M. C. Vidal-Carou, *Food Chem.*, 1996, **57**, 569–573.
- 143 A. Béné, A. Hayman, E. Reynard, J. L. Luisier and J. C. Villettaz, *Sensors Actuators, B Chem.*, 2001, **72**, 204–207.
- 144 H. M. Awwad, J. Geisel and R. Obeid, *J. Chromatogr. B Anal. Technol. Biomed. Life Sci.*, 2016, **1038**, 12–18.
- 145 Z. Wang, B. S. Levison, J. E. Hazen, L. Donahue, X. Li and S. L. Hazen, *Anal. Biochem.*, 2015, **35**, 1–18.
- 146 Y. Wang, M. E. Bollard, H. Keun, H. Antti, O. Beckonert, T. M. Ebbels, J. C. Lindon, E. Holmes, H. Tang and J. K. Nicholson, *Anal. Biochem.*, 2003, **323**, 26–32.
- 147 W. J. Yang, Y. W. Wang, Q. F. Zhou and H. R. Tang, *Sci. China, Ser. B Chem.*, 2008, **51**, 218–225.
- 148 W. J. Dyer, *J. Fish. Res. Board Canada*, 1945, **6**, 351–358.
- 149 C. H. Castell, B. Smith and W. J. Dyer, *J. Fish. Res. Board Canada*, 1974, **31**, 383–389.

- 150 D. Marinov, J. Rey and M. W. Sigrist, *Appl. Opt.*, 2008, **47**, 1956–1962.
- 151 L. Du, J. R. Lane and H. G. Kjaergaard, *J. Chem. Phys.*, 2012, **136**, 184305–8.
- 152 S. Armenta, N. M. M. Coelho, R. Roda, S. Garrigues and M. de la Guardia, *Anal. Chim. Acta*, 2006, **580**, 216–222.
- 153 S. A. Arnold, J. Crowley, N. Woods, L. M. Harvey and B. McNeil, *Biotechnol. Bioeng.*, 2003, **84**, 13–19.
- 154 T. N. K. Zu, S. Liu, E. S. Gerlach, K. L. Germane, M. D. Servinsky, D. M. Mackie and C. J. Sund, *J. Raman Spectrosc.*, 2017, **48**, 1852–1862.
- 155 S. M. Ewanick, W. J. Thompson, B. J. Marquardt and R. Bura, *Biotechnol. Biofuels*, 2013, **28**, 1–8.
- 156 K. V. Hackshaw, J. S. Miller, D. P. Aykas and L. Rodriguez-Saona, *Molecules*, 2020, **25**, 1–23.
- 157 M. I. Santos, E. Gerbino, E. Tymczyszyn and A. Gomez-Zavaglia, *Foods*, 2015, **4**, 283–305.
- 158 M. E. Hefni, M. Bergström, T. Lennqvist, C. Fagerström and C. M. Witthöft, *Anal. Bioanal. Chem.*, 2021, **216**, 1–12.
- 159 H. Abaibou, G. Giordano and M. A. Mandrand-Berthelot, *Microbiology*, 1997, **143**, 2657–2664.
- 160 T. W. Smith, New application of gas phase vibrational spectroscopy in biochemistry and microbiology, PhD thesis, University of Sheffield, 2017.
- 161 T. W. Smith and M. Hippler, *Anal. Chem.*, 2017, **89**, 2147–2154.
- 162 S. Alahmari, X. W. Kang and M. Hippler, *Anal. Bioanal. Chem.*, 2019, **411**, 3777–3787.
- 163 R. Sander, *Atmos. Chem. Phys.*, 2015, **15**, 4399–4981.
- 164 M. Hippler, C. Mohr, K. A. Keen and E. D. McNaghten, *J. Chem. Phys.*, 2010, **133**, 044308–8.
- 165 M. Hippler and G. D. Metcalfe, *Bunsen-Magazin*, 2020, **22**, 102–5.
- 166 A. M. Giovannozzi, F. Pennechi, P. Muller, P. B. Tivola, S. Roncari and A. M. Rossi, *Anal. Bioanal. Chem.*, 2015, **407**, 8423–8431.
- 167 D. K. Veirs and G. M. Rosenblatt, *J. Mol. Spectrosc.*, 1987, **121**, 401–419.
- 168 C. Pinske and F. Sargent, *Microbiology*, 2016, **5**, 721–737.
- 169 J. C. Cox, M. T. Madigan, J. L. Favinger and H. Gest, *Arch. Biochem. Biophys.*, 1980, **204**, 10–17.
- 170 M. Sakaguchi and A. Kawai, *Bull. Japanese Soc. Sci. Fish.*, 1977, **43**, 437–442.
- 171 R. O. N. Grosz and G. Stephanopoulos, *Biotechnol. Bioeng.*, 1983, **25**, 2149–2163.

172 M. Roggiani and M. Goulian, *J. Bacteriol.*, 2015, **197**, 1976–1987.